



HAL
open science

A numerical study of the influence of grain shape on the mechanical behaviour of granular materials : application : load transfer above underground conduits

Krzysztof Szarf

► To cite this version:

Krzysztof Szarf. A numerical study of the influence of grain shape on the mechanical behaviour of granular materials : application : load transfer above underground conduits. Mechanics of materials [physics.class-ph]. Université de Grenoble, 2012. English. NNT : 2012GRENI095 . tel-01195754

HAL Id: tel-01195754

<https://theses.hal.science/tel-01195754>

Submitted on 8 Sep 2015

HAL is a multi-disciplinary open access archive for the deposit and dissemination of scientific research documents, whether they are published or not. The documents may come from teaching and research institutions in France or abroad, or from public or private research centers.

L'archive ouverte pluridisciplinaire **HAL**, est destinée au dépôt et à la diffusion de documents scientifiques de niveau recherche, publiés ou non, émanant des établissements d'enseignement et de recherche français ou étrangers, des laboratoires publics ou privés.

THÈSE

Pour obtenir le grade de

DOCTEUR DE L'UNIVERSITÉ DE GRENOBLE

Spécialité: **Matériaux, Mécanique, Génie Civil, Electrochimie**

Arrêté ministériel: 7 août 2006

Présentée par

KRZYSZTOF SZARF

Thèse dirigée par **Pascal Villard**

et codirigée par **Gaël Combe**

préparée au sein du **Laboratoire 3S-R**

dans l'École Doctorale Ingénierie – Matériaux Mécanique

Environnement Énergétique Procédés Production (I-MEP²)

A Numerical Study of the Influence of Grain Shape on the Mechanical Behaviour of Granular Materials. Application: Load Transfer above Underground Conduits

Thèse soutenue publiquement le **18.12.2012**,
devant le jury composé de:

Fabrice Émeriault

Prof. Grenoble-INP, 3SR – Grenoble, Président

Jean-Noël Roux

Ing. en Chef IFSTTAR, Laboratoire Navier - Champs sur Marne, Rapporteur

Zbigniew Sikora

Prof. dr hab. inż. dr h.c., Politechnika Gdańska – Gdańsk, Rapporteur

Farhang Radjaï

Dr CNRS, LMGC – Montpellier, Examineur

Pascal Villard

Prof. UJF, 3SR – Grenoble, Directeur de thèse

Gaël Combe

MCF UJF, 3SR – Grenoble, Co-Directeur de thèse



Acknowledgments

I would like to thank all those who influenced the final shape of this work, or the fact that it even exists.

My very special thanks go to my supervisors: Prof. Pascal Villard and MCF Gaël Combe, without whose support and assistance I would not be where I am today.

I would like to express my gratitude to Prof. Cino Viggiani and Prof. Christian Geindreau for creating an opportunity for me to come here, and Prof. Zbigniew Sikora back in Gdańsk for pushing me towards actually doing it.

I wish to acknowledge the help provided by my friends and colleagues from 3SR – your support was truly appreciated.

I am also thankful to all the CEGEO participants – the program was a valuable source of useful advice.

Last but not least, to my family and my friends – thank you for always being there for me.

Zwiemy je ziarnkiem piasku.

A ono siebie ani ziarnkiem, ani piasku.

*Obywa się bez nazwy
ogólnej, szczególnej,
przelotnej, trwałej,
mylnej czy właściwej.*

We call it a grain of sand,

but it calls itself neither grain nor sand.

*It does just fine without a name,
whether general, particular,
permanent, passing,
incorrect, or apt.*

Na nic mu nasze spojrzenie, dotknięcie.

Nie czuje się ujrzane i dotknięte.

*A to, że spadło na parapet okna,
to tylko nasza, nie jego przygoda.*

*Dla niego to to samo, co spaść na cokolwiek,
bez pewności, czy spadło już,
czy spada jeszcze.*

Our glance, our touch mean nothing to it.

It doesn't feel itself seen and touched.

*And that it fell on the windowsill
is only our experience, not its.*

*For it, it is no different from falling on anything else
with no assurance that it has finished falling
or that it is falling still.*

(...)

(...)

Wisława Szymborska,
„Widok z ziarnkiem piasku” (fragment)

From: Wisława Szymborska,
“View with a Grain of Sand”
translated by Stanisław Barańczak

Abstract

This study was devoted to the influence of grain shape on the mechanical behaviour of granular materials and its effect on load transfer over underground pipes. Shape of convex polygons and concave clumps of discs was generalised with a geometrical parameter α . In the study a Discrete Element Modeling (DEM) approach was used. Biaxial compression of granular assemblies revealed that mechanical and geometrical properties like porosity, macroscopic friction or shear localisation depends both on α and on grain (non-)convexity.

The intergranular load transfer over a flexible pipe was studied both experimentally (2D rods in a plain strain apparatus) and numerically (DEM). The experiments showed that the pipe has no significant impact on the macroscopic behaviour of the assembly. The numerical model complied with the experiments and revealed that the arching effect in a sheared granular medium exists above the pipe and is magnified with the increase of α of the grains.

Résumé

Cette étude porte sur l'influence de la forme des particules sur le comportement mécanique des matériaux granulaires, et les mécanismes de transfert de charge qui s'y développent, notamment dans les cas des conduits enterrés. La géométrie des particules (polygones de forme convexe ou assemblage de particules de forme concave constitués de plusieurs disques superposés et indissociables) a été caractérisée par un coefficient de forme α . Cette étude est basée sur une approche numérique par éléments discrets. Des simulations numériques de l'essai de compression biaxiale montrent que les caractéristiques macroscopiques ou géométriques de l'échantillon granulaire, tel que l'angle de frottement macroscopique, la compacité, ou la nature des bandes de cisaillement, dépendent fortement du coefficient de forme α et de la convexité ou non convexité des grains.

Les mécanismes de transfert de charge au dessus d'un conduit souple ont été étudiés expérimentalement (rouleaux bidimensionnels en condition de déformation plane) et numériquement (MED). Les expérimentations réalisées montrent que la présence du conduit à peu d'influence sur le comportement macroscopique de l'assemblée granulaire lors d'une sollicitation biaxiale. Les résultats du modèle numérique convergent avec les résultats expérimentaux et mettent en évidence la présence des mécanismes de transfert de charge au dessus du conduit dont les intensités dépendent du coefficient de forme α .

Contents

Abstract	ii
Résumé	ii
Glossary of Symbols	vii
Introduction	1
1 Particle Shape in Granular Materials	3
1.1 Particle Shape Description	3
1.2 Examples of Particle Shape Influence for Sands	4
1.3 Particle Shape Modeling in DEM	8
1.4 Particle Contact Management: Clumps and Polygons	10
1.4.1 Clumps: Grains Made of Discs	10
1.4.2 Polygons: 2D Shadow Overlap Method	11
1.5 Molecular Dynamics Overview	13
1.6 Law of Motion	14
1.6.1 Leapfrog Algorithm	15
1.6.2 Third-Order Gear Predictor–Corrector Algorithm	15
1.7 Contact Laws	16
1.7.1 Normal Contact Law	16
1.7.2 Tangential Contact Law	17
2 Influence of Grain Shape	19
2.1 CEGEO Project	19
2.2 Convex and Concave Grains	28
2.3 Conclusions	33
3 Application: Arching Effect Above Buried Pipes	45
3.1 Theory and Practice	46
3.1.1 Pipe Stiffness	46
3.1.2 Marston-Spangler	47
3.1.2.1 Stiff Pipe in a Ditch	47
3.1.2.2 Pipe in an Embankment	48
3.1.3 Flexible Pipe	50
3.1.3.1 Iowa Formula	50
3.1.3.2 Internal Forces and Pipe Failure	52
3.1.3.2.1 Beam Theory	52
3.1.3.2.2 Marston-Spangler	53
3.1.3.2.3 Ring Compression	54

3.1.4	Pipe Experiments and Modeling	54
3.1.5	Arching Effect	55
3.2	Elastic Pipe Modeling in DEM	56
3.2.1	Parallel Bond Contact Law	56
3.2.2	Numerical Model of Elastic Pipe	57
3.2.3	Analytical Validation of the Numerical Model: Cantilever Beam Loading	59
3.2.3.1	Vertical Loading: Bending	59
3.2.3.2	Axial Loading: Compression and Traction	61
3.2.4	Validation of the Numerical Model with Experimental Results and Analytical Solution of Simple Compression Test on Pipe	62
3.2.4.1	Young's Modulus Estimation	62
3.2.4.2	Point Loading of the Pipe: Simple Compression	64
3.2.4.3	Point Loading of the Pipe: Oedometric Compression	67
3.3	$1\gamma 2\varepsilon$ Experiments	70
3.3.1	Description of the $1\gamma 2\varepsilon$ Apparatus	70
3.3.2	Assessment of Grain Displacement	72
3.3.2.1	Methodology	73
3.3.3	Experimental Program	75
3.3.4	Oedometric Tests Results	77
3.3.4.1	Macroscopic Results	77
3.3.4.2	Kinematic Analysis	78
3.3.5	Biaxial Test Results	78
3.3.5.1	Macromechanical Response	78
3.3.5.2	Kinematic Analysis	79
3.3.5.2.1	Strains	79
3.3.5.2.2	Displacement Fields	84
3.3.5.2.3	Localisation of Shear	89
3.3.6	Conclusions	92
3.4	Modeling of an Elastic Pipe in Granular Material	92
3.4.1	Simulation Protocol and Parameters	92
3.4.2	Numerical Simulations Performed	93
3.4.2.1	Macromechanical Response	93
3.4.2.1.1	Biaxial Compression	93
3.4.2.1.2	Oedometric Compression	96
3.4.2.2	Kinematic Analysis	97
3.4.2.2.1	Strains	97
3.4.2.2.2	Displacement Fields	105
3.4.2.2.3	Localisation of Shear	110
3.4.2.3	Arching Effect Assessment	110
3.4.2.3.1	Stress Comparison	110
3.4.2.3.2	Stress Direction	116
3.5	Conclusions	117

A Shadow Overlap Method	127
A.1 Method Description	127
A.1.1 Predetection	128
A.1.2 Contact Detection	129
A.1.3 Contact Geometrical Position	130
A.2 Block Schemes	132
B Particle Area	136
B.1 Clump Area	136
B.2 Polygon Area	138
C Castigliano Theorem	140
D $1\gamma 2\varepsilon$ Results	143
D.1 Displacement Fields	143
D.2 Mean Displacement Field Subtracted from Displacement Field	149
D.3 Strain Localisation	155
D.4 Volumetric Strains	159
D.5 Horizontal and Vertical Strains	163
D.6 PVC Pipe Unloading after Biax-4-PVC-Pipe Test	165
E DEM Pipe in Soil Simulation Results	166
E.1 Displacement Fields	167
E.2 Mean Displacement Field Subtracted from Displacement Field	171
E.3 Strain Localisation	176
E.4 Stress Direction	184
Bibliography	192

Glossary of Symbols

Negative ε denotes dilation (extension)
 Positive ε denotes contraction (compression)
 Positive rotations are counterclockwise

DEM		Discrete Element Method
MD		Molecular Dynamics
DIC		Digital Image Correlation
$1\gamma 2\epsilon$		Plane Strain Apparatus located in 3SR Laboratory in Grenoble
α	$[-]$	Grain shape parameter
R_1	$[m]$	Radius of a grain circumscribed circle
R_2	$[m]$	Radius of a grain inscribed circle
f_n	$[N]$	Normal contact force
f_t	$[N]$	Tangential contact force
k_n	$[\frac{N}{m^3}]$	Normal contact stiffness
k_t	$[\frac{N}{m}]$	Tangential contact stiffness
h	$[m]$	Particle overlap
ϕ_μ	$[deg]$	Microscopic friction angle
μ	$[-]$	Microscopic friction coefficient
k_n^{pb}	$[\frac{N}{m^3}]$	Parallel bond normal stiffness
k_t^{pb}	$[\frac{N}{m^3}]$	Parallel bond tangential stiffness
\bar{R}^{pb}	$[-]$	Distance between two parallel bonds
κ	$[-]$	Stiffness parameter
I	$[-]$	Inertial Number
ρ^{iso}	$[-]$	Solid fraction in the isotropic state
z^*	$[-]$	Corrected coordination number

GLOSSARY OF SYMBOLS

ε_1	[-]	Vertical strain
ε_V	[-]	Volumetric strain
σ_0	[Pa]	Isotropic stress
σ_1	[Pa]	Vertical stress
σ_3	[Pa]	Horizontal stress
η	[-]	$\eta = \frac{\sigma_1 - \sigma_3}{\sigma_1 + \sigma_3} = \sin\phi$
$\phi_{threshold}$	[deg]	Residual macroscopic friction angle
ϕ_{peak}	[deg]	Maximum macroscopic friction angle
S_t	[-]	Shear localisation indicator
E	[Pa]	Young's modulus
h	[m]	Pipe wall thickness
ϕ_{μ}^{wood}	[deg]	Microscopic friction angle between wooden rods
ϕ_{μ}^{PVC}	[deg]	Microscopic friction angle between PVC rods
μ_{int}	[-]	Microscopic friction coefficient between grains and pipe
NCC	[-]	Normalised Correlation Coefficient

Introduction

Granular materials are ubiquitous in the universe. Many branches of engineering deal with materials consisting of separate particles on a daily basis: civil engineering, mining engineering, environmental engineering, agricultural engineering or pharmacy to name but a few. Granular materials consist of a large number of solids. Some examples of such materials are: sand, gravel, ore, coal, solid waste, rice, PVC pellets, capsules.

Granular materials come in many shapes and sizes, their chemical composition can be very diverse. Due to the energy dissipation occurring whenever discrete particles constituting the material interact with each other, the mechanical behaviour of granular materials differs from the behaviour of solids or liquids. The scientific investigations of this behaviour can be dated back at least to the works of Coulomb nearly 200 years ago (Coulomb, 1821). Currently the granular materials are studied by many communities, especially physicists of condensed matter and solid mechanics researchers.

The behaviour of a dense granular assembly under stress is determined by a number of factors: grain size distribution (Voivret, 2008), grain arrangement (Sazzad and Suzuki, 2010), the loading history (Calvetti et al., 1997), the mechanical properties of each of the grains (Cheng et al., 2005). Other important factor influencing the assembly behaviour is the geometry of the particles composing it (Santamarina and Cho, 2004). In case of soils the shape of the grains is determined by their geological history: conditions during the formation of the minerals, chemical and biological effects, abrasion etc. In case of anthropogenic particles the shape is determined by the production process.

The shape of the grains seems to be a trivial thing, very often it can be quickly determined by an amateur with no tools or training and correctly described with common words like “rounded” or “flat”. Then again, its contribution to the behaviour of granular assembly is difficult to determine. The fact that angular sands have higher values of macroscopic friction angle than rounded sands is clear to any geotechnical engineer. At the same time, the real reason behind that difference and the significance of each particular aspect of shape are yet to be determined.

The basic problem rising before a researcher trying to understand the effect of grain shape in granular materials is how to control the experimental parameters, the particle shape itself. In a physical experiment one can change the grading curve of the assembly, change the type of the material or to use some particles of uniformed shape, for example manufactured spheres. Subtle changes of shape are virtually impossible.

The second problem in experimental shape effect study is how to track the behaviour of the particular grains in order to be able to understand the phenomenon. Although testing various assemblies as a whole provides us with some general concepts of grain shape influence on the mechanical behaviour of granular materials, the microscopic insight seems to be necessary to fully understand that behaviour origins.

Nowadays, the computerisation of science offers ways to seek solutions to these questions. We are able to perform numerical simulations of granular assembly where all the features of

the medium can be modified and the response can be studied in both macro- and microscale. This range of possibilities creates other problems: how to narrow down the scope of a research in order to obtain information about a certain aspect of the problem and how to relate it to reality.

In this work it was decided to study the effects of particle shape on the mechanical behaviour of dense granular assembly in the framework of Discrete Element Method. In order to model an engineering problem: load transfer over an elastic pipe, in this case the load transfer over a buried elastic pipe, it was necessary to apply a granular model more complicated than commonly used assemblies of discs or spheres. These simple shapes cannot imitate the real behaviour of granular soils by themselves because the round particles rotate with little effort under load and it limits the maximal and residual strength of the assembly. Among different techniques used for real soil modeling in discrete element methods one should mention rolling resistance (Gilabert et al., 2007; Plassiard, 2007) and use of complex particle shapes, mainly polygons (polyhedra) (Matuttis et al., 2000; Azéma et al., 2009) or clusters of discs (spheres) (Jensen et al., 1999; Salot et al., 2009). These two complex-shape modeling techniques are not equivalent; The clusters are easy to model while polygonal grains are more complex; Clusters made of reasonably small number of discs per particle are concave, while polygons can easily be both relatively complex and convex. The arising question is what is the influence of the cluster concavity in comparison with polygon convexity on the behaviour of granular media.

This work is divided into two main parts: investigations of the influence of particle shape on the mechanical behaviour of granular materials and application of the model to an engineering problem. The description of particle shape in granular materials is given in the first chapter. Presented there are other researchers' findings in the field of grain shape influence, methods of describing the shape commonly used in geology, as well as the numerical DEM model which was used to perform the study. The specific polygon particle contact strategy used in this model is presented in details in Appendix A.

The second chapter is devoted to numerical simulations of assemblies of granular materials made of grains of different shapes. Two popular tactics to model granular particles in 2D were compared: disc clustering and the use of polygons. The goal was to observe the effects of grain sphericity and convexity on the behaviour of the assembly. Two families of grains, clumps and polygons, were tested in multiple shape variants. The assemblies of grains of one type were studied in the isotropic state and after loading in a vertical compression test with constant lateral pressure.

In the last chapter of this work the experiments and numerical simulations of an unpressurised elastic pipe buried in granular material are presented. This situation is typical for some engineering constructions, such as drain pipes, culverts or tunnels. Such constructions can be designed to interact with the surrounding material to take advantage of the arching effect which transfers the load from the elastic body to the soil envelope. The experiments were performed in a plane strain apparatus using analogue soil, which made it possible to take images during the tests. The Digital Image Correlation technique was applied in order to obtain information about kinematic behaviour of the samples. The same numerical model as presented in the second chapter of this work was used to perform simulations of an elastic pipe in granular material under load. The goal of this part of the study was to observe the stress repartition. Higher resolution, step-by-step results of the experiments and numerical simulations are presented in Appendices D and E.

Chapter 1

Particle Shape in Granular Materials

1.1 Particle Shape Description

Granular materials consist of grains of different size and usually no two grains are identical. The question of size distribution is well known (Wilun, 2009; Muir Wood and Maeda, 2008) and can be answered using coefficients like mean size D_{50} and coefficient of uniformity C_u . The classification of grain shapes is more complex; There are different ways of grain shape classification. One of the methods is to describe the shape of a grain using three parameters: sphericity, roundness and smoothness, (Wadell, 1932; Krumbein and Sloss, 1951; Barrett, 1980). Sphericity describes how close a shape of the grain resembles a sphere. Roundness describes the curvature of the angles of the grain. Smoothness describes how rough the grain surface is.

The measurements of these parameters are based on quantifying the inscribed and circumscribed spheres of a grain, Figure 1.1. In order to assess the grain sphericity one compares the radius of the largest inscribed sphere R_2 with the smallest circumscribed R_1 :

$$Sphericity = \frac{R_2}{R_1}. \quad (1.1)$$

Higher values characterise more spherical grains.

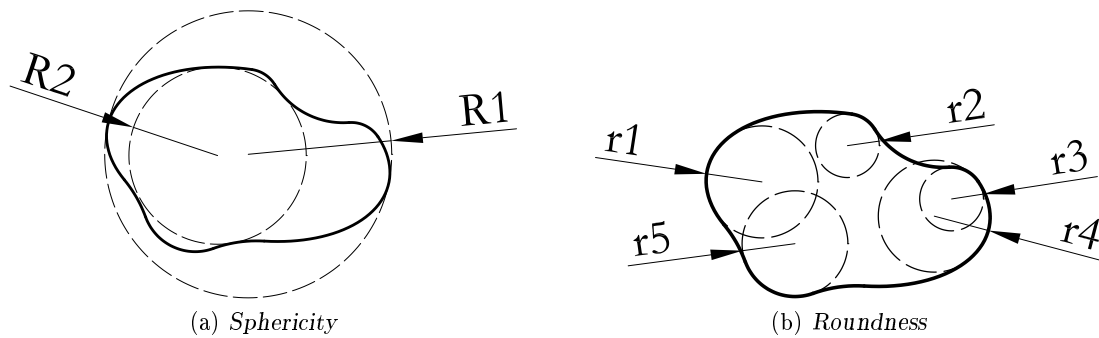


Figure 1.1: Measurements of sphericity and roundness parameters for an exemplary grain. In this case the sphericity is equal to 0.62 while the roundness is equal to 0.51

Grain roundness can be defined as a ratio between the mean curvature of the surface features and the largest inscribed sphere:

$$Roundness = \frac{\sum r_i}{N R_2}, \quad (1.2)$$

where N is the number of angles of the particle and r_i is their curvature radius. Lower values of roundness describe grains with sharp angles. In Figure 1.2 some examples of the real grains shapes are classified with regard to these two parameters.

The measurement itself can be carried out in many ways: by direct measurements of the grains using a microscope or a magnifying glass, by automated digital image analysis or by comparison of the grains against shape templates, for example as in (Krumbein and Sloss, 1951).

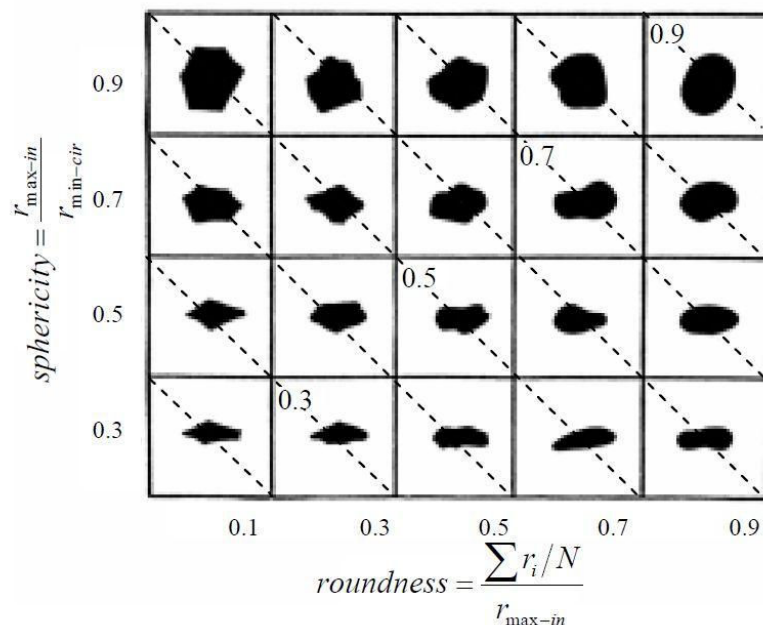


Figure 1.2: Chart presenting some natural grain shapes with different values of sphericity and roundness, originally from (Krumbein and Sloss, 1951), modified by (Cho et al., 2006)

Other ways to describe the particle shape are Fourier analysis and fractal analysis (Orford and Whalley, 1983). These methods were not used in this study and will not be discussed further.

1.2 Examples of Particle Shape Influence for Sands

The form of the geomaterials depends on their geological history. The geological processes by definition occurs on a large area, but the particular combination that lead to creation of some type of soil is unique and characteristic for a much smaller region. Since soil mechanics is studied worldwide, there exist a number of reference materials that has been tested intensively. One of these reference sands is RF Hostun that has been the focus of numerous studies in the 3S-R laboratory in Grenoble for many years: (Desrues, 1984; Doanh et al., 1997; Desrues and Viggiani, 2004). Other well known examples are Ottawa sand or Ticino sand. Compilations of the experimental results on these sands are an invaluable source of information on the topic.

Youd gathered the experimental results on sands (Youd, 1973) to conclude that the maximum and minimum void ratio is affected by the angularity of the particles and the grading curve uniformity, Figure 1.3. In both the dense and loose samples more angular grains formed assemblies with larger number of voids.

In Cho's paper (Cho et al., 2006) there is a compilation of experiments on many types of sands in the context of their shape. They obtained linear dependence of the sample void ratio on the roundness and sphericity of the particles, Fig. 1.4a, and a linear dependence of the critical

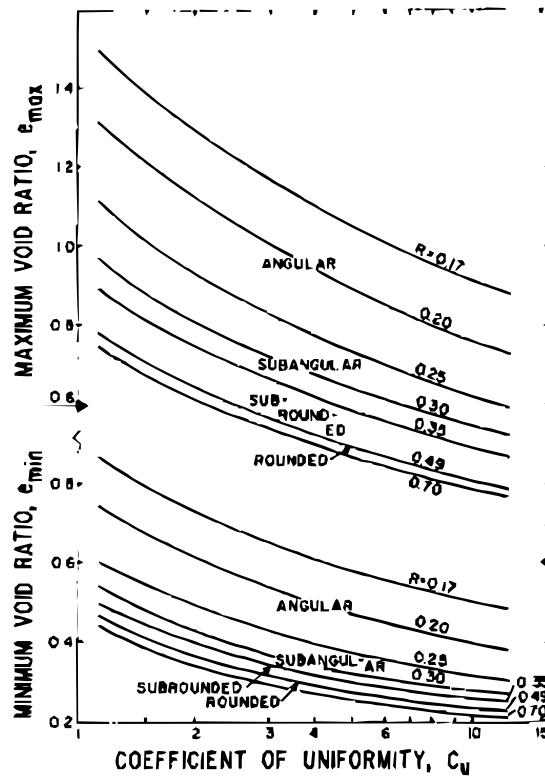
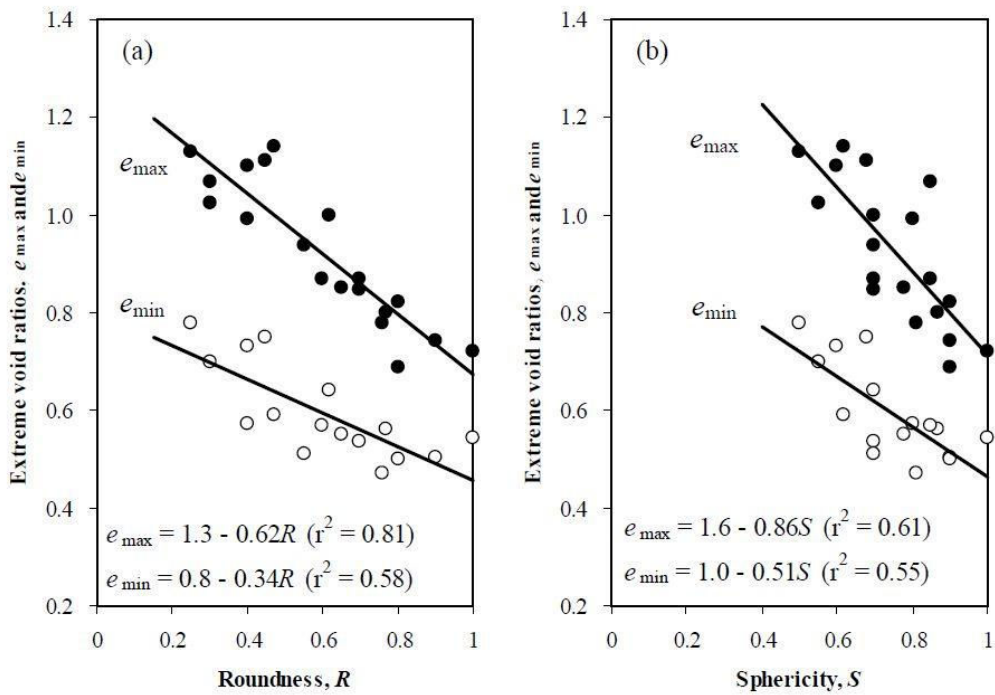
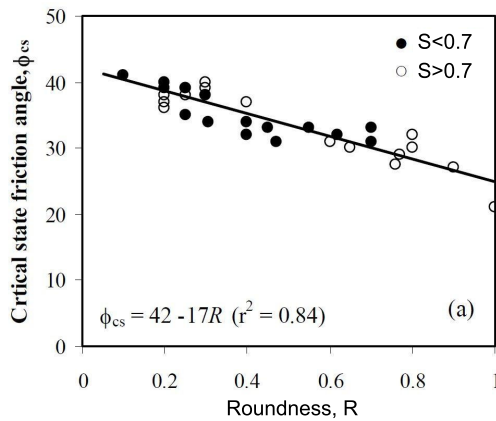


Figure 1.3: Relationship between particle roundness, sample coefficient of uniformity and extreme values of density for various sands, after (Youd, 1973)

friction angle in function of roundness, Fig. 1.4b. Soils with higher roundness or higher sphericity were forming denser assemblies. The residual strength of specimens consisting of grains with more angular shape was higher than those consisting of rounded particles.



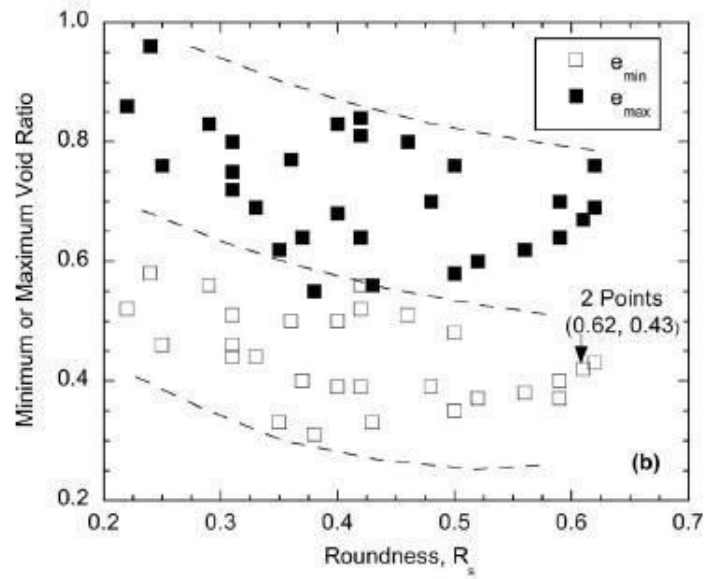
(a) Void ratio



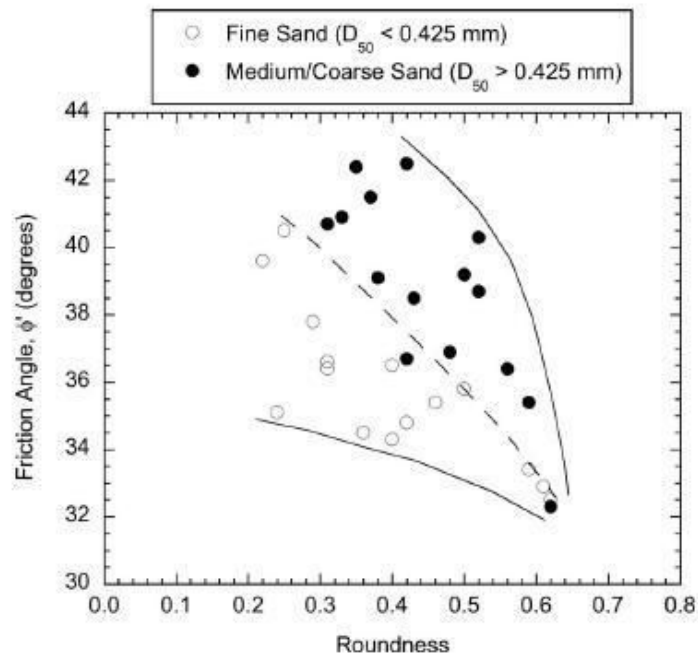
(b) Critical friction angle

Figure 1.4: Relationship between particle roundness and sphericity, and the void ratio and friction angle for various sands, after (Cho et al., 2006)

In Bareither's paper, (Bareither et al., 2008), the authors tested a large number of natural sands from the area of North America and obtained similar results on the relation between particle roundness and void ratio, Figure 1.5a, and a slightly different relation for the friction angle, Fig. 1.5b.



(a) Void ratio



(b) Critical friction angle

Figure 1.5: Relationship between particle roundness and the void ratio and friction angle for various sands, after (Bareither et al., 2008)

These comparisons show influence of the grain shape on the granular materials but the scatter of the data points suggest that there are other parameters influencing the porosity and friction angle of the granular soils.

1.3 Particle Shape Modeling in DEM

Generally speaking, there are two approaches to particle modeling in DEM. The first one is to use simple shapes like discs or spheres. This approach usually incorporates some numerical procedures that are supposed to make the simple granular model more similar to the real behaviour of the material. Sometimes these procedures, although effective, have little physical meaning. The second approach is to use complicated shapes that would resemble real particles more. This approach can be very expensive in terms of computation time.

Contact detection is the most CPU encumbering task in DEM. Contact detection between simple entities like discs or spheres is also simple, so the computational cost of modeling with simple shapes is low. This allows using large numbers of particles or extending the duration of simulation, while keeping the time of computation reasonably short. Some examples of this approach are: (Cundall and Strack, 1979; Radjaï et al., 1996; Åström et al., 2000; Iwashita and Oda, 2000; Krut and Rothenburg, 2004) (use of discs in 2D) and (Suiker and Fleck, 2004; Abe et al., 2006) (use of spheres in 3D). Even so, these approaches are usually too much simplified to model granular materials like sands properly without any additions. Example of such an addition is rolling resistance. It is a contact law that mimics the imbrications of the particles in contact which discs and spheres are lacking (Zhou et al., 2001; Estrada et al., 2011). The idea of reducing circular particle rotation was brought further up to a point of blocking the rotations completely (Calvetti et al., 2003), which is physically discussible but proved to be effective.

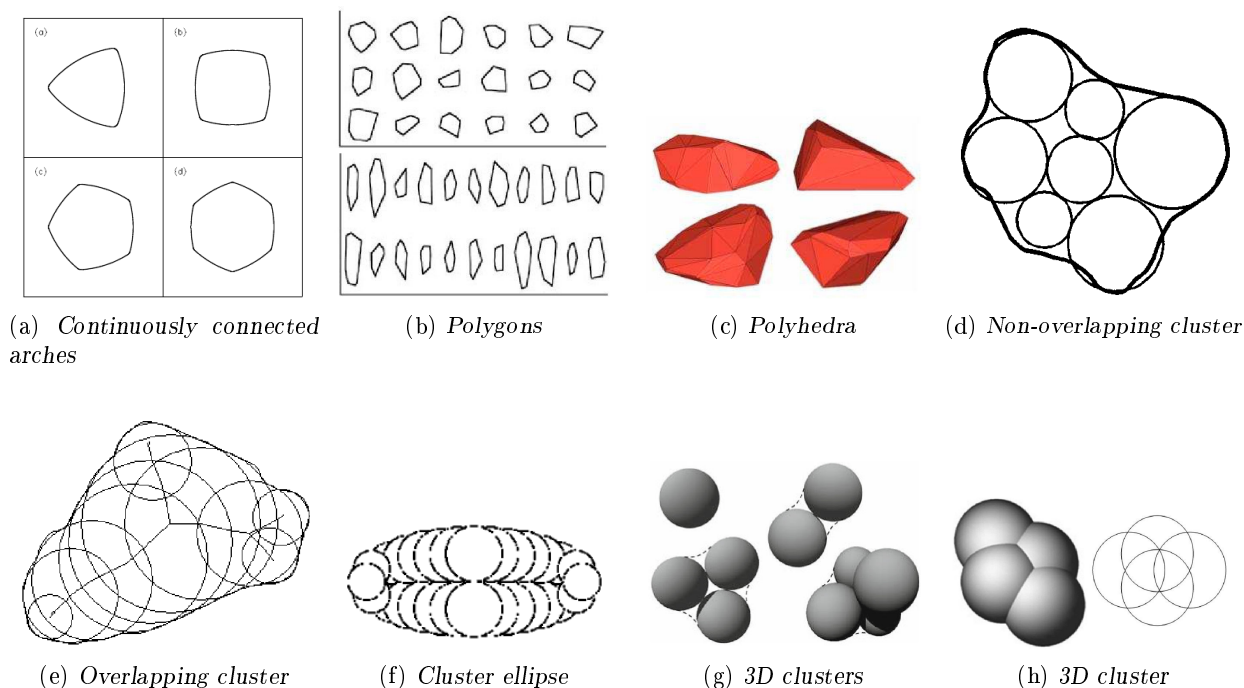
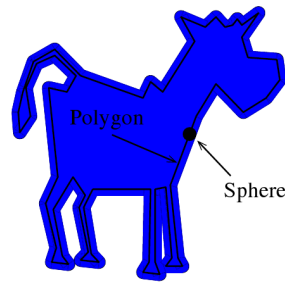


Figure 1.6: *Examples of some particles used in discrete element modeling, images after: (Potapov and Campbell, 1998; Noguier-Lehon et al., 2003; Azéma et al., 2009; Jensen et al., 1999; Das, 2007; Emeriault and Claquin, 2004; Salot et al., 2009; McDowell et al., 2011)*

(i) *Minkowski sum*Figure 1.6: *Examples of some particles used in discrete element modeling, image after: (Alonso-Marroquin, 2008)*

The second concept has been realised in many different ways, see Figure 1.6. One idea is to define complex grains as geometric shapes other than circles or spheres, for example as ellipses (Ting, 1992; Rothenburg and Bathurst, 1992), super-quadrics (Cleary and Sawley, 2002), continuously connected arches (Potapov and Campbell, 1998), superellipsoids (Delaney and Cleary, 2010) or 2D polygons and 3D polyhedra (Matuttis et al., 2000; Nougier-Lehon et al., 2003; Azéma et al., 2009). Contacts between particles like these are generally speaking more complex than contacts between spheres or discs, use more resources and are more difficult to code.

Other idea is to connect multiple simple particles together in order to obtain one complex solid called a cluster or a clump. There exist a number of papers using different clusters of discs trying to approach the actual shape of the real grains as close as possible: Jensen (Jensen et al., 1999) proposed approximating the shape of grains with assemblies of three discs that although touch each other, do not overlap. This idea was extended by Matsushima (Matsushima and Saomoto, 2002; Matsushima et al., 2009) and Ashmawy (Ashmawy et al., 2003; Das, 2007); The extended methods used bigger number of overlapping discs of various sizes to cover all the area (or volume) of a grain. Depending of the complexity of the grain shape the +95% grain coverage was obtained with 10 to 15 discs in 2D or 100 to 300 spheres in 3D. The method of filling an arbitrary shape with multiple simple particles has been used to model ellipses and ellipsoids as well: (Emeriault and Claquin, 2004) (up to 32 discs in one ellipse), (Markauskas and Kačianauskas, 2011) (11 spheres). As one can see, the drawback of these models is the large number of discrete bodies per particle. One must note that the contacts between grains consisting of multiple simple shapes are still simple.

One can also decide to keep the number of simple shapes per particle low and to accept the particle shapes might be far from ones found naturally in soils: (Salot et al., 2009) (clumps of two to four spheres), (McDowell et al., 2011) (clumps of four overlapping spheres on a single plane).

There are also some modeling tactics that link elements from the above-mentioned groups, for example spheropolygons (Alonso-Marroquin, 2008) which are basically polyhedra with spherical corners.

Extreme cases of the two approaches: oversimplification and surplus of details ought to be avoided with the exception of certain well justified circumstances. The optimum solution seems to be placed somewhere in between: a model that is simple on one hand, but which do not neglect some fundamental features of the granular medium and avoids excessive numerical tricks.

In order to build such a “middle ground” model, one must understand what elements of the medium can be simplified and which are critical and need to be present.

1.4 Particle Contact Management: Clumps and Polygons

At each step a granular sample consists of thousands of intergranular contacts. That is the reason why the way a DEM code deals with contacts might be the most important aspect in terms of software performance. In general the problem consists of the following questions:

- a) how to decide whether the contact actually occurred,
- b) where the contact point is located.

1.4.1 Clumps: Grains Made of Discs

The question of circle-circle (sphere-sphere as well) collision/intersection detection and the geometric position of such a contact is simple. If the distance AB between the centres of the two discs is bigger than the sum of the radii, there is no contact. Otherwise, the contact occurs, and the point of contact is placed on the vector connecting the centres, as in the equation below and in Fig. 1.7.

$$\| AB \| \leq r_A + r_B \quad (1.3)$$

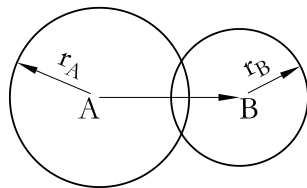


Figure 1.7: Contact between two discs or two spheres can be identified by comparing the distance between the centres of the particles with the sum of the radii

In this study some complex shapes were created by combining three overlapping discs into a single rigid body called *clump*. In this case, contacts between two grains are simply multiple contacts between discs and the contact criterion is the same as (1.3). The difference is that in case of disc particles in contact only tangential force is causing the moment of force on the grain, while in case of clumps it is both normal and tangential forces. The case of disc contact is presented in Figure 1.8a. The moment of force with respect to the grain centre is expressed as:

$$M_{centre}^{disc} = M_T = \mathbf{l}_T \times \mathbf{f}_T. \quad (1.4)$$

The case of clump contact is presented in Figure 1.8b. The moment of force with respect to the grain centre is expressed as:

$$M_{centre}^{clump} = M_N + M_T = \mathbf{l}_N \times \mathbf{f}_N + \mathbf{l}_T \times \mathbf{f}_T. \quad (1.5)$$

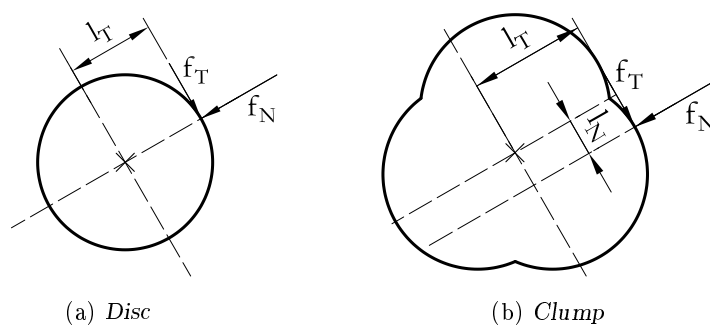


Figure 1.8: Forces acting on the grain are causing moment of force with respect to the mass centre of the particle. In case of disc the axis of normal forces is going through the grain centre, which is usually not the case in clump

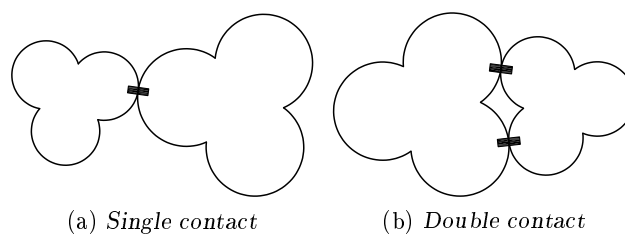


Figure 1.9: Examples of contact between two clumps. The contacts are treated the same way as in case of separate discs

In Figure 1.9 some examples of possible clump contacts are presented. The location of the contact points in case of clump contact is determined the same way as in case of discs.

1.4.2 Polygons: 2D Shadow Overlap Method

Other type of grains used in our simulations were irregular symmetric convex polygons. A contact between two polygons is more complicated than a contact between two discs. Since the problem of polygon contact detection (also called collision detection) is very common in computer science (computer graphics and animation, motion planning, game development), there are many algorithms dealing with it, for example Gilbert-Johnson-Keerthi distance algorithm (Gilbert et al., 1988), various space partitioning algorithms (Ganter and Isarankura, 1993), separating axis theorem (SAT) (Gottschalk et al., 1996).

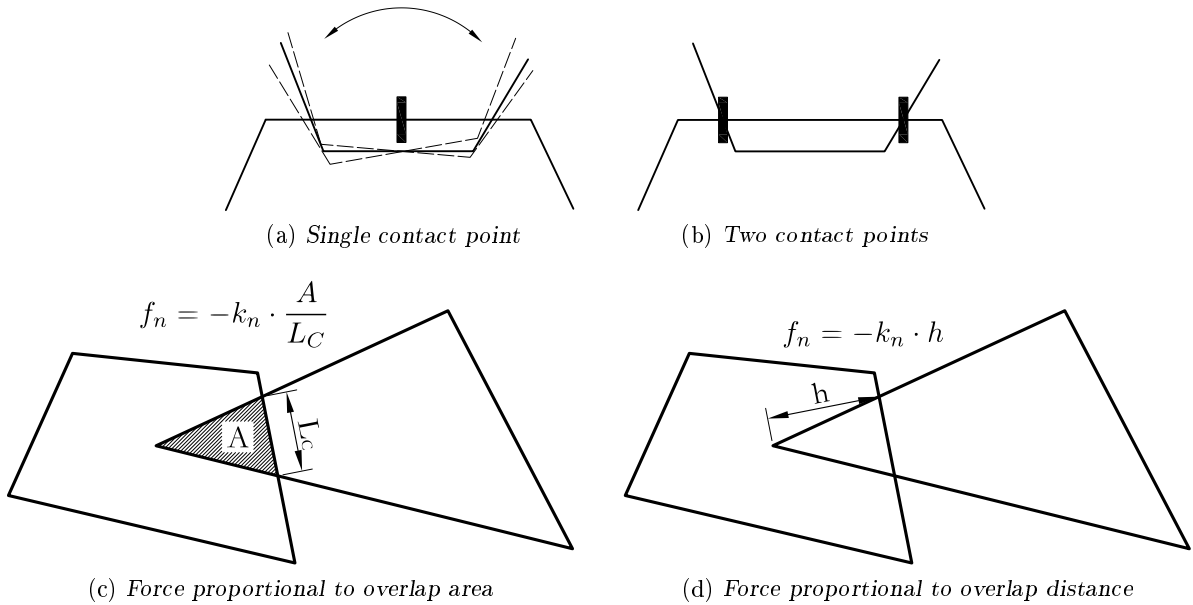


Figure 1.10: Difference between a standard polygon contact treatment (left) and the one introduced in Moreau's Shadow Overlap Method (right). More on contact force computation in Section 1.7

In this study a *Shadow Overlap Method* was used. The method was developed by Jean-Jacques Moreau for the Contact Dynamic code (Saussine et al., 2006) and adapted to Molecular Dynamics code (Charalampidou et al., 2009; Szarf et al., 2011). The contact detection in this method is based on the well-known separating axis theorem¹, but the treatment of the contact point and contact force is innovative.

In DEM a typical way to model a contact between two convex polygons is to introduce a single force (Fig. 1.10a) proportional to overlap area of polygons in contact (Fig. 1.10c) (Matuttis et al., 2000; Alonso-Marroquin et al., 2005).

In Shadow Overlap Method in case of a contact between faces of two polygons *two* contact points are introduced, see Figure 1.10b. This assures fast stabilisation of the contact point in comparison with the methods using a single force where the contact is wobbly (compare Fig. 1.10a and 1.10b). In case of contact between a corner and a face a single force is used as it is typically done in other approaches.

The second difference is that the value of the contact force is proportional to the overlap *distance*, not *area*, see Figure 1.10d.

The algorithm of the Shadow Overlap Method used in this study is presented in details in Appendix A. It can be regarded as three separate tasks performed one after another for each pair of neighbouring particles in order to determine whether the given particles are in contact or not, what is the type of contact (single or double point of contact) and where these points are located.

The contacts between two polygons are presented in Figure 1.11.

¹Any two non-overlapping polytopes (generalization of a polygon in n-dimensions) can always be separated by a plane that is either parallel to a face of one of the polytopes or parallel to an edge of each. (Schneider and Eberly, 2002)

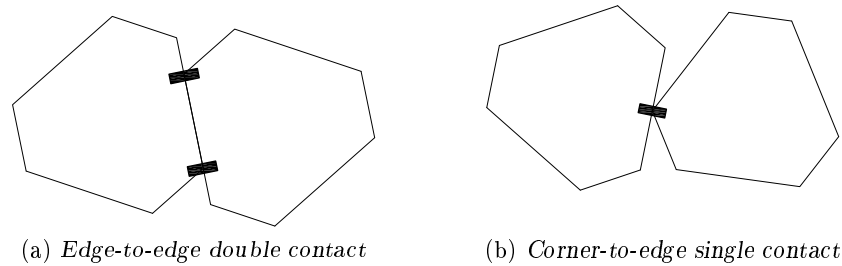


Figure 1.11: *Examples of the contacts between two polygons*

The third type of contact, corner-to-corner, is in fact always represented as either corner-to-edge or edge-to-edge.

1.5 Molecular Dynamics Overview

Discrete Element Method (DEM) is a common name for a group of numerical methods able to simulate the behaviour of a group of interacting particles. It is used in various fields of science and engineering. *Molecular Dynamics* approach to DEM was introduced by Cundall (Cundall, 1971) as a proposition for rock mechanics problem solving, and subsequently developed to cover granular media modelling (Cundall and Strack, 1979).

The principle of DEM is to describe the behaviour of a granular medium under external loading by means of individual particle movements and their interactions. Disturbances such as external loading propagate through a particle assembly causing changes of particle positions, velocities, values of forces interacting at the contact points, and rearrange the contact network. The mathematical description of the medium behaviour is based on motion laws (described in Section 1.6), drawn from Newton's second law of motion and on contact laws (described in Section 1.7). The motion laws are applied to each particle while the contact laws act at the point of contact. Calculations are made in time steps as presented in Figure 1.12. In each step motion laws are solved to obtain new positions and new contacts, which are used as an input to the force-displacement contact laws that result in new contact forces.

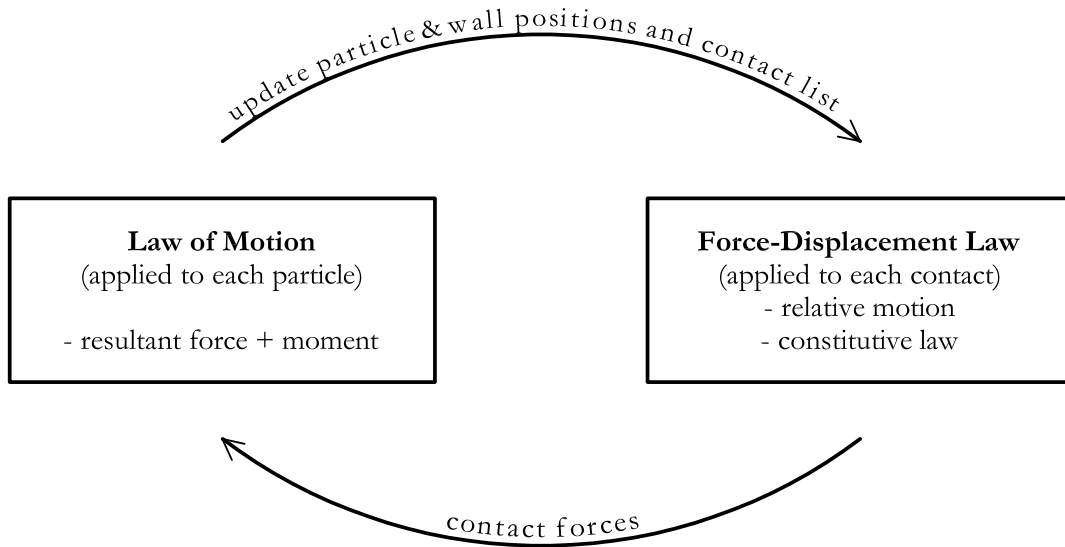


Figure 1.12: Typical time step in DEM (modified after (PFC^{2D} Manual, 2004))

1.6 Law of Motion

The equations (1.6) and (1.7) are drawn from Newton's second law of motion. The method consists of numerically solving these ordinary differential equations over time.

$$M\vec{x}_i = \sum_j \vec{F}_{j \rightarrow i} + \vec{r}, \quad (1.6)$$

$$\underline{\underline{I}}\vec{\theta}_i = \sum_j \vec{\Gamma}_{j \rightarrow i} + \vec{m}_r, \quad (1.7)$$

where:

M	is the mass of the particle i	$[kg]$,
$\underline{\underline{I}}$	is the inertia matrix of the particle i	$[kg \cdot m^2]$,
\vec{x}_i	is the acceleration of the particle i	$[\frac{m}{s^2}]$,
$\vec{\theta}_i$	is the angular acceleration of the particle i	$[\frac{rad}{s^2}]$,
$\vec{F}_{j \rightarrow i}$	is the force acting from j to i	$[N]$,
$\vec{\Gamma}_{j \rightarrow i}$	is the moment of force $\vec{F}_{j \rightarrow i}$ with respect to the mass centre of the particle i	$[N \cdot m]$,
\vec{r}	is the external force (e.g. gravity)	$[N]$,
\vec{m}_r	is the moment of the external force \vec{r} with respect to the mass centre of the particle i	$[N \cdot m]$.

There are many explicit integration schemes applicable to the equations (1.6) and (1.7). In this study two different codes were used, each one using a different integration method. While PFC^{2D}

makes use of Verlet *leapfrog* integration method (PFC^{2D} Manual, 2004; Allen and Tildesley, 1994), the code applied for polygons uses the third-order Gear *predictor-corrector* method (Haile, 1992; Allen and Tildesley, 1994).

1.6.1 Leapfrog Algorithm

Leapfrog algorithm consists of calculating the positions at “full” time steps, $t = k\Delta t$ while the velocities are calculated at “half” time steps: $t = (k + \frac{1}{2})\Delta t$, $k = 0, 1, 2, \dots$. The equation (1.6) is integrated using a centred finite-difference over one time step Δt :

$$\vec{x}_i(t) = \frac{1}{\Delta t} \left(\vec{x}_i(t + \frac{\Delta t}{2}) - \vec{x}_i(t - \frac{\Delta t}{2}) \right). \quad (1.8)$$

The equation (1.6) is then inserted into equation (1.8) in order to obtain velocity at the next half-time step:

$$\vec{x}_i(t + \frac{\Delta t}{2}) = \vec{x}_i(t - \frac{\Delta t}{2}) + \left(\frac{\sum_j \vec{F}_{j \rightarrow i} + \vec{r}}{M} \right) \Delta t. \quad (1.9)$$

Finally, the computed velocities are used to update the positions of the particles:

$$\vec{x}_i(t + \Delta t) = \vec{x}_i(t) + \vec{x}_i(t + \frac{\Delta t}{2}) \Delta t. \quad (1.10)$$

The rotation of the particles is integrated in analogical way using equation (1.7).

1.6.2 Third-Order Gear Predictor–Corrector Algorithm

On the contrary, this integration algorithm allows us to obtain positions and velocities at the same instant. The prediction of the trajectory at time $t + \Delta t$ is obtained from the truncated Taylor series expansion:

$$\vec{x}_i^P(t + \Delta t) = \vec{x}_i(t) + \vec{x}_i(t) \Delta t + \frac{1}{2} \vec{x}_i(t) \Delta t^2, \quad (1.11)$$

$$\vec{x}_i^P(t + \Delta t) = \vec{x}_i(t) + \vec{x}_i(t) \Delta t, \quad (1.12)$$

$$\vec{x}_i^P(t + \Delta t) = \vec{x}_i(t). \quad (1.13)$$

The predicted positions are used as an input to the contact laws in order to obtain the values of force. The new forces are inserted to Newton’s equation, which has to be solved in order to obtain the corrected values of acceleration, velocity and position. It is a second-order equation of the form $\ddot{x} = f(x, \dot{x})$. In case of the third-order Gear method the correction coefficients are $C0 = 0$, $C1 = 1$, $C2 = 1$. The final form of the equations is the following:

$$\vec{x}_i^C(t + \Delta t) = \frac{\sum_j \vec{F}_{j \rightarrow i} + \vec{r}}{M}, \quad (1.14)$$

$$\vec{x}_i^C(t + \Delta t) = \vec{x}_i^P(t + \Delta t) + \frac{1}{2} \Delta t \left(\vec{x}_i^C(t + \Delta t) - \vec{x}_i^P(t + \Delta t) \right), \quad (1.15)$$

$$\vec{x}_i^C(t + \Delta t) = \vec{x}_i^P(t + \Delta t). \quad (1.16)$$

As one can see, the equations (1.16) equal to (1.11) and (1.15) are equivalent to the so-called velocity form of the Verlet’s algorithm, (Allen and Tildesley, 1994).

1.7 Contact Laws

In this study, the intergranular forces were computed using classical contact laws for DEM. At each contact point normal and tangential contact laws were applied to determine the contact forces basing on the relative position of the contacting particles. Apart from the two standard laws a third one, so called *parallel bond* contact law, was introduced in the second part of the study to model an elastic body (see Section 3.2.1).

1.7.1 Normal Contact Law

The value of the normal contact force is proportional to the overlap between the two particles in contact. The overlap distance is defined as:

$$h = d_{ij} - r_i - r_j \quad (1.17)$$

where:

$$\begin{aligned} d_{ij} & \text{ is the distance between the centres of the particles } i \text{ and } j \text{ in contact} & [m], \\ r_k & \text{ is the radius of a given particle} & [m]. \end{aligned}$$

The force equation can be expressed as

$$f_n = -hk_n \quad (1.18)$$

where:

$$\begin{aligned} f_n & \text{ is the resulting normal force} & [N], \\ k_n & \text{ is the normal spring stiffness} & \left[\frac{N}{m}\right], \end{aligned}$$

so that if $h < 0$ then $f_n > 0$, otherwise $f_n = 0$.

The normal contact force f_n can be damped with a viscous dashpot in order to dissipate energy. The normal forces are computed with a law described by a Kelvin-Voigt rheological model (see Fig. 1.13).

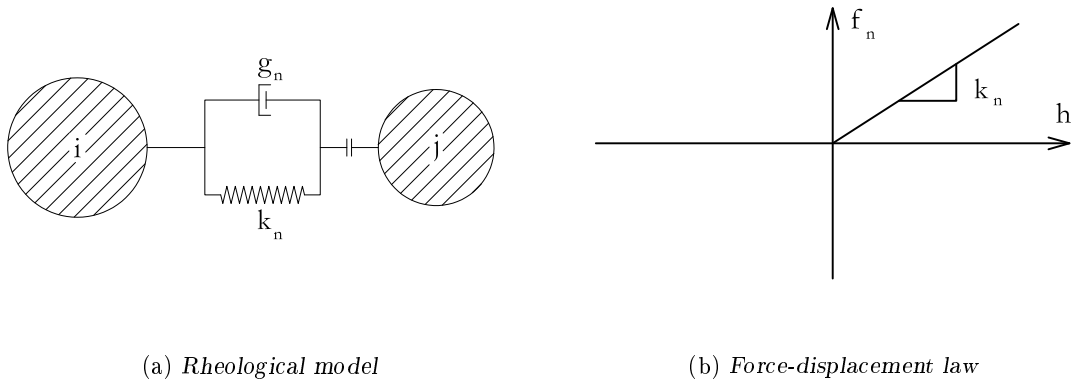


Figure 1.13: Normal contact force

In that case, the force value is computed according to the following equation:

$$f_n = -hk_n + v_n g_n \quad (1.19)$$

where:

$$\begin{aligned} v_n & \text{ is the relative normal velocity of the particles in contact} & \left[\frac{m}{s}\right], \\ g_n & \text{ is the dashpot damping constant} & \left[\frac{kg}{s}\right]. \end{aligned}$$

Value of g_n is given by $g_n = \beta_n 2\sqrt{mk_n}$. Where β_n is the value of the critical damping ratio. The

normal force is pushing two overlapping particles away from each other. The damping introduced in equation (1.19) is supposed to help reaching the equilibrium state faster in such way, that its sign is opposing the change of overlap. Unfortunately it can cause problems by introducing artificial pulling forces (Radjaï and Dubois, 2011). The solution implemented in PFC^{2D} is local damping similar to the one proposed by Cundall (Cundall and Strack, 1979). In this case, the damping is applied to each particle, not to each contact. Additional term is introduced to the Newton's equation and it assumes the form of:

$$M\ddot{x}_i = F_i + r + F_d. \quad (1.20)$$

The damping force F_d depends on the velocity of the particle:

$$F_d = -\alpha |F_i| \operatorname{sgn}(\dot{x}_i), \quad (1.21)$$

where α is the damping constant and sgn function gives only the sign (+ or -) of a scalar.

This damping is working very effectively but is acceptable only for quasi-static situations. In other cases some mass forces appear that lead to non-physical behaviour.

1.7.2 Tangential Contact Law

Tangential forces are computed according to an elastic-perfectly plastic law. Between two time steps t_1 and t_2 there is a relative tangential displacement change δU_t resulting in an increment of tangential force δf_t :

$$\delta f_t = k_t \delta U_t = k_t v_t^{ij} dt \quad (1.22)$$

where:

- v_t^{ij} is the relative tangential velocity of the particles in contact,
- δf_t is the increment of the resulting tangential force.

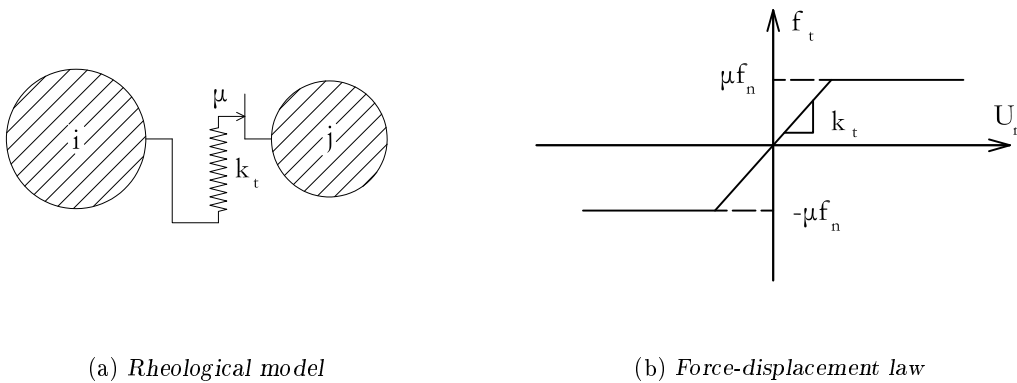


Figure 1.14: Tangent contact force

The sum of the increments over increasing time steps equals:

$$f_t = \sum \delta f_t \quad (1.23)$$

but as the tangential forces obey Coulomb friction:

$$|f_t| > \mu f_n \rightarrow f_t = \text{sgn}(f_t) \cdot \mu f_n \quad (1.24)$$

where μ is the intergranular friction coefficient.

Chapter 2

Influence of Grain Shape

The work presented in this chapter was focused on the study of grain shape influence on the mechanical behaviour of particle assemblies by means of Discrete Element Method. This work was reported during two conferences (STPMF 2009 (Szarf et al., 2009a) and Powders and Grains 2009 (Szarf et al., 2009b)) and two papers in international journals (Szarf et al., 2011; CEGEO et al., 2012). Therefore an unusual format was adopted for this chapter: after a short introduction and presentation of the studies, the two papers are reproduced *in extenso*. To end the chapter, new specific results on the effect of grain shape on the micromechanical behaviour are presented.

2.1 CEGEO Project

The work presented hereafter was part of an interlaboratory research program CEGEO¹ organised in cooperation between French laboratories LMGC², 3SR³ and LTDS⁴ from 2007 to 2010. The name of the program stands for “Changement d’Echelle dans les GEO-matériaux” (Change of Scale in Geomaterials). Among other topics in the research program (micromechanical aspects of granular media failures, kinematical localisation in granular media, boundary condition effect on the mechanical properties of granular materials, capillarity in non-saturated granular media), the collaboration focused on studying the particle shape influence in granular media. The project assumed using various DEM codes with some common framework concerning shape definition, granulometry, testing protocol. It was decided to model one group of shapes, the clumps of three discs, twice using independent Molecular Dynamics and Contact Dynamics codes.

As explained in the introduction of this thesis, Section 1.1, different geometric parameters can be used to describe a grain shape. In the collaborative research program CEGEO, it was decided to use a simple shape parameter equivalent with sphericity, equation (1.1):

$$\alpha = 1 - \frac{R_2}{R_1}, \quad (2.1)$$

where the radii R_1 and R_2 are respectively defined as radii of a smallest circumscribed circle and a largest inscribed circle (see Fig. 2.1).

¹<http://www.granuloscience.com/CEGEO/>

²Laboratoire de Mécanique et Génie Civil (Laboratory of Mechanics and Civil Engineering), Montpellier, France

³Laboratoire Sols, Solides, Structures – Risques (Soils, Solids, Structures – Risk Laboratory), Grenoble, France

⁴Laboratoire de Tribologie et Dynamique des Systèmes (Tribology and System Dynamics Laboratory), Lyon, France

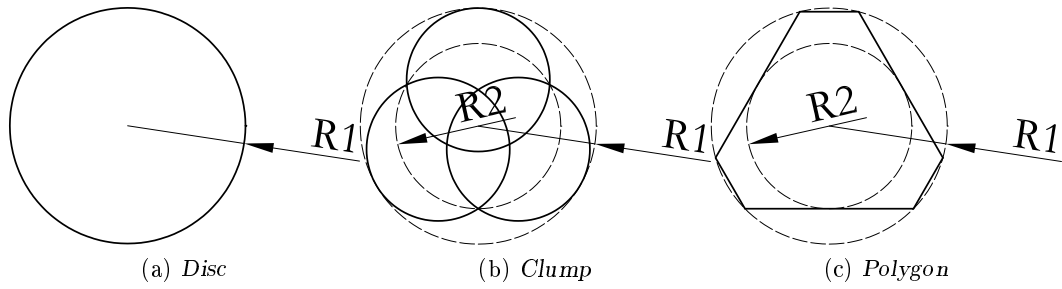


Figure 2.1: Definition of the shape parameter α . Particles (b) and (c) based on the same circles have the same $\alpha = 0.30$ but different shape

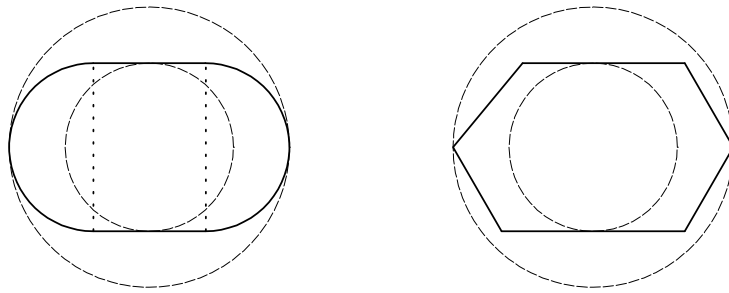


Figure 2.2: Other particle shapes used in CEGEO research program: clump made of two discs connected with a rectangle (left) and elongated polygon (right). The shape parameter α of these particles is equal to 0.40

The shape types presented in Figure 2.1: clumps of three discs and irregular polygons with three axes of symmetry are presented in this thesis. The CEGEO program used two other grain shapes as well: convex clumps consisting of two discs connected with a rectangle of the same size and elongated convex irregular polygons, Fig. 2.2.

Two numerical approaches were used to simulate granular samples consisting of these shapes, Fig. 2.3. The research teams of Montpellier and Lyon used the *Contact Dynamics* approach (Jean and Moreau, 1992) to model clumps of three discs, elongated clumps and elongated polygons. The research team of 3SR used a *Molecular Dynamics*-like approach to model clumps of three discs and polygons with three axes of symmetry.

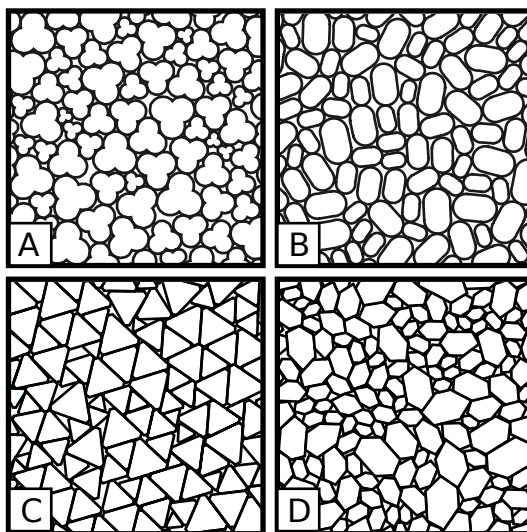


Figure 2.3: Fragments of the samples used in the CEGEO shape influence study (CEGEO et al., 2012)

Some common ground rules were set: same grading of the samples, same boundary conditions⁵, same interparticular friction coefficient, same sample preparation method⁶, similar inertial number⁷ for the mechanical tests etc. Thanks to that, in spite of using different approaches and multiple numerical codes, it was possible to show similarities between the samples made of very different grain shapes but characterised with the same sphericity parameter. The samples submitted to biaxial loading⁸ showed the linear evolution of the residual macroscopic angle of friction $\phi_{threshold}$ with α .

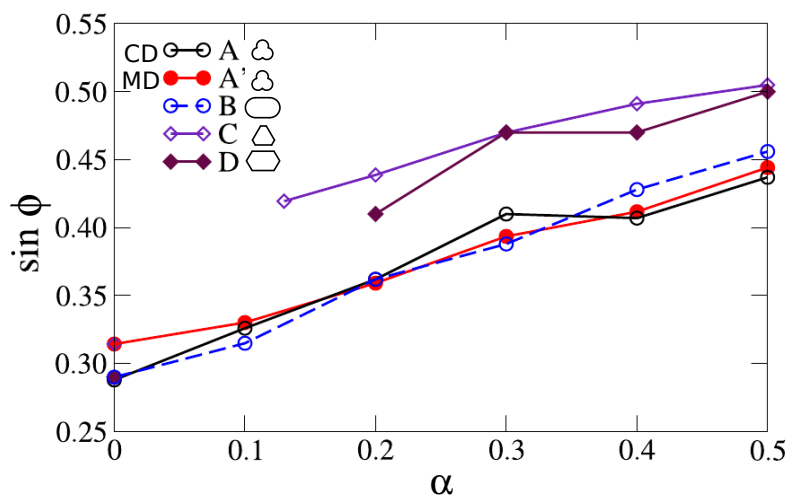


Figure 2.4: Macroscopic friction angle at the threshold of samples consisting of 5000 particles subjected to biaxial compression (CEGEO et al., 2012)

⁵Rigid walls

⁶Isotropic compression with no intergranular friction

⁷Dimensionless relation between the forces of inertia and the forces applied (Roux and Chevoir, 2005)

⁸Vertical compression with constant vertical strain rate and constant horizontal stress. In such conditions the sample is free to contract or to dilate, depending on the initial porosity and/or coordination number

The Figure 2.4 presents the evolution of $\phi_{threshold}$ depending on the grain shape and on α . Each sample shows the same linear dependence of macroscopic friction angle at the critical state with the sphericity coefficient α , but with higher values for angular shapes (polygons denoted C and D). These results highlights that even if α is a low-order shape parameter, it is enough to grasp the hierarchy of shapes.

Another interesting point in the collaborative research work was the comparison of the influence of α on different internal parameters like the mean coordination number or the packing fraction. These two parameters analysed in frictionless particle assemblies submitted to isotropic loading revealed some nontrivial evolution. A simple analytical model of the packing fraction at the isotropic state $\rho^{iso} = f(\alpha)$ was successfully proposed. The model was based on the geometrical description of grain self-porosity (which depends on α) and the voids between grains. Moreover, the results of that collaborative work showed that for three-disc clump shapes the results of Contact Dynamics and Molecular Dynamics approaches are the same, qualitatively for ϕ^* (Fig. 2.4) and quantitatively for ρ^{iso} (Fig. 2.5).

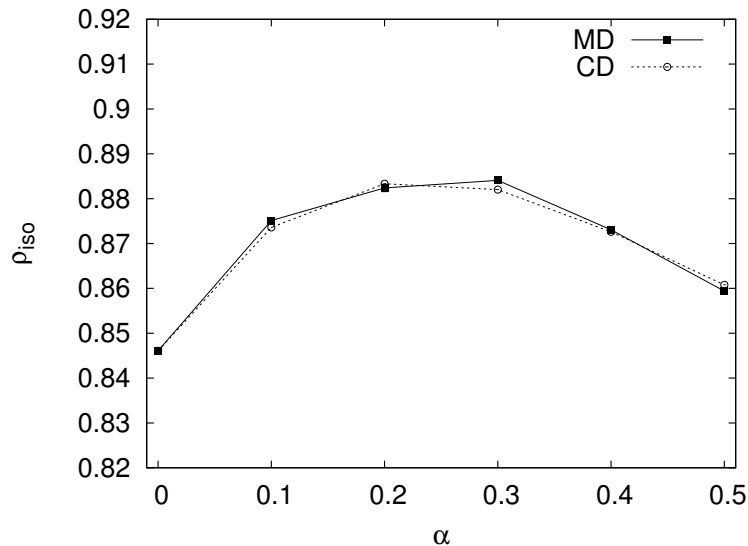


Figure 2.5: *Evolution of solid fraction in the isotropic state with changing sphericity of clump grains. Comparison of numerical assemblies created in Contact Dynamics and Molecular Dynamics methods*

The paper describing the study (CEGEO et al., 2012) is available hereafter, with an exception that α was denoted there as η .

Particle shape dependence in 2D granular media

CEGEO^(a), B. SAINT-CYR^{1,4}, K. SZARF², C. VOIVRET⁵, E. AZÉMA¹, V. RICHEFEU², J.-Y. DELENNE⁶, G. COMBE², C. NOUGUIER-LEHON³, P. VILLARD², P. SORNAY⁴, M. CHAZE³ and F. RADJAI¹

¹ *University Montpellier 2, CNRS, LMGC UMR 5508 - Place Eugène Bataillon, F-34095 Montpellier cedex, France, EU*

² *UJF-Grenoble 1, Grenoble-INP, CNRS UMR 5521, 3SR Lab. - B.P. 53, F-38041 Grenoble cedex 09, France, EU*

³ *University of Lyon, Ecole Centrale de Lyon, LTDS UMR CNRS 5513 - 36 avenue Guy de Colongue, F-69134 Ecully cedex, France, EU*

⁴ *CEA, DEN, SPUA, LCU - F-13108 Saint Paul Lez Durance, France, EU*

⁵ *SNCF Innovation and Research Immeuble Lumière - 40 Avenue des Terroirs de France, F-75611 Paris cedex 12, France, EU*

⁶ *IATE, UMR 1208 INRA-CIRAD-Montpellier Supagro-UM2 - 2 place Pierre Viala, F-34060 Montpellier cedex 01, France, EU*

received 10 February 2012; accepted in final form 25 April 2012
published online 30 May 2012

PACS 45.70.-n – Granular systems

PACS 81.05.Rm – Porous materials; granular materials

PACS 61.43.Hv – Fractals; macroscopic aggregates (including diffusion-limited aggregates)

Abstract – Particle shape is a key to the space-filling and strength properties of granular matter. We consider a shape parameter η describing the degree of distortion from a perfectly spherical shape. Encompassing most specific shape characteristics such as elongation, angularity and non-convexity, η is a low-order but generic parameter that we used in a numerical benchmark test for a systematic investigation of shape dependence in sheared granular packings composed of particles of different shapes. We find that the shear strength is an increasing function of η with nearly the same trend for all shapes, the differences appearing thus to be of second order compared to η . We also observe a non-trivial behavior of packing fraction which, for all our simulated shapes, increases with η from the random close packing fraction for disks, reaches a peak considerably higher than that for disks, and subsequently declines as η is further increased. These findings suggest that a low-order description of particle shape accounts for the principal trends of packing fraction and shear strength. Hence, the effect of second-order shape parameters may be investigated by considering different shapes at the same level of η .

Copyright © EPLA, 2012

The hard-sphere packing is at the heart of various models for the rheology and (thermo)dynamical properties of amorphous states of matter including liquids, glasses and granular materials [1,2]. Such models reflect both the purely geometrical properties of sphere packings, *e.g.* the order-disorder transition with finite volume change [3], and emergent properties arising from collective particle interactions, *e.g.* force chains and arching in static piles [4]. As to non-spherical particle packings, rather recent results suggest that such packings exhibit higher shear strength than sphere packings [5–15], and may approach unusually high packing fractions [2,16–18]. However, a systematic

and quantitative investigation of shape dependence is still largely elusive since particle shape characteristics such as elongation, angularity, slenderness and non-convexity are described by distinct groups of parameters, and the effect of each parameter is not easy to isolate experimentally.

In order to evaluate the shape dependence of general granular properties such as packing fraction, shear strength and internal structure for particles of different shapes, we designed a numerical benchmark test that was simulated and analyzed by the members of a collaborative group (CEGEO). The idea of this test is that various non-spherical or non-circular shapes can be characterized by their degree of distortion from a perfectly spherical or circular shape. Let us consider an arbitrary 2D shape as sketched in fig. 1. The border of the particle is fully

^(a) Collaborative group “Changement d’Echelle dans les Géomatériaux” (scale change in geomaterials).

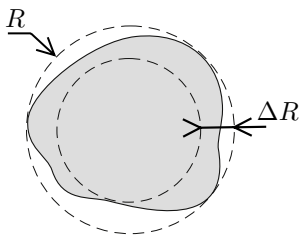


Fig. 1: An arbitrary particle shape represented by a concentric pair of circumscribing and inscribed circles.



Fig. 2: Four different shapes belonging to the same η -set with $\eta = 0.4$: trimer (A), rounded-cap rectangle (B), truncated triangle (C), and elongated hexagon (D).

enclosed between two concentric circles: a circumscribing circle of radius R and an inscribed circle of radius $R - \Delta R$. We define the η -set as the set of all shapes with borders enclosed between a pair of concentric circles (spheres in 3D), touching both circles and having the same ratio

$$\eta = \frac{\Delta R}{R}. \quad (1)$$

Four different particle shapes belonging to the same η -set are shown in fig. 2. A non-zero value of η corresponds to non-convexity for A-shape, elongation for B-shape, angularity for C-shape, and a combination of angularity and elongation for D-shape.

The parameter η is obviously a rough low-order shape parameter; see also [19]. But, encompassing most specific shape parameters, it provides a general framework in which shape dependence may be analyzed among particles of very different shapes. Within an η -set, each specific shape may further be characterized by higher-order parameters. The issue that we address in this letter is to what extent the packing fraction and shear strength are controlled by η and in which respects the behavior depends on higher-order shape parameters.

The benchmark test is based on the four shapes of fig. 2. The A-shape (trimer) is composed of three overlapping disks touching the circumscribing circle and with their intersection points lying on the inscribed circle; the B-shape (rounded-cap rectangle) is a rectangle touching the inscribed circle and juxtaposed with two half-disks touching the circumscribing circle; the C-shape (truncated triangle) is a hexagon with three sides constrained to touch the inscribed circle and all corners on the circumscribing circle; and the D-shape (elongated hexagon) is an irregular hexagon with two sides constrained to touch the inscribed circle and two corners lie on the circumscribing circle. The range of geometrically defined values of η for a given

shape (defined by a construction method) has in general a lower bound η_0 . For A and B, the particle shape changes continuously from a disk, so that $\eta_0 = 0$ whereas we have $\eta_0 = 1 - \sqrt{3}/2 \simeq 0.13$ for C and D.

Two different discrete element methods (DEM) were used for the simulations: contact dynamics (CD) and molecular dynamics (MD). In the CD method, the particles are treated as perfectly rigid [20] whereas a linear spring-dashpot model was used in MD simulations with stiff particles ($k_n/p_0 > 10^3$, where k_n is the normal stiffness and p_0 refers to the confining pressure) [21]. The trimers were simulated by both methods for all values of η . We refer below as A (for CD) and A' (for MD) to these simulations. The packing C was simulated by MD whereas the packings B and D were simulated by CD. In CD simulations, the coefficient of restitution was set to zero. In MD simulations, the damping parameter was taken very close to the critical damping coefficient so that the restitution coefficient was also negligibly small [22]. Note that in quasi-static flow, the relaxation time of the particles is short enough (compared to the inverse shear rate) to allow for efficient dissipation of kinetic energy in each time step. For this reason, in contrast to granular gases, the exact values of the damping parameters or restitution coefficients have practically no influence on the numerical data analyzed below [23].

For each shape, several packings of 5000 particles were prepared with η varying from 0 to 0.5. To avoid long-range ordering, a size polydispersity was introduced by taking R in the range $[R_{min}, R_{max}]$ with $R_{max} = 3R_{min}$ and a uniform distribution of particle volumes. A dense packing composed of disks ($\eta = 0$) was first constructed by means of random deposition in a box [24]. For other values of η , the same packing was used with each disk serving as the circumscribing circle. The particle was inscribed with the desired value of η and random orientation inside the disk. This geometrical step was followed by isotropic compaction of the packings inside a rectangular frame. The gravity g and friction coefficients between particles and with the walls were set to 0 during compaction in order to avoid force gradients. Figure 3 displays snapshots of the packings for $\eta = 0.4$ at the end of isotropic compaction¹.

The isotropic samples were sheared by applying a slow downward velocity on the top wall with a constant confining stress acting on the lateral walls. During shear, the friction coefficient μ between particles was set to 0.5 and to 0 with the walls. The shear strength is characterized by the internal angle of friction φ defined by

$$\sin \varphi = \frac{\sigma_1 - \sigma_2}{\sigma_1 + \sigma_2}, \quad (2)$$

where the subscripts 1 and 2 refer to the principal stresses. $\sin \varphi$ increases rapidly from zero to a peak value before relaxing to a constant material-dependent value $\sin \varphi^*$,

¹Animation videos of the simulations can be found at www.cgp-gateway.org/ref012.

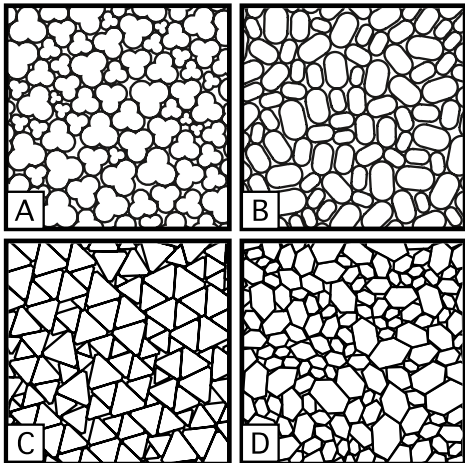


Fig. 3: Snapshots of the simulated packings in the densest isotropic state for $\eta = 0.4$.

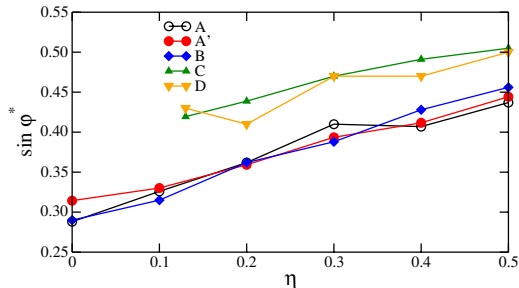


Fig. 4: (Colour on-line) Shear strength $\sin \varphi^*$ of packings composed of various particle shapes (see fig. 2) as a function of η .

which defines the shear strength at large strain at a steady stress state.

Figure 4 shows the dependence of $\sin \varphi^*$ with respect to η for our different shapes. Remarkably, $\sin \varphi^*$ increases with η at the same rate for all shapes. The data nearly coincide between the A and B shapes, on the one hand, and between C and D shapes, on the other hand. This suggests that non-convex trimers and rounded-cap rectangles, in spite of their very different shapes, belong to the same family (rounded shapes). In the same way, the truncated triangles and elongated hexagons seem to belong to the family of angular particles and exhibit a shear strength slightly above that of rounded shapes. Note also that the results are robust with respect to the numerical approach as the packings A and A' were simulated by two different methods.

The increase of shear strength with η may be attributed to the increasing frustration of particle rotations as the shape deviates from a disk [11,25]. Since the particles may interact at two or three contact points (A-shape) or through side-to-side contacts (shapes B, C and D), the kinematic constraints increase with η and frustrate the particle displacements by rolling. The restriction of rolling

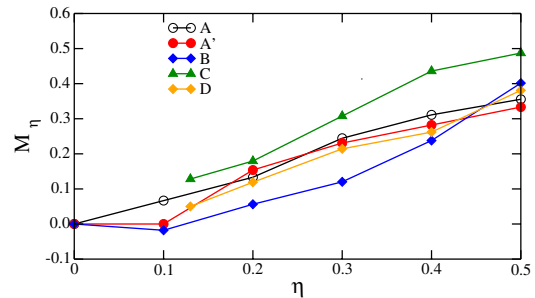


Fig. 5: (Colour on-line) Friction mobilization in the steady state as a function of η for different particle shapes.

leads to enhanced role of friction in the mechanical equilibrium and relative sliding of particles during deformation. A related static quantity is the mean friction mobilization defined by $M = \langle f_t / (\mu f_n) \rangle$, where f_t is the magnitude of the friction force, f_n is the normal force, and the average is taken over all force-bearing contacts in the system.

To evaluate the effect of particle shape, we consider the parameter

$$M_\eta = \frac{M(\eta)}{M(\eta=0)} - 1 \quad (3)$$

as a function of η for different shapes, where $M(\eta=0)$ is the friction mobilization for circular particles. Figure 5 shows that M_η is a globally increasing function of η for all shapes. The parameter η appears also in this respect to account for the global trend of friction mobilization, and the differences observed in fig. 5 among different shapes are rather of second order.

We also observe that the proportions of double and triple contacts for A-shape packings and the proportion of side-to-side contacts for other shapes increase with η . For non-circular particles, one should distinguish the coordination number Z , defined as the mean number of contacting neighbors per particle, from the “contact coordination number” Z_c defined as the mean number of contacts per particle. Obviously, for the calculation of both Z and Z_c only the force-bearing contacts and non-floating particles are taken into account [26]. We have $Z = Z_c \simeq 4$ for the disks in the initial state prepared with $\mu = 0$. This value corresponds to an isostatic state in which one expects $Z = 2N_f$, where N_f is the number of degrees of freedom of a particle [27]. For frictionless disks, we have $N_f = 2$ (two translational degrees of freedom), leading to $Z = 4$. For non-circular shapes, we have $N_f = 3$ since the rotational degrees of freedom take part in the mechanical equilibrium of the particles. Hence, if isostaticity holds also for non-circular frictionless particles, we expect $Z = 6$. We observe instead $Z < 5$ for all our packings. However, we find $Z_c \simeq 6$ for $\eta \neq 0$ if each side-to-side contact is counted twice, representing two independent constraints. This result is consistent with the isostatic nature of a packing of frictionless non-circular particles and shows that the packings of non-circular shape are

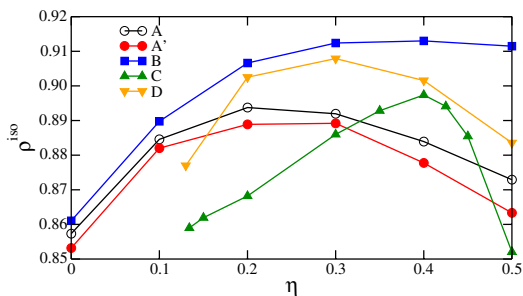


Fig. 6: (Colour on-line) Packing fraction in the isotropic state as a function of η for different particle shapes.

not under-constrained as previously suggested [28]. For $\mu = 0.5$, the packings are no more isostatic and Z and Z_c vary only slightly with η with values in the range 3 to 4 for Z and in the range 4 to 5 for Z_c in the course of shearing.

We now focus on the packing fraction which crucially depends on particle shape. Figure 6 shows the packing fraction ρ^{iso} in the initial isotropic state as a function of η . We observe a non-trivial behavior for all particle shapes: the packing fraction increases with η , passes by a peak depending on each specific shape and subsequently declines. For the B-shape a sharp decrease of ρ^{iso} occurs beyond $\eta = 0.5$ as was shown in [10].

This unmonotonic behavior of packing fraction was observed by experiments and numerical simulations for spheroids as a function of their aspect ratio [2,16,17,28–30]. The decrease of the packing fraction is attributed to the excluded-volume effect that prevails at large aspect ratios and leads to increasingly larger pores which cannot be filled by the particles [29]. The observation of this unmonotonic behavior as a function of η for different shapes indicates that it is a generic property depending only on deviation from circular shape. This behavior may thus be explained from general considerations involving the parameter η but with variations depending on second-order shape characteristics.

A plausible second-order parameter is

$$\nu = \frac{V_p}{\pi R^2}, \quad (4)$$

where V_p is the particle volume in 2D. Its complement $1 - \nu$ is the “self-porosity” of a particle, *i.e.* the unfilled volume fraction inside the circumscribing circle. Keeping the radius R of the circumscribing circle constant, $\rho^{iso} = V_p/V$ varies with η as a result of the relative changes of V_p and the mean volume V per particle. The free (pore) volume per particle is $V_f = V - V_p$.

At $\eta = 0$, the free volume V_f is only composed of *steric voids*, *i.e.* voids between three or more particles, and the packing fraction is given by $\rho(0) = \pi R^2/V(0)$. For $\eta > 0$, the void patterns are more complex but can be described by considering the generic shape of particles belonging to a given η -set. The borders of a particle involve “hills”, which are the parts touching the circumscribing circle, and

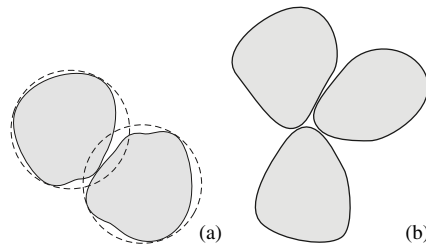


Fig. 7: Pore volume reduction by (a) overlap between self-porosities; (b) steric pores.

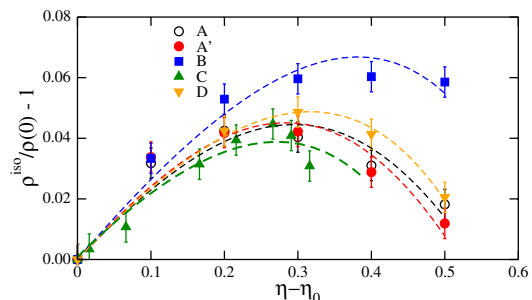


Fig. 8: (Colour on-line) Normalized packing fractions fitted by eq. (6).

“valleys” touching the inscribed circle. The volume V per particle varies with η by two mechanisms. First, the hills of a particle may partially fill the valleys of a neighboring particle, fig. 7(a). Secondly, the steric voids between the hills shrink as η increases due to the increasing local curvature of the touching particles, fig. 7(b). To represent this excess or loss of pore volume due to the specific jamming configurations induced by particle shapes, we introduce the function $h(\eta)$ by setting

$$V(\eta) = V(\eta_0) - \pi R^2 h(\eta), \quad (5)$$

with $h(\eta_0) = 0$. With these assumptions, the packing fraction is expressed as

$$\rho(\eta) = \frac{\nu(\eta)\rho(\eta_0)}{1 - h(\eta)\rho(\eta_0)}. \quad (6)$$

The function $\nu(\eta)$ is known for each shape but $h(\eta)$ needs to be estimated. A second-order polynomial approximation

$$h(\eta) = \alpha(\eta - \eta_0) + \beta(\eta - \eta_0)^2 \quad (7)$$

together with eq. (6) allows us to recover the correct trend and to fit the data as shown in fig. 8. The error bars represent the variability at η_0 assumed to be the same for all other values of η . The parameter α ensures the increase of packing fraction with η at low values of the latter and it basically reflects the shrinkage of steric pores (fig. 7(b)) whereas β accounts for the overlap between circumscribing circles (fig. 7(a)) and is responsible for the subsequent decrease of the packing fraction.

The fitting parameters in fig. 8 are $\alpha \simeq 1.30, 1.29, 1.14, 1.17$ and $\beta \simeq 1.23, 1.20, 0.23, 0.20$ for C, A, D and B shapes, respectively with increasing peak value. Note that the values of β are considerably smaller for B and D that have an elongated aspect and for which the overlapping of self-porosities prevails as compared to A and C for which the shrinkage of the initial pores is more important.

In summary, our benchmark simulations show that a low-order shape parameter η , describing deviation with respect to circular shape, controls to a large extent both the shear strength and packing fraction of granular media composed of non-circular particles in 2D. The shear strength is roughly linear in η whereas the packing fraction is unmonotonic. Our simple model for this unmonotonic behavior is consistent with the numerical data for all shapes. It is governed by a first-order term in η for the shrinkage of the initial steric pores and a second-order term in η for the creation of large pores by shape-induced steric pores. The effect of higher-order shape parameters may be analyzed also in this framework in terms of differences in packing fraction and shear strength among various shapes belonging to the same η -set. An interesting issue to be addressed in future is whether a generic second-order parameter accounting for such differences exists. Another aspect that merits further investigation is the joint effects of size polydispersity and particle shape. The shear strength is independent of particle size polydispersity as a result of the capture of force chains by the class of larger particles [31]. But the packing fraction and force and contact anisotropy depend on both shape and polydispersity.

We thank B. CAMBOU and F. NICOT for stimulating discussions. We also acknowledge financial support of the French government through the program PPF CEGEO.

REFERENCES

- [1] BINDER K. and KOB W., *Glassy Materials and Disordered Solids* (World Scientific) 2005.
- [2] MAN W., DONEV A., STILLINGER F., SULLIVAN M., RUSSEL W., HEEGER D., INATI S., TORQUATO S. and CHAIKIN P., *Phys. Rev. Lett.*, **94** (2005) 198001.
- [3] TORQUATO S., TRUSKETT T. M. and DEBENEDETTI P. G., *Phys. Rev. Lett.*, **84** (2000) 2064.
- [4] RADJAI F., WOLF D. E., JEAN M. and MOREAU J., *Phys. Rev. Lett.*, **80** (1998) 61.
- [5] OUADFEL H. and ROTHENBURG L., *Mech. Mater.*, **33** (2001) 201.
- [6] MIRGHASEMI A., ROTHENBURG L. and MARYAS E., *Geotechnique*, **52** (2002) 209.
- [7] NOUGUIER-LEHON C., CAMBOU B. and VINCENS E., *Int. J. Numer. Anal. Methods Geomech.*, **27** (2003) 1207.
- [8] AZÉMA E., RADJAI F., PEYROUX R. and SAUSSINE G., *Phys. Rev. E*, **76** (2007) 011301.
- [9] AZÉMA E., RADJAI F. and SAUSSINE G., *Mech. Mater.*, **41** (2009) 721.
- [10] AZÉMA E. and RADJAI F., *Phys. Rev. E*, **81** (2010) 051304.
- [11] ESTRADA N., AZÉMA E., RADJAI F. and TABOADA A., *Phys. Rev. E*, **84** (2011) 011306.
- [12] AZÉMA E. and RADJAI F., *Phys. Rev. E*, **85** (2012) 031303.
- [13] NOUGUIER-LEHON C., *C. R. Méc.*, **338** (2010) 587.
- [14] SAINT-CYR B., DELENNE J.-Y., VOIVRET C., RADJAI F. and SORNAY P., *Phys. Rev. E*, **84** (2011) 041302.
- [15] SZARF K., COMBE G. and VILLARD P., *Powder Technol.*, **208** (2011) 279.
- [16] DONEV A., STILLINGER F., CHAIKIN P. and TORQUATO S., *Phys. Rev. Lett.*, **92** (2004) 255506.
- [17] DONEV A., CISSE I., SACHS D., VARIANO E., STILLINGER F., CONNELLY R., TORQUATO S. and CHAIKIN P., *Science*, **303** (2004) 990.
- [18] JIAO Y., STILLINGER F. H. and TORQUATO S., *Phys. Rev. E*, **81** (2010) 041304.
- [19] PÖSCHEL T. and BUCHHOLTZ V., *Phys. Rev. Lett.*, **71** (1993) 3963.
- [20] RADJAI F. and RICHEFEU V., *Mech. Mater.*, **41** (2009) 715.
- [21] COMBE G. and ROUX J.-N., *Discrete numerical simulation, quasistatic deformation and the origins of strain in granular materials*, in *Proceedings of Deformation Characteristics of Geomaterials*, edited by DI BENEDETTO H. et al. (A. A. Balkema) 2003, pp. 1071–1078.
- [22] BRILLIANTOV N. V., SPAHN F., HERTZSCH J.-M. and PÖSCHEL T., *Phys. Rev. E*, **53** (1996) 5382.
- [23] ROUX J.-N. and CHEVOIR F., *Dimensional analysis and control parameter*, in *Discrete-element Modeling of Granular Materials*, edited by RADJAI F. and DUBOIS F. (ISTE-Wiley) 2011, Chapt. 8, pp. 223–253.
- [24] VOIVRET C., RADJAI F., DELENNE J.-Y. and YOUSOUFI M. S. E., *Phys. Rev. E*, **76** (2007) 021301.
- [25] ESTRADA N., TABOADA A. and RADJAI F., *Phys. Rev. E*, **78** (2008) 021301.
- [26] COMBE G. and ROUX J.-N., *Construction of granular assemblies under static loading*, in *Discrete-element Modeling of Granular Materials*, edited by RADJAI F. and DUBOIS F. (ISTE-Wiley) 2011, Chapt. 6, pp. 153–180.
- [27] AGNOLIN I. and ROUX J.-N., *Phys. Rev. E*, **76** (2007) 061302.
- [28] DONEV A., CONNELLY R., STILLINGER F. and TORQUATO S., *Phys. Rev. E*, **75** (2007) 051304.
- [29] WILLIAMS S. and PHILIPSE A., *Phys. Rev. E*, **67** (2003) 051301.
- [30] SACANNA S., ROSSI L., WOUTERSE A. and PHILIPSE A., *J. Phys.*, **19** (2007) 376108.
- [31] VOIVRET C., RADJAI F., DELENNE J.-Y. and EL YOUSOUFI M. S., *Phys. Rev. Lett.*, **102** (2009) 178001.

2.2 Convex and Concave Grains

In the present study the emphasis was put on the mechanical behaviour of dense and loose granular assemblies made of clumps of three discs, Fig. 2.1b, and convex polygons with three axes of symmetry, Fig. 2.1c. It is worth noting that these polygons can be seen as an envelope of clumps. More information about these two shapes can be found in Appendix B.

In CEGEOS's paper (CEGEO et al., 2012) these shape groups were denoted as A' and C. From this point the clump samples previously denoted A' will be referred to as either *C.xx* or *clumps*, with *.xx* denoting the value of the sphericity factor α . The polygons previously denoted as C will be referred to as *P.xx* or *polygons*.

In Figure 2.6 the shapes used in the study are presented. The values of α used in the study ranged from 0.0 to 0.5. For clumps $\alpha = 0.0$ denotes a disc while $\alpha = \sqrt{3} - 1 \approx 0.73$ is the maximum possible value and denotes three discs in contact without any overlap. For polygons the minimum value is $\alpha = 1 - \sqrt{3}/2 \approx 0.13$ (hexagon) while the maximum $\alpha = 0.5$ (equilateral triangle).

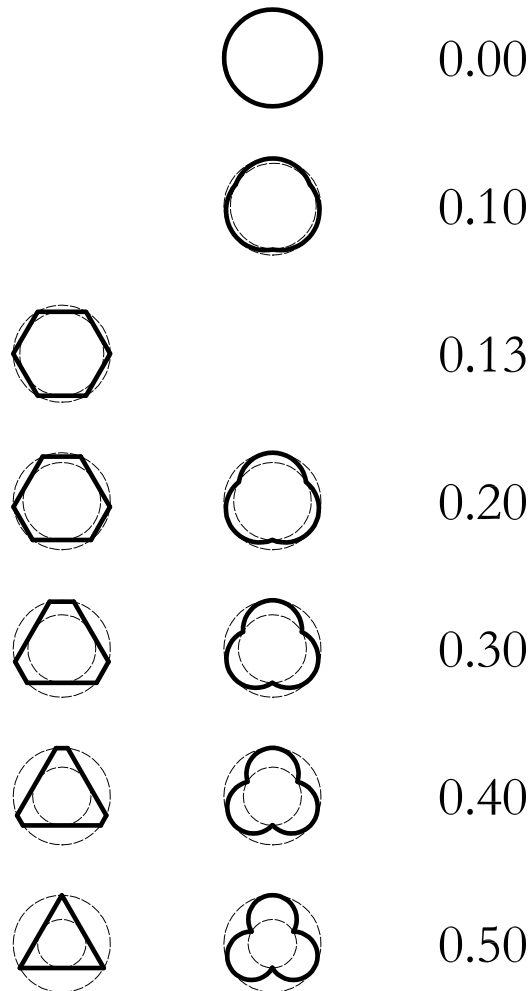
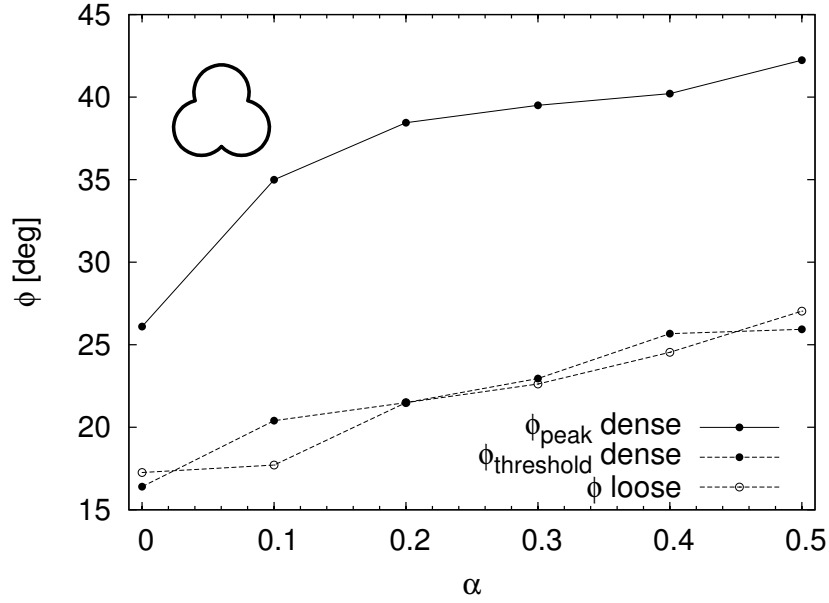
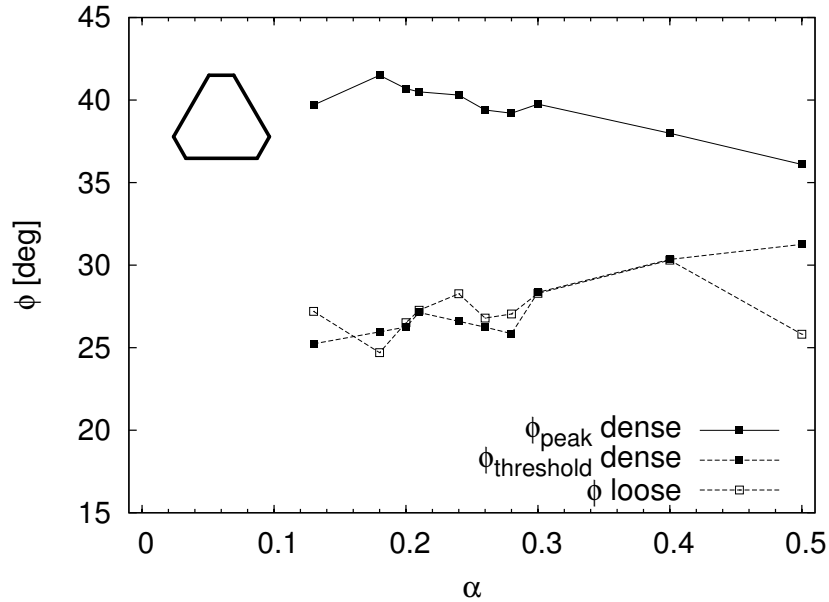


Figure 2.6: Particle shapes used in the study. The outer radius of particles R_1 is constant. The left column presents polygonal grains, the right one clumps. Values of shape parameter α are given for each shape. Note the absence of polygons $\alpha = 0.00$ and $\alpha = 0.10$, as well as clumps $\alpha = 0.13$



(a) Clumps



(b) Polygons

Figure 2.7: Evolution of macroscopic friction angles ϕ of samples submitted to vertical biaxial compression in function of α . ϕ_{peak} was measured at the peak of stress while $\phi_{threshold}$ was measured at the stress critical state

The mechanical behaviour of the samples consisting of the particles listed above observed in the numerical biaxial compression tests showed that initially ($\varepsilon_1 < 3\%$) the concavity of the particles predominates for dense samples⁹. The Figure 2.7 clearly shows that the macroscopic friction angle ϕ_{peak} measured at the peak of stresses increases with α for clumps, but not for polygons; Dense samples containing polygonal particles responded to the loading with a shear strength decreasing with α . This difference is even more remarkable because dense samples of

⁹Samples prepared without intergranular friction: $\mu = 0.0$

polygons and clumps displayed the same coordination number value¹⁰ in the isotropic state (on average number $z^* \simeq 6$). This difference in the mechanical behaviour can be explained by the mobilization of tangential contact forces that increase with the degree of sphericity for assemblies made of concave clumps, but not for convex polygons.

For large macroscopic strains (critical stress state), the behaviour with α is different than at the peak. The trend of evolution of $\phi_{threshold}$ (and ϕ for loose assemblies¹¹) is the same whatever the particle shape or the initial density of the sample. It seems that the sphericity parameter α is the deciding factor, not the particle concavity.

Some additional observations were made on the influence of the grain shape on the strain localisation. Localisation in the form of shear bands is a ubiquitous failure mechanism in granular materials (Desrues and Chambon, 2002). In Figure 2.8 two examples of strain localization maps are presented.

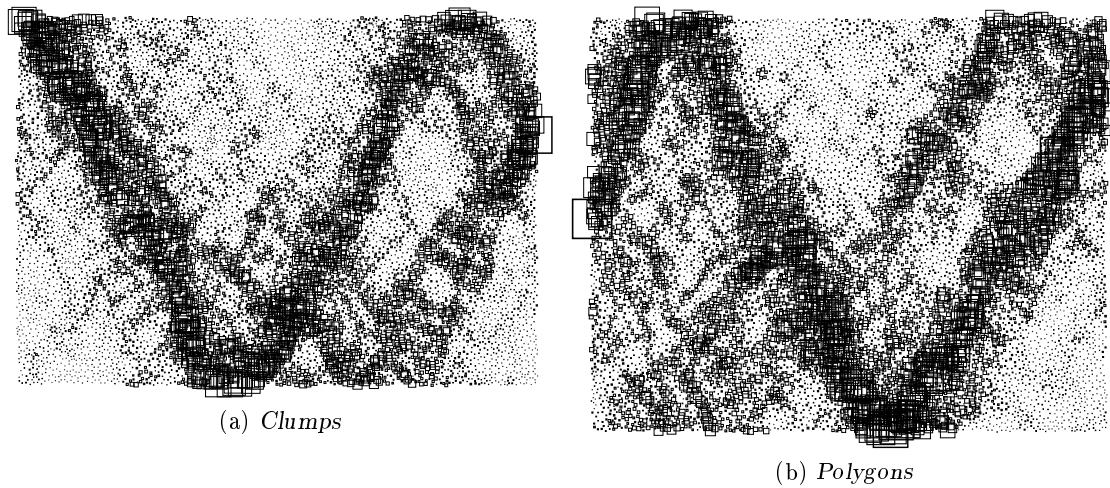


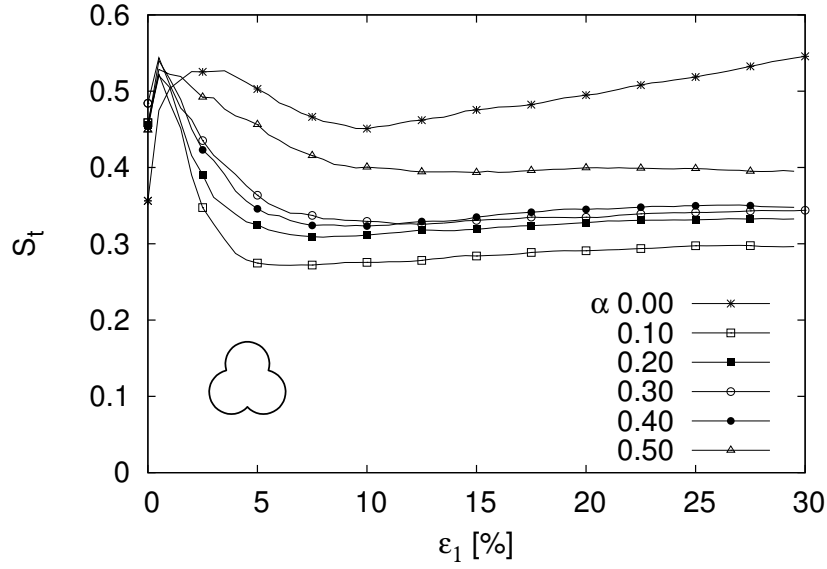
Figure 2.8: *Shearmaps on samples made of grains with $\alpha = 0.3$. $\varepsilon_1 = 0 - 13.5\%$*

To quantify the influence of particle shape on the shear localisation a localization indicator S_t proposed by (Sornette et al., 1993) was used. The indicator can be seen as a proportion of the sheared area to the total area of the sample. Apart from presenting it locally as in Figure 2.8, one can also compute it globally. In Figure 2.9 the evolution of the global S_t value during the biaxial tests on assemblies of different particles is presented. The overall shape of the curves resembles that of the macroscopic stress-strain curves: the value of S_t increases at the beginning of the compression and reaches its maximum along with the peak stress, and then declines to a plateau.

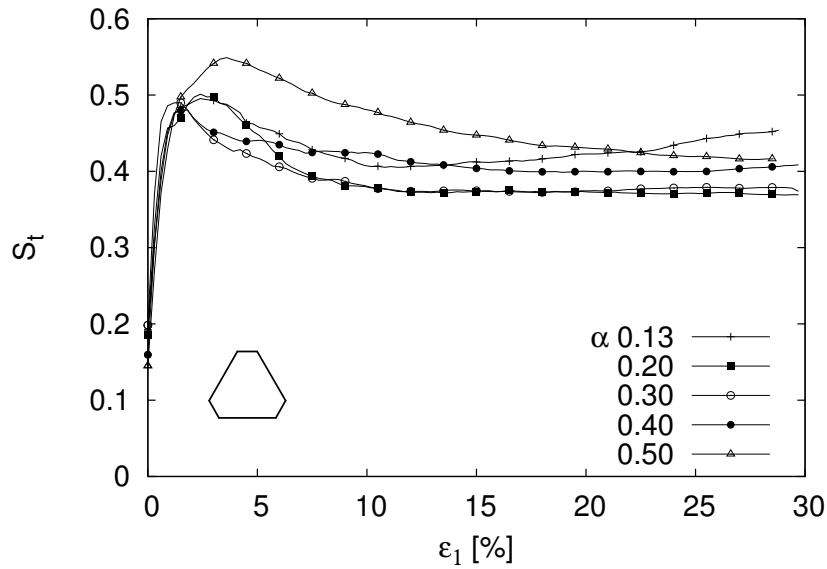
Comparison of the localisation maps and the localisation curves reveals that the plateau in Figure 2.9 is correlated with a concentration of the deformation in a band. The amount of sheared area of the assembly is increasing when α increase in the samples of clumps, Fig. 2.9a, with an exception of discs that seemed not to localise much. In clumps α is directly related to the size of concavities; More concave grains interlock more and the thickness of the shear bands is larger.

¹⁰Average number of contacts per particle, floating particles excluded

¹¹Samples prepared with intergranular friction: $\mu = 0.5$



(a) Clump samples



(b) Polygon samples

Figure 2.9: Evolution of the shear localisation indicator throughout a vertical compression test. The curves represent a mean of four samples consisting of grains of the same type

A clear trend for samples made of polygons is more difficult to determine but one might say that except for samples of hexagons $\alpha \approx 0.13$, the amount of sheared area increased with α as well, Fig. 2.9b. Moreover it seems that while in the case of clump samples the S_t value drops down to a plateau rapidly, in samples consisting of polygons the process is slower and the plateau stabilises for larger values of ε_1 . The second remark is that the residual value of S_t is generally higher in polygons, meaning wider localisation bands.

As a synthesis of these remarks, the samples made of clumps behaves more like a “brittle” material whereas samples made of polygons are more “ductile” in a way that they resemble dry sand behaviour.

Apart from the localisation of strains, it was also interesting to investigate the spatial distri-

bution of interparticle contacts that were maintained during the loading. The persisting contacts can be divided into two groups based on the relative movement of the particles in contact. Two rounded particles remaining in contact can either roll, slip, or roll and slip at the same time.

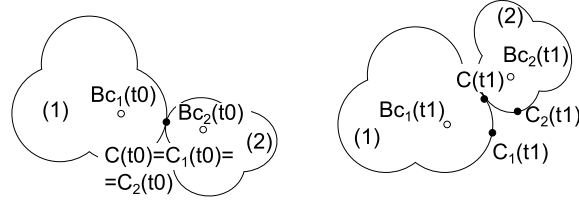


Figure 2.10: Sketch of a single, persisting contact between two clumps (1) and (2). On the left: configuration at time $t = t_0$, on the right: configuration after a displacement occurred, time $t = t_1$. $Bc_1(t_1)$ and $Bc_2(t_1)$ denotes the actual position of the centres of discs in contact. Here the sign of the distance $d[C_1(t_1), C(t_1)]$ is positive while $d[C_2(t_1), C(t_1)]$ is negative

Let us consider two grains that remain in contact during deformation of the assembly (see Fig. 2.10). Before the relative displacement occurred, the initial point of contact $C(t_0)$ was identical with the two points on the perimeter of the grains, C_1 and C_2 . After the change of positions and orientations of the grains in relation to each other, these points moved to positions $C_1(t_1)$ and $C_2(t_1)$ while the point of contact was placed at $C(t_1)$. By comparing these distances between the new contact position and the points on the perimeter that were in contact previously, one can separate contacts where rolling without sliding occurred according to the following relation:

$$|d[C_1(t_1), C(t_1)] + d[C_2(t_1), C(t_1)]| = 0, \quad (2.2)$$

where:

- $C(t_1)$ is the current position of the current contact point,
- $C_i(t_1)$ is the current position of the initial contact point,
- $d[A, B]$ is the arch length between two given points A and B,

This criterion was made softer by accepting the sliding contacts where the amount of sliding $|d[C_1(t_1), C(t_1)] + d[C_2(t_1), C(t_1)]|$ is less than 10% of the maximum sliding as rolling. This threshold value was chosen arbitrarily (Lanier and Combe, 1995).

In Figure 2.11 the contacts that remained between 13 and 13.5% ϵ_1 are presented. It appears that the sliding contacts are placed in the zones of localisation, and their direction is, generally speaking, perpendicular to the length of the zone forming characterising bridges (Tordesillas, 2007). The large zones of unbroken rolling contacts are the rigid blocks that do not deform much during the loading. In this image it is also visible that in the localisation bands smaller number of contacts is maintained.

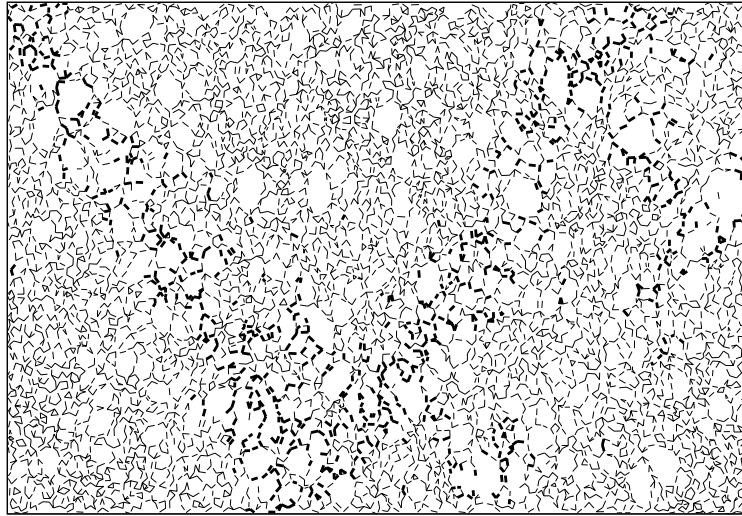


Figure 2.11: *Rolling and sliding contacts in the sample of $\alpha = 0.3$ dense clumps between 13 and 13.5% ε_1 . Each persisting contact is denoted with a line connecting the discs in contact. The rolling with sliding contacts are denoted with a bold line*

2.3 Conclusions

The investigations of samples consisting of particles with different grain shapes revealed that the form governs a number of important features of granular media like porosity or shear resistance. Moreover the effects can be quantified using a simple sphericity parameter as was proposed by CEGEO for the initial solid fraction.

Cooperation between multiple research groups proved that the observed shape effect was independent of numerical approach, and that it is common for different shapes. It is also remarkable that simulations incorporating very simple grain shapes and very simple contact laws were capable of reproducing behaviour of real materials.



Polygons vs. clumps of discs: A numerical study of the influence of grain shape on the mechanical behaviour of granular materials[☆]

K. Szarf, G. Combe^{*}, P. Villard

Université de Grenoble, Laboratoire Sols, Solides, Structures, Risques (3SR) UJF, G-INP, CNRS UMR 5521, Domaine Universitaire BP53 38041 Grenoble Cedex 9, France

ARTICLE INFO

Keywords:

Granular materials
DEM
Grain shape
Clumps of discs
Polygons
Shear localisation

ABSTRACT

We performed a series of numerical vertical compression tests on assemblies of 2D granular material using a Discrete Element code and studied the results with regard to the grain shape. The samples consist of 5000 grains made from either 3 overlapping discs (clumps – grains with concavities) or six-edged polygons (convex grains). These two grain type have similar external envelope, which is a function of a geometrical parameter α . In this paper, the numerical procedure applied is briefly presented followed by the description of the granular model used. Observations and mechanical analysis of dense and loose granular assemblies under isotropic loading are made. The mechanical response of our numerical granular samples is studied in the framework of the classical vertical compression test with constant lateral stress (biaxial test). The comparison of macroscopic responses of dense and loose samples with various grain shapes shows that when α is considered a concavity parameter, it is therefore a relevant variable for increasing mechanical performances of dense samples. When α is considered an envelope deviation from perfect sphericity, it can control mechanical performances for large strains. Finally, we present some remarks concerning the kinematics of the deformed samples: while some polygon samples subjected to a vertical compression present large damage zones (any polygon shape), dense samples made of clumps always exhibit thin reflecting shear bands.

© 2010 Elsevier B.V. All rights reserved.

1. Introduction

A typical numerical approach to discrete element modeling of granular materials is to use simple shapes of particles (discs in 2D [1] or spheres in 3D [2]). Although the computation time is short using this method, these models cannot reflect some of the more complex aspects of real granular media behaviour, such as high shear resistance or high volumetric changes [3]. In order to model these mechanisms properly, physical phenomena (resistance to inter-granular rolling [4–6]) or other grain shapes (sphere aggregates [7] or polyhedral grains [8]) must be used. The influence of grain shape is not yet fully understood. In this article, we will present our findings concerning the influence of grain shape (grain concavity in particular) on the mechanical behaviour of granular assemblies. We compared two groups of grains – convex irregular polygons and non-convex aggregates of three overlapping discs.

2. Granular model

The granular model used consists of 5000 polydisperse 2D frictional particles. Two kinds of grain shape are used: convex irregular polygons

with six edges and non-convex particles made of aggregates of three overlapping discs called *clumps*. These two shapes were chosen because of the similarity of their global contour (polygonal grains can be seen as a polygonal envelope of clumps made of three discs). As shown in Fig. 1, particle shape is defined by a parameter $\alpha = \frac{\Delta R}{R_1}$, where R_1 denotes the ex-circle radius of the particle and ΔR is the difference between the ex-circle and the in-circle radii, [9,10]. The in-circle must be fully contained in the particle. For non-convex clumps, α ranges from 0 (circle) to 0.5. For convex polygonal grains, α ranges from $1 - \frac{\sqrt{3}}{2} \approx 0.13$ (regular hexagons) to 0.5 (equilateral triangles). Some of the shapes used are presented at the bottom of Fig. 1. For each chosen α , granular samples are made of polydisperse particles: the polydispersity of grains is determined by the radii of the grain ex-circle. In each sample, the chosen radii R_1 are such that the areas of the ex-circles are equally distributed between $S_m = \pi(R_m)^2$ and $S_M = \pi(R_M)^2 = \pi(3R_m)^2$.

3. Discrete Element Method

Two-dimensional numerical simulations were carried out using the Discrete Element Method according to the principles of *Molecular Dynamics* (MD) [11]. Two codes were used: PFC^{2D} by ITASCA [12] for clump simulation and a code capable of dealing with polygonal particles that was developed at the laboratory. Both codes use the same contact laws for contact forces computations [13]: grains interact in their contact points with a linear elastic law and Coulomb friction. The normal

[☆] This paper was written as part of a CEGEO research project (<http://www.granuloscience.com/CEGEO/>).

^{*} Corresponding author.

E-mail address: gael.combe@ujf-grenoble.fr (G. Combe).

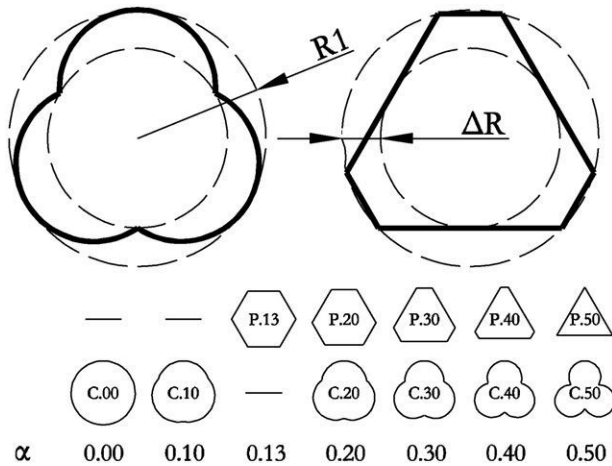


Fig. 1. Particle shape definition: $\alpha = \frac{\Delta R}{R_1}$ and examples of clump and polygon particle shapes used.

contact force f_n is related to the normal interpenetration (or overlap) h of the contact

$$f_n = k_n \cdot h \quad (1)$$

as f_n vanishes if contact disappears, i.e. $h=0$. The tangential component f_t of the contact force is proportional to the tangential elastic relative displacement, according to a stiffness coefficient k_t . The Coulomb condition $|f_t| \leq \mu f_n$ requires an incremental evaluation of f_t in every time step, which leads to some amount of slip each time one

of the equalities $f_t = \pm \mu f_n$ is imposed (μ corresponds to the contact friction coefficient). A normal viscous component as opposed to the relative normal motion of any pair of grains in contact is also added to the elastic force f_n . Such a term is often introduced to facilitate the mechanical equilibrium approach [14]. In case of frictional assemblies under quasi-static loading, the influence of this viscous force (which is proportional to the normal relative velocity, using a damping coefficient g_n) is not significant [15] (elastic energy is mainly dissipated by Coulomb friction). Finally, the motion of grains is calculated by solving Newton's equations using either a leap-frog (in PFC^{2D}) or third-order predictor–corrector discretisation scheme [16] (in the in-house software). This constitutes the only known difference between the two codes.

The principles of disc contact detection are well known [13,17], and contact detection for clumps was solved in the same way: contact occurs at a point, the normal force value f_n is calculated with Eq. (1) and its direction connects the centers of discs in contact, Fig. 2(a). Contact detection and contact force calculations between polygons do not use classical methods based on the area overlap between polygons [18–21]. The *shadow overlap* technique proposed by J.J. Moreau [22], which was originally applied within the *Contact Dynamic* approach [23] for convex polygonal particles, was used. In our study this technique was adapted to the MD approach. Three types of geometrical contact can exist between polygons: Corner-to-Corner, Corner-to-Edge (CE) and Edge-to-Edge (EE). Corner-to-Corner contacts are geometrically (or mathematically) realistic but never occur in our simulations because of the numerical rounding errors. When dealing with (EE) contact, contact detection involves two contact points and their associated overlaps h , Fig. 2(b). This is the main difference compared to the classical method (area overlap

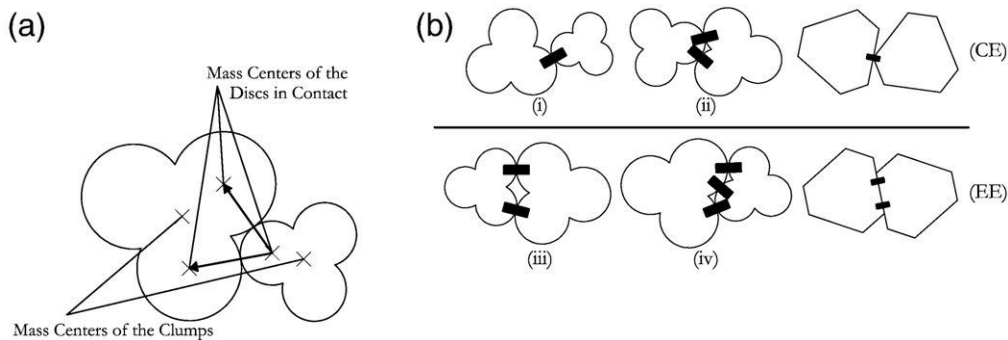


Fig. 2. Contacts between the particles; contact definition and classification. (a) Definition of a contact between clumps. Normal contact vector connects the centers of the discs in contact. (b) Various types of possible contacts between clumps. Analogy between clump and polygon contacts: corner-to-edge (CE) and edge-to-edge (EE) groups. Note that for a contact between two polygon edges two contact points are considered while only one if there is a contact between a corner and an edge.

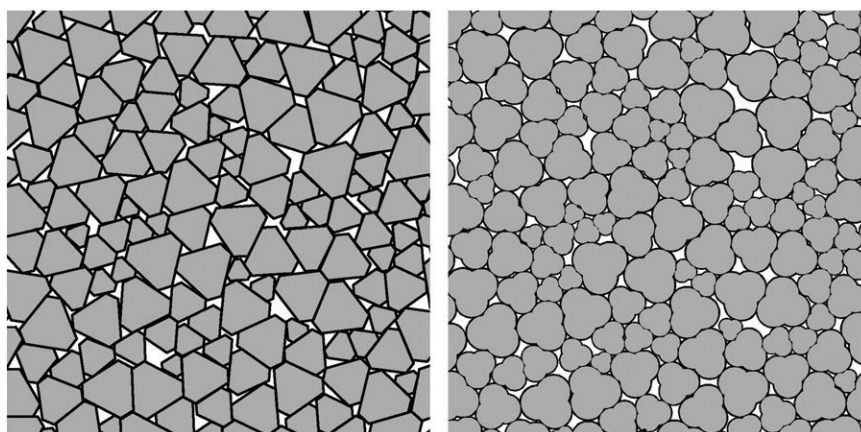


Fig. 3. Fragments of two confined dense samples with $\alpha=0.3$. Sample P.D.30 on the left and C.D.30 on the right.

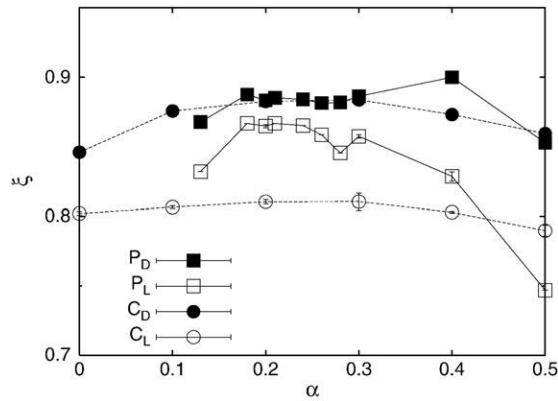


Fig. 4. Solid fraction ξ of the samples under isotropic loading versus α . Error bars correspond to standard deviation calculated using of four samples. The round and square symbols represent samples made of clumps and polygons, respectively. The black and white symbols represent dense and loose samples, respectively. This convention will be maintained hereafter.

calculations) where only one contact is considered between the edges.

Finally, we may be interested in the main contact law parameters: the normal and tangential stiffness, k_n and k_t , and the friction coefficient μ . Assuming that samples would first be loaded with a 2D isotropic stress $\sigma_0 = 10$ kN/m, the normal stiffness of contact k_n was calculated according to the dimensionless 2D stiffness parameter $\kappa = k_n / \sigma_0$ [15,24–26]. κ expresses the mean level of contact deformation, $1/\kappa = h / \langle 2R \rangle$, where $\langle R \rangle$ is the mean particle radius. In our simulations, κ was arbitrarily set to 1000. As a comparison, a sample made of glass beams under isotropic loading of 100 kPa reaches $\kappa = 3000$. The tangential stiffness k_t can be expressed as a fraction of the normal stiffness, $\tilde{k} = k_t / k_n$, $\tilde{k} > 0$. $\tilde{k} > 1$ may exhibit specific behaviour where Poisson coefficient of grain assemblies become negative [27–30]. Running several numerical simulations with various \tilde{k} , $0 < \tilde{k} \leq 1$, [25] have shown that if $0.5 \leq \tilde{k} \leq 1$, the macroscopic behaviour remains similar. Thus we arbitrarily set \tilde{k} to 1.

4. Sample preparation – isotropic compression

Granular samples of 5000 grains are prepared in three steps: preparations start with a random spatial distribution of particle position inside a square made of four rigid walls. Secondly, the particles expand slowly until $\sigma_0 = 0.5$ kN/m is reached. Finally, samples are isotropically loaded by wall displacement up to $\sigma_0 = 10$ kN/m. To obtain samples with different solid fractions, we may use various values of the intergranular friction coefficient μ during the preparation [31]. When μ is set to zero, samples isotropically loaded up to $\sigma_0 = 10$ kN/m are dense and the Solid fraction is maximal. When a strictly positive value of μ is used instead, samples become looser and Solid fraction decreases. In our study dense samples were prepared with $\mu = 0$ and the loose ones with μ equal 0.5. 16 different samples (4 dense, 4 loose made of clumps and 4 dense, 4 loose made of polygons) for each α value were prepared.¹ Dense samples will be written as C_D or P_D respectively for Clumps and Polygons. Loose samples will be denoted as C_L or P_L . A subscript can be added. It then corresponds to the decimal part of the shape number α . As an example, fragments of two dense samples with $\alpha = 0.30$, $C_{D,30}$ and $P_{D,30}$, are displayed in Fig. 3.

¹ All the analyses presented in this article were carried out on mean results calculated over 4 samples of each density and each α . Associated Standard Deviations will always be given, even if they are too small to be significant.

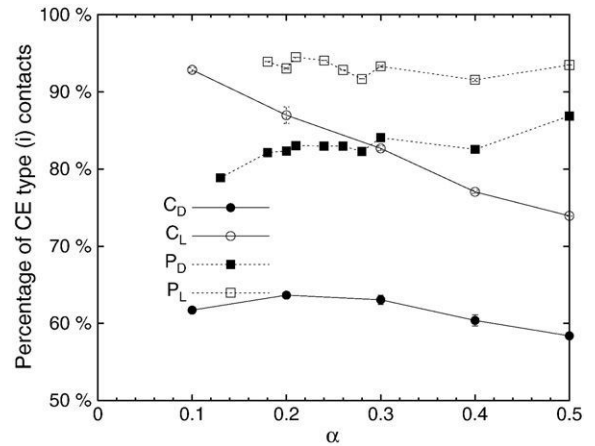


Fig. 5. Corner-to-edge contacts ((CE) see Fig. 2(b)) percentage in the isotropic state, ε_i . Comparison between clumps and polygons.

For both clumps and polygons, contact between particles can occur at more than one contact point. There are four contact possibilities for clumps: single contact Fig. 2(b)(i) double contact involving three discs Fig. 2(b)(ii), double contact involving four discs Fig. 2(b)(iii) and triple contact Fig. 2(b)(iv). By analogy with polygon contacts (Edge-to-Edge or Corner-to-Edge, Fig. 2(b)), all these contacts between clumps can be merged into two groups, (CE) and (EE). In the (CE) group, grains involved in a single contact (i) may rotate without sliding. Double contact (ii) allows rotation with sliding and eventually friction. Rotation and sliding of polygons meeting at a single contact point are not correlated. Group (EE) contacts block the rotation of the grains. In the case of rotation of grains, contacts of this type would be lost. Therefore, the shape of the grains can be regarded as macro roughness.

For samples subjected to isotropic loading, we focus on two internal parameters that mainly determine the mechanical behaviour: the Solid fraction ξ and the coordination number z^* . Fig. 4 shows the evolution of ξ with α for dense and for loose samples. For C_D samples, ξ evolution is bell-shaped and maximum Solid fraction is reached for $0.2 \leq \alpha \leq 0.3$. Similar observations were made by [9,10]. This also seems to be the case for C_L samples although the amplitude of the bell-shaped curve appears to be lower. The geometrical origin of these results deals with the grain shape (concavity and grains envelope) and imbrication and the interlocking between grains, but appears to be complex to establish. While we might think that when two grains are in contact with a single point of contact (contact (CE)-type (i), Fig. 2(b)), this would tend to increase the local porosity and thus reduce the overall Solid fraction; this does not seem to be the case:

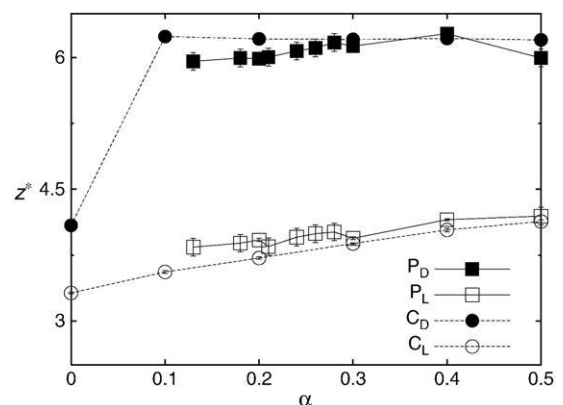


Fig. 6. Coordination number z^* values vs. α under isotropic loading. The round and square symbols represent samples made of clumps and polygons, respectively. The black and white symbols represent dense and loose samples, respectively.

Fig. 5 shows clearly that for C_D samples, the proportion of contact (CE)-type (i) is at its maximum for $0.2 \leq \alpha \leq 0.3$ in the case of dense samples and decreases linearly with α in the case of C_L samples. This completely goes against the ξ trend, even if it is clearly established that when ξ is high (C_D samples), the proportion of (CE)-type (i) contacts is lower than in the case where the Solid fraction is low (C_L samples).

For samples made of polygons, the dependence of ξ on α is not clear either. For P_D samples, ξ is almost constant for $0.2 \leq \alpha \leq 0.3$. If we exclude the $P_{D,40}$ sample, which behaves in a peculiar way, we can notice that for samples made of grains with regular shapes, corresponding to $\alpha = 0.13$ and $\alpha = 0.5$, the Solid fraction ξ is smaller than for samples made of grains which have shape irregularities ($0.13 < \alpha < 0.5$). The relationship between ξ and the percentage of (CE)-type (i) contact is again impossible to establish. Furthermore, it is worth observing that when $0.2 \leq \alpha \leq 0.3$, C_D and P_D samples show very similar Solid fraction. Here, grain envelope seem to be a clever interpretation of α parameter than grain imbrication, which is only relevant for clumps. Finally, we should note that the angle of friction used during the preparation does not seem to have a major influence on the Solid fraction of samples made of polygons when $0.2 < \alpha < 0.3$.

For samples subjected to isotropic loading, we studied the coordination number z^* corresponding to the mean number of contacts per grain. Here only grains that have two or more compression forces, and therefore take part in the load transfer, were considered. For samples made of frictionless perfectly rigid discs, $z^* = 4$ [32]. Because κ is not infinite in our study, in the samples made of frictionless circular particles ($C_{D,00}$), $z^* = 4.093 \pm 0.005$ is greater but still very close to the reference value. z^* is evaluated for clumps and polygons

and both dense and loose samples. The dependence of z^* according to α is shown in Fig. 6. For C_L samples, z^* increases linearly with α , like P_L samples, but for C_L , it can be directly correlated to the percentage of (CE)-type (i) contacts which decrease with α , and then increase z^* . For dense samples, the percentage of (CE)-type (i) contacts did not vary too much. z^* is constant for C_D and P_D samples.

5. Macromechanical response of granular assembly loaded in vertical compression test

The samples were tested in a 2D strain controlled vertical compression test, also called *biaxial test*. Vertical stress σ_1 was applied by increasing the compressive vertical strain ε_1 while lateral σ_3 remained constant. The loading velocities were chosen according to the dimensionless inertial number $I = \dot{\varepsilon}_1 \sqrt{\frac{\langle m \rangle}{\sigma_3}}$ [26] where $\dot{\varepsilon}_1$ denotes the strain rate and $\langle m \rangle$ the typical mass of a grain. It describes the level of dynamic effects in the sample. For quasi-static evolutions, the value of I should be low. I value was set to $5 \cdot 10^{-5}$ for clumps and for polygons samples, regardless of the code used. During the vertical compression in both dense and loose samples, the same value of contact friction coefficient $\mu = 0.5$ was used. The mechanical responses of the samples are plotted on η vs. ε_1 charts and shown in Fig. 7. $\eta = t/s$, $t = (\sigma_1 - \sigma_3)/2$ is half of the deviator stress and $s = (\sigma_1 + \sigma_3)/2$ is the mean stress. Extracted from $\eta - \varepsilon_1$ curves shown in Fig. 7, friction angles at the peak ϕ_p and at the threshold ϕ_t are given Fig. 8(a). Average dilatancy angles extracted from Fig. 9 are presented in Fig. 8(b).

For dense samples made of clumps, C_D , we can observe in Fig. 7(a) that the macroscopic shear resistance increases with α . Although

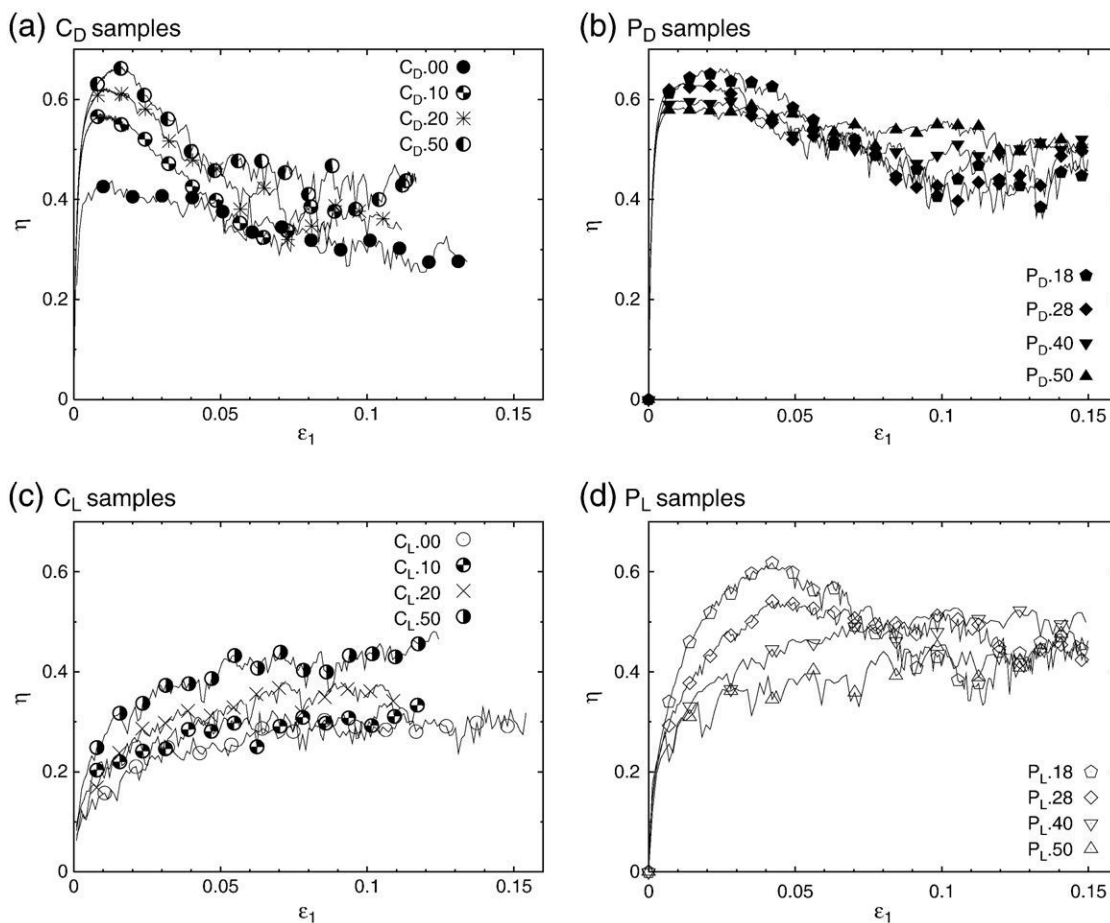


Fig. 7. Macroscopic $\eta - \varepsilon_1$ curves for some of the samples.

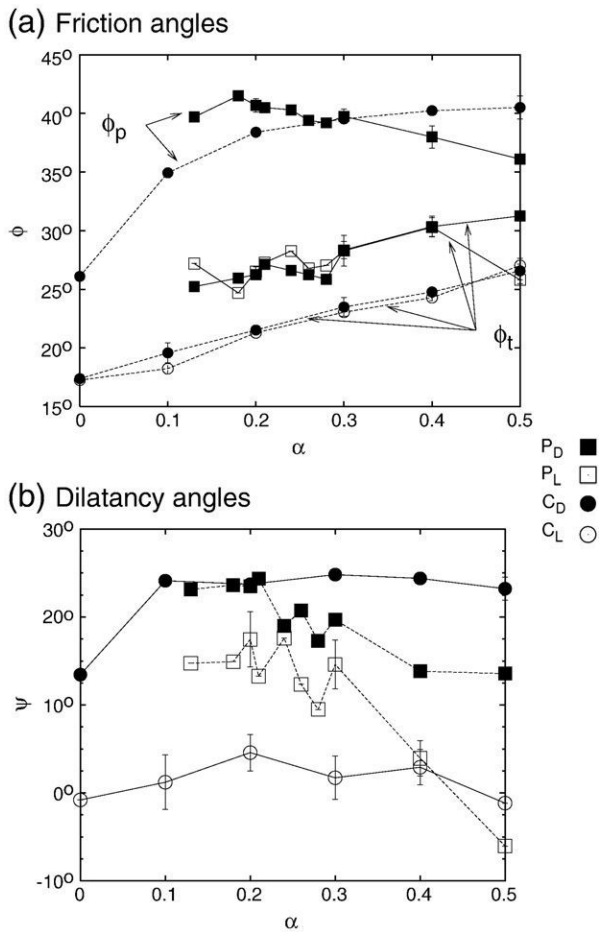


Fig. 8. (a) Friction angles vs. α for clumps and polygons samples. The two upper curves correspond to friction angles at the peak ϕ_p of dense samples. The four other curves show friction angles at the threshold ϕ_t , either for dense or loose samples. (b) Dilatancy angles for all the samples; Values of the angles for dense samples were calculated at the peak, between [1.5–2.5%] ε_1 ; For loose ones, the range was [6–7%] ε_1 .

$C_{D,10}$ implies grains with a small α , the mechanical response of the sample exhibits remarkable increase of the maximum deviator in comparison to disc samples $C_{D,00}$ where rotations of particles are not potentially disturbed by the grain shape. For C_L samples, there is no peak value of the friction angle, $\phi_p = \phi_t$ Fig. 7(c). Thus, for all clump samples, both peak ϕ_p and threshold ϕ_t friction angle values increase along with α . ϕ_t increases proportionally with α while the increase of ϕ_p is nonlinear and seems to be asymptotic for $\alpha \geq 0.4$.

For P_D samples, ϕ_p values slightly decrease linearly along α , while ϕ_t values increases, Fig. 8(a).

For P_L samples, we can notice in Fig. 7(d) that the macroscopic curves show typical behaviour similar to that of loose samples when $\alpha < 0.3$ and a typical behaviour characteristic of dense samples for $\alpha > 0.3$. This kind of behaviour deals with the values of the initial Solid fraction of the samples shown in Fig. 4 where we can observe that ξ values for P_D and P_L samples are very close when $\alpha \leq 0.3$. If we focus only on ϕ_t for P_L samples, we can observe (Fig. 8(a)) an increase of the friction angle with α , except for samples made of triangles, $\alpha = 0.5$, which always behave in a specific way.² In conclusion, it can be noted that adding some shape irregularity by increasing α always leads to an increase of the macroscopic angle of friction in the critical state. This is the case for clumps and polygons with a constant microscopic friction angle μ .

This influence of grain geometry is in line with a previous study by Salot et al. [7]. Lastly, as we can see in Fig. 7, α does not explicitly influence Young's modulus. E is linked to the rigidity matrix and therefore to z^* [33], which is constant for dense samples (Fig. 6).

Similarly, particle concavity does not particularly influence the average dilatancy angle ψ values ($\sin \psi = \frac{d\varepsilon_1 + d\varepsilon_3}{d\varepsilon_1 - d\varepsilon_3}$) of dense and loose clump samples (Fig. 8(b)). On the other hand, ψ is lower for polygons with higher values of α (closer to triangular shape) than for those more similar to hexagons.

In Fig. 9, volumetric changes in some samples are illustrated. For both dense clump and polygon samples, Fig. 9(a) and (b), the volume³ increases mainly during vertical compression, after a small contraction due to the stiffness of the contacts [15]. The volumetric increase for C_D samples is quite similar from one α to another (Fig. 9(a)). On the other hand, α clearly influences the volumetric change of P_D samples but this influence seems erratic. Nevertheless, P_D samples show greater total dilatancy than C_D samples. C_L samples (Fig. 9(c)) behave like loose sands and contract all throughout the compression test. It is more complex for P_L samples (Fig. 9(d)) for which the setting-up process remains problematic for some values of α .

6. Micromechanical analysis

From the macroscopic results exposed in the previous section, two main observations can be established: for dense samples made of clumps, the evolution of the angle of friction at the stress peak ϕ_p varies significantly with α . The geometrical imbrication between grains in contact, which depend on α , may be one of the micromechanical origins of these results. Secondly, for all samples, dense or loose, made of clumps or polygons, it was established that the angle of friction ϕ_t at the end of biaxial tests increases with α and is independent of the initial state. This result is a proof of the role of the grain envelope in the mechanical behaviour rather than some inter-granular imbrication considerations. In this section we will try to gather evidence for these proposals.

6.1. Contact proportion evolution for dense samples made of clumps

Single contacts are mainly involved in all the grains samples tested, Fig. 5 ((CE) contacts for polygons or (CE)-type (i) contacts for clumps – Fig. 2(b)). During loading, it can be noted that the percentage of single contacts increases. Because dense samples were prepared with no friction, Solid fraction of each assemblies of grains subjected to isotropic loading is constant and always maximal. As a consequence, even if samples can exhibit slight contractancy (related to dimensionless contact stiffness κ , [34]), the total number of contacts in each sample during a vertical compression systematically decreases. Therefore, in order to compare different contact type proportions in different phases of the test, we suggest balancing the decrease in the total number of contacts using the coefficient $\omega^* = N_{\varepsilon_b}^*/N_{\varepsilon_a}^*$, $N_{\varepsilon_a}^*$ and $N_{\varepsilon_b}^*$ represent the total number of neighbouring contacts⁴ at the given vertical strains ε_1 (ε_a or ε_b) in the samples. Here, we suggest focusing on the evolution of two new contact groups for clumps:

- (SC) single contact between grains, known as *simple* contact,
- (CC) multiple contacts between grains, hereafter called *complex* contacts.

These two new groups can be examined in Fig. 10.

We observed the evolution of clump contact numbers of each group between two successive stages by normalising this evolution

³ For convenience we resort to the vocabulary pertaining to 3D triaxial tests.

⁴ When two grains are in contact via 1, 2 or 3 contact points, only one contact is counted.

² Note that triangle is the only shape with 3 edges.

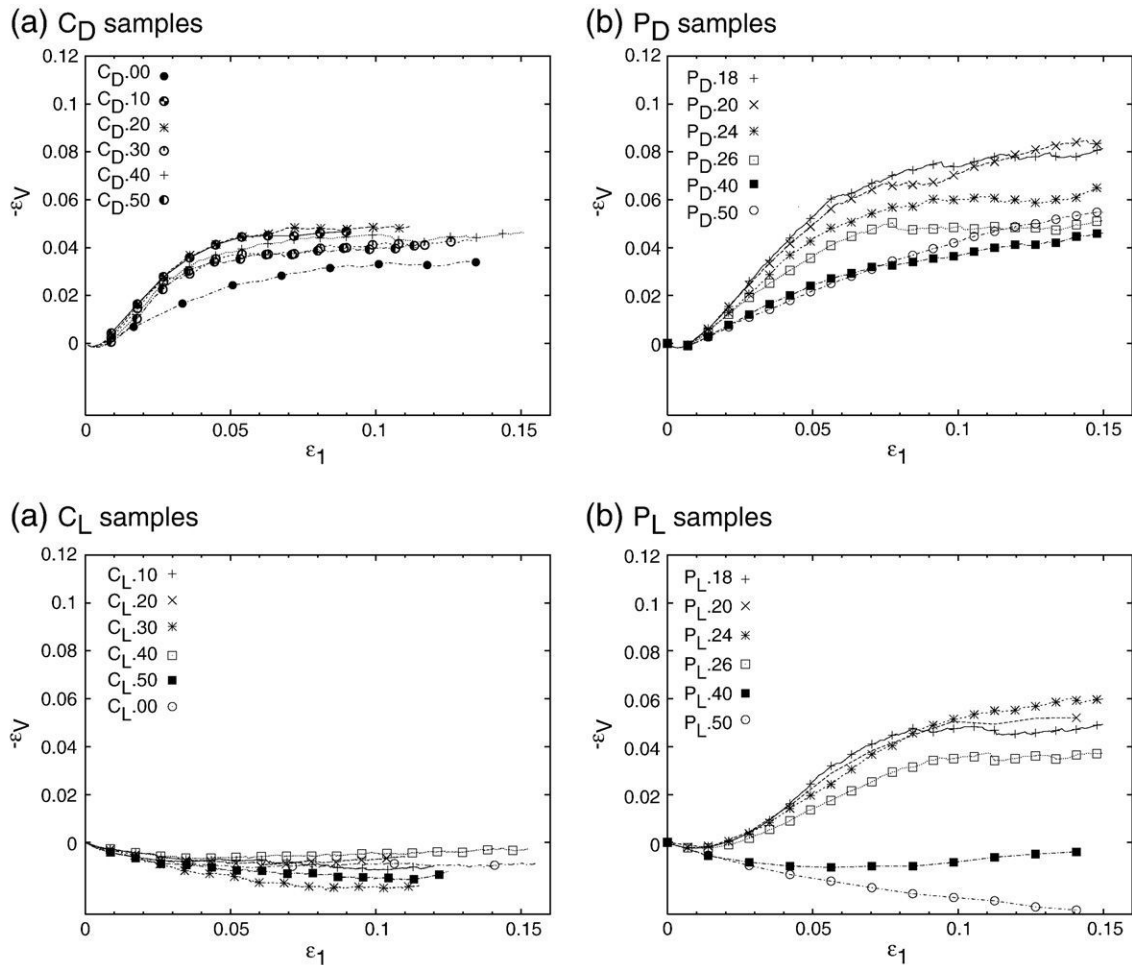


Fig. 9. Volumetric changes (computed in 2D corresponding to the area) during vertical compression for loose and dense samples made of clumps and of polygons. Positive $-\varepsilon_v$ implies an increase of the sample volume.

with ω^* . We thus defined a new variable $\lambda = \omega^* \cdot N_{\varepsilon_a} / N_{\varepsilon_b}$, where N_{ε_a} and N_{ε_b} denote the number of (SC) or (CC) on two different levels ε_a and ε_b of the vertical strain ε_1 . In Fig. 11(a), λ evolution is calculated between $\varepsilon_a = \varepsilon_i$ (isotropic state) and $\varepsilon_b = \varepsilon_p$ (maximum stress deviator). We can observe that for $\alpha = 0.10$, λ is smaller than 1 for (CC) and greater than 1 for (SC). This can be regarded as a transformation of (CC) into (SC) between these two stages. If all the complex contacts transformed into simple, graphic points were at an equal distance from 1, $1 - \lambda_{(CC)} = \lambda_{(SC)} - 1$. If $1 - \lambda_{(CC)} > \lambda_{(SC)} - 1$, it means that some complex contacts transform into simple contacts but some of them also disappear.

When α goes to 0.5, these transformations are still active but with less intensity. Geometrical imbrications between clumps increase with α and are “more difficult to lose” during the biaxial tests. It is also interesting to observe that λ seems to reach a threshold when

$\alpha \geq 0.4$, Fig. 11(a). This last observation can be correlated to the evolution of ϕ_p , which also reaches a threshold for the same value of α , Fig. 8(a).

Focusing on λ between the peak and the critical state, $\varepsilon_a = \varepsilon_p$ and $\varepsilon_b = \varepsilon_c$, Fig. 11(b), we can observe that the increase of simple contacts is small for every α ($\lambda_{(SC)} - 1 \leq 0.1$) and complex contacts are mainly lost $1 - \lambda_{(CC)} > 0.1$, especially when α is small. The greater α is, the smaller the proportion of complex contacts lost (grain imbrications are destroyed less). This may be a clue that ϕ_t of clumps increases with α , as seen in Fig. 8(a). Nevertheless, some new investigations on the evolution of contact orientations are proposed in the next section.

6.2. Evolution of contact fabric for C_D samples

Contact direction and its evolution during the vertical compression tests are often analysed [35]. Focusing on the first part of the mechanical behaviour, from the isotropic state to the stress peak for example, it is well known that in dense samples, contacts are mainly lost in the extension direction and gained in the direction of compression. [36]. In Fig. 12(a) to (d), for two values of α , we present statistical analysis of the evolution of contact direction by the evaluation of $\mathcal{P}(\theta) = N_{\varepsilon_b}(\theta) / N_{\varepsilon_a}(\theta)$, where ε_a and ε_b correspond to two successive vertical strains levels and where $N_{\varepsilon_x}(\theta)$ is the number of contacts in the direction θ . $\mathcal{P}(\theta) = 1$ expresses that the number of contacts in the direction θ remains constant between the two configurations studied. If $\mathcal{P}(\theta) < 1$, contacts are lost and if $\mathcal{P}(\theta) > 1$,

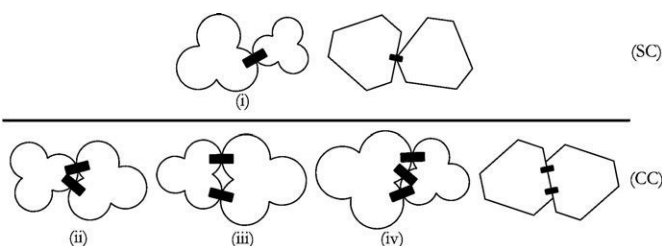


Fig. 10. Contact types for clumps and polygons: simple contacts (SC) and complex contacts (CC).

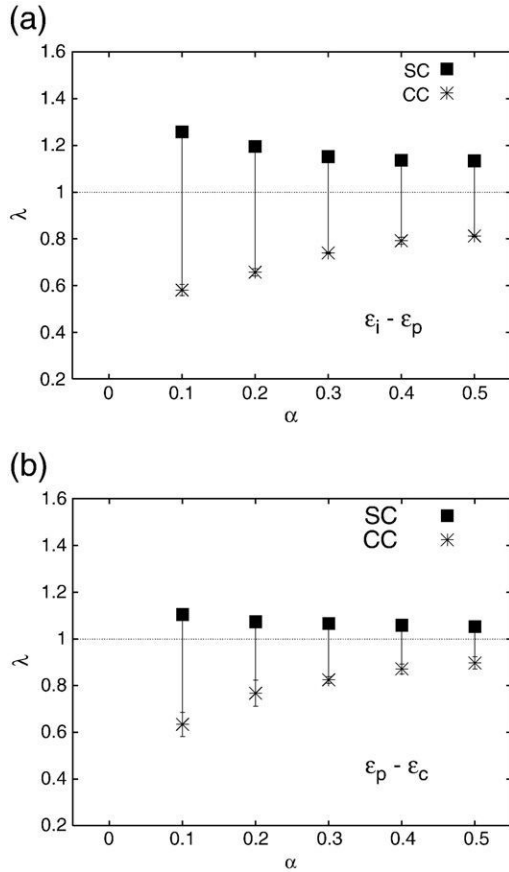


Fig. 11. Transformation of complex clump contacts into simple contacts, quantified by λ and evaluated between the ϵ_i and ϵ_p for figure (a), and between ϵ_p and ϵ_c for figure (b).

contacts are gained in the direction θ . Integrated over θ , $\langle \mathcal{P} \rangle$ is a global evaluation of the proportion of gained or lost contacts.

We focus on the evolution of contact anisotropy between the isotropic state and the peak, Fig. 12(a) for $\alpha=0.2$ and Fig. 12(c) for $\alpha=0.5$, we can observe that there is no contact gain in any direction: in the compression direction, the number of contacts remains constant $\mathcal{P}(\theta) \approx 1$ and the number of contacts decreases in the extension direction $\mathcal{P}(\theta) < 1$. The mean value of \mathcal{P} over θ is smaller than 1 for both α discussed here and also for the other α studied. During the vertical compression of C_D , sample contacts are mainly lost. Finally, we noticed that the greater α is, the smaller the amount of contacts lost in the extension direction. By analysing the contacts change in direction between the peak and the critical state, ϵ_p to ϵ_c , Fig. 12(b) and (d), opposite tendencies emerge: contacts are mainly lost in the compression direction and gained in the extension direction, with a less intensive effect for $\alpha=0.5$, Fig. 12(d). At this stage of analysis, we are not yet able to distinguish the nature of the contacts involved in these observations. An analysis of clustered contacts, as outlined below, is thus necessary.

We now suggest the same contact direction analysis but for (SC) and (CC) groups (simple and complex contacts). Statistical analysis of the evolution of contact orientation from the isotropic state ϵ_i to the peak ϵ_p for (SC) and (CC) groups is shown in Figs. 12(e) to (h). On one hand, Fig. 12(e) and (f) show that in the compression direction (SC) contacts are gained ($\alpha=0.2$) or are kept ($\alpha=0.5$). (SC) contacts are mainly lost in the extension direction, with a more pronounced amplitude when α is small. On the other hand, we can observe that (CC), Figs. 12(g) and (h), are lost in every direction with some variations depending on θ . Nevertheless, complex contacts are more persistent when α is greater ($\langle \mathcal{P} \rangle$ is greater for $\alpha=0.5$ because of grain imbrications).

The statistical analysis of the evolution of contact direction between the peak ϵ_p and the critical state ϵ_c shown in the Figs. 12(i) to (l) confirms the tendency shown in Figs. 12(b) and (d): simple and complex contacts are lost in the compression direction. For (SC) with $\alpha=0.2$, $\langle \mathcal{P} \rangle = 1$, Fig. 12(i): although the number of (SC) decreases in the compression direction and increases in the extension direction, the number of simple contacts remains constant during the mechanical test from the peak to the critical state. When $\alpha=0.5$, the number of simple contacts decreases ($\langle \mathcal{P} \rangle = 0.9$, especially in the compression direction. Complex contacts are the ones that are lost the most ($\langle \mathcal{P} \rangle$ is always lower than 1, regardless of the value of α). Nevertheless, it is desirable to make a distinction based on α : the amount of (CC) lost is smaller for $\alpha=0.5$ ($\langle \mathcal{P} \rangle = 0.8$, Fig. 12(k)) than for $\alpha=0.2$ ($\langle \mathcal{P} \rangle = 0.7$, Fig. 12(l)). The proportion of (CC) lost in the compression direction is bigger for $\alpha=0.2$, like if vertical contact chains were more unstable or less persistent when α tends to 0.

Further studies, taking into account the intensity of contact forces and their propensity to be stronger in the case of complex contacts [37] would provide more certainty about possible links between the observations made above and improvement of the mechanical property ϕ_t measured at ϵ_c , Fig. 8(a).

6.3. Evolution of comparative contact proportions in compression tests for clumps and polygons

Focusing on the critical phase only, contact observations are now based on the division into two contacts groups corner-to-edge (CE) and edge-to-edge (EE) (Fig. 2(b)). The evolution of (CE) contacts according to α is shown in Fig. 13. (EE) contacts can be easily deduced by subtracting (CE) contacts percentage from 100%. On one hand, the percentage of (CE) contacts does not depend on the initial Solid fraction of the sample; dense and loose samples exhibit a similar trend. On the other hand, (CE) contact percentages for C_D and C_L samples decrease linearly with α . A different tendency is observed for P_D and P_L samples where the contact percentage remains more or less the same except for $\alpha=0.5$. We can even observe that when $\alpha=0.5$, (CE) contacts and (EE) contact percentages are close: for this special value of α , clump and polygon envelopes converge.

6.4. Influence of shape on local strain analysis

We focused on the strain localisation in the samples in order to study the macroscopic rupture and its origin. Two approaches were used: *local strain maps* and *shear localisation indicator* S_2 [38]. By comparing particle kinematics in the isotropic state $\epsilon_i = \epsilon_i = 0$ and in the deformed stage ϵ_1 , we calculated local strains using Delaunay triangulation as in [36] (Delaunay triangle corners correspond to the mass centers of particles). Using the second strain invariant, $I_{e_d} = \epsilon_I - \epsilon_{II}$, where ϵ_I and ϵ_{II} are respectively the major and the minor principal strains, we illustrate the shear localisation in Fig. 14. We should notice that such shear localisation patterns, also called shear bands, are often observed on granular materials confined by more or less rigid boundaries, or even numerical or experimental considerations [36,39–41]. Even if the number of shear bands depends on the macroscopic strain levels applied to samples, different patterns (multiple shear zones) seem to exist when periodic boundary conditions are used [42].

The shear localisation indicator S_2 is defined as

$$S_2 = \frac{1}{N_t} \frac{\left(\sum_{i=1}^{N_t} I_{e_d} \right)^2}{\sum_{i=1}^{N_t} I_{e_d}^2}, \quad (2)$$

where I_{e_d} is the second invariant of the strain tensor and N_t is the total number of Delaunay triangles. In a sense, value of S_2 can be regarded as a percentage of a distorted sample area.

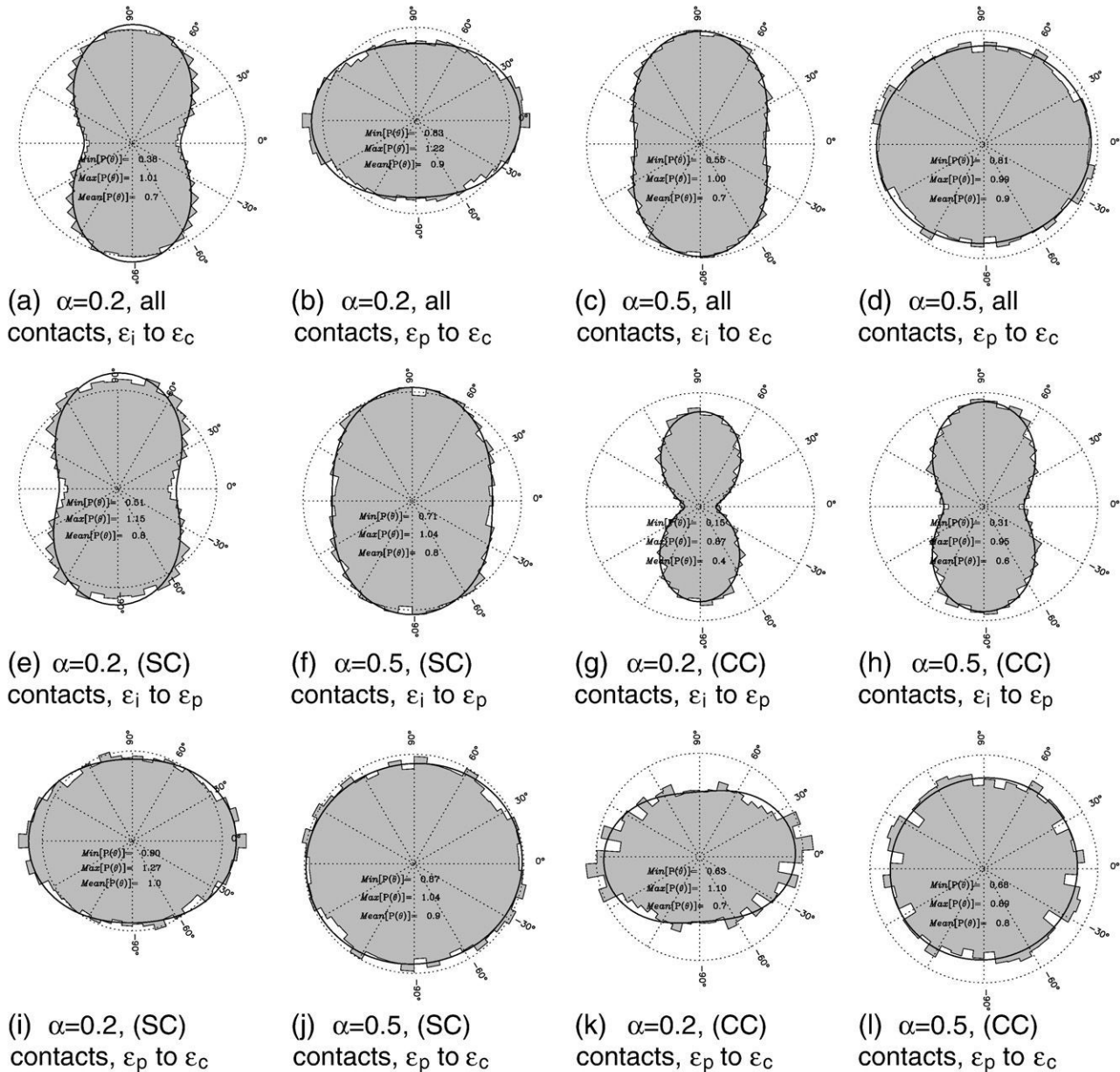


Fig. 12. C_D samples. Histogram analysis of the evolution of contact directions for all the contacts (panels (a) to (d)) or for (SC) and (CC) (panels (e) to (l)). Histograms calculated over 25 classes of 7.2° each, between two successive strains levels: ε_i to ε_p for the panels (e) to (h) and ε_p to ε_C for the figures (i) to (l). When all the contacts are taken into account (panels (a) to (d)), the statistics are calculated over approximately 40,000 contacts for the isotropic state, 30,000 contacts at the peak and 29,000 at the critical state. The circle radius drawn in dashed line is 1.

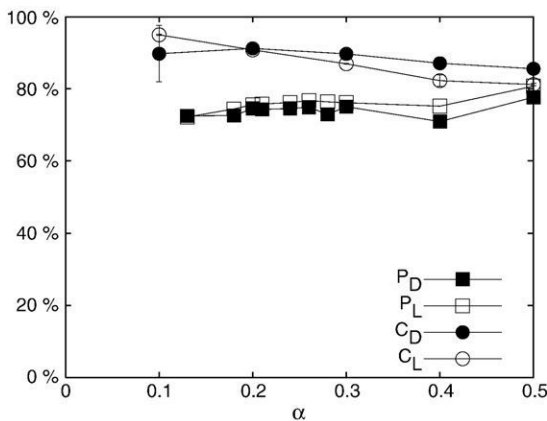


Fig. 13. Corner-to-edge contacts ((CE) see Fig. 2(b)) percentage at critical state, ε_c . Comparison between clumps and polygons.

Fig. 15 gives the evolution of S_2 according to ε_1 for several dense and loose samples made of clumps and polygons. Regardless of the sample studied, the sheared area always reaches a maximum which is at least greater than 50%. From evolution of S_2 , we may encounter two types of behaviour: samples for which S_2 reaches a maximum and then decreases and stabilises, and a second type where S_2 increases asymptotically towards a maximum.

We have observed that when S_2 reaches a maximum and later decreases to reach a threshold value, it always corresponds to samples which were identified as dense samples because $\phi_p > \phi_t$ (for example $C_{D,50}$, $P_{D,24}$, $P_{L,28}$ samples of the Fig. 14). On the contrary, when $\phi_p \sim \phi_t$, samples can be classified as loose samples. In this case, S_2 continuously increases from $\varepsilon_1 = 0$ to 10% to eventually reach a threshold close to $S_2 \approx 60\%$.

In the case of dense samples, the asymptotic value of S_2 is interesting because it clearly shows higher values for P_D samples than for C_D samples. Coupling this quantitative result with the qualitative

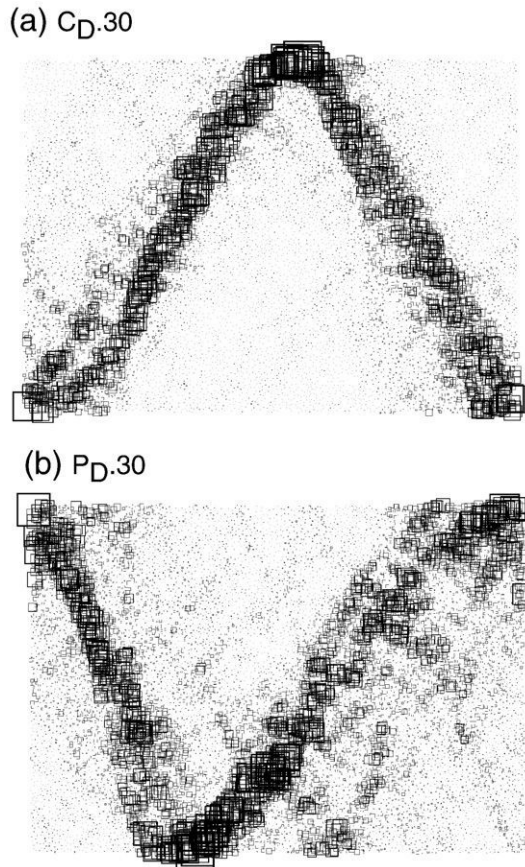


Fig. 14. Shear maps on dense samples made of grains with $\alpha=0.3$ calculated from the isotropic state to $\varepsilon_1 = 13.5\%$. Black square symbols are proportional to the amplitude of the second invariant of the strains I_{e_2} .

observation of shear maps like in the Fig. 14, it is obvious that localised zones in P_D samples are wider than in C_D samples. This result is consistent with the overall dilatancy of samples: P_D samples globally expand more than C_D ones. For loose samples, the sheared area always corresponds to approximately 60% of the samples, regardless of the grain shape.

7. Conclusions and discussion

The aim of this article was to present some new investigations on the mechanical influences of particle shape in granular assemblies in

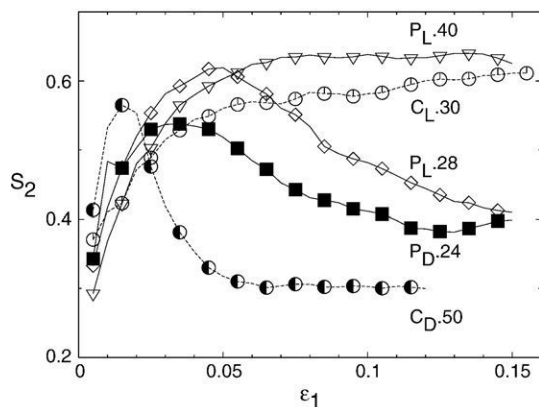


Fig. 15. Shear indicator evolution during a vertical compression.

the framework of numerical simulations performed with Discrete Element Method. First, a grain geometry parameter α was defined by the CEGEO research team. For particles called clumps, made of 3 overlapping discs, α is a measure of the grain concavity. 6-edged convex polygonal grains were also ruled by α . The overall envelope depending on α for each type of particles used in the studied granular model was the common feature. Our numerical simulations were performed with the Discrete Element Method adapted to each grain shape. For particles made of discs (clumps), the commercial code PFC^{2D} by ITASCA was used. For polygonal particles, we developed our own computer code which implements special contact detection between objects in the framework of Molecular Dynamic approach. In this article, we highlighted that changing the grain geometry, influences granular assembly mechanical behaviour under the classical vertical compression test in 2D. More complex grain shapes allow higher levels of internal friction angle and large volumetric strains to be reached compared to simple discs. Some clear differences in the behaviour of polygon (convex) and clump (non-convex) assemblies were shown. We should also note that the particle shapes chosen also demonstrate similarities, caused by the global envelope, that justify the comparison. The generation and compaction of granular assemblies were presented. By using two extreme values of the inter-granular friction angle μ , dense and loose samples were prepared, both for samples made of clumps and polygons.

Firstly, by focusing on the macroscopic mechanical behaviour of our granular model we show that loose samples composed of polygons with low values of α present behaviour typical to moderately dense granular samples. For these granular materials, the initial contracting stage was not only due to contact stiffness, but was also influenced by large inter-granular reorganisation. Apart from this, loose and dense samples of all shapes behaved as expected (loose samples only show contracting behaviour while dense ones mostly exhibit major dilatancy), showing similar behaviour when discussing friction residual angles ϕ_r or contact percentages. All samples show higher values of internal friction angles ϕ_p and ϕ_c than samples made of only circular grains where each particle is a disc. The correlations between shape parameter α and friction angles are different for clumps and polygons. On one hand, for dense clump samples ϕ_p increases with α and seems to reach an asymptotic value $\phi_p = 40^\circ$. On the other hand, ϕ_p linearly decreases when α shifts from 0.13 to 0.5. In this case, the particular case of the triangular shape ($\alpha=0.5$) is also discussed briefly. The overall dilatancy of clump samples is greater than that of disc assemblies, but spectacularly smaller than dilatancy of polygons.

Secondly, on the granular scale, we suggested correlating macroscopic observations by means of contact evolution analysis, which led us to introduce several groups of contacts between particles. Thus, we observed that multiple contacts between clumps transform into simple contacts and that this process depends on the size of concavities, i.e. α . We tend to associate this with an increase of shear resistance in the case of dense granular samples made of clumps. However, for a better understanding of the role of α in the magnitude of contact forces and their influence on the macroscopic repercussions, complementary studies need to be carried out.

Focusing on granular assembly failure, we studied the localisation of shear bands and tried to characterise it by a scalar. It was observed that reflecting shear bands were thinner in dense samples made of clumps than in those made of polygons, regardless of the α type, thus highlighting the evident effects of the geometrical imbrications of clumps. Polygon samples gradually create wide shear bands, while for samples made of clumps, the appearance of shear bands are more immediate.

Although the meaning and implications of the parameters α have been presented in this article, it needs to be clarified further. Nevertheless, from the comparisons between polygons and clumps, two trends seem to emerge: for very dense samples made of clumps, a large α naturally implies imbrications between particles. α is thus a

measure of clump concavity. With the simulations exposed in this article, we can deduce that the larger the concavities are, the higher the angle of friction at the peak ϕ_p is.

For the samples made of polygons, this does not apply. Indeed, there are no imbrications between the grains and α is thus a measure of grain sphericity. We have shown that in dense samples made of polygons, the percentage of a single contact in the isotropic state increases with α . In corollary, we can observe that the angles of friction peak decrease slightly with α .

For loose samples P_L or C_L , or for P_D and C_D samples close to the critical state, ϕ_t is the parameter which characterises the failure. We have shown that for large strains, contacts between grains are mostly single. Therefore, clump imbrications are less involved in the evolution of ϕ_t . Furthermore, ϕ_t , which increases linearly with α , increases with the same rate regardless of the grain shape. α should thus be only regarded as a parameter of spherical grains.

Acknowledgments

This study was carried out as part of a CEGEO research project (<http://www.granuloscience.com/CEGEO/>). The authors would like to express special thanks to F. Radjai, C. Nouguier for fruitful discussions and to F. Nicot for his very useful suggestions. The authors are indebted to J.J. Moreau for his guidance on algorithm for contact detection between polygon objects.

References

- [1] J. Lanier, M. Jean, Experiments and numerical simulations with 2D-disks assembly, Powder technology (special issue on Numerical simulations of discrete particle systems) 109 (2000) 206–221.
- [2] C. Thornton, J. Lanier, Uniaxial compression of granular media: numerical simulations and physical experiment, in: R.P. Behringer, J. Jenkins (Eds.), *Powders and Grains 97*, Balkema, Rotterdam, 1997, pp. 223–226.
- [3] M. Oda, K. Iwashita (Eds.), *Mechanics of Granular Materials, An Introduction*, A.A. Balkema, ISBN: 90-5410-461-9, 1999.
- [4] K. Iwashita, M. Oda, Rotational resistance at contacts in the simulation of shear band development by DEM, *ASCE Journal of Engineering Mechanics* 124 (1998) 285–292.
- [5] A. Tordesillas, D.C. Stuart, Incorporating rolling resistance and contact anisotropy in micromechanical models of granular media, *Powder Technology* 124 (2002) 106–111.
- [6] F. Gilabert, J.-N. Roux, A. Castellanos, Computer simulation of model cohesive powders: influence of assembling procedure and contact laws on low consolidation states, *Physical Review E (Statistical, Nonlinear, and Soft Matter Physics)* 75 (2007) 011303.
- [7] C. Salot, P. Gotteland, P. Villard, Influence of relative density on granular materials behavior: DEM simulations of triaxial tests, *Granular Matter* 11 (4) (2009) 221–236.
- [8] E. Azema, F. Radjai, R. Peyroux, G. Saussine, Force transmission in a packing of pentagonal particles, *Physical Review E (Statistical, Nonlinear, and Soft Matter Physics)* 76 (1) (2007) 011301.
- [9] B. Saint-Cyr, C. Voivret, D.J.-Y., F. Radjai, P. Sornay, Effect of shape nonconvexity on the shear strength of granular media, in: *Powders and grains 2009*, AIP Conference Proceedings, Materials Physics & Applications, vol. 1145, Golden, CO USA, 2009, pp. 389–392.
- [10] K. Szarf, G. Combe, P. Villard, Influence of the grains shape on the mechanical behavior of granular materials, in: *Powders and grains 2009*, AIP Conference Proceedings, Materials Physics & Applications, vol. 1145, Golden, CO USA, 2009, pp. 357–360.
- [11] D. Rapaport, *The Art of Molecular Dynamics Simulation*, Cambridge University Press 0-521-82568-7, 1995.
- [12] Itasca Consulting Group Inc., PFC^{2D}, Particle Flow Code in Two Dimensions-User's Guide, Itasca Consulting Group Inc., 1999.
- [13] P.A. Cundall, O.D.L. Strack, A discrete numerical model for granular assemblies, *Géotechnique* 29 (1) (1979) 47–65.
- [14] A. Atman, P. Claudin, G. Combe, Departure from elasticity in granular layers: investigation of a crossover overload force, *Computer physics communications* 180 (4) (2009) 612–615.
- [15] J.-N. Roux, G. Combe, On the meaning and microscopic origins of “quasistatic deformation” of granular materials, *Proceedings of the EM03 ASCE conference*, CD-ROM published by ASCE, Seattle, 2003.
- [16] M. Allen, D. Tildesley, *Computer simulation of liquids*, Oxford Science Publications, 1994.
- [17] S. Luding, Stress distribution in static two-dimensional granular media in the absence of friction, *Physical Review E (Statistical, Nonlinear, and Soft Matter Physics)* 55 (4) (1997) 4720–4729.
- [18] M. Hopkins, On the ridging of intact lead ice, *Journal of Geophysical Research* 99 (C8) (1994) 16,351–16,360.
- [19] H.-G. Matuttis, Simulation of the pressure distribution under a two-dimensional heap of polygonal particles, *Granular matter* 1 (2) (1998) 83–91.
- [20] F. Alonso-Marroquin, S. Luding, H.J. Herrmann, I. Vardoulakis, The role of the anisotropy in the elastoplastic response of a polygonal packing, *Physical Review E (Statistical, Nonlinear, and Soft Matter Physics)* 71 (2005) 051304.
- [21] F. Alonso-Marroquin, H.J. Herrmann, Calculation of the incremental stress-strain relation of a polygonal packing, *Physical Review E (Statistical, Nonlinear, and Soft Matter Physics)* 66 (2) (2002) 021301, doi:10.1103/PhysRevE.66.021301 <http://dx.doi.org/10.1103/PhysRevE.66.021301>.
- [22] J. Moreau, Private communication (2006).
- [23] G. Saussine, C. Cholet, P.-E. Gautier, F. Dubois, C. Bohatier, J. Moreau, Modelling ballast behaviour under dynamic loading. Part 1: A 2D polygonal discrete element method approach, *Computer Methods in Applied Mechanics and Engineering* 195 (2006) 2841–2859.
- [24] G. Combe, J.-N. Roux, Discrete numerical simulation, quasistatic deformation and the origins of strain in granular materials, in: H. DiBenedetto, T. Doanh, H. Geoffroy, C. Sauzeat (Eds.), *3rd International Symposium on Deformation Characteristics of Geomaterials*, Lyon, France, 2003, pp. 1071–1078.
- [25] G. Combe, <http://pastel.paristech.org/00000051>/Origines microscopiques du comportement quasi-statique des matériaux granulaires, Ph.D. thesis, École Nationale des Ponts et Chaussées, Champs-sur-Marne, France (2001). URL <http://pastel.paristech.org/00000051/>.
- [26] J.-N. Roux, F. Chevoir, Discrete numerical simulation and the mechanical behavior of granular materials, *Bulletin des Laboratoires des Ponts et Chaussées* 254 (2005) 109–138.
- [27] B. Emeriault, B. Cambou, A. Mahboudi, Homogenization for granular materials: non reversible behaviour, *Mechanics of cohesive-frictional materials* 1 (1996) 199–218.
- [28] B. Cambou, P. Dubujet, F. Emeriault, F. Sidoroff, Homogenization for granular materials, *European J. of Mechanics A/Solids* 14 (1995) 255–276.
- [29] J. Bathurst, L. Rothenburg, Micromechanical aspects of isotropic granular assemblies with linear contact interactions, *Journal of Applied Mechanics* 55 (1988) 17–23.
- [30] J. Bathurst, L. Rothenburg, Note on a random isotropic granular material with negative poisson's ratio, *International Journal Engineering Science* 26 (1988) 373–383.
- [31] B. Chareyre, P. Villard, Dynamic spar elements and DEM in two dimensions for the modeling of soil-inclusion problems, *Journal of Engineering Mechanics* 131 (2005) 689–698.
- [32] I. Agnolin, J.-N. Roux, Internal states of model isotropic granular packings. I. Assembling process, geometry, and contact networks, *Physical Review E (Statistical, Nonlinear, and Soft Matter Physics)* 76 (6) (2007) 061302.
- [33] I. Agnolin, J.-N. Roux, Internal states of model isotropic granular packings. III. Elastic properties, *Physical Review E: Statistical, Nonlinear, and Soft Matter Physics* 76 (6) (2007) 061304.
- [34] J.-N. Roux, G. Combe, Quasistatic rheology and the origins of strain, *Comptes Rendus de l'Académie des Sciences, Série IV - Physics-Astrophysics (Comptes Rendus Physique)* 3 (2) (2002) 131–140.
- [35] R. Behringer, J. Jenkins (Eds.), *Powders and Grains 97* – International Conference on Powders & Grains – (3rd – 1997 – Durham, N.C., USA), A.A. Balkema, Rotterdam, 1997.
- [36] F. Calvetti, G. Combe, J. Lanier, Experimental micromechanical analysis of a 2D granular material: relation between structure evolution and loading path, *Mechanics of Cohesive-frictional materials* 2 (1997) 121–163.
- [37] E. Azéma, F. Radjai, R. Peyroux, Force transmission in a packing of pentagonal particles, *Physical Review Letter* 76 (2007) 011301.
- [38] A. Sornette, P. Davy, D. Sornette, Fault growth in brittle–ductile experiments and the mechanics of continental collisions, *Journal of geophysical research* 98 (1993) 12111–12140.
- [39] J. Lanier, Étude expérimentale des lois de comportements en grandes déformations à l'aide d'une presse réellement tridimensionnelle, *Cahier du groupe français de Rhéologie* 4 (1976) 53–57.
- [40] J. Lanier, M. Jean, Experiments and numerical simulations with 2D-disks assembly, *Power Technology* 109 (2000) 206–221.
- [41] J. Desrués, G. Viggiani, Strain localization in sand: an overview of the experimental results obtained in Grenoble using stereophotogrammetry, *International Journal for Numerical and Analytical Methods in Geomechanics* 28 (2004) 279–321.
- [42] M. Kuhn, K. Bagi, Specimen size effect in discrete element simulations of granular assemblies, *Journal of Engineering Mechanics* 135 (2009) 485–492.

2.3. CONCLUSIONS

Chapter 3

Application: Arching Effect Above Buried Pipes

Having observed how the change of grain shape affects the mechanical behaviour of granular material and how behaviour of assemblies of complex shapes is closer to real granular soils than behaviour of assemblies of discs, it was interesting to apply this experience to a real engineering problem.

Underground pipes are widely used in various fields of engineering. Among the typical pipe application is transport of fluids under pressure (oil, gas, water) or with a free surface (sewage, drains). Moreover, the large pipes can be used as tunnels or culverts in order to allow water flow or animal crossing under railroad or highway embankments. The interaction between the pipe and surrounding soil is complex and depends on a number of parameters like geometry and mechanical properties of the pipe, geological conditions, loading. Historically due to the poor understanding of this complex interactions the buried pipes were typically thick and stiff and did not incorporate the soil response in their mechanical behaviour. With the introduction of new materials like sheet steel or plastic new design methods were developed which allowed constructing flexible conduits which interacted with the surrounding soil in transferring the load. This study is focused on the load transfer above a flexible buried unpressurised pipe.

The materials used nowadays in underground pipes can differ, but generally can be divided into three major groups: concrete/ceramics, metal and plastics. Various types of plastics are used, the most common ones being: PE (Polyethylene) and HDPE (High Density Polyethylene), PVC (Polyvinyl Chloride), PP (Polypropylene) and GRP (Glass-Reinforced Plastic). The type of the material used depends on the particular task the conduit is supposed to perform. For example in leechate collection systems under ore heaps the wastewater is chemically reactive and the pipe material must be resistant.

When comparing the pipe stiffness to the stiffness of the surrounding material (envelope), the pipes can be stiff or flexible. The stiff pipe failure mode is rapid wall crushing that occurs when the stress in the pipe exceeds the strength of the pipe material. In case of flexible pipes the walls can locally buckle or the ring deflection of the pipe can be too high. The second fail mode can lead to pipe inversion. In some applications like water collection systems under landfills the hydraulic properties of the buried pipes are more important than the mechanical performance and since a replacement of a pipe can be difficult, inversion of the pipe can sometimes be accepted.

3.1 Theory and Practice

There exist a number of design methods applicable for buried pipes. The design methods are based on the engineering experience and observations of real construction and comply with the limit state design approach. In general the pipes can be considered as flexible or stiff and the pipes can be buried in a narrow ditch or placed on a plane. These factors influence the repartition of load over the pipe affecting the so called *arching effect*. The typical approach is to consider the pipe in plane strain conditions.

3.1.1 Pipe Stiffness

The aforementioned stiff and flexible pipe distinction can be quantified experimentally using the S parameter (Kunecki, 2006). The stiffness of the pipe can be expressed as a relation between a force acting on a pipe sample and the resulting deformation.

$$S = \frac{F \cdot f}{L \cdot dv} \quad (3.1)$$

where:

S	is the pipe stiffness	$[Pa]$,
F	is the force acting on a unit of length of the pipe	$[N]$,
L	is the length of the pipe sample	$[m]$,
dv	is the deflection of the pipe	$[m]$,
f	is a deflection coefficient	$[-]$.

The deflection coefficient includes a correction factor for ovality of the deformed specimen and is given with the following formula:

$$f = 10^{-5} \cdot \left(1860 + 2500 \frac{dv}{d_m} \right) \quad (3.2)$$

where:

d_m is the diameter of the pipe $[m]$.

The European Committee for Standardization in EN codes and the International Organization for Standardization in ISO standards use the following pipe stiffness definition:

$$S = \frac{E \cdot I}{d_m^3} \quad (3.3)$$

where:

E	is the Young's modulus of the pipe	$[Pa]$,
I	is the moment of inertia of the pipe wall section, $I = h^3/12$	$[m^3]$,
d_m	is the diameter of the pipe	$[m]$.

Different codes propose different experimental protocols to measure the pipe stiffness. For example international code ISO 9969 suggests a compression of three equal specimens between two parallel, horizontal walls to obtain 3% of deflection:

$$S_i = \frac{0.0186 + 0.025 \cdot Y_i \cdot F_i}{D_w \cdot L_i \cdot Y_i} \quad (3.4)$$

where:

F_i	is the force corresponding to 3% of deformation of i-th sample	$[kN]$,
L_i	is the length of the i-th pipe sample	$[m]$,
D_w	is the internal diameter	$[m]$,
Y_i	is the deflection corresponding to 3% of pipe deformation	$[m]$.

American code ASTM F894 suggests stiffness measurement at the 5% deflection level; The stiffness in this code is expressed in $[psi]$. German DIN 16961 code uses (3.3) modified by changing the pipe diameter with radius, $S[Pa]$.

3.1.2 Marston-Spangler

The classical method for pipe design is the Marston-Spangler method based on the works of (Marston, 1930) and (Spangler, 1933). Marston postulated that the load acting on the pipe comes from the external loading (like traffic or landfill) and the weight of the soil above the pipe. The soil weight contribution depends on the parameters of the soil but also on the installation conditions. Spangler introduced the so-called bedding factor that takes into account the dimensions of the ditch and the contact between the pipe and the ditch. The theory is based on considerations of forces acting on a virtual slice of soil placed within a prism above the pipe.

3.1.2.1 Stiff Pipe in a Ditch

Marston considered a narrow and deep trench excavated in the residual soil. He considered a band of soil over the pipe as in Figure 3.1 (Moser, 2001; Kunecki, 2006).

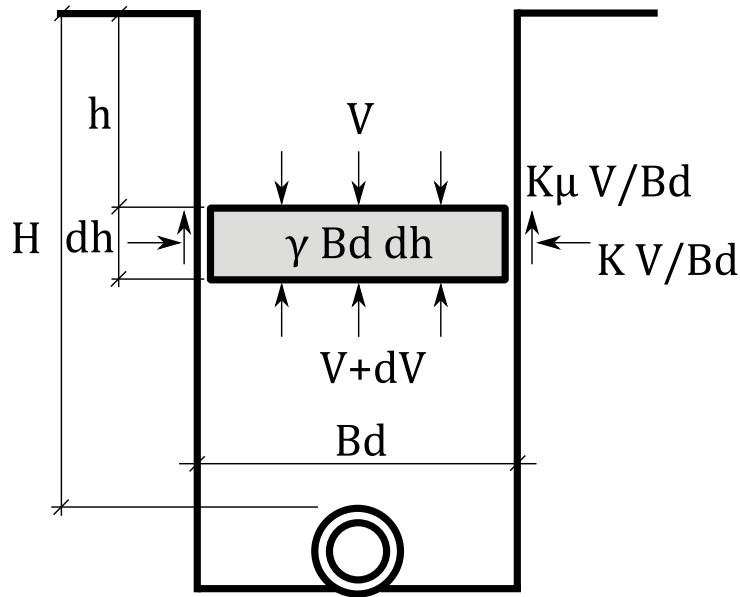


Figure 3.1: The basis of Marston approach, a pipe in a ditch and the loads acting on a strip of soil above it

The settlements of the backfill and the pipe are resulting in shearing forces on the sides of the trench. Cohesion is neglected as it needs time to recreate and cohesionless scenario is less favourable for the pipe. The force on the top of the band $V \left[\frac{N}{m} \right]$ is countered by the force on the bottom, $V + dV$. The differential volume of soil is B_d by dh by one unit of length. Its weight is computed by multiplying the volume by the soil specific weight γ . The horizontal pressure acting on the band is equal to $K \frac{V}{B_d}$, K being the earth pressure coefficient, and the shearing pressure is:

$$F_s = K\mu \frac{V}{B_d} \text{ [Pa]}, \quad (3.5)$$

where μ is the friction coefficient between the walls of the trench and the backfill. To equilibrate the vertical forces acting on the strip of soil:

$$V + \gamma B_d dh = V + dV + 2 \cdot K\mu \frac{V}{B_d} \cdot dh. \quad (3.6)$$

Solution of the equation above for the vertical load at the depth H (the top of the pipe) is the following:

$$W_d = \frac{\gamma B_d^2}{2K\mu} (1 - e^{-2K\mu H}). \quad (3.7)$$

Typically the load is expressed in the form:

$$W_d = \gamma B_d^2 C_d \left[\frac{N}{m} \right], \quad (3.8)$$

with the coefficient:

$$C_d = \frac{1 - e^{-2K\mu \frac{H}{B_d}}}{2K\mu}. \quad (3.9)$$

In the above considerations the earth pressure coefficient K is usually identified with the Rankine's coefficient of active earth pressure $K_a = \frac{1 - \sin\phi}{1 + \sin\phi}$ and the friction coefficient is identified with the internal friction angle $\mu = \tan\phi$ which is not necessarily true (Christensen, 1967). The parameter C_d is a function of $\frac{H}{B_d}$ and $K\mu$ and usually is plotted for different soils in the form of a nomogram (Moser, 2001).

3.1.2.2 Pipe in an Embankment

Apart from a narrow trench situation of Marston (Marston, 1930), Spangler (Spangler, 1933) considered a trench of infinite width as well. This situation is typical for pipes laid on the ground and buried with a backfill or under an embankment. The approach was the same as in the case of a narrow ditch except that a strip of soil selected from a prism was as wide as the external diameter of the pipe, not as wide as a ditch.

Spangler distinguished two scenarios: the ground around the pipe settles more than the top of the pipe (Fig. 3.2b and 3.2d) or the top of the pipe settles more (Fig. 3.2c). The first case may occur for stiff pipes while the second for flexible pipes or in case when a trench is shallow and buried under an embankment. The first situation was called "projection condition"; In this case the shearing stress are acting downwards and are adding additional load on the pipe. The second case was called "ditch conditions"; In the second case the direction of shearing is opposite (upwards), as in the case of a narrow trench, and the load on the pipe is reduced.

Moreover, Spangler also concluded that there exists a certain level above the pipe where there are no shearing forces. Above this level the settlements of the prism above the pipe and the prisms at the sides are the same. This so-called plane of equal settlements defines an "incomplete conditions" when the plane level actually exists in the embankment and "complete conditions" when the equal settlement plane is above the top of the embankment (in other words is virtual) and the shearing between the prisms occurs along the whole height of the soil mass. All the situations described by Marston are schematically presented in Figure 3.2.

The load equation in case of a pipe buried under an embankment is the following:

$$W_c = \gamma B_c^2 C_c, \quad (3.10)$$

where:

- W_c is the load at the top of the pipe $\left[\frac{N}{m} \right]$,
- γ is the specific weight of the backfill soil $\left[\frac{N}{m^3} \right]$,
- B_c is the diameter of the pipe (the width of the soil prism above) $[m]$,
- C_c is the loading coefficient $[-]$.

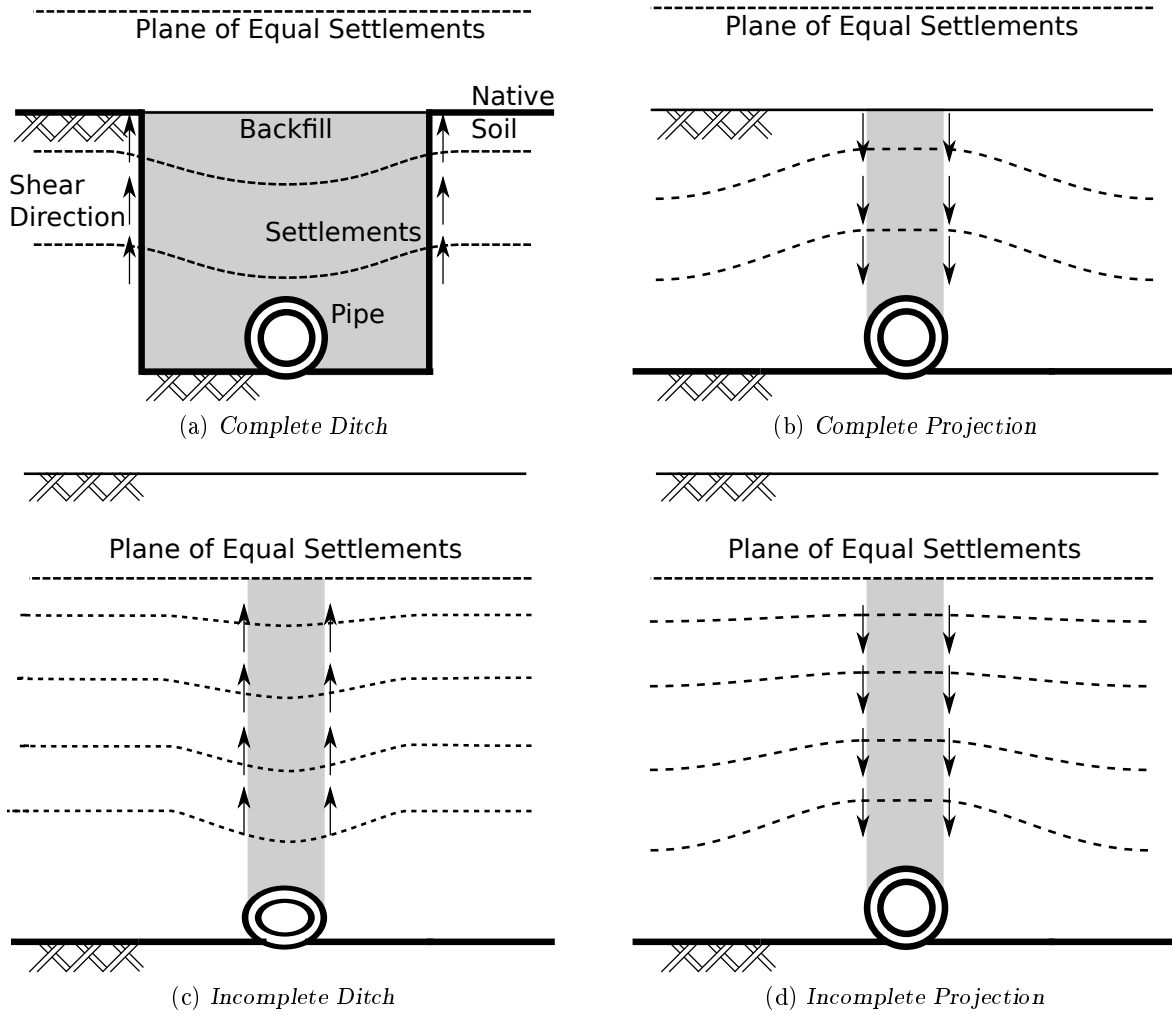


Figure 3.2: Four situations described by Marston and Spangler. Ditch and projection conditions depends whether the shearing stresses are overloading or unloading the pipe; Complete and incomplete conditions depends on the existence of a plane of equal settlements (dashed line). The native soil is denoted with a bold line, backfill level with a thin line, the soil prism in grey

The C_c coefficient can be defined in different ways depending on the direction of shearing and whether the conditions are complete or not. For complete conditions (no real plane of equal settlements) the coefficient is:

$$C_c = \frac{e^{\pm 2K\mu \frac{H}{B_c}} - 1}{\pm 2K\mu}. \quad (3.11)$$

The plus sign appears for the complete projection while the minus sign for the complete ditch.

For incomplete conditions the coefficient is expressed with the equation:

$$C_c = \frac{e^{\pm 2K\mu \frac{H}{B_c}} - 1}{\pm 2K\mu} + \left(\frac{H}{B_c} - \frac{H_e}{B_c} \right) \cdot e^{\pm 2K\mu \frac{H}{B_c}}, \quad (3.12)$$

where H_e is the distance between the top of the pipe and the level of plane of equal settlements [m].

The sign convention is the same as above: plus sign for incomplete projection.

As in the case of ditch case loading coefficient, equation (3.9), the values of the C_c are usually presented in the form of nomograms. The determination of the plane of equal settlements is difficult as it is depending on the stiffness of the pipe, stiffness of the backfill and residual soil, loading and so on. The typical approach is to use tabulated values of a *settlement ratio* r_{sd} which are based on years on engineering practice.

3.1.3 Flexible Pipe

The use of flexible pipes increased with introduction of modern materials like plastic. The classical methods developed for stiff pipes were not predicting the loads acting on the flexible pipes well. Flexible pipe under vertical compression deflects and starts pushing the soil on either side causing passive earth pressure. The large vertical displacements allows the arching effect to develop in the backfill soil. Marston-Spangler method neglected the horizontal stress. In the framework of this method it is possible to consider special case of a pipe in a ditch with a stiffness equal to the stiffness of the soil. In this case, the distribution of load will be dependant only on the geometry of the system:

$$W_c = W_d \cdot \frac{B_c}{B_d}. \quad (3.13)$$

Using the equation (3.8) it is possible to obtain a so-called Marston load equation for flexible pipes:

$$W_c = \gamma B_c B_d C_d, \quad (3.14)$$

but it does not predict the flexible pipe loading much better than a simple prism load equation: $W_c = \gamma B_c H$.

The design of flexible unpressurized pipes complying with the limit state approach takes into account three criteria: deflection, wall-crushing force in the pipe, buckling. These criteria can be verified in different ways.

3.1.3.1 Iowa Formula

Iowa formula (Spangler and Shafer, 1941) is a classical method used to asses the deflections of the pipe. It takes into account the soil-structure cooperation. The assumptions made by Spangler are that the load is uniformly distributed over the entire top part of the pipe; The pressure at the bottom is uniformed as well, but only in the zone of contact between the pipe and the base described with a bedding angle α ; The horizontal pressure at the sides of the pipe acts parabolically over $\beta = 100^\circ$ angle and is dependant on the horizontal deformation of the pipe (see Fig. 3.3).

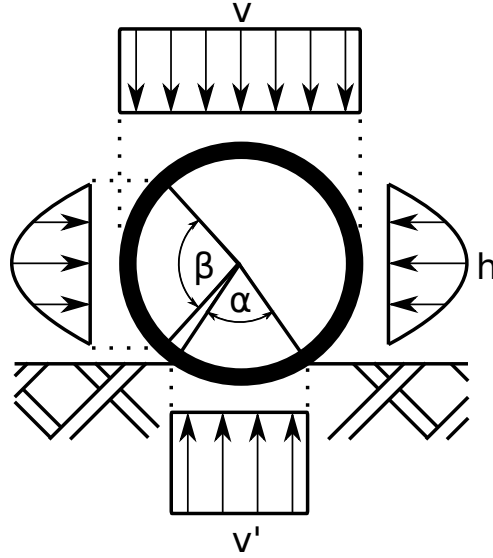


Figure 3.3: *Distribution of loads acting on the pipe in Iowa method (Spangler and Shafer, 1941). The pipe is located on top of residual soil where α describes the bedding angle and buried under backfill soil*

The vertical pressure at the top is given with the following formula:

$$v = \frac{W_c}{2R}, \quad (3.15)$$

where:

- v is the vertical pressure on top of the pipe $[Pa]$,
- W_c is the load as in Marston (3.10) $[\frac{N}{m}]$,
- R is the radius of the pipe $[m]$.

The soil reaction at the bottom of the pipe is:

$$v' = \frac{v}{\sin\alpha}, \quad (3.16)$$

where:

- α is the bedding angle of the pipe $[^\circ]$.

The Spangler's equation (Iowa formula) is therefore:

$$\delta x = \frac{D_l K W_c R^3}{EI + 0.061eR^4}, \quad (3.17)$$

where:

- δx is the total horizontal deformation of the pipe $[m]$,
- D_l is the deflection lag factor $[-]$,
- K is the bedding constant $[-]$,
- W_c is the Marston load $[\frac{N}{m}]$,
- R is the radius of the pipe $[m]$,
- E is the pipe material Young's modulus $[Pa]$,
- I is the pipe wall moment of inertia per one meter of the pipe $[\frac{m^4}{m}]$,
- e is the modulus of the passive resistance of soil $[\frac{N}{m^3}]$.

The coefficients K , D_l and e are empirical. The constant e was later modified to represent a real property of the soil (Watkins and Spangler, 1958). Watkins introduced a modulus of soil

reaction:

$$E' = eR, \quad (3.18)$$

therefore creating a Modified Iowa Formula:

$$\delta x = \frac{D_l K W_c R^3}{EI + 0.061 E' R^3}. \quad (3.19)$$

Originally the bedding constant K depended on the angle of bedding assuming an equal contact in all the contact zone. This is actually very rarely true. The contact between the pipe and the residual soil depends on the technology used to prepare the bedding. It is technically difficult to cut a circular groove of a precise radius for kilometres of pipes, and a groove of larger diameter is not supporting the pipe properly. In the engineering practice the pipe is typically laid on the ground and the backfill is dumped on top of it with little compaction to avoid reducing the permeability. In such a situation there are large voids below the pipe under the haunches which causes a reduction of the pipe strength and can be a cause of pipe collapse. Some engineering tactics were developed to avoid this problem, for example flushing the backfill under the pipe, but also changing the bedding shape. In (Willardson and Watkins, 2002) it was shown that a triangular groove supporting the pipe in two points is almost as effective as a well prepared circular bedding, while being much easier to construct in the field. Nevertheless, in the classical situation considered by Spangler the values of bedding angle α ranging from 0° to 180° were related to the K values ranging from 0.110 to 0.083, commonly 0.1.

The deflection lag factor D_l takes into account the consolidation of the soil at the sides of the pipe changing with time. Under constant load the deflection of a flexible pipe can increase by 30% in 40 years, (Warman et al., 2009). Typically the values of D_l range between 1.0 and 1.5.

Possibly the most important parameter in Iowa formula is the soil reaction modulus (Moser, 2001). It was often tried to identify it with oedometric modulus with factors like $M = (0.7 - 1.5) \cdot E'$ (Krizek, 1971) or $M = (1.0) \cdot E'$ (Hartley and Duncan, 1987). Typically the values of E' are taken from tables and depend on the type of soil and the level of compaction.

3.1.3.2 Internal Forces and Pipe Failure

There is a number of methods to compute the internal forces in the walls of the pipe. If the stress in any place of the wall exceeds the yield stress or maximum stress of the pipe wall material the wall can be crushed which leads to failure. Typical pipe failure modes are presented in Figure 3.4. The mode depends on the stiffness of the pipe and the surrounding soil.

3.1.3.2.1 Beam Theory In case of point loading of a pipe the internal forces can be determined in the framework of beam theory. In Appendix C a method based on the beam theory is presented. The normal and tangential stresses are negligible while the bending moment is significant. The internal moment can be expressed with a following equation:

$$M = P_v R \left(\sin \theta - \frac{2}{\pi} \right), \quad (3.20)$$

where:

P_v is the vertical force acting on the pipe [N],

θ is the angle [deg]

The extreme internal moments are located at $\theta = 0^\circ$ and $\theta = 90^\circ$:

$$M(\theta = 0^\circ) = -\frac{2}{\pi} P_v R, \quad (3.21)$$

$$M(\theta = 90^\circ) = \left(1 - \frac{2}{\pi}\right) P_v R. \quad (3.22)$$

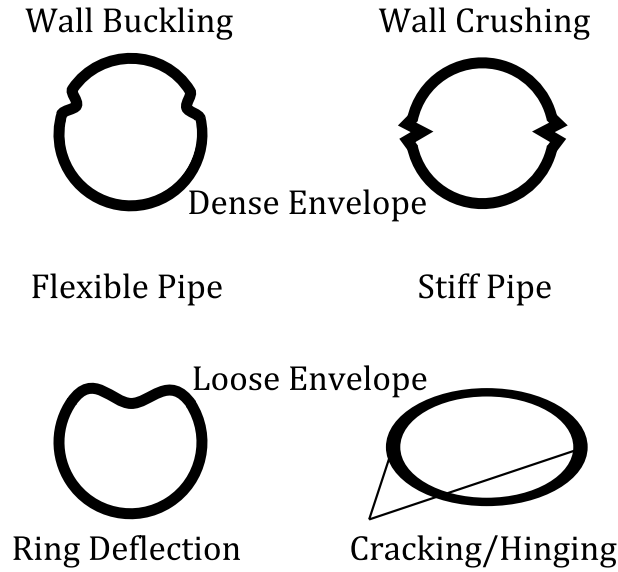


Figure 3.4: Failure modes in underground pipes (modified after (Watkins et al., 1980))

3.1.3.2.2 Marston-Spangler The Marston-Spangler method gives the following values of normal compressive force in the wall:

$$T_c = 0.7P_v R, \quad (3.23)$$

$$T_h = 0.7P_v R, \quad (3.24)$$

where:

- T_c is the normal force in the top and bottom parts of the pipe [N],
- T_h is the normal force in the side parts of the pipe [N],
- P_v is the vertical force acting on the pipe [N].

The bending moments in the pipe are given with the following formulas:

$$M_c = 0.02P_v R^2, \quad (3.25)$$

$$M_h = -0.02P_v R^2, \quad (3.26)$$

where:

- M_c is the moment of force in the top, bottom and both sides of the pipe [Nm] (12, 3, 6 and 9 o'clock positions, see Fig. 3.5),
- M_h is the moment of force at 1:30, 4:30, 7:30 and 10:30 positions [Nm].

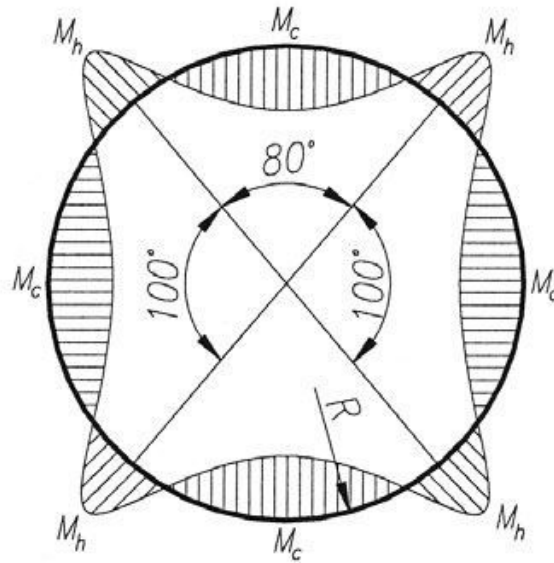


Figure 3.5: *Bending moment diagram given by Spangler (after (Kunecki, 2006))*

3.1.3.2.3 Ring Compression Other classical approach to compute the forces in the pipe walls is to use the ring compression theory stating that the compression force in the wall is equal to radial pressure acting on the wall multiplied by the radius

$$T = P \cdot R. \quad (3.27)$$

Ring compression method neglects the influence of bending moments in the wall of the pipe.

Other methods based on the ring compression theory and engineering experience were developed by American Association of State Highway and Transportation Officials (AASHTO method) and Canadian Highway Bridge Design Code (CHBDC method) and are described in (Iron and Institute, 1994). These three methods can be used to design large constructions (diameters up to 7.7 [m], arch spans greater than 3 [m]) and shapes other than circular, and thus are applicable to culverts, arches and tunnels. These methods neglect the influence of bending moments in the wall of the construction and focus on the axial forces in the wall.

3.1.4 Pipe Experiments and Modeling

The study of buried pipe behaviour was always based on the engineering practice. Full scale experiments and instrumentation of real constructions are an important part of new design method development and improvement of parameters in the existing methods.

In (Arockiasamy et al., 2006) the authors performed field testing of shallow buried large HDPE and PVC pipes under highway truck loading. The experimental results were compared with theoretical values obtained using modified Iowa method and FEM simulations.

In (McAfee and Valsangkar, 2008) an induced trench conditions were tested, that is a situation where a highly compressive material (geofoam, sawdust) is placed above a pipe in projection conditions to induce soil arching and improve the performance of the construction. In this paper Marston-Spangler theory was compared with centrifuge experiments, numerical modeling and field tests.

In (Calvetti et al., 2004) the authors presented 3D pipe modeling in DEM method in the context of landslide damaging pipes, which was continued in (di Prisco and Galli, 2006). This work proved that discrete element method is able to simulate buried pipe behaviour.

3.1.5 Arching Effect

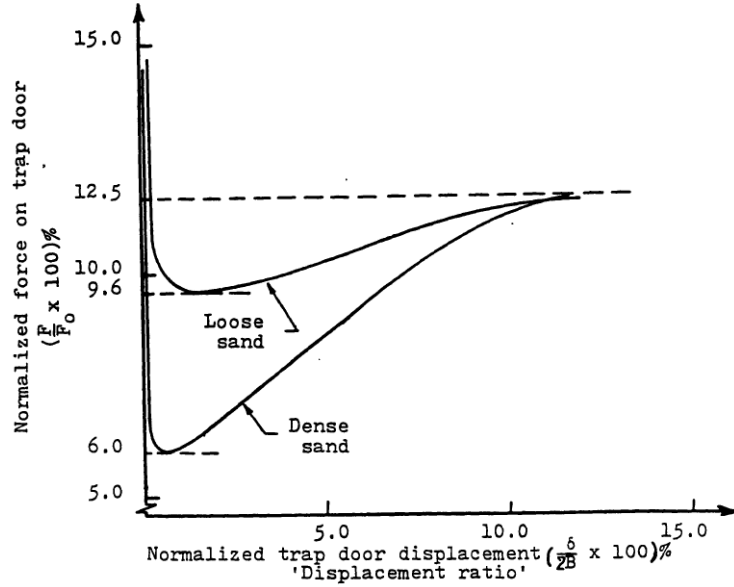


Figure 3.6: *Experimental results in Terzaghi trap door experiment (after (Tien, 1996)). The force acting on the trap is quickly reducing along with the lowering of the trap and then rise again to some residual level*

The shearing between two soil prisms described by Marston comes from the fact that one soil prism is settling more than the other. As was said before, the direction of shear can result in the pipe load reduction or increase, depending on the situation. Similar situation occurs in many other situations except buried pipes, for example in grain silos or between the heads of foundation piles. This phenomenon is called arching effect and was studied intensively since the times of Marston. Terzaghi generalised the problem (Terzaghi, 1943) by studying a trap door problem. In his experiments a rectangular door was moved down from under a granular assembly, a situation similar to opening a valve at the bottom of a grain silo. The load on the door was observed to be smaller than the theoretical load coming from the weight of the grain prism above it. It was concluded that the load was transferred from the yielding soil mass to the stationary soil around the trap door. As in the case of Marston, Terzaghi assumed vertical surfaces of shearing between the soil prisms. Considering equilibrium of a yielding soil strip above a trap Terzaghi obtained a solution for cohesive soil:

$$\sigma_v = \frac{B \left(\gamma - \frac{c}{B} \right)}{K \tan \phi} \left(1 - e^{-K \tan \phi \frac{z}{B}} \right) + q \cdot e^{-K \tan \phi \frac{z}{B}}, \quad (3.28)$$

where:

σ_v	is the vertical stress	$[Pa]$,
z	is the depth	$[m]$,
c	is the cohesion	$[Pa]$,
ϕ	is the friction angle of the soil	$[deg]$,
q	is the loading at the top of the soil assembly	$[Pa]$,
B	is the width of the trap door	$[m]$.

Terzaghi observed that along with the lowering of the trap door the load transfer was greatest in the beginning of the test and was smaller after some large displacement, Figure 3.6.

3.2 Elastic Pipe Modeling in DEM

The idea of the study was to perform physical experiments and to reproduce them numerically in order to study soil arching in the context of particle shape. The analogue soil was modeled using the method described in the previous chapter, but in order to create a model of an elastic pipe, additional contact law had to be introduced.

3.2.1 Parallel Bond Contact Law

Generally speaking in 2D this model consists of a pair of links transmitting forces (N , T) and moment of force (M) between the two connected cylinders of length t . One should think of elastic springs distributed regularly between two bonded particles. The parallel bonds transfer forces up to a limit when it brakes. The bonds are described by five numerical parameters:

1. Parallel bond normal stiffness $k_n^{pb} [\frac{N}{m^3}]$, similar to contact normal stiffness
2. Parallel bond tangential stiffness $k_t^{pb} [\frac{N}{m^3}]$, similar to contact tangential stiffness
3. Normal strength of the bond $N^{pb} [\frac{N}{m^2}]$, describing the breaking point of the bond
4. Tangential strength of the bond $T^{pb} [\frac{N}{m^2}]$, describing the breaking point of the bond
5. The distance between a parallel bonds and particle centre $R^{pb} [m]$, the physical size of the bond. It can be represented as a dimensionless ratio between the size of the bond and size of the particles in contact: $\bar{R}^{pb} [-] = \frac{R^{pb}}{\min(R_A; R_B)}$

In order to create the bond, two particles must overlap or at least be in contact. Initially the forces in the bond are equal zero. After the bond is created, the two particles can change their relative position. The bond forces are computed relating to the increment of displacement from the initial state when the bond was created. The bonds work in parallel with the standard normal and tangential contact laws described in Sec. 1.7 The bond can be broken but this feature of the model was not used in the current study. A single parallel bond connecting two particles A and B can be regarded as a beam of length $R_A + R_B - d$ (where d denotes the particle overlap), height $2R^{pb}$ and width equal to the length of the particles t . A sketch of the parallel bond is presented in Figure 3.7.

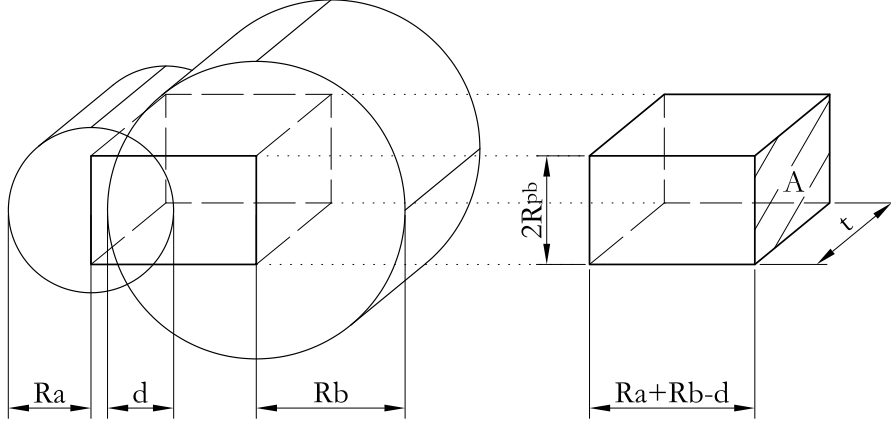


Figure 3.7: Parallel bond between two particles. The bond is a finite rectangular parallelepiped of lengths $R_A + R_B - d$, $2R^{pb}$ and t

The normal force increment in a given timestep is computed the following way:

$$\Delta F_n^{pb} = k_n^{pb} \cdot A \cdot \Delta U_n, \quad (3.29)$$

where:

$$\begin{array}{ll} A \quad [m^2] & \text{is the cross-section area of the bond; } A = 2R^{pb} \cdot t, \\ \Delta U_n \quad [m] & \text{is the normal relative displacement between the particles in contact.} \end{array}$$

The tangential force increment is computed using:

$$\Delta F_t^{pb} = k_t^{pb} \cdot A \cdot \Delta U_t. \quad (3.30)$$

and the moment of force between two particles by:

$$\Delta \bar{M} = k_n^{pb} \cdot I \cdot \Delta \theta, \quad (3.31)$$

where:

$$\begin{array}{ll} I \quad [m^4] & \text{is the moment of inertia of the bond cross-section; } I = \frac{2}{3} \cdot t \cdot (2R^{pb})^3, \\ \Delta \theta \quad [-] & \text{is the change of relative orientation of the particles.} \end{array}$$

3.2.2 Numerical Model of Elastic Pipe

Elastic pipe was created with circular particles of the same diameter D connected together with *parallel bonds* into a single body, see Figure 3.8. In order to obtain similar mechanical behaviour,

the geometry of the bonds was related to the geometry of the pipe, while the numerical parameters describing the bonds were related to the mechanical properties of the material. This way, the height is expressed with the following equation:

$$\bar{R}^{pb} = \frac{h}{D}. \quad (3.32)$$

This relation ensures that a given beam geometry can be modelled correctly regardless of the size of the particles used.

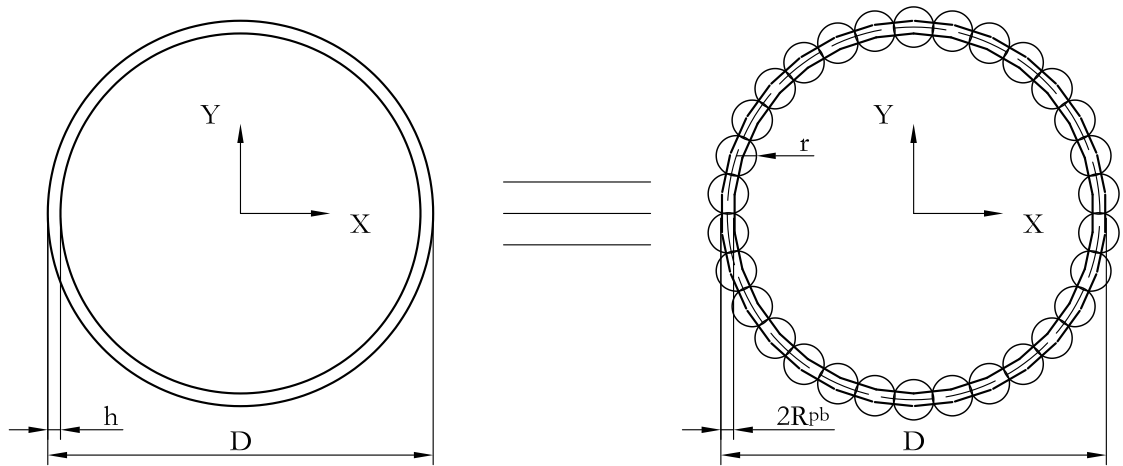


Figure 3.8: A numerical model of an elastic pipe. The model consists of a number of particles bound with parallel bonds. The distance between the bonds correspond to the thickness of the pipe while the number and diameter of the particles can be different

The bond stiffness is related to the stiffness of the material:

$$k_n^{pb} = \frac{E}{D}, \quad (3.33)$$

$$k_t^{pb} = \frac{G}{D}. \quad (3.34)$$

By default the parallel bond works together with the normal and tangential contact laws (see Section 1.7) which can affect the behaviour of the pipe. This is due to the fact that the stiffness of the elastic body becomes different in tension where only parallel bonds carry all the load and

different in compression or bending where the load is shared in parallel with the contact bonds. One can conclude that the solution to this problem would be to use k_n and k_t equal to zero, but in PFC^{2D} the contact stiffness is calculated as a mean of the stiffnesses of two bodies in contact:

$$k = \frac{k^A \cdot k^B}{k^A + k^B}. \quad (3.35)$$

In the particular case of pipe buried in granular material, using different values of contact stiffness for soil and for pipe would result in different stiffness of the pipe-soil interface with little physical meaning, especially if one would be equal to zero.

Because of this problem, it was therefore decided to keep realistic values of contact stiffness but to cancel the contact bonds inside the pipe. The contact bonds were countered by introducing additional forces everywhere where a force resulting from a contact bond between the pipe particles occurred. That way the elastic behaviour of the pipe was modelled with parallel bonds only, without any influence of the pipe's k_n and k_s . Therefore the values of these parameters could have been chosen to present proper soil-pipe and soil-soil interface behaviour.

3.2.3 Analytical Validation of the Numerical Model: Cantilever Beam Loading

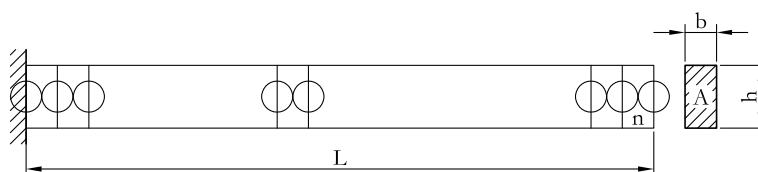


Figure 3.9: *Parallel bond notation in simple case of a cantilever beam*

The parallel bond behaviour was validated by studying a simple case of elastic cantilever beam. It was decided to study three cases: bending, tension and compression. The beam was modelled with a number of discs forming a single horizontal line. Initially the discs were in contact (which is a necessary condition to create a parallel bond) with no overlap. The discs were connected together with the parallel bonds and the position and orientation of the first disc was blocked in order to obtain a fixed support. The bonds were not supposed to be broken and so their strength was set to be very high. The beam was loaded with the external forces gradually to reduce vibrations of the beam. When the load reached the maximum value, a number of additional calculation steps were made in order to obtain an equilibrium state.

b [m]	h [m]	L [m]	E [Pa]
0.1	0.2	2.0	$20 \cdot 10^8$

Table 3.1: *Cantilever beam characteristic*

For all the cases the same geometry and stiffness of the beam was used, see Table 3.1 and Figure 3.9. The self-weight of the beam was neglected.

3.2.3.1 Vertical Loading: Bending

The beam was loaded with an uniformly distributed vertical load q . The value of the load was the same in all the tests. The beam was modelled with different number of particles. This caused

3.2. ELASTIC PIPE MODELING IN DEM

change of the particle diameter. Since the beam was subjected to bending, no overlap between the particles occurred and there was no influence of the k_n and k_s parameters. The numerical parameters used are summarised in Table 3.2.

n	D [m]	\bar{R}^{pb} [-]	k_n^{pb} [N/m ³]	q [N/m]
20	0.1	2.0	2e10	100.0
50	0.04	5.0	5e10	100.0

Table 3.2: Numerical parameters of the elastic beams subjected to transverse loading

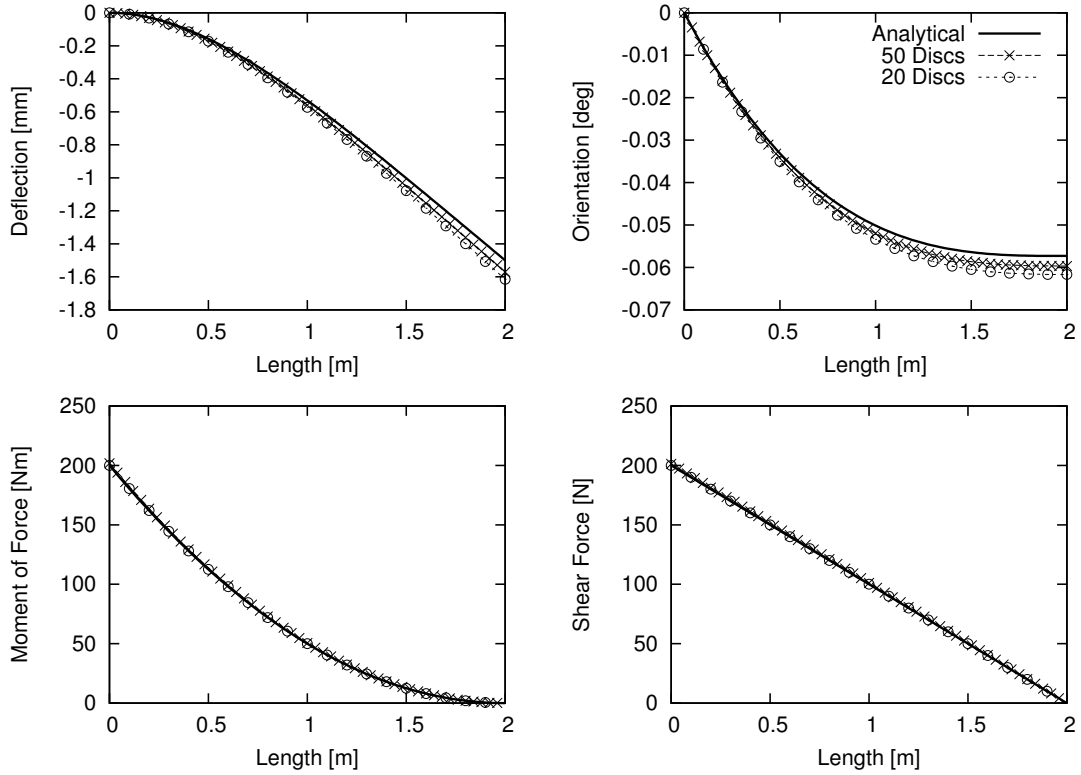


Figure 3.10: Results of cantilever beam loaded with uniform load compared with the analytical solutions

The final positions and orientations of the particles can be compared with the analytical equations describing the deflections and slope of a beam. The forces in the parallel bonds correspond to internal forces that can also be obtained analytically. The analytical solutions of a cantilever beam are given by the following equations:

$$\delta(x) = \frac{q \cdot x^2}{24EI} (6L^2 - 4Lx + x^2) \quad (3.36)$$

$$\theta(x) = \frac{q \cdot x}{6EI} (3L^2 - 3Lx + x^2) \quad (3.37)$$

$$M(x) = -\frac{q}{2} (L^2 - 2Lx + x^2) \quad (3.38)$$

$$T(x) = q \cdot (x - L) \quad (3.39)$$

where $\delta(x)$ is the beam deflection, I is the moment of inertia of the beam cross-section (in this case $I = \frac{b \cdot h^3}{12}$), $\theta(x)$ is the beam slope, $M(x)$ represent the internal moment of force while $T(x)$ is the shear force in the beam.

As one can see in Figure 3.10, the result of the model is in agreement with the analytical solution of the internal forces. The difference between the exact solution of the particle displacement and the model is less then 8% for a model consisting of 20 particles and less then 5% for a model consisting of 50 discs, see the extreme values in Table 3.3.

n	$\delta_{min}[mm]$	$\theta_{min}[deg]$	$M_{max}[Nm]$	$T_{max}[N]$
20	-1.614	-0.0617	200.000	200.000
50	-1.570	-0.0597	201.868	201.323
analytical	-1.500	-0.0573	200.000	200.000

Table 3.3: Result of the beam bending

3.2.3.2 Axial Loading: Compression and Traction

A beam of the same geometry as described before was loaded axially with a point force at the tip of the beam that was either compressing or extending the beam. In this case of loading the contact bonds were taking part in load transfer by default. As it was mentioned previously in Section 3.2.2, the contact bonds were countered by introducing additional forces with the same value and opposite direction.

n	D [m]	$\bar{R}^{pb}[-]$	$k_n^{pb}[N/m^3]$	$k_n[N/m]$	F [N]
20	0.1	2.0	2e10	10e7	± 500.0
50	0.04	5.0	5e10	10e7	± 500.0
50	0.04	5.0	5e10	10e4	± 500.0

Table 3.4: Numerical parameters of the elastic beams subjected to axial loading

n	$k_n[N/m]$	F [N]	$\Delta U[m]$	Analytical	N [N]	Analytical
20	10e7	+500.0	2.4817e-5	2.5e-5	-500.0026	-500.0
20	10e7	-500.0	-2.5187e-5	-2.5e-5	499.9972	500.0
50	10e7	+500.0	2.3939e-5	2.5e-5	-500.0061	-500.0
50	10e7	-500.0	-2.6082e-5	-2.5e-5	499.9931	500.0
50	10e4	+500.0	2.3939e-5	2.5e-5	-500.0061	-500.0
50	10e4	-500.0	-2.6083e-5	-2.5e-5	499.9931	500.0

Table 3.5: Resulting displacement and forces of the elastic beams subjected to axial loading compared with the theoretical values

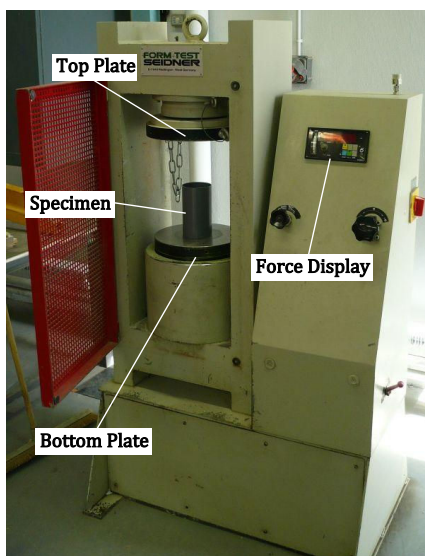
Table 3.4 gathers the numerical parameters of the beams used. Table 3.5 present the result of the numerical simulations. These tests proved that the number of balls and the value of contact stiffness has very little influence on the final result of axial loading which are in agreement with the expected values.

3.2.4 Validation of the Numerical Model with Experimental Results and Analytical Solution of Simple Compression Test on Pipe

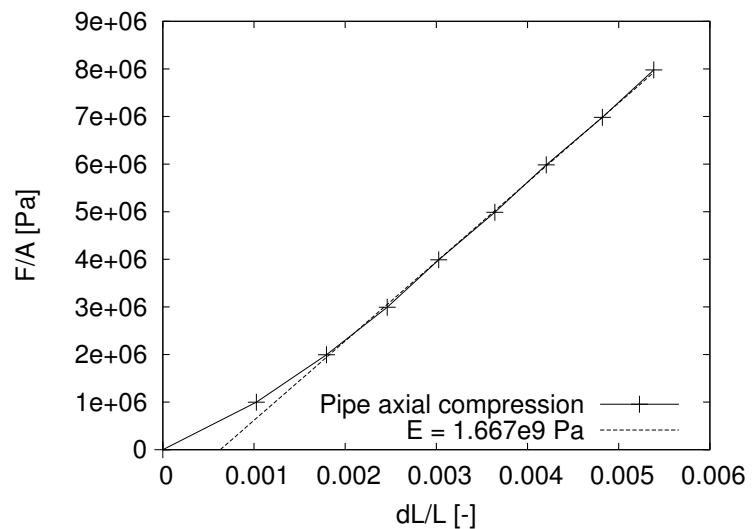
A next approach to validation of the model was to conduct laboratory experiments and compare the results with the numerical model and analytical solution.

The analytical solution may be obtained basing on the beam theory and using the Castigliano theorem described in Appendix C. The idea behind the solution is to treat a circular pipe as a curved beam. The analytical solution is valid only for small strains and was compared with the results in the initial, elastic phase of compression test. In order to obtain the deformations of the beam one must give the value of the elastic modulus of the material.

3.2.4.1 Young's Modulus Estimation



(a) Hydraulic press



(b) Axial compression result

Figure 3.11: Young's modulus estimation with axial compression of a 22.5cm pipe fragment. The deformation of the specimen were measured with an external gauge, not visible in the image

PVC is a synthetic material with very high range of application, from vinyl records to plastic windows and electric cable coating. The mechanical properties of plastic materials depend on the chemical composition that can vary greatly. The specimens used in the experiments were cut from a commercially available plumbing pipe of unknown mechanical properties. Because of that it was decided to obtain the necessary values experimentally by performing simple laboratory tests. All the specimens were prepared from the same piece of PVC pipe in order to assure the consistency of the results. The wall thickness of the pipe was equal to 3.3mm with the outer diameter equal to 100mm.

To derive the value of Young's modulus, two types of experiments were made. The first experiment consisted of axial compression of a PVC pipe while the second was a simple compression performed on multiple specimens.

The axial compression specimen was manually cut to be 22.5cm long with parallel top and bottom. It was placed in a hydraulic press without any lubrication of the contact surfaces and compressed. The specimen axial deformation was measured with analogue gauges (see Fig. 3.11a). The resulting stress-strain curve is presented in Figure 3.11b. Because of the imperfections of

the pipe surfaces and friction between the specimen and the plates, the beginning of the curve is disturbed. The value of a Young's modulus fitted in that experiment results is equal to $16.7e8Pa$.

The second experiment consisted of a vertical compression of an elastic ring. In these tests four samples were used. All the samples were mechanically cut in order to obtain smooth and parallel surfaces at the ends. The specimens had different lengths: 6.3, 6.0, 6.0 and 2.2cm. The results of all the samples were normalised to correspond to specimen of 6.0cm length. The wall thickness and outer diameter were the same as in the previous experiment. During the experiment the sample was loaded between two vertical plates with an electric press (see Fig. 3.12a). The displacements of the top plate were measured using an analogue gauge. The force applied on the pipe was measured with a ring force gauge. Specimens were also photographed during the loading and unloading and the digital images acquired that way were used to verify the precision of the pipe deformation measurements. The results can be observed in Figure 3.12b.

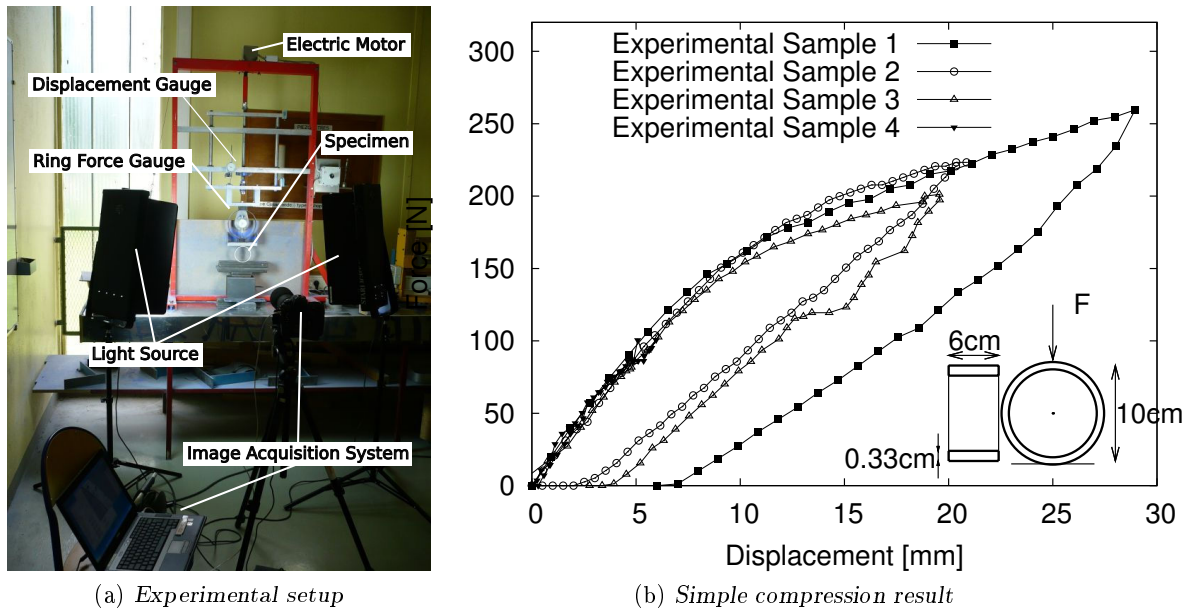


Figure 3.12: Young's modulus estimation with simple compression. The test was performed on four samples that were loaded up to different extent in the apparatus presented in Figure 3.12a. The sample was photographed in order to perform digital image correlation

Since in this kind of experiment the Young's modulus cannot be calculated directly, an analytical equation (C.12) described in more details in Appendix C was used.

$$E = \left(\frac{\pi}{4} - \frac{2}{\pi} \right) \cdot \frac{F \cdot R^3}{\delta Y \cdot I} \quad (3.40)$$

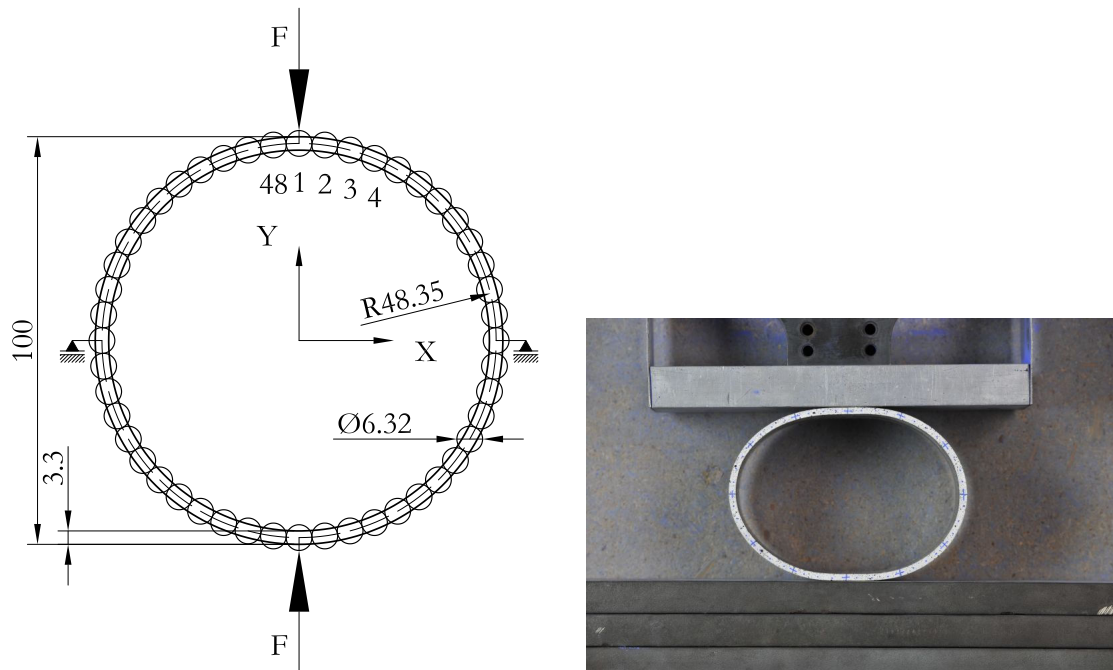
The Young's modulus characterising the initial, linear part of the curves extracted from these tests was equal to $20.2e8Pa$. It was decided to use the value of the second group of experiments rounded down to $20.0e8Pa$ because of the repeatability of the results, some imperfections of the sample used in the axial compression and because those results were closer to the ones found in literature ($24.50e8Pa$ in (Alves and Martins, 2009), $33.78e8Pa$ in (Titov, 1984)) then the value obtained from the axial loading.

3.2.4.2 Point Loading of the Pipe: Simple Compression

Knowing the value of the Young's modulus it was possible to perform numerical simulations of the experimental situation described in Section 3.2.4.1, simple compression of an elastic ring. The comparison was made by comparing the force-displacement curves obtained during the experiments and from numerical simulations, and the deformations of the compressed pipe.

The experiments were recorded with series of digital photographs in order to be able to follow the change of shape of the specimen by means of Digital Image Correlation (DIC). A number of points distributed regularly on the front face of the specimen was chosen and then followed. That way it was possible to obtain a force-displacement curve and the deformations of all the body, and later to reproduce the behaviour with the numerical model.

The geometrical parameters of the pipe were reproduced in a DEM model. The pipe was 6.0cm long, had an external diameter of 10cm and its wall thickness was equal to 0.33cm. In DEM it was modelled with 48 discs touching each other but without any overlap (48 parallel bonds), as shown in Figure 3.13a. The mechanical properties of PVC were function of Young's modulus as described before. The Young's modulus was equal $20.0 \cdot 10^8 Pa$. A circular pipe was loaded with a vertical point force acting directly on the pipe. All these data are presented in Table 3.6.



(a) Pipe geometry used in the validation of the numerical model. The model is divided into 48 sections

(b) PVC pipe during simple compression. The specimen in the experiment had 48 marks on the front face, as well as a speckle pattern, to facilitate the correlation performance

Figure 3.13: Experimental setup of simple compression was reproduced in the numerical model. The neutral axis of the pipe is defined by the radius R equal to $\frac{D-h}{2}$. The distance between the parallel bonds $2R^{pb}$ is equal to the pipe wall thickness. The displacements of the two particles at the sides of the pipe are fixed in the direction of Y

	n	D	h	b	E	F_{max}
Simple compression						
Sample 2	-	100mm	3.3mm	60mm	$20.2 \cdot 10^8 Pa$	223.256N
DEM	48	100mm	3.3mm	60mm	$20.0 \cdot 10^8 Pa$	250.000N

Table 3.6: Parameters of the elastic pipe simple compression

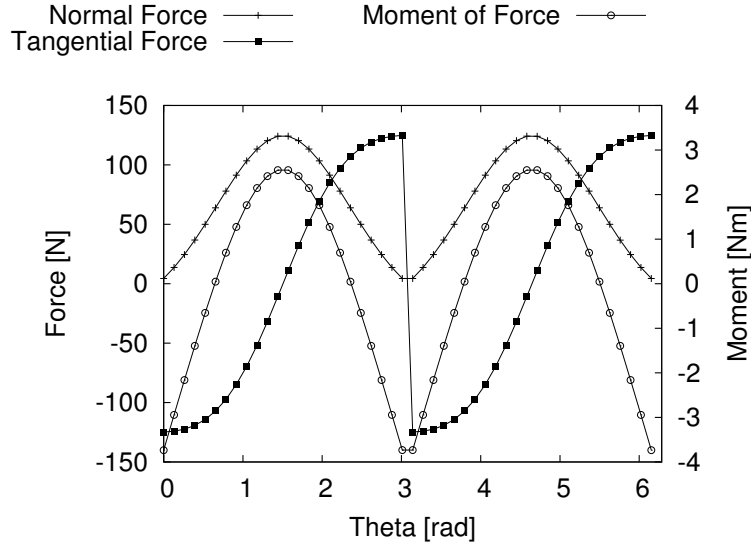


Figure 3.14: Forces in the parallel bonds representing internal forces in the elastic pipe under a single force $F=250N$ acting on the top

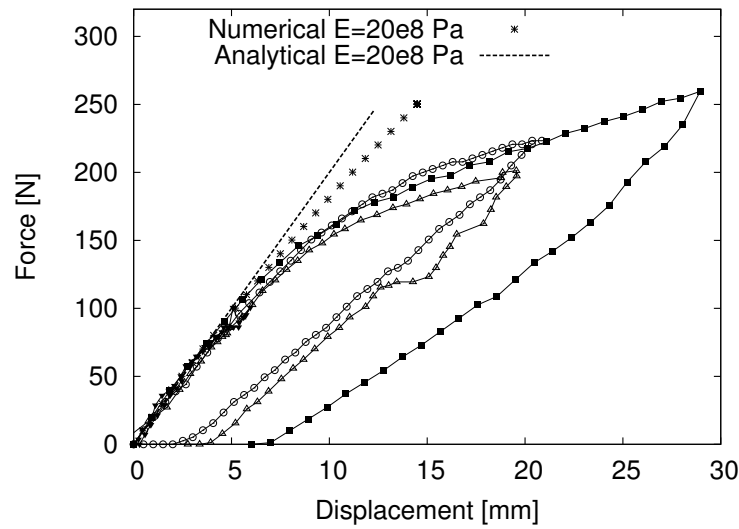


Figure 3.15: Force-displacement curve of a circular pipe simple compression. Comparison between experimental and a numerical results

The contact forces between the particles forming the pipe were disabled by introduction of additional forces with equal value but an opposite direction. That way only the parallel bonds

were taking part in the transfer of load. Therefore forces in parallel bonds were corresponding to the internal forces inside the elastic body.

The resulting internal forces are presented in Figure 3.14 while the comparison of the force-displacement curve is presented in Figure 3.15.

As one can see, the model is reproducing the pipe behaviour well in the elastic domain. In this domain it was possible to make a comparison between the three types of result: experimental, numerical and analytical. The following parameters were put into equations (C.12), (C.13), (C.14) and (C.15):

E [Pa]	R [m]	b [m]	h [m]	F [N]
$20.0 \cdot 10^8$	0.04835	0.060	0.0033	51.92

Table 3.7: Geometrical parameters

In the experiment the elastic pipe was placed on a fixed metal base and loaded from the above. In this case the values of displacement computed from the equations (C.12) and (C.13) must be doubled because the derivation in the appendix assume different boundary conditions.

For the given geometry the moment of inertia is computed as for a rectangle: $I = \frac{bh^3}{12}$ where b is the pipe length and h is the wall thickness.

The analytical values were as following:

$$\delta Y = 2 \cdot 0.5 \cdot \left(\frac{\pi}{4} - \frac{2}{\pi} \right) \cdot \frac{51.92 \cdot 0.04835^3}{20.0 \cdot 10^8 \cdot \frac{0.06 \cdot 0.0033^3}{12}} = 2.430mm \quad (3.41)$$

$$\delta X = 2 \cdot 0.5 \cdot \left(\frac{2}{\pi} - \frac{1}{2} \right) \cdot \frac{51.92 \cdot 0.04835^3}{20.0 \cdot 10^8 \cdot \frac{0.06 \cdot 0.0033^3}{12}} = 2.231mm \quad (3.42)$$

$$M(\theta = 0^\circ) = -\frac{2}{\pi} \cdot \frac{51.92}{2} \cdot 0.04835 = -0.7991Nm \quad (3.43)$$

$$M(\theta = 90^\circ) = \left(1 - \frac{2}{\pi} \right) \cdot \frac{51.92}{2} \cdot 0.04835 = 0.4561Nm \quad (3.44)$$

It is worth noting that the same value of vertical displacement as in the analytical solution can be obtained using Blake's analytical formula (Blake, 1959):

$$\delta Y = \frac{F\lambda}{E} \left(1.788\lambda^2 + 3.091 \frac{0.637}{1 + 12\lambda^2} \right), \quad (3.45)$$

$$\lambda = \frac{R}{h}.$$

$$\delta Y = \frac{51.92 \cdot \frac{0.04835}{0.0033}}{0.06 \cdot 20.0 \cdot 10^8} \left(1.788 \cdot \frac{0.04835^2}{0.0033^2} + 3.091 \cdot \frac{0.637}{1 + 12 \cdot \frac{0.04835^2}{0.0033^2}} \right) = 2.433mm \quad (3.46)$$

The comparison of the results in case of simple loading (see Tab. 3.8) show that the vertical and horizontal deformation of the model are in agreement with the experimental results with less than 5% of difference. The extreme bending moment in the pipe is similar in both the analytical and numerical solutions, with an error smaller than 10%.

	E[Pa]	δY [mm]	δX [mm]	$M(\theta = 0^\circ)$ [Nm]	$M(\theta = 90^\circ)$ [Nm]
Experiment	20.2e8	-2.41mm	+2.14mm	—	—
Analytical	20.0e8	-2.43mm	+2.23mm	-0.7991	0.4561
Analytical Blake	20.0e8	-2.43mm	—	—	—
Model	20.0e8	-2.52mm	+2.24mm	-0.7288	0.4688

Table 3.8: Comparison of the result of a simple compression of elastic pipe under 51.92N of vertical load

Finally, the overall shape of the pipe captured in the pictures can be compared with the particle position in DEM, Fig. 3.16. This comparison was made for the external force equal to 51.92N.

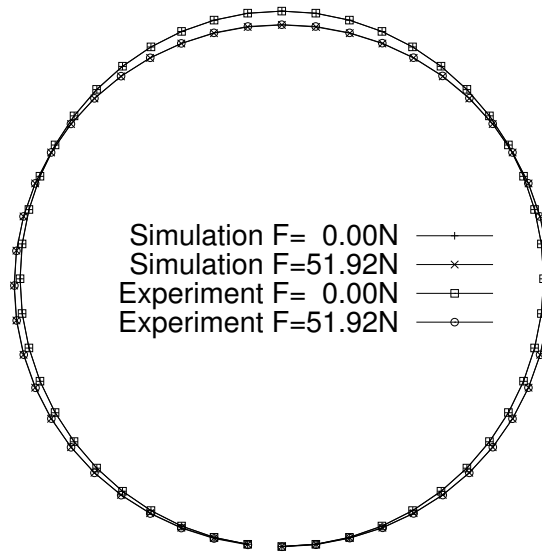
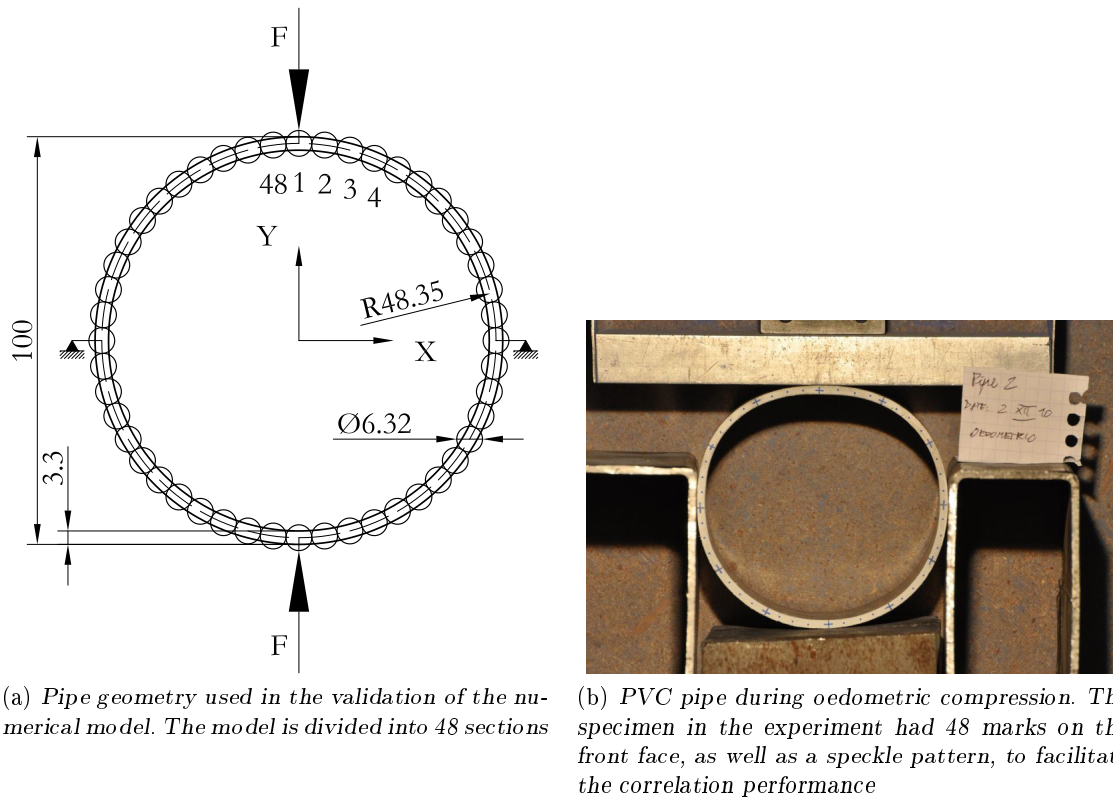


Figure 3.16: Pipe shape in the experiment and in DEM simulation in initial and final shape. Each point correspond to mass centre of a disc or to a point on the front face of the pipe

3.2.4.3 Point Loading of the Pipe: Oedometric Compression

In order to test the ability of the numerical model to represent the behaviour of the pipe in other boundary conditions, another type of experiment was made: vertical compression in 2D oedometric conditions. This experiment was performed with the same apparatus as the simple compression described before but this time the PVC pipe specimen was mounted in a rigid steel box prior to loading that blocked the lateral displacements of the pipe walls. The front face of the sample was clear and marked with 48 regularly spaced points and crosses to allow DIC point tracking. The contact surface between the specimen and steel was not lubricated in any way. This experimental setup was reproduced in the computer model as described before. The difference was that the horizontal displacements of the discs on the side of the pipe were blocked, see Figure 3.17a. The parameters of the experiment and its counterpart in the simulation are presented in Table 3.9



(a) Pipe geometry used in the validation of the numerical model. The model is divided into 48 sections

(b) PVC pipe during oedometric compression. The specimen in the experiment had 48 marks on the front face, as well as a speckle pattern, to facilitate the correlation performance

Figure 3.17: Experimental setup of oedometric compression was reproduced in the numerical model. The neutral axis of the pipe is defined by the radius R equal to $\frac{D-h}{2}$. The distance between the parallel bonds $2R^{pb}$ is equal to the pipe wall thickness. The displacements of the two particles at the sides of the pipe are fixed in the direction of X and Y

	n	D	h	b	E	F_{max}
Oedometric compression						
Specimen 1	-	100mm	3.3mm	60mm	$20.2 \cdot 10^8 Pa$	480.26N
DEM	48	100mm	3.3mm	60mm	$20.0 \cdot 10^8 Pa$	500.00N

Table 3.9: Parameters of the elastic pipe oedometric compression

The result of the simulations is presented in Figures 3.18 and 3.19. As one can see, the model is able to reproduce the behaviour of the pipe well in both boundary conditions. The force-displacement curve obtained from discrete element simulation is similar to the one obtained during the experiment. The small difference between the curves can be attributed to a contact between the pipe and rigid walls on the sides which were not ideally parallel to each other.

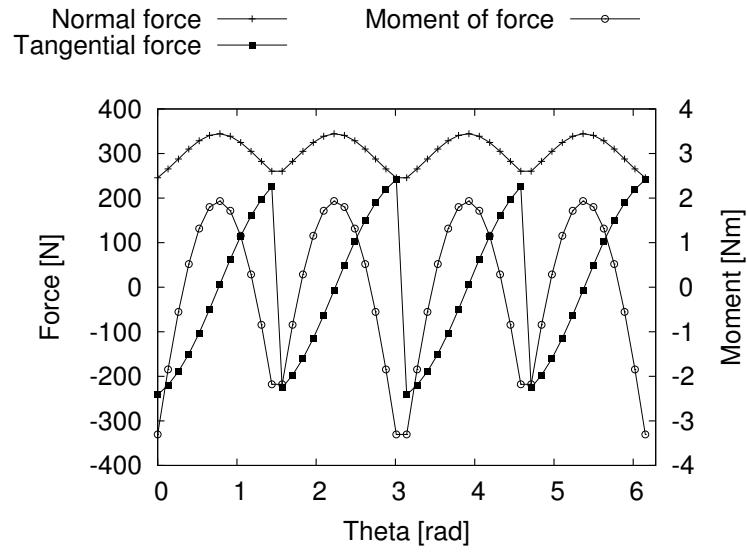


Figure 3.18: *Internal forces in an elastic pipe under a single force $F=500\text{N}$ acting on the top with horizontal displacements blocked*

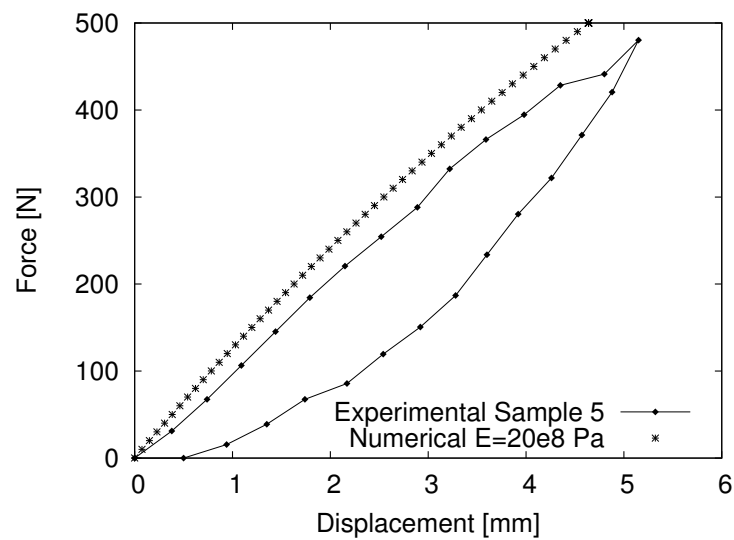


Figure 3.19: *Force-displacement curve of a circular pipe oedometric compression. Comparison between experimental and numerical results*

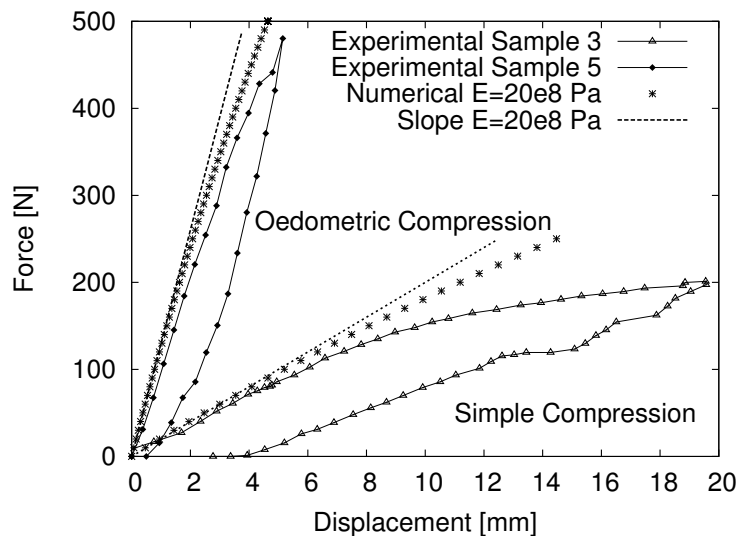


Figure 3.20: Comparison between simple and oedometric compression of pipe. The experimental results were reproduced with a numerical model. The slope of the elastic part of the curves is equal to $3 \cdot 10^5 [Pa]$ in case of simple compression and $2 \cdot 10^6 [Pa]$ in case of oedometric compression

3.3 $1\gamma 2\varepsilon$ Experiments

A number of physical experiments was performed and later reproduced in numerical simulations in order to observe the arching effect above the buried pipes.

3.3.1 Description of the $1\gamma 2\varepsilon$ Apparatus

The tests were performed using an apparatus located in the 3S-R laboratory in Grenoble called $1\gamma 2\varepsilon$ (see Fig. 3.21). The name of the device describes the conditions that can be controlled in that apparatus: two directions of strain ε_x and ε_y , and one shearing angle γ . The device consists of four walls connected together with hinges, forming a vertical rigid parallelogram AOBC around a sample. The right bottom corner of the apparatus, denoted O in the sketch, is fixed. Each wall is made of five sliding sections and therefore it is able to extend and contract evenly. The apparatus is equipped with 6 force sensors (3 perpendicular and 3 parallel to the wall surfaces) placed in the three hinges of the frame (A,B,C) and 5 LVDTs measuring the length change of every wall and the tilt angle of the two vertical walls. The information coming from the sensors are processed by a PC and are used to impose stress or strain conditions onto the sample using 5 electric motors running linear actuators that change the length (top vertical, top horizontal, bottom vertical and bottom horizontal motors: TV, TH, BV, BH in Figure 3.21) and orientation of the walls (shearing motor: Sh in the figure). The horizontal wall lengths range from 56 to 67cm while the vertical ones from 42 to 54cm. The maximum stress the apparatus can impose on a sample is equal to 250kPa.

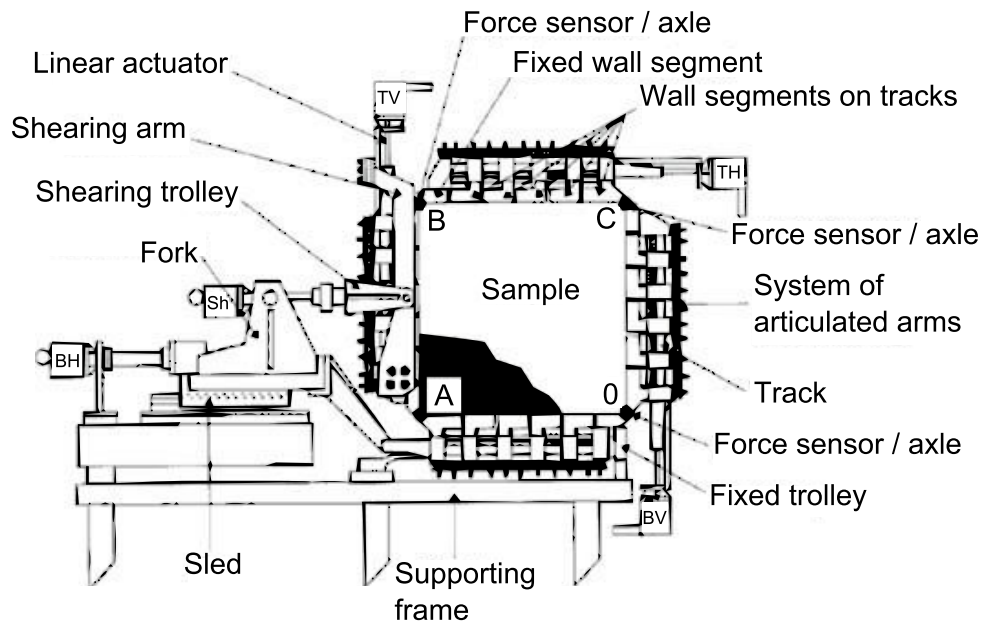


Figure 3.21: $1\gamma_2\varepsilon$ apparatus

The device uses mainly the well known Schneebeli material (Schneebeli, 1956), a bi-dimensional analogue of soil consisting of 6-cm-long circular rods of various diameters. The apparatus is quite versatile and was used in numerous studies: (Joer et al., 1992; Calvetti et al., 1997; Sibille and Froiio, 2007; Hall et al., 2010; Tengattini, 2010) to mention just a few. In course of these studies other specimens were tested in the $1\gamma_2\varepsilon$ apparatus: hexagonal rods made of aluminium (Lirer et al., 2005), wooden rectangles (Charalampidou et al., 2009), large circular and bean-shaped blocks of rubber (Le Ngoc, 2011). In the current study, besides a 6cm piece of PVC pipe (Fig. 3.22a), two types of the analogue material were used: an assembly of PVC rods and a mixture of ash wood rods (Fig. 3.22b).



(a) Elastic PVC pipe



(b) Granular material: PVC grains (left), wooden grains (right)

Figure 3.22: The materials used in the $1\gamma_2\varepsilon$ experiments. The length of all the elements is 6cm

It is possible to perform various types of plane-strain tests in the $1\gamma 2\epsilon$ apparatus:

- oedometric compression (horizontal or vertical), when two parallel walls remain stationary and the remaining move towards the sample,
- biaxial test (horizontal or vertical), when the stress on two parallel walls is kept constant and the sample is loaded by the third wall movement,
- shear test, when the tilt angle is changed and the stress on top wall remain constant.

For the last type of the test, the walls, otherwise smooth, are equipped with equally spaced fixed metal bars with dimensions corresponding to the size of Schneebeli material that distribute shearing stresses equally.

The design of the device leaves the front face of the sample unobstructed and flat. That allows performing image acquisition throughout the experiments without any disturbances which is very useful to study the kinematic field of the sample.

3.3.2 Assessment of Grain Displacement

Recording the experiments with digital images enabled the use of *Digital Image Correlation* method to analyse the results. It is “essentially a mathematical tool for assessing the spatial transformation (including translations and distortions) between two digital images” (Viggiani and Hall, 2008).

This technique consists of comparing two digital images before and after a deformation in order to evaluate the change in surface characteristics and to deduce the behaviour of the specimen.

The DIC technique is very universal and can be applied in many various fields, both in 2D and 3D cases, to recognize patterns (medical imaging, face recognition, dactyloscopy) or measure deformations, strains and displacements (experimental mechanics, engineering) (Sutton et al., 2009). In this work 2D-DIC was used.

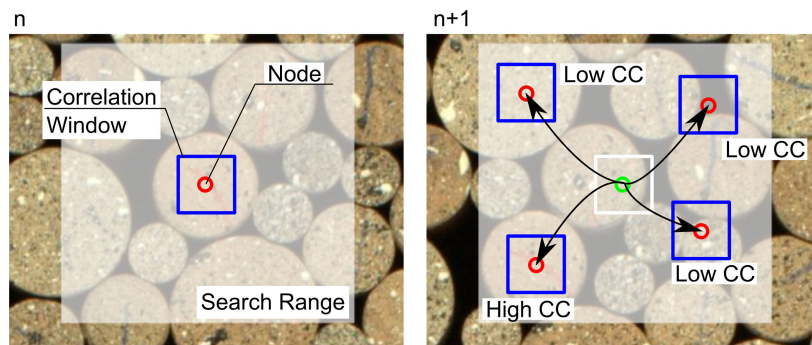


Figure 3.23: *Digital Image Correlation* method consists of finding a matching motif on two images. A node is defined on the reference image n containing some characteristic features of the image, like for example specimen surface texture. Around the node a correlation window is defined. The motif inside the correlation window is searched for in the second image $n+1$ within some area called a search range. The motif is compared with various fragments of the image and for each comparison a correlation coefficient is computed. The best match have the highest correlation coefficient. Finally a displacement vector can be drawn between the initial and final position of the node

3.3.2.1 Methodology

To apply DIC method an experimental device that allows direct observation is needed. $1\gamma 2\varepsilon$ meets that requirement as its front face is open. The specimen surface must have distinguishable features, like for example contrasting areas of colour, and should be flat. Usually a fine black-and-white speckle pattern is applied on the surface of a specimen to enhance the natural contrast of the material. In this study the wooden particles were painted with a pattern like this. The face of the elastic pipe specimen was painted white, then speckled with fine black points and marked with additional 48 equally distributed crosses, see Figure 3.24. The PVC grains were not painted in any way as each rod had a different shade of grey.



Figure 3.24: *Elastic pipe surrounded by wooden grains at the beginning of a vertical compression with constant lateral pressure. The contrast of the front face of the pipe was increased by spraying fine black speckles over a white background and marking 48 points and crosses*

The principle of correlation is very simple and was summarised in Figure 3.23. In the beginning the user defines a position of a point in the first image that is supposed to be found in the second image, for example a centre of a specific grain. The DIC code contains that point of interest inside a *correlation window* that describe the size of a motif which will be looked for. The correlation window in general should be big enough to have some characteristic patterns of colour inside that would be easy to find on a second image but not too big to avoid covering space outside an exemplary grain.

After defining a box around a specific point, the code search for a best match between the motif taken from the initial image and the deformed one. Theoretically the small motif might be compared with the entire image surface, but it would be impractical. In most of the cases one can expect that a given grain moved in some specific direction and can give an approximate magnitude of the displacement. There is no need to compare the motif with far corners of the image. The user can specify a *search range* around the initial position of the motif and to limit the search.

The comparison is made by computing some metrics for each piece of the image inside the specified range and the best one is chosen at the end. After finishing this procedure one gets the information about the displacements of the original motif.

There are different metrics that allow quantifying whether two images match or not. One example, used in this study, is the *Normalised Correlation Coefficient* (NCC). Its function is

given by the following equation:

$$NCC(x, y) = \frac{\sum_{x=1}^n \sum_{y=1}^m (I_1(x, y) - \bar{I}_1) (I_2(x + u, y + v) - \bar{I}_2)}{\sqrt{\sum_{x=1}^n \sum_{y=1}^m (I_1(x, y) - \bar{I}_1)^2 \sum_{x=1}^n \sum_{y=1}^m (I_2(x + u, y + v) - \bar{I}_2)^2}} \quad (3.47)$$

Where:

- I_1 and I_2 are the grey level functions before and after deformation,
- \bar{I}_1 and \bar{I}_2 are the mean of I_1 and I_2 ,
- x, y are the local spatial coordinates,
- u, v are the local displacement coordinates.

Theoretically the correlation is perfect when the correlation coefficient is equal to 1.

In the simple DIC approach described above, transformations are expressed as integer values. The actual movements are much more complicated: they consist of translations, rotations and deformations at the same time, and none of these is integer. To overcome this problem, DIC codes usually offer so-called *sub-pixel refinement*, (Sutton et al., 2009). It is a numerical method whereby the initial integer transformation is improved and its non-integer value is found. That might be done by approximating a discrete function of the correlation coefficient and finding its maximum. The approximation can be realised in different ways. A simple example is shown in Figure 3.25. In this example, three neighbouring values of NCC are interpolated with a quadratic function, which is very simple and fast.

Another, more accurate but also more complicated method, is to approximate the grey level functions of the images instead of NCC. Doing that produces much more precise results if only because the original images have much higher resolution than the correlation coefficient fields.

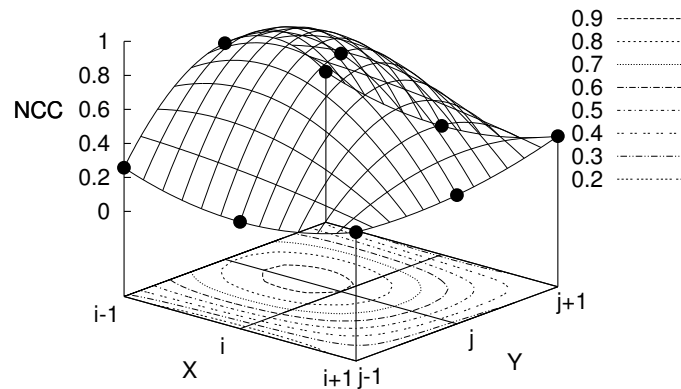


Figure 3.25: *Sub-pixel refinement example. Nine discrete values of correlation coefficient are approximated with a parabolic surface in order to find a maximum value. The position of this maximum is expressed with a real number*

A number of commercial and academic codes exist to carry out DIC. The program used in this work was developed by Steven Hall and is called *Photowarp* and was used previously in different works, for example (Hall et al., 2010) (Tengattini, 2010).

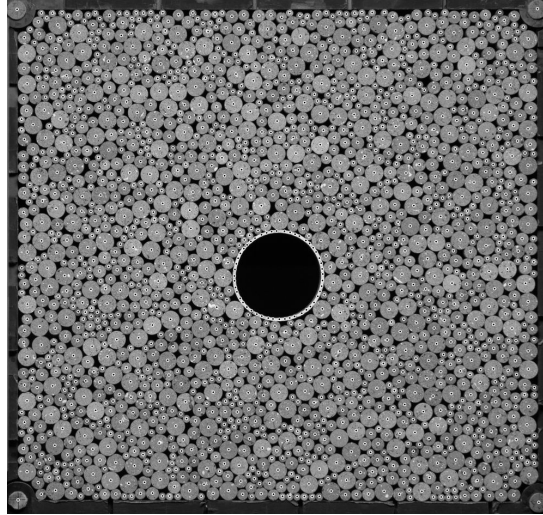


Figure 3.26: *Initial position of the points used in the digital image correlation. In this case the points were placed in the centre of each particle, in the corners of the experimental apparatus and around the perimeter of the pipe*

The DIC codes are capable of tracking big numbers of specific motifs relatively quickly. In this study specific points were defined in the corner of the $1\gamma 2\varepsilon$ in order to follow the strains of the experimental apparatus and on the front face of the pipe on its perimeter to follow the deformation of the pipe. Apart from these points, the granular material was tracked as well. In case of wooden grains, the points were placed in the mass centre of each particle, see Figure 3.26. In case of PVC the resolution of the images was too small to do the same, therefore a number of points of the highest contrast was chosen. These points covered all the area of the sample evenly.

3.3.3 Experimental Program

The $1\gamma 2\varepsilon$ apparatus was used to perform six tests with two different types of material: three tests with each type of particles. Two vertical compression tests without a pipe were done as a reference. These tests were followed by four tests with a circular PVC pipe placed inside the sample. Each type of granular sample was loaded vertically either in oedometric conditions or in biaxial conditions with constant lateral pressure.

The experiments performed in $1\gamma 2\varepsilon$ were recorded as series of digital images. The images were taken in specified time intervals, each 30s. The specimens that included a pipe were loaded with different velocities. The PVC particles used in the experiments had diameters of 1.5, 3.0 and 3.5mm, while the mixture of ash wood rods had diameters of 8.0, 10.0, 12.0 and 20.0mm. The microscopic intergranular friction angle between the wooden rods is equal to $\phi_{\mu}^{wood} = 25.5^{\circ} \pm 2^{\circ}$ while it is $\phi_{\mu}^{PVC} = 22.0^{\circ}$ between the PVC ones (Joer, 1991).

The information concerning all the experiments in the $1\gamma 2\varepsilon$ were summarised in Table 3.10.

3.3. $1\gamma 2\varepsilon$ EXPERIMENTS

	<i>Test</i>	Material	Pipe	Loading velocity	Image interval	Test name
Biaxial	1	PVC	NO	$2.0 \frac{cm}{h}$	none	Biax-1-PVC-NoPipe
	2	Wood	NO	$2.5 \frac{cm}{h}$	none	Biax-2-Wood-NoPipe
Biaxial	3	Wood	YES	$2.5 \frac{cm}{h}$	30s	Biax-3-Wood-Pipe
	4	PVC	YES	$5.1 \frac{cm}{h}$	30s	Biax-4-PVC-Pipe
Oedometric	5	Wood	YES	$5.1 \frac{cm}{h}$	30s	Oedo-5-Wood-Pipe
	6	PVC	YES	$5.1 \frac{cm}{h}$	30s	Oedo-6-PVC-Pipe

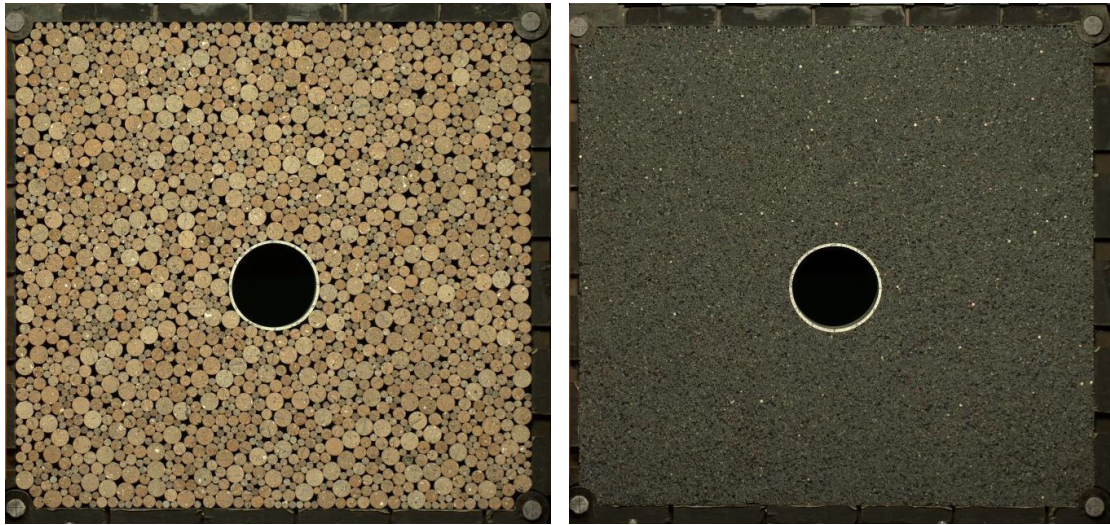
Table 3.10: *Description of the $1\gamma 2\varepsilon$ experiments*

The experimental protocol of a vertical compression with constant lateral pressure can be summarised in steps:

- **Sample preparation** The material is gradually placed inside the apparatus, one handful after another, without any additional densification. The rods are distributed evenly in all the width of the frame in order to avoid building steep, unstable slopes. In case of an experiment with a pipe it is placed inside the sample in the same time as the grains. The few last centimetres on the top of the sample are built by placing the rods one by one. The top surface of the sample must be flat to ensure full contact of the sample with the top wall. To be sure that the strains occur in one plane the front face of the sample is flattened as well. The flat front face is also critical for the subsequent particle recognition: rods protruding from the sample cast shadows on the surrounding rods. The flattening procedure causes a slight densification of the assembly;
- **Isotropic compression** The three moving walls (L,R,T) compress the sample isotropically in order to reach a certain level of stress on every wall, in this case $\sigma_0 = 50kPa$;
- **Vertical compression with constant lateral pressure** In the vertical compression test the top plate moves down with a low, constant velocity (in this case $\leq 1 \frac{mm}{min}$ which corresponds to $I \simeq \frac{0.1cm/min}{50cm} \sqrt{\frac{14g \cdot 2cm}{50kPa \cdot 6cm \cdot 50cm}} \simeq 1 \cdot 10^{-8}$ which ensures the quasi-static conditions), lateral pressure is kept constant and equal to the isotropic pressure from the previous step. This step is finished when the maximum width of the apparatus frame is reached or when the pipe deformation is big enough to create a risk of sudden breaking which could be dangerous to the apparatus;

The sample in the vertical compression test was prepared as previously. The loading itself was performed differently and there was no initial isotropic phase:

- **Oedometric compression** During the test the vertical walls remain in the same position while the top wall moves down with a constant velocity. Next the sample is unloaded in the same manner;

(a) *Sample of wooden rods*(b) *Sample of PVC rods*Figure 3.27: *Images of $1\gamma 2\epsilon$ samples at the beginning of biaxial tests*

3.3.4 Oedometric Tests Results

3.3.4.1 Macroscopic Results

The experiments were performed starting from no vertical stress (some horizontal stress was recorded by the sensors due to the weight of the sample). Initially the top plate of the apparatus was not in contact with the sample and was lowered with a constant velocity. The moment when the stresses (both vertical and horizontal) began to increase was arbitrarily chosen as a start of the oedometric compression. That is the reason why the experimental stress curves in Figure 3.28 are not ideally starting from $0Pa$.

During the oedometric test made on both wooden and PVC particles, the stress on the walls of the apparatus rose quickly while the pipe specimen or the granular material did not deform or displace much. Nevertheless, the sample consisting of PVC grains deformed more than the sample made of wood.

The measurements of stress allowed us to obtain the coefficient of earth pressure at rest $K_0 = \frac{\sigma_3}{\sigma_1}$. It is equal to 0.6 for the sample made of wooden particles and 0.5 for the sample consisting of PVC grains.

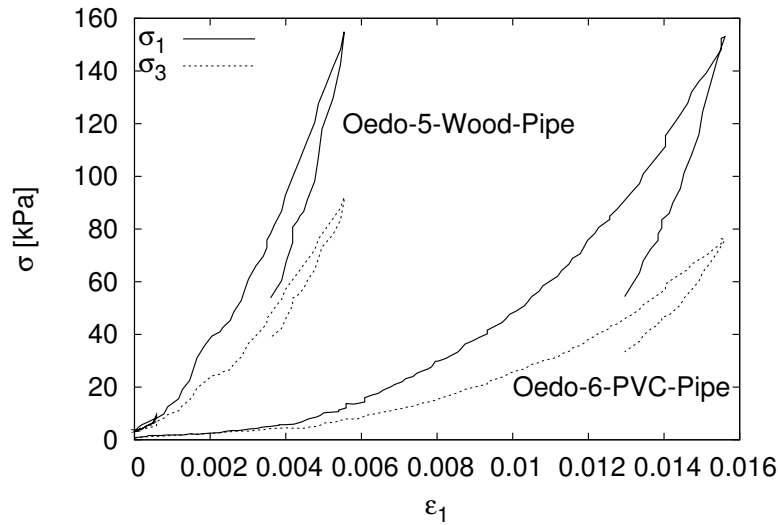


Figure 3.28: $1\gamma 2\varepsilon$ oedometric compression results of tests *Oedo-5-Wood-Pipe* and *Oedo-6-PVC-Pipe* consisting of two types of materials with a circular, elastic pipe inside. Elastic modulus of the wooden sample is equal $28 \cdot 10^6 Pa$ while for the PVC sample it is equal to $10 \cdot 10^6 Pa$

3.3.4.2 Kinematic Analysis

The front face of the sample was photographed in regular time intervals using a static digital camera during the experiments. The images obtained that way were used to acquire information about the kinematic behaviour of the assembly with DIC tools, see Section 3.3.2.

During the observation of the experiments it seemed there was very little deformation of the pipe. The measurements of the sample- and pipe area revealed that during the *Oedo-5-Wood-Pipe* experiment the volumetric strain of the apparatus reached -0.55% (negative value denoting contraction) while in the elastic pipe it was equal -0.2% . In the experiment *Oedo-6-PVC-Pipe* the maximum values of ε_V were equal to -1.56% and -0.23% respectively.

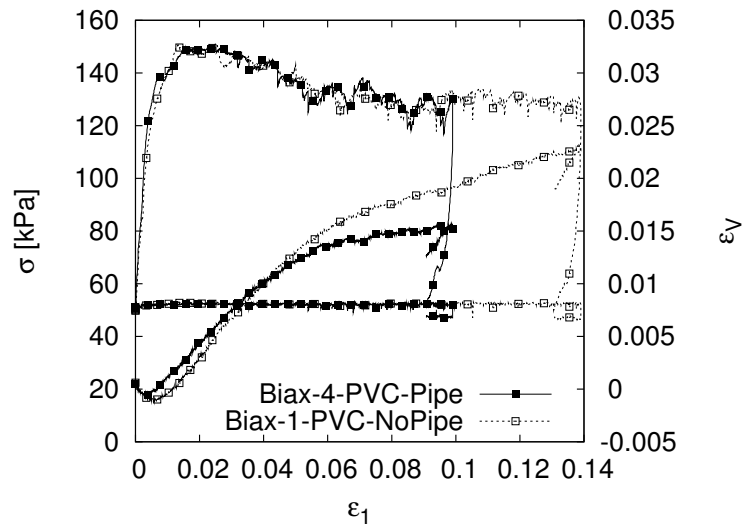
These results show that the majority of the overall deformation occurred in the granular material, not in the elastic pipe, which deformed approximately the same amount in both the tests. The sample made of wooden particles was more dense than the sample made of PVC.

3.3.5 Biaxial Test Results

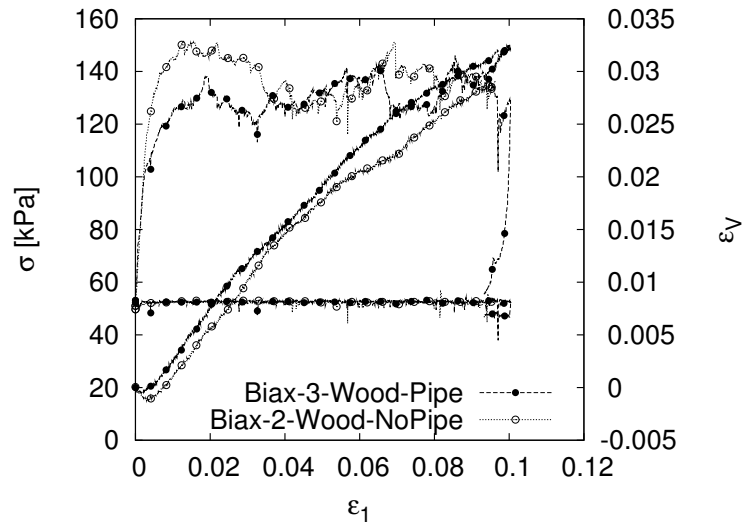
3.3.5.1 Macromechanical Response

The macroscopic results of the vertical compression tests show that the presence of a PVC pipe in the central part of the assembly does not influence the overall behaviour of the specimen, see Fig. 3.29. Even though the samples were prepared in the same way, it is virtually impossible to assure that their density is the same, hence the differences in the volumetric strain curves.

The elastic modulus of the sample of wood was equal to $22 \cdot 10^6 Pa$ while in case of PVC its value was lower: $15 \cdot 10^6 Pa$. The macroscopic friction angle at the peak was equal to 30° for the samples made of PVC rods and 30° and 26.4° for the samples made of wood, without and with the pipe specimen respectively. As for the friction angle at the threshold, the values of all the tests were similar and were about 26.4° as well. The macroscopic behaviour of these samples is characteristic for dense assemblies of cohesionless material like sand.



(a) PVC rods



(b) Wooden rods

 Figure 3.29: $1\gamma 2\varepsilon$ experiment results of two types of materials with or without a circular, elastic pipe inside

Please note that in both the boundary conditions, oedometric and biaxial, the maximum level of stress reached was similar.

3.3.5.2 Kinematic Analysis

3.3.5.2.1 Strains

During the experiments it was decided to photograph all the area of the sample with a single camera. Because the maximum size of the $1\gamma 2\varepsilon$ apparatus walls is about $60 \times 60\text{cm}$, a scale of an image taken with a 24MPx camera was approximately $1\text{mm} = 6\text{px}$. That means that the smallest PVC rod diameter was $\approx 9\text{px}$ and a rectangle inscribed inside that rod was a square smaller than $7 \times 7\text{px}$. Therefore it was not large enough to carry out reliable correlation on

each rod separately. A better choice was to study the full deformation field of such a sample by treating it as a continuum. What it actually means is that a number of points was defined over all the area of the image and a DIC was carried out for each grid node between two given images.

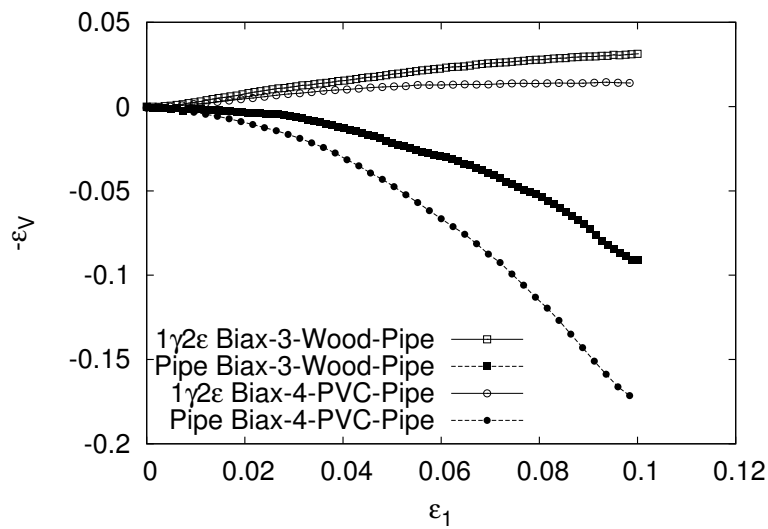
The samples made of wooden rods have grains big enough to carry out a correlation by treating the assembly as a discrete medium. With the same scale of the image as previously, the wooden rods have between 48 and 160px of diameter, which is enough to fit a correlation window inside a single grain.

Apart from observing the kinematics of the granular medium, a separate correlation was done using only the points on the front face of the pipe specimens. This allowed us to monitor the change of shape of the pipe.

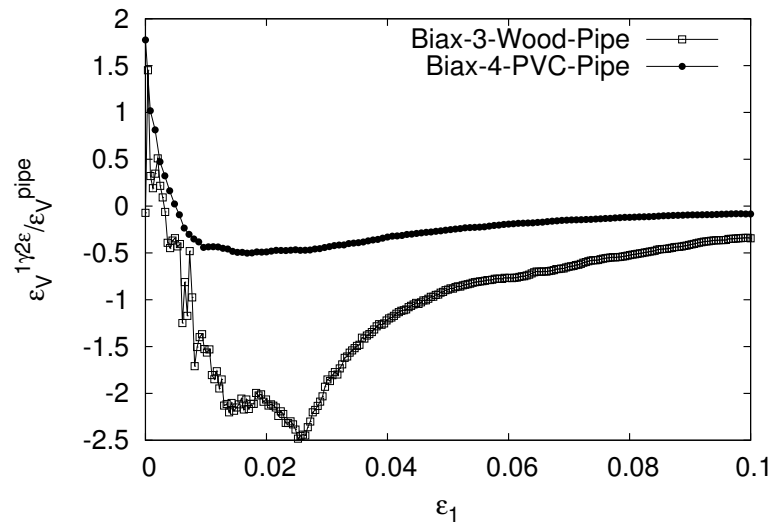
To each correlation four points representing the corners of the apparatus were added. They allowed verifying the size of the frame independently from the LVDTs in the apparatus and (since one of the corners is fixed) the quality of correlation as well.

Each biaxial test sample was loaded up to 10% of vertical strain ε_1 of the apparatus.

Having photographed the size of the sample and the size of the PVC pipe inside it was interesting to present the comparison of the volumetric strains of these two, see Figure 3.30. As one can see, the elastic pipe model was behaving differently then the whole assembly: it was contracting during all the test, Fig. 3.30a. In order to investigate the relation between the strains of the apparatus and the strains of the pipe specimen, it was decided to plot the $\frac{\varepsilon_V^{1\gamma 2\varepsilon}}{\varepsilon_V^{pipe}}$: Figure 3.30b. The sample made of wooden grains was causing the pipe to deform in a less symmetric shape because a smaller number of grains was in contact with the pipe. This caused the disturbances in the first part of the curve. On the other hand, the sample made of PVC rods was acting in a more equally distributed way and thus the shape of the pipe and the resulting change of volume were much more smooth. The behaviour presented in that figure shows that the elastic pipe was compressing more then the surrounding granular material.



(a) Volumetric strain of the sample and pipe



(b) Comparison between volumetric strains

Figure 3.30: During vertical compression test in $1\gamma 2\varepsilon$ the volumetric strains of the apparatus and the pipe specimen were different. The whole sample was dilating ($\varepsilon_V > 0$) while the PVC pipe was contracting ($\varepsilon_V < 0$). The figures present the values of the strains and the relation between them throughout the test

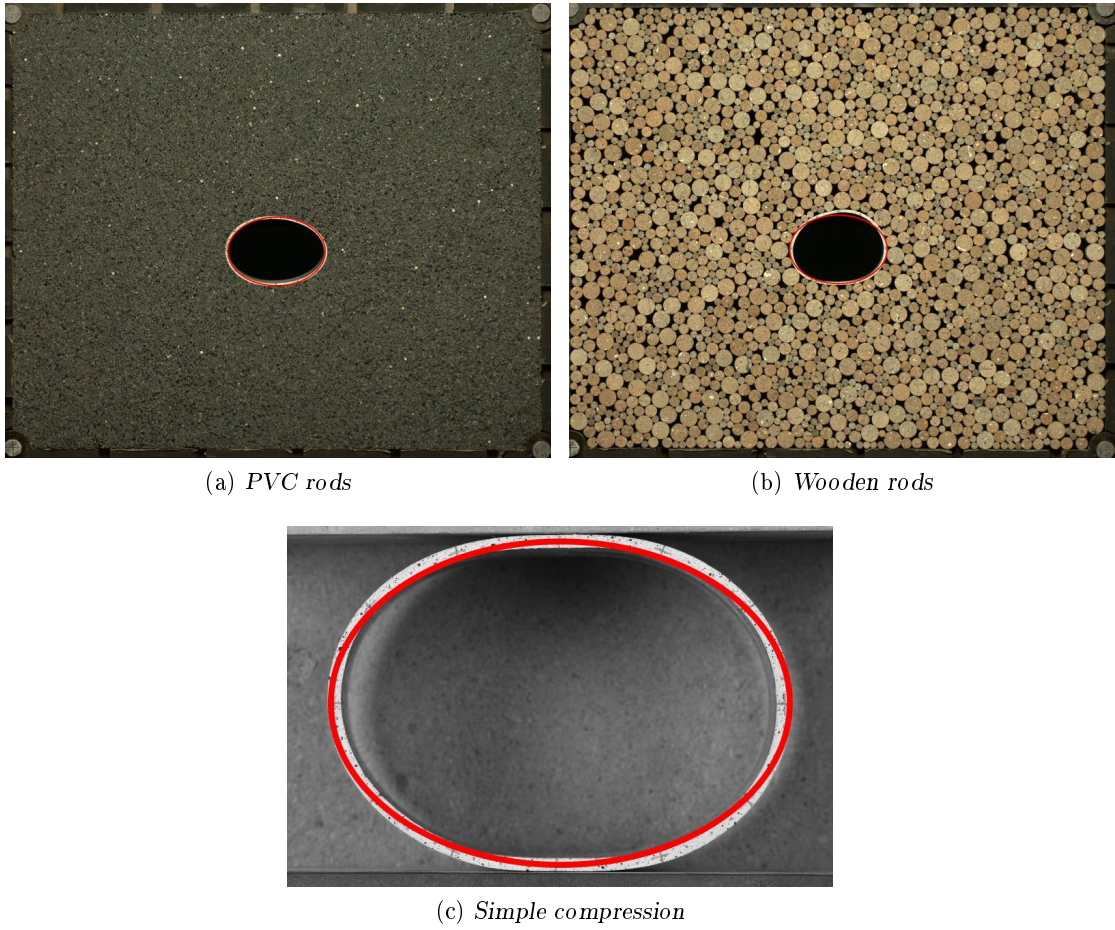


Figure 3.31: Images of the loaded samples. An ellipse with the same value of eccentricity was superposed over each pipe

The shape of the pipe specimens during loading resembled an ellipse, see Figure 3.31. Therefore it was decided to compare the change of volume of the pipes during the experiments with the change of volume of a circle transforming into ellipse with the same perimeter. There is no simple way to express the perimeter of an ellipse. A Maclaurin expansion up to its fifth term was used here (Maclaurin, 1774):

$$P_{ellipse} = 2\pi a \left(1 - \left[\frac{1}{2} \right]^2 \cdot \frac{e^2}{1} - \left[\frac{1 \cdot 3}{2 \cdot 4} \right]^2 \cdot \frac{e^4}{3} - \left[\frac{1 \cdot 3 \cdot 5}{2 \cdot 4 \cdot 6} \right]^2 \cdot \frac{e^6}{5} - \left[\frac{1 \cdot 3 \cdot 5 \cdot 7}{2 \cdot 4 \cdot 6 \cdot 8} \right]^2 \cdot \frac{e^8}{7} \right), \quad (3.48)$$

$$e = \sqrt{1 - \frac{b^2}{a^2}}, \quad (3.49)$$

where a is the major, horizontal axis while b is the minor, vertical axis and e is ellipse eccentricity. Supposing that during the compression the perimeter remains constant, $P_{ellipse} = P_{circle}$, it was possible to obtain a relation between ε_V and ε_1 , Fig. 3.32.

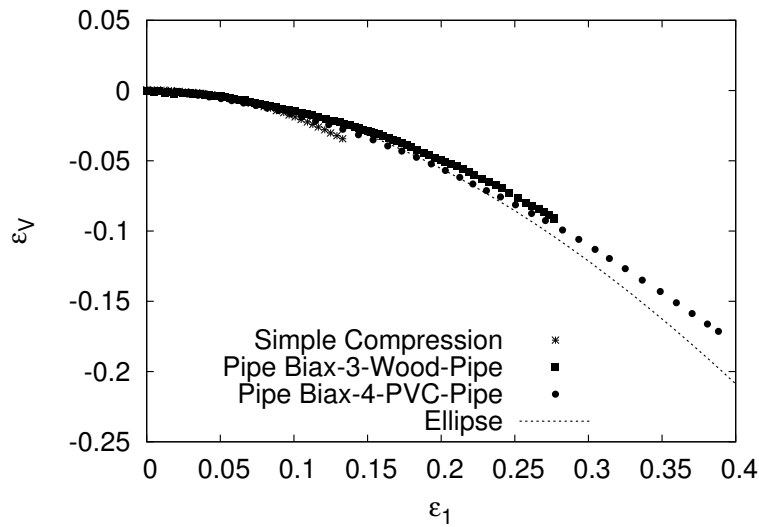
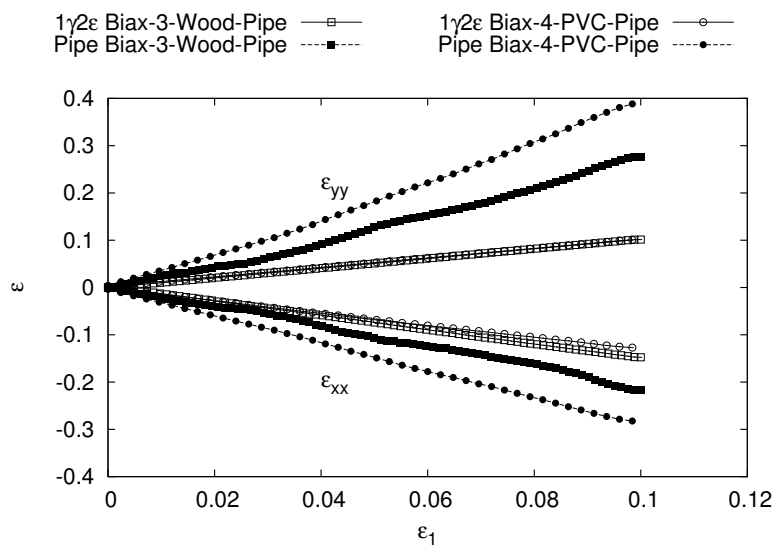


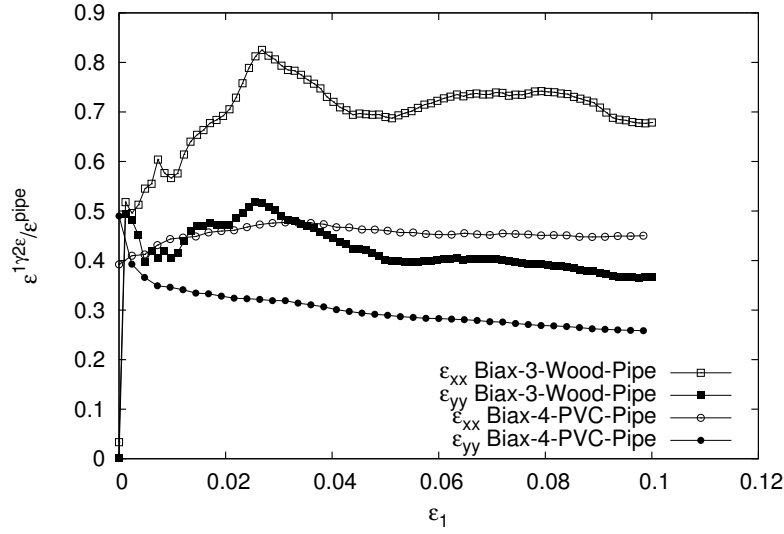
Figure 3.32: Comparison of the volumetric strains between experiments on an elastic pipe with theoretical behaviour of an ellipse. The vertical strains ε_1 are not the strains of the experimental apparatus but the strains of the pipe

As one can see, the behaviour of the elastic pipe in all the three experiments, simple compression discussed previously (Section 3.2.4.2) and vertical compression with constant lateral loading, is almost the same as the behaviour of the mathematical model, especially in the initial phase of the loading.



(a) Strain of the sample and pipe

Figure 3.33: During vertical compression test in $1\gamma 2\varepsilon$ the strains of the apparatus and the pipe specimen were different. The figures present the values of the strains and the relation between them throughout the test. The figure is continued on the next page



(b) Comparison between strains

Figure 3.33: During vertical compression test in $1\gamma 2\varepsilon$ the strains of the apparatus and the pipe specimen were different. The figures present the values of the strains and the relation between them throughout the test

The same approach was used to study the vertical and horizontal strains of the pipe in reference to the strains of the experimental apparatus. Figure 3.33 shows that the pipe was cumulating the strains more than the surrounding material. This effect is more pronounced in the sample made of PVC rods.

3.3.5.2.2 Displacement Fields

Knowing the positions and displacements of each grain (or randomly chosen points covering the entire sample) it was possible to obtain fields of displacement, presented in Figures 3.34 and 3.35 (see Appendix D.1 for larger, scalable images). The centre of coordinates was placed at the bottom of the pipe.

The aforementioned figures are difficult to analyse. A more clean view of the behaviour of the assembly can be obtained by presenting the same fields after subtracting the mean field of displacement \bar{u}_i , as it is presented in Figures 3.36 and 3.37 (see Appendix D.2 for larger, scalable images and zoom the region above the elastic pipe).

$$u_i = u'_i + \bar{u}_i \quad (3.50)$$

$$u'_i = u_i - \bar{u}_i \quad (3.51)$$

$$\bar{u}_i = \mathbf{X}_i \boldsymbol{\varepsilon} \quad (3.52)$$

where:

- u_i is the displacement of a grain i ,
- \bar{u}_i is the mean field of displacement,
- u'_i is the fluctuation around the mean field,
- \mathbf{X}_i is the initial position of the grain i ,
- $\boldsymbol{\varepsilon}$ is the strain tensor.

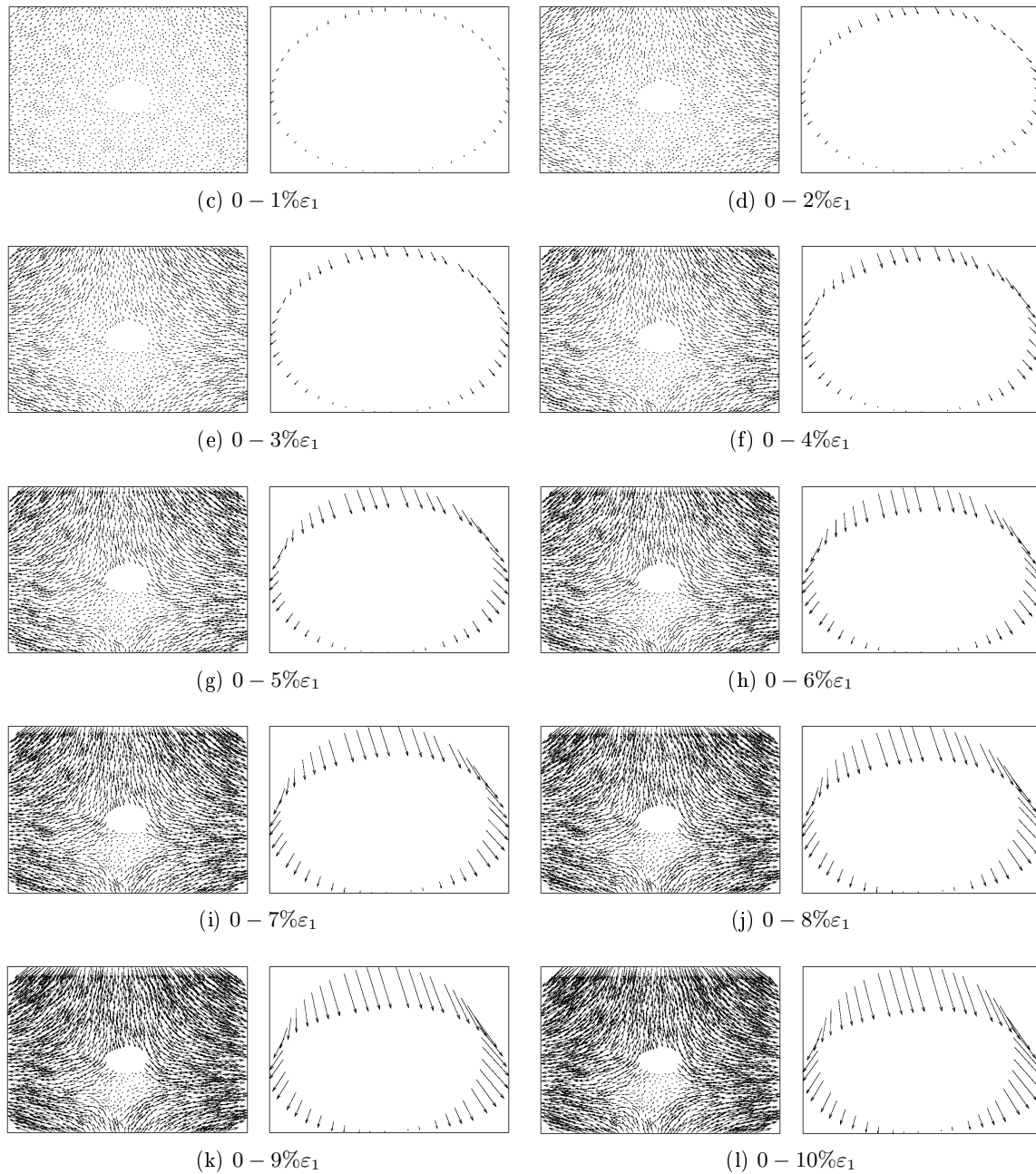


Figure 3.34: Wooden grains with a PVC pipe, displacement fields. The longest arrow of particle displacement is equal to 58mm; The biggest displacement of a point on a pipe is equal to 26mm

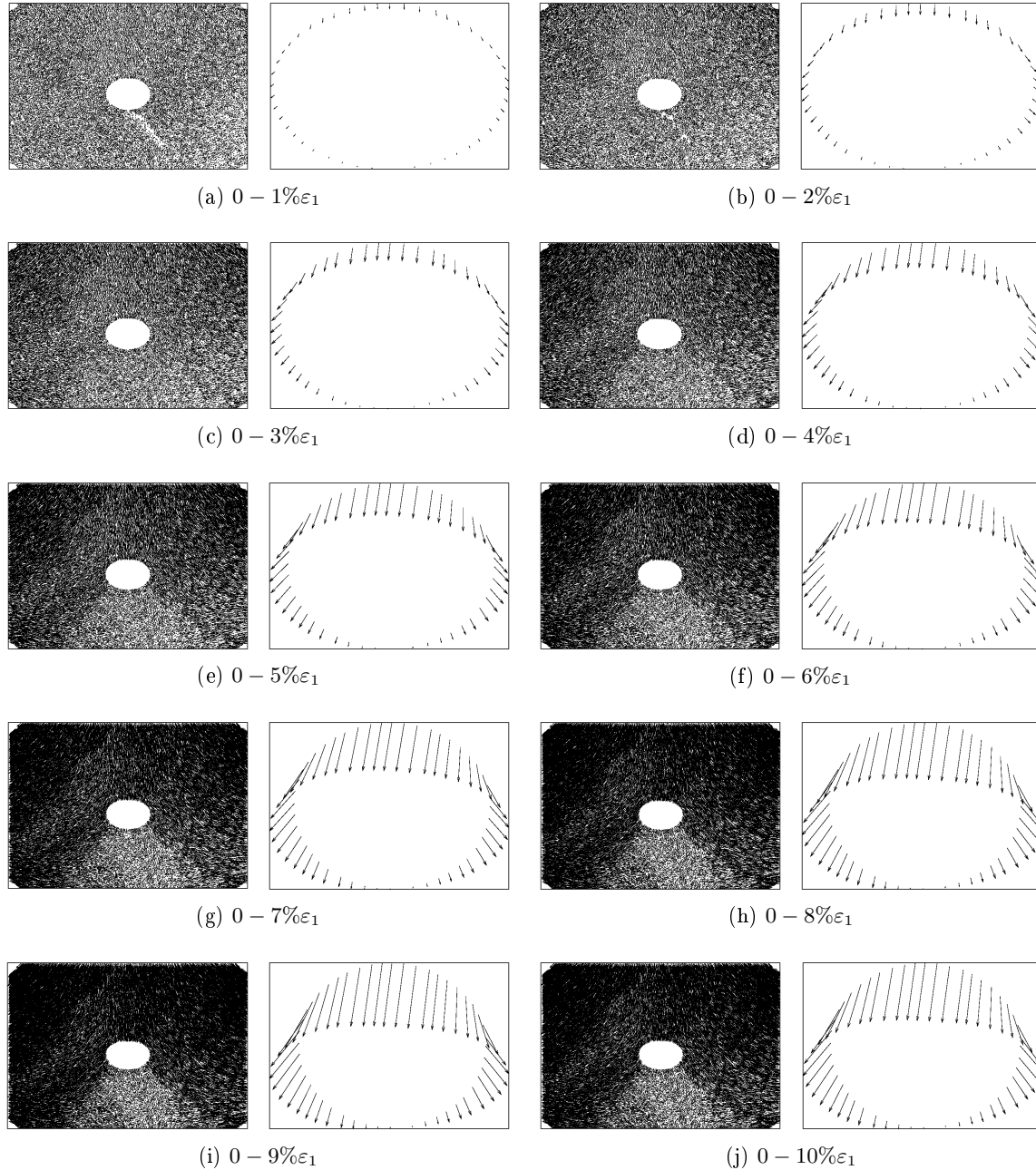


Figure 3.35: PVC grains with a PVC pipe, displacement fields. The longest arrow of particle displacement is equal to 51mm and it was reduced three times in the images for a clearer presentation; The biggest displacement of a point on a pipe is equal to 34mm

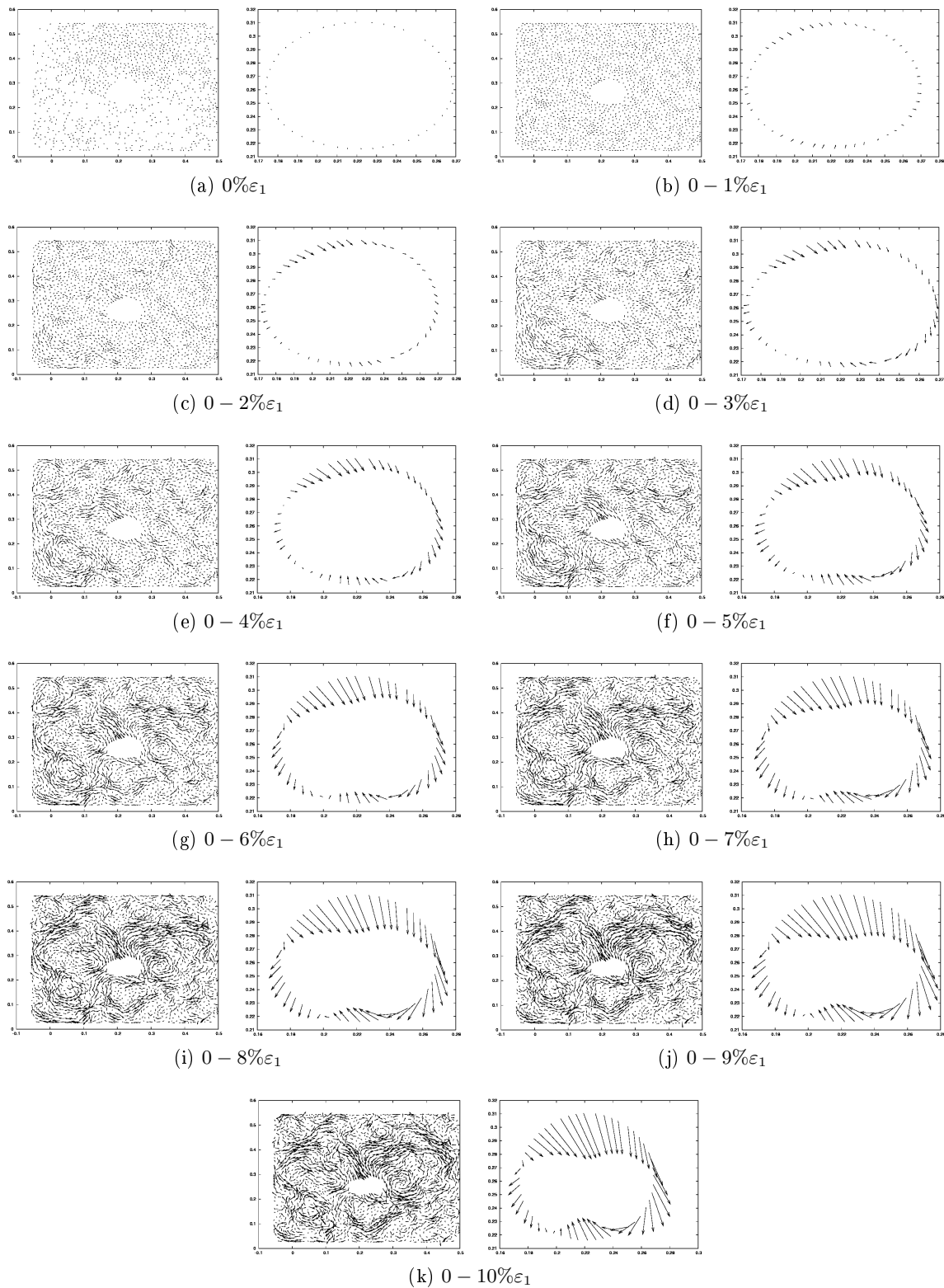


Figure 3.36: Wooden grains with a PVC pipe, a mean field of displacement was subtracted from the displacement field. The longest arrow of displacement in the figures correspond to 4cm

3.3. $1\gamma 2\varepsilon$ EXPERIMENTS

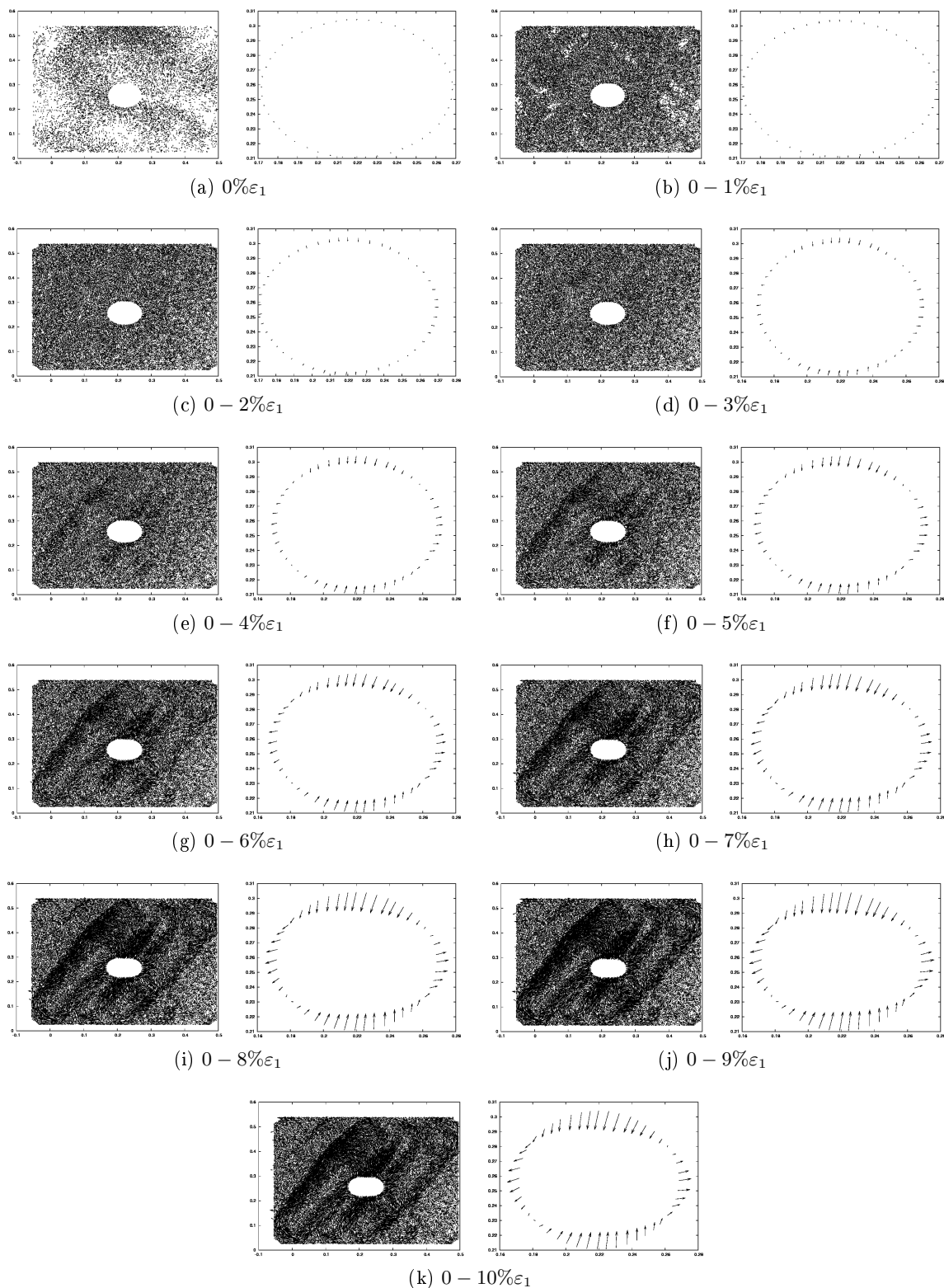


Figure 3.37: PVC grains with a PVC pipe, a mean field of displacement was subtracted from the displacement field. The longest arrow of displacement in the figures correspond to 1cm

This subtraction allows us to see that indeed, as shown with the macroscopic plots of the strains, the pipe is deflecting more than the surrounding grains.

3.3.5.2.3 Localisation of Shear

The images of displacement vectors reveal some discontinuities that are due to the localisation zones. A better look into these localisations can be obtained by plotting the second strain invariant in the same way as was previously done on the pages 30 and 40. The results are presented in Figures 3.38 and 3.39 (see Appendix D.3 for larger, scalable images). Please note that the symbols inside the pipe are artifacts of triangulation, not actual indicators of shear.

It is visible that the shear localisation zones are reflected by the walls, they intersect each other and also seem to go through the PVC pipe specimen. It is discussable whether the presence of a PVC pipe changes the shear localisation patterns or not. The localisation bands seem to go through the pipe instead of going around, at least in the first phases of the test.

In course of this study the images were not taken during Biax-1-PVC-NoPipe and Biax-2-Wood-NoPipe experiments. A similar experiment in the same apparatus with the same PVC rods was done previously (Viggiani and Hall, 2008) and a resulting maximum shear strain is presented in Figure 3.40. It is clear that the shearing pattern, although unique to every experiment, is similar in both the cases, with and without an elastic pipe.

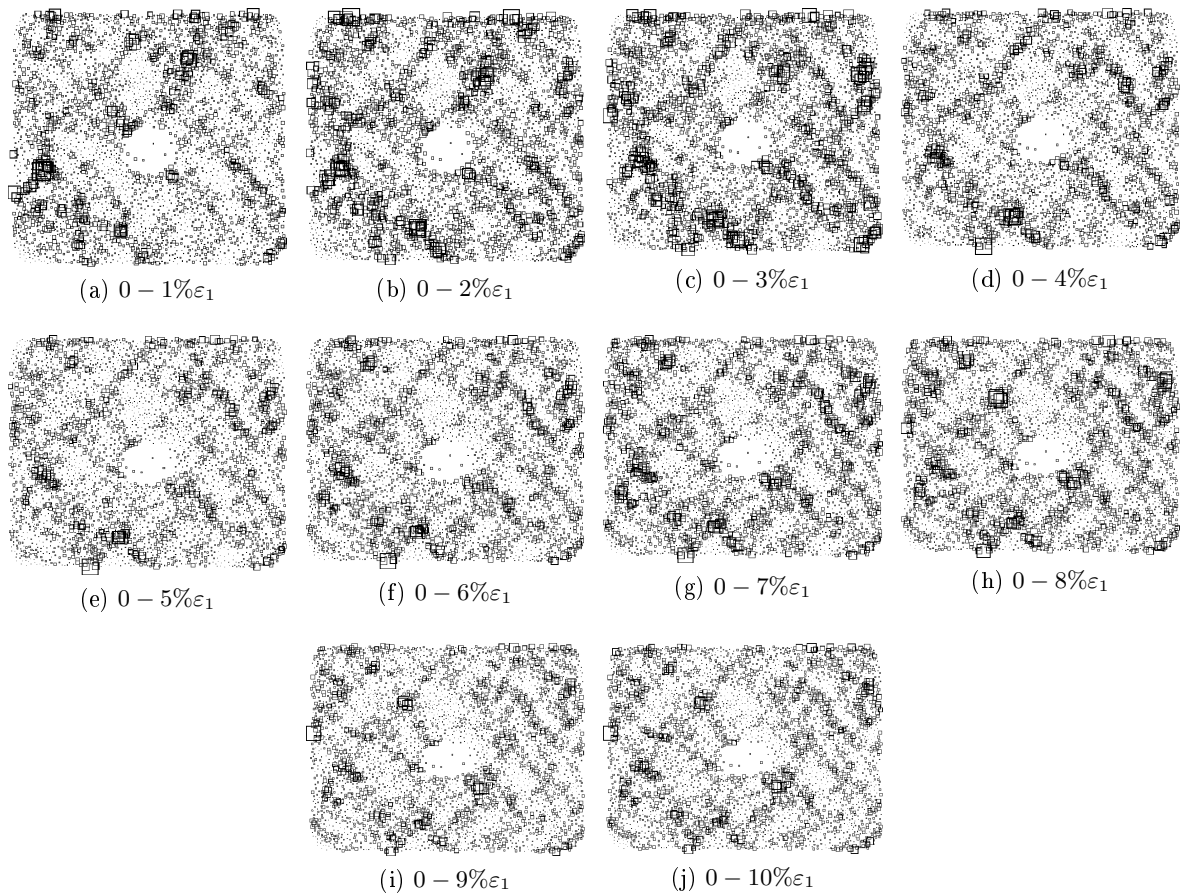


Figure 3.38: Wooden grains with a PVC pipe, shear localisation. For the maximum strain the biggest symbol correspond to 300% while the mean is equal to 35%

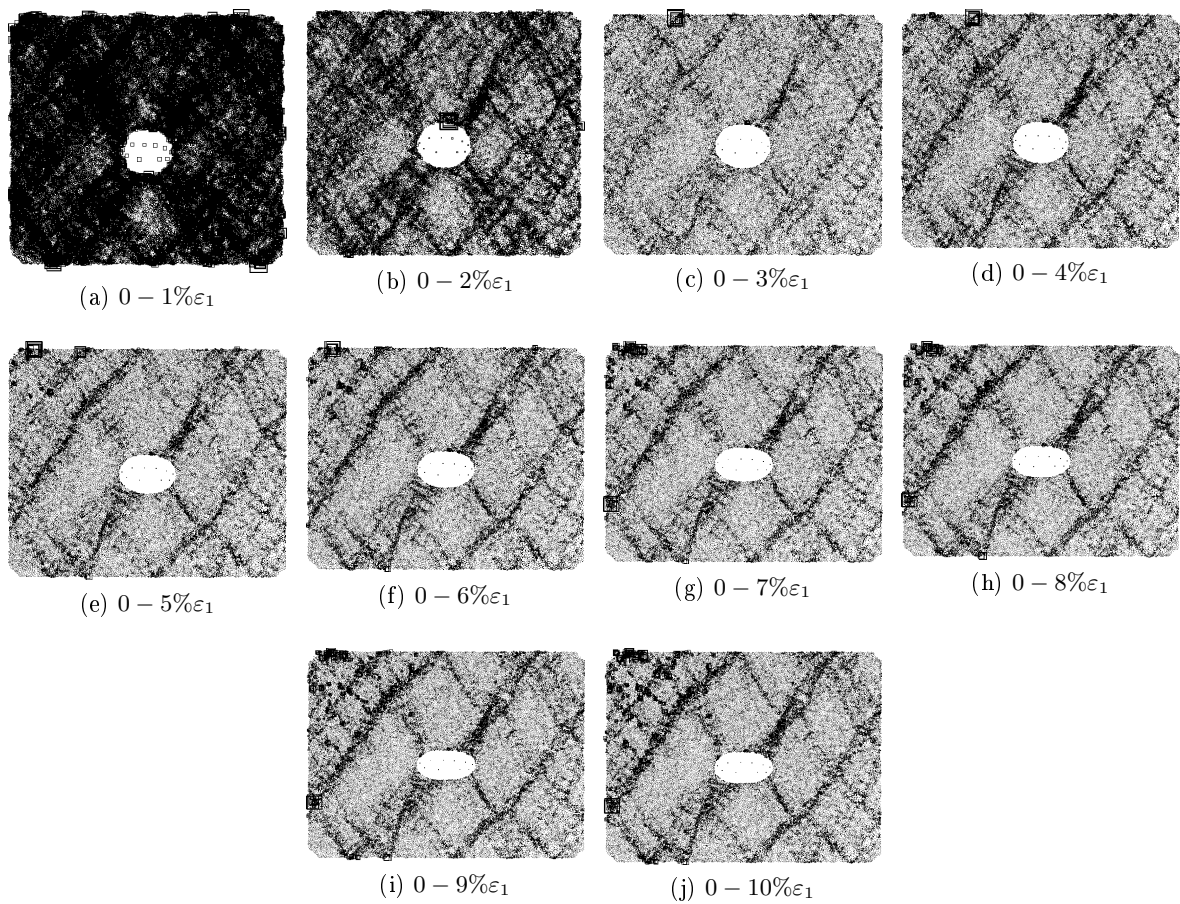


Figure 3.39: *PVC grains with a PVC pipe, shear localisation. For the maximum strain the biggest symbol correspond to 2500% while the mean is equal to 32%*

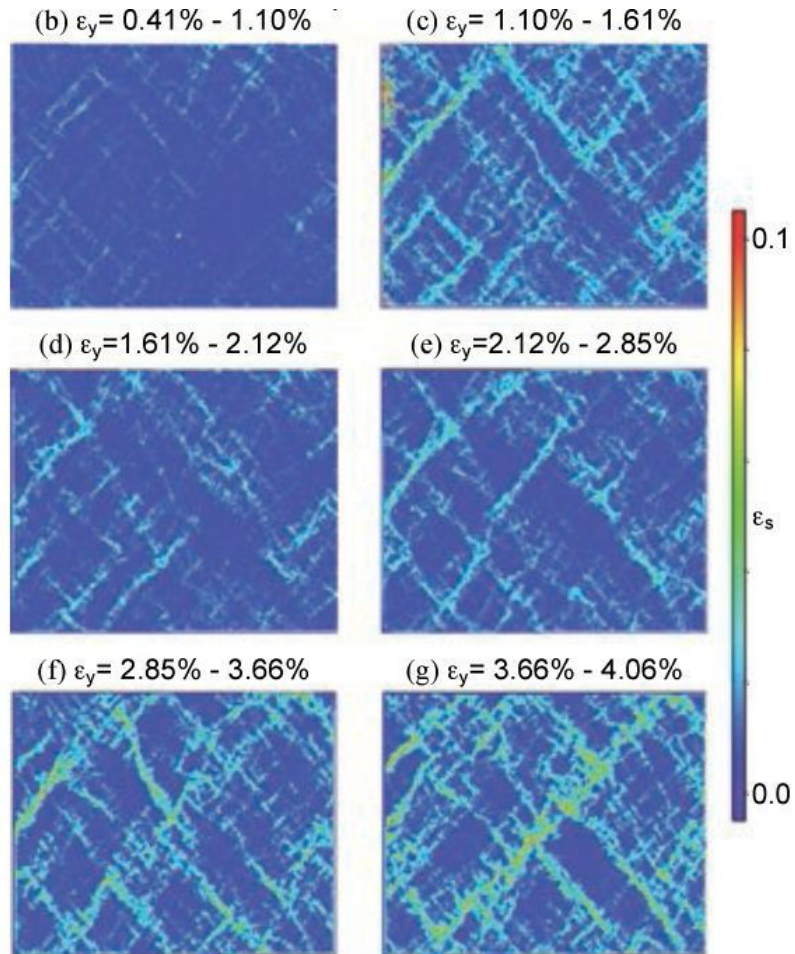


Figure 3.40: Shear strain during a vertical compression of PVC Schneebeli material in $1\gamma 2\epsilon$. The DIC code Photowarp revealed shear localisation zones similar to the ones obtained by us with the PVC pipe inside. Image reproduced from (Viggiani and Hall, 2008), courtesy of Viggiani and Hall

3.3.6 Conclusions

The experimental program in $1\gamma 2\varepsilon$ consisted of tests in two different boundary conditions and with two different types of granular material. The main purpose of these experiments was to study the influence of an elastic pipe placed inside the specimen and to create a point of reference for the numerical modeling. The tests were recorded with the use of the sensors built in the apparatus and on multiple digital images as well.

The stress-strain macroscopic curves show little influence of the elastic pipe specimen on the behaviour of the sample. The similar behaviour was obtained both in terms of volume change and the shear resistance. The similarity was bigger for a sample made of small PVC grains which is due to the much larger number of particles in these tests.

The digital images were analysed using DIC software. It allowed us to see that during vertical compression with constant lateral pressure the strains in the pipe were bigger than in the apparatus. The opposite was observed in oedometric conditions, where the volumetric strains of the pipe constituted a fraction of the global strains.

The digital image correlation revealed shear localisation in the samples. It was consistent with previous results obtained in this apparatus and shown little influence of the elastic pipe on the localisation patterns.

3.4 Modeling of an Elastic Pipe in Granular Material

The final step of this study was to incorporate the pipe model described in Section 3.2.2 into the granular model described in Chapter 1 in order to perform numerical experiments similar to those in $1\gamma 2\varepsilon$ (see Section 3.3) and to obtain proofs of arching effect over the elastic pipe.

3.4.1 Simulation Protocol and Parameters

The numerical simulations were done in PFC^{2D}. The simulation protocol was similar to the one described in the previous chapter:

1. Initially a single large disc was placed and fixed inside a rectangular box as a placeholder for the elastic pipe. The box was 0.5 by 0.5m while the centre of the disc was at (0.25, 0.20). The radius of the large disc was equal to the radius of the elastic pipe increased by the radius of the discs forming the pipe;
2. The particle growing phase was the same as previously, except that it did not affect the temporary particle in the middle;
3. Next, the large disc in the middle of the sample was replaced with an elastic pipe consisting of 48 particles, as described in Section 3.2.2. Translation and rotation of the discs forming the pipe were blocked;
4. The sample was isotropically compressed by rigid walls with no friction between the walls and the grains. The sample was compressed until the stress on the walls reached $\sigma_0 = 50.0kPa$;
5. The grains forming the pipe were set free.

Samples prepared in that way were subsequently loaded in a vertical compression test with constant lateral pressure. As in the case of physical test, a sample was tested in oedometrical conditions as well.

The numerical parameters of the particles of soil once again were computed according to the dimensionless stiffness parameter κ (page 36). For sake of comparability it was decided to keep the same value of $\kappa = 1000$ as in the previous part. In the new simulations the pressure level was five times higher than before, therefore the normal contact stiffness of the soil was chosen to be equal to $k_n = 50000[\frac{kN}{m}]$. The tangential stiffness of contact was decided to be equal to the normal one, as in (Szarf et al., 2011).

The stiffness of the elastic pipe model was computed basing on the Young's modulus of the PVC pipe as described previously (Section 3.2.2). The effects of contact stiffness between the particles of the pipe were countered with additional forces. This way it was possible to model the interactions between the soil and the pipe in the simplest way: there was no difference between soil – soil and soil – pipe contacts. It was decided to use two different values of the microscopic friction parameter between the particles of the soil and the particles of the pipe. The values of μ_{int} used were equal to 0.5 and 0.0.

Apart from the standard pipe stiffness additional tests with other Young's modulus values were performed. While the reference simulations were modeling a pipe made of PVC, the other stiffnesses used were resembling soft plastic and concrete.

3.4.2 Numerical Simulations Performed

Biaxial compression and oedometric tests were carried out:

Twelve vertical compression tests with constant lateral loading were performed for different values of shape parameter in order to evaluate the influence of the shape of grains on the arching effect. The simulations are summarised in Table 3.11. Apart from these twelve tests one grain shape ($\alpha = 0.5$) was chosen to be used in vertical compression tests with the value of Young's modulus of the pipe ten times lower (test C05d-p0-e7) and ten times higher (test C05d-p0-e9) than the $20.0e8Pa$ used in the other tests. In the tests with different pipe stiffness values the friction coefficient between the pipe and the soil μ_{int} was zero.

$\alpha =$	0.0	0.1	0.2	0.3	0.4	0.5
$\mu_{int} = 0.0$	C00d-p0	C01d-p0	C02d-p0	C03d-p0	C04d-p0	C05d-p0
$\mu_{int} = 0.5$	C00d-p5	C01d-p5	C02d-p5	C03d-p5	C04d-p5	C05d-p5

Table 3.11: Description of the twelve vertical compression simulations with pipe performed in PFC^{2D}. Each sample consisted of 5000 clumps of a given type and a pipe model made of 48 discs. The microscopic friction between the pipe and the surrounding material was different. Young's modulus of the pipe was equal to $20.0e8Pa$

The vertical compression simulation in oedometric conditions was performed with $\alpha = 0.5$ clumps, with no friction on the pipe boundary and with standard pipe stiffness $E = 20e8Pa$; The name of the oedometric test was C05d-p0-oed.

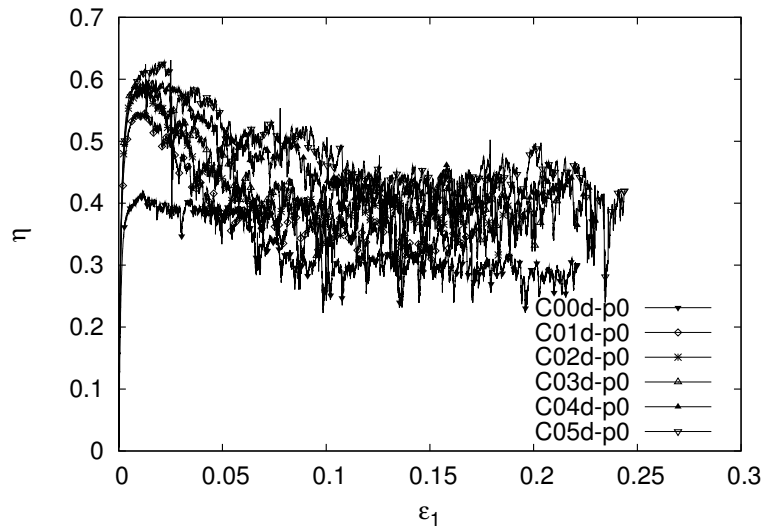
3.4.2.1 Macromechanical Response

3.4.2.1.1 Biaxial Compression

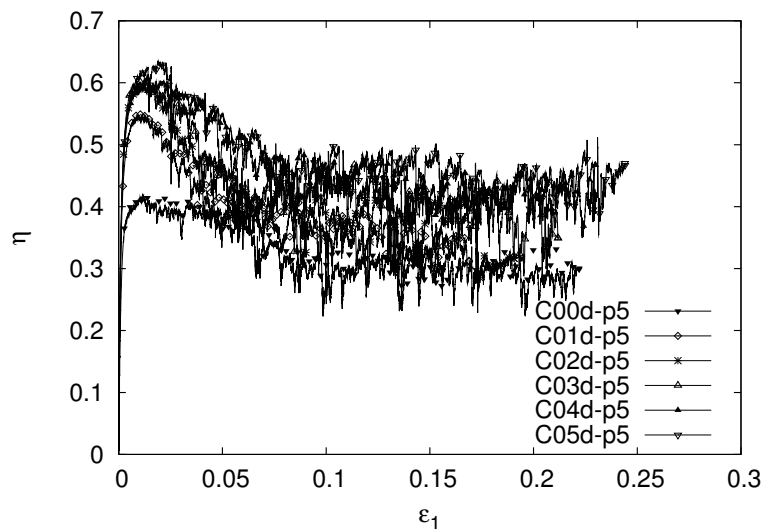
Influence of Grain Shape The comparison of the macroscopic results of the numerical compression tests with the results obtained from biaxial tests without pipe described in Chapter 1 show that the presence of the pipe have little influence on the behaviour of the sample, compare Figures 3.41a, 3.41b and 3.41c. A similar result was obtained in the $1\gamma 2\varepsilon$ experiments, Figure 3.42. The shape of the curves and the peak and threshold values of the stress obtained are

3.4. MODELING OF AN ELASTIC PIPE IN GRANULAR MATERIAL

similar in the simulations and the experiments for the numerical sample made of discs (*C0d*), which shows much lower values of the friction angle both at the peak and at the threshold than the rest of numerical samples made of clumps.

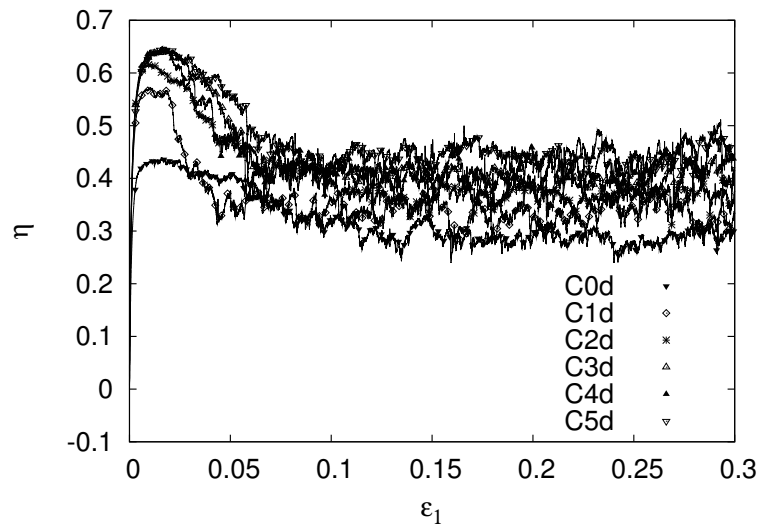


(a) Simulation with pipe, $\mu_{int} = 0.0$



(b) Simulation with pipe, $\mu_{int} = 0.5$

Figure 3.41: Comparison of the numerical macroscopic results of vertical compression tests on clumps with and without circular elastic pipe inside the sample. The graphics show tests performed with pipe inside. The two simulations differ by the value of the friction coefficient between the granular material and the pipe



(c) Simulation without pipe

Figure 3.41: Comparison of the macroscopic results of vertical compression tests on clumps with and without circular elastic pipe inside the sample. The graphic recalls the macroscopic response of granular material without the intrusion

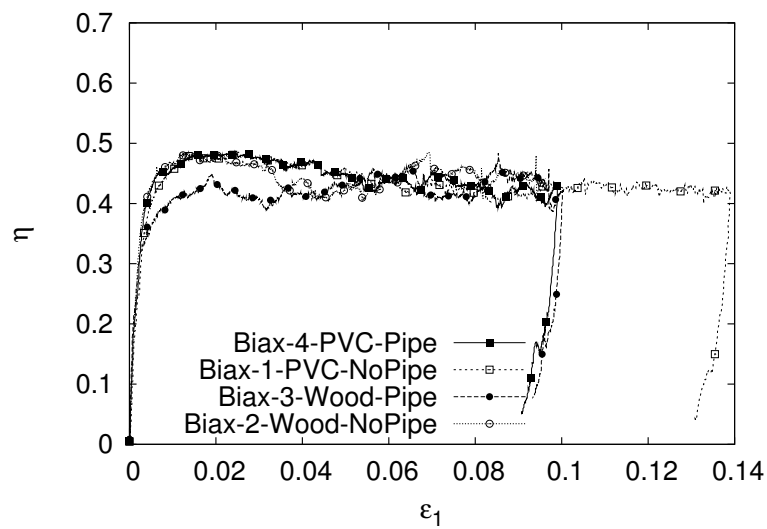


Figure 3.42: $1\gamma 2\epsilon$ experiment results of two types of materials with or without a circular, elastic pipe inside

Influence of Pipe Stiffness For the chosen values of pipe and soil rigidity there seems to be little influence on the global strength of the sample, see Figure 3.43. Both the peak and residual friction angle are unaffected by the change of the stiffness of the pipe.

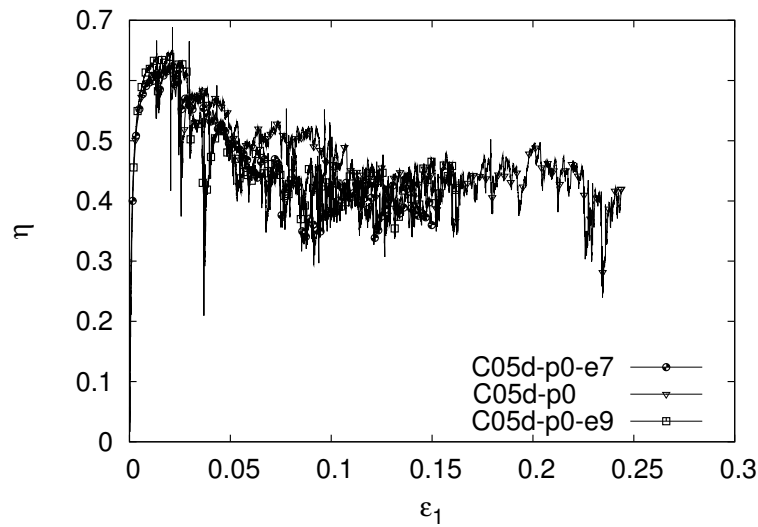


Figure 3.43: Comparison of the macroscopic results of numerical biaxial compression with clump $\alpha = 0.5$ samples including pipes of different stiffness: $20e7Pa$, $20e8Pa$ and $20e9Pa$

3.4.2.1.2 Oedometric Compression The numerical results of vertical compression in oedometric conditions are presented in Figure 3.44. The curves are not starting from $0Pa$ due to the sample preparation method which was based on the grain growing procedure. Even though the isotropic compression performed in all the other numerical tests prior to loading was omitted, the grain growing phase induced some stress on the walls.

There was little grain displacement in the numerical sample, the original contact network in the sample did not change and the sample behaved almost elastically. The stress curves even though seem to be linear in fact are slightly curved.

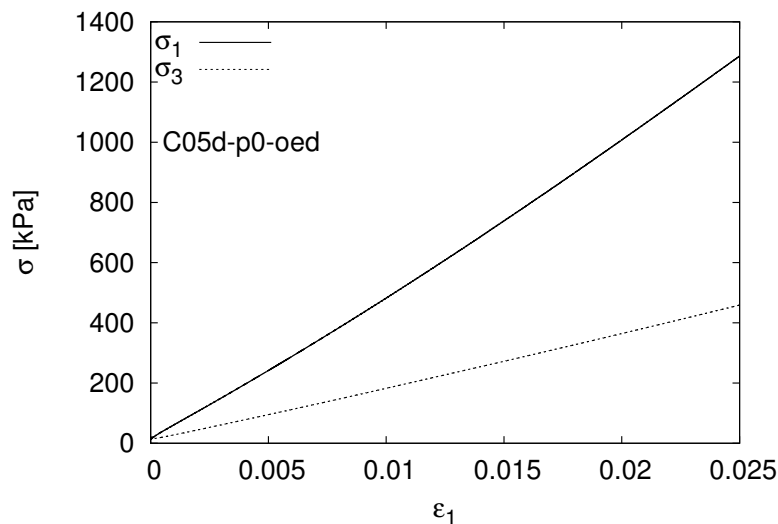


Figure 3.44: Oedometric compression stresses in a numerical simulation *C05d-p0-oed*

Globally it can be noted that the earth pressure coefficient at rest computed for the $\alpha = 0.5$

clump simulation was equal to $K_0 = 0.35$ while in the experiments it was 0.6 and 0.5 for wooden and PVC grains respectively. Apart from that it is clear that the shape of the experimental curves is much more curved.

3.4.2.2 Kinematic Analysis

3.4.2.2.1 Strains

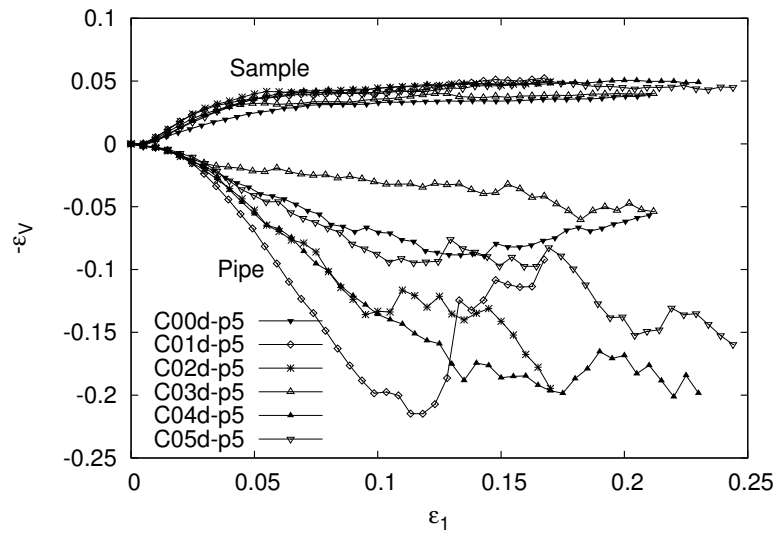
As in the previous experimental Section 3.3.5.2, it was decided to compare the strains of the whole assembly with the strains of the pipe.

Biaxial Compression

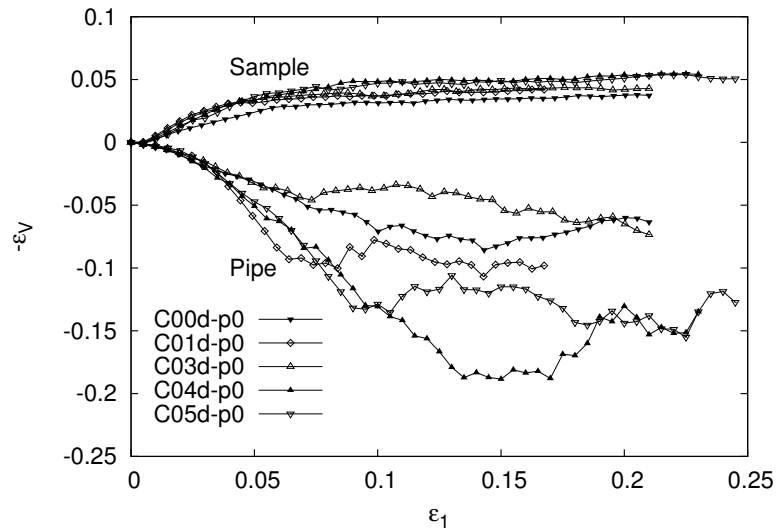
Grain Shape Influence The study of volumetric strains, Figures 3.45 and 3.46, reveal the same behaviour as in the physical experiment in $1\gamma 2\varepsilon$, Figure 3.30. The pipes were contracting while the whole assembly was dilating. In all the numerical samples (α ranging from 0.0 to 0.5), the change of volume of the pipe was similar to the one observed in the experiment until 10% of ε_1 . After that, the value of ε_V stagnated at different levels for different α values. Different values of final volumetric strain are probably linked with different patterns of localisation more than with the shape of the soil particles.

In Figure 3.46 the ratio between the strains of the assembly and the strains of the pipe $\frac{\varepsilon_V^{1\gamma 2\varepsilon}}{\varepsilon_V^{pipe}}$ is presented. The shape of the curves is similar to the shape of the curve obtained from a $1\gamma 2\varepsilon$ test with wooden grains, Fig. 3.30b. In both the test with wooden grains and numerical simulation with clumps, the number of particles in contact with the pipe was small while in the experiment with PVC grains the contact number was much higher. The irregularity of contact probably led to sudden change of volume.

Apart from that, the comparison of the curves in Figures 3.45 and 3.46 do not reveal any particular influence of the grain shape and the interface friction on the volume change of the sample.



(a) *Frictional pipe-soil interface*



(b) *Frictionless pipe-soil interface*

Figure 3.45: Values of the strains throughout the simulations of vertical compression test with constant lateral loading for different samples of clumps. The whole sample was dilating ($\epsilon_V > 0$) while the pipe was contracting ($\epsilon_V < 0$)

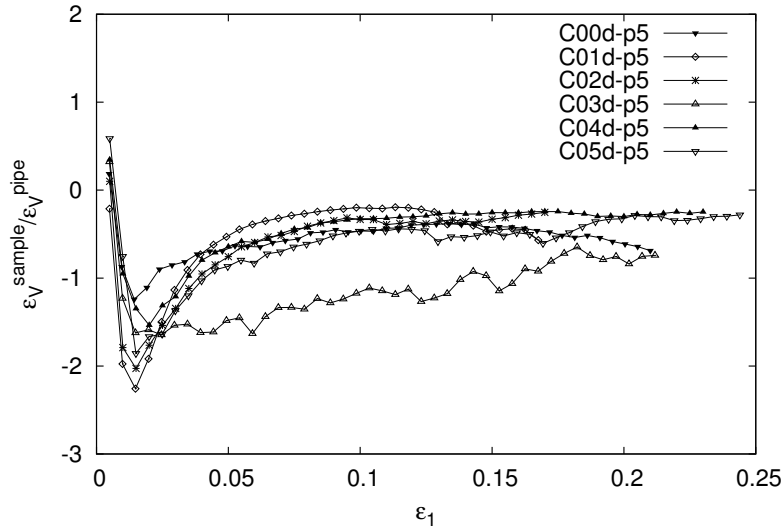
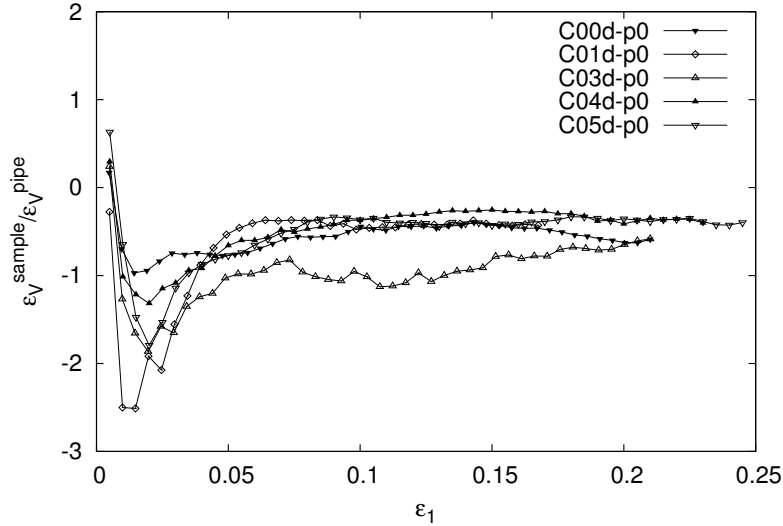

 (a) *Frictional pipe-soil interface*

 (b) *Frictionless pipe-soil interface*

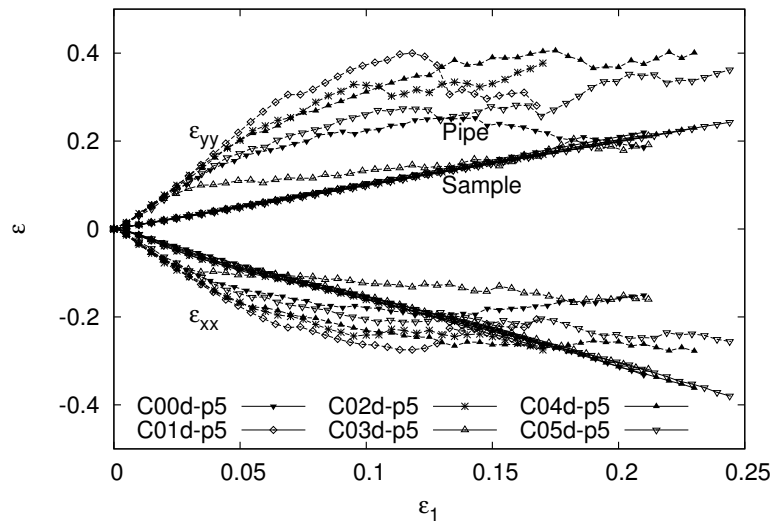
 Figure 3.46: *Relation between the volumetric strain values throughout the simulations for different samples of clumps*

The investigation of the strains of the numerical samples was completed with the figures showing the evolution of horizontal and vertical strains ε_{xx} and ε_{yy} : Fig. 3.47. As observed previously in the physical test, Figure 3.33, the pipe sample was strained more than the surrounding material. In case of physical test, the sample was compressed up to 10% of ε_1 while in the numerical tests, the vertical strain rose more. In the later phases of the simulations the horizontal strains of the pipe became lower than the horizontal strains of the whole sample for all the shapes of the particles and both the friction coefficients on the boundary between the pipe and the soil. In the later phases of the compression the majority of strain was localised in shearbands and did not affect pipe.

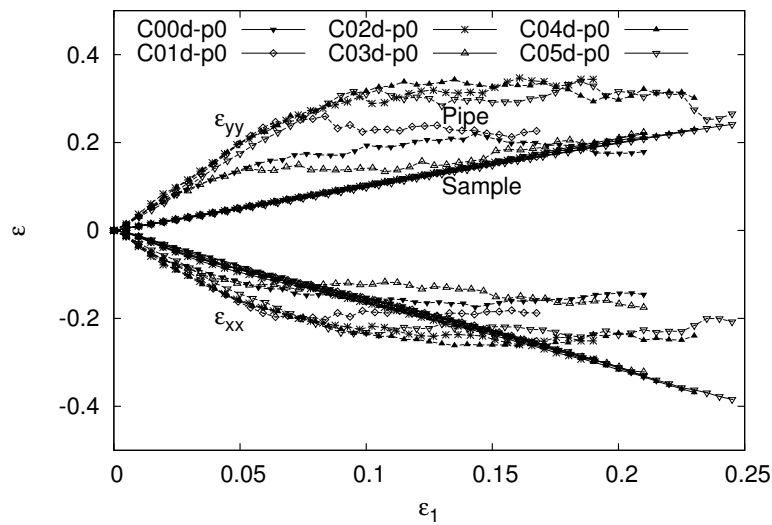
In order to determine the influence of the friction at the pipe interface the curves presented

3.4. MODELING OF AN ELASTIC PIPE IN GRANULAR MATERIAL

the curves in Fig. 3.47 were split into four separate Figures: 3.48a and 3.48b for the samples with $\mu_{int} = 0.5$ and 3.49a and 3.49b for the samples with $\mu_{int} = 0.0$. Apart from the samples of $\alpha = 0.3$ that behaved differently in the previous strain plots as well, it seems that all the clump shapes act in the similar way regardless of the friction coefficient at the pipe boundary.



(a) *Frictional pipe-soil interface*



(b) *Frictionless pipe-soil interface*

Figure 3.47: Values of the horizontal and vertical strains throughout the simulations for different samples of clumps. The strains of the granular sample are linear comparing to the strains of the pipe

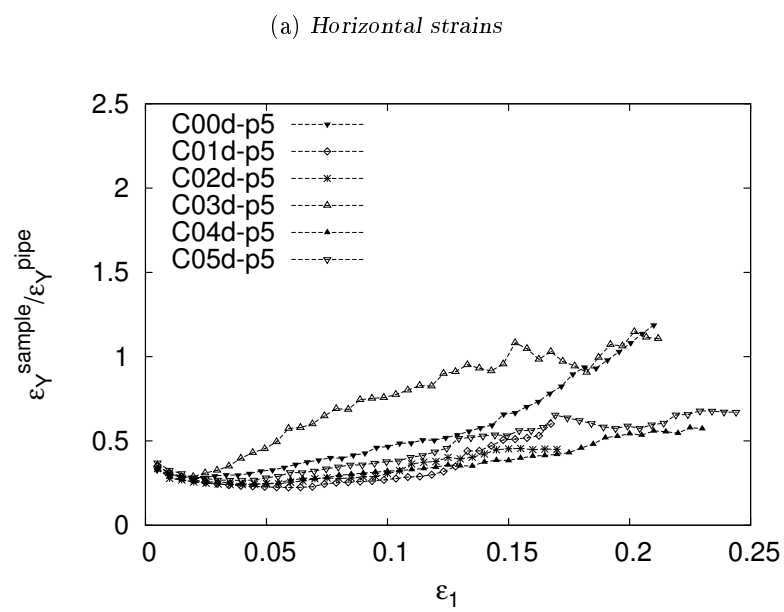
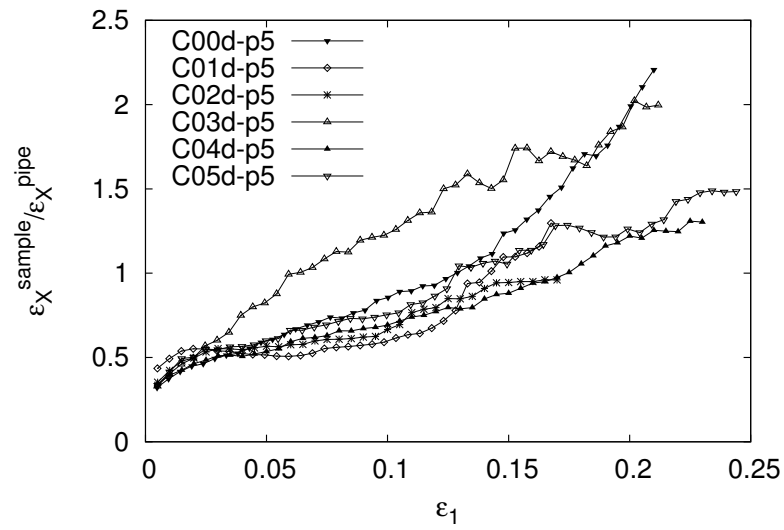
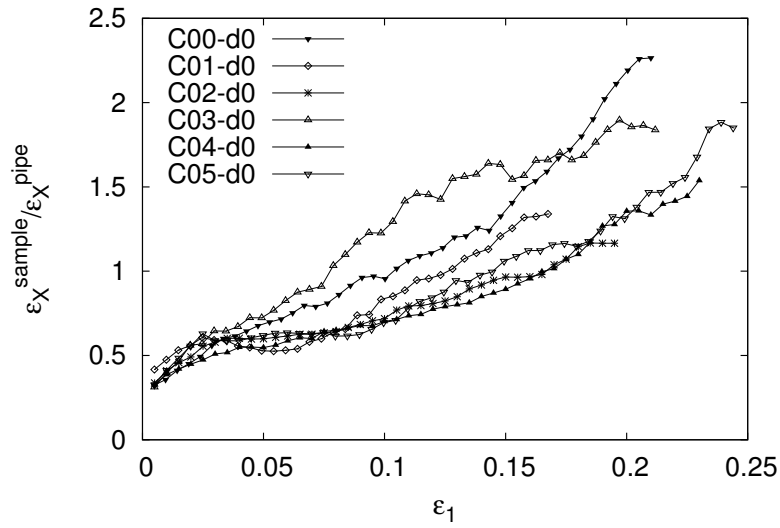
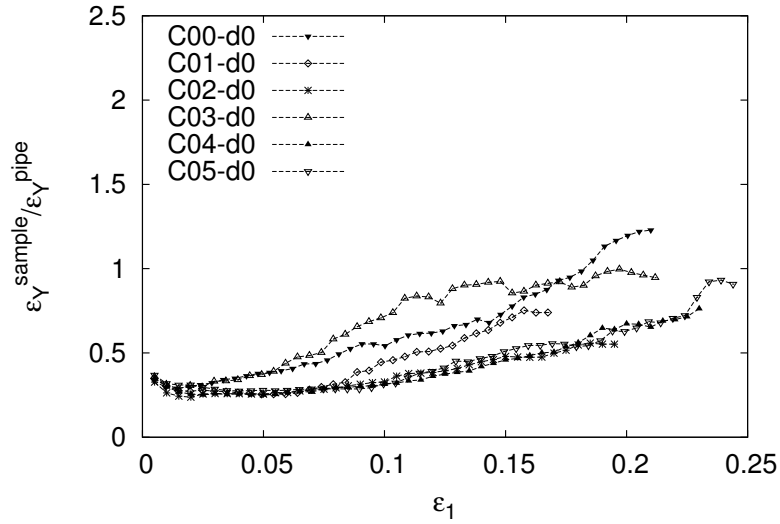


Figure 3.48: Relation of the strains throughout the simulations for different samples of clumps with friction at the pipe boundary



(a) Horizontal strains



(b) Vertical strains

Figure 3.49: Relation of the strains throughout the simulations for different samples of clumps without friction at the pipe boundary

Pipe Stiffness Influence Different behaviour of the pipe with different stiffness was observed and presented in Figures 3.50 and 3.51. While the behaviour of the granular samples remained the same, the stiffness of the pipe influenced the behaviour of the pipe obviously. The strains of the softer pipe C05d-p0-e7 were higher than the reference pipe C05-p0. The pipe with 20GPa of Young's modulus C05d-p0-e9 did not change the shape practically at all, Fig. 3.50a. Because of that, it was pointless to present the comparison of the strains of the stiff pipe and the sample for the pipe C05d-p0-e9; The small strains in the divisor of the ratio $\frac{\varepsilon_V^{\text{sample}}}{\varepsilon_V^{\text{pipe}}}$ resulted in large values and therefore were omitted in Figure 3.50b.

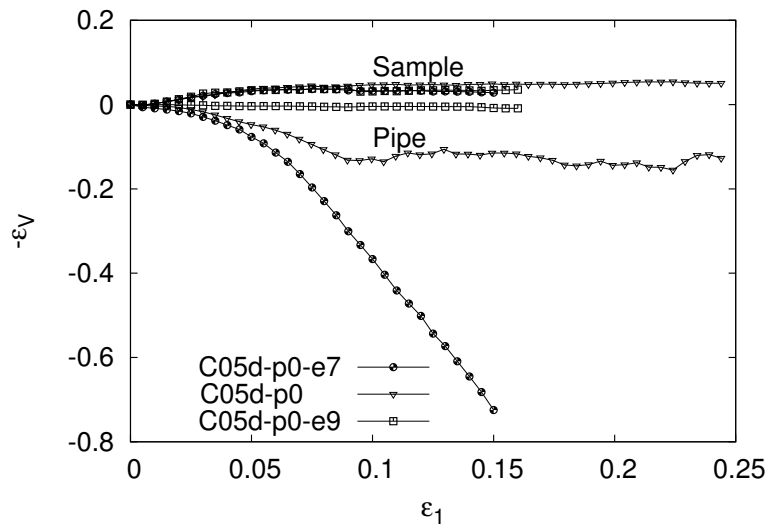
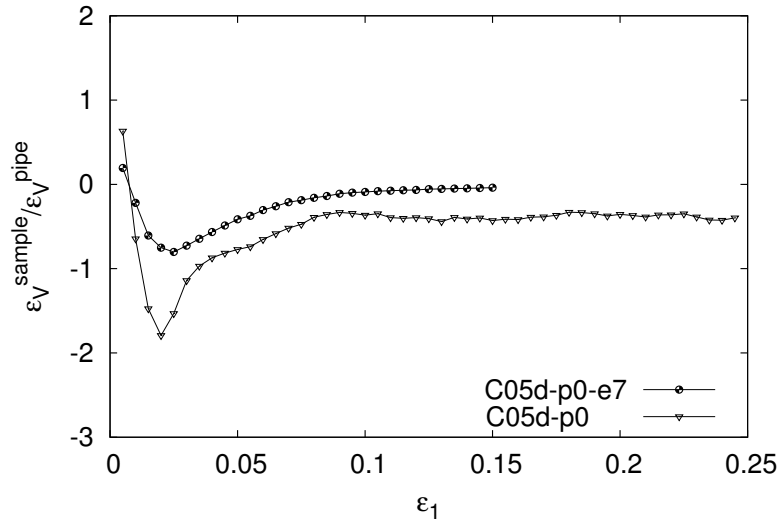
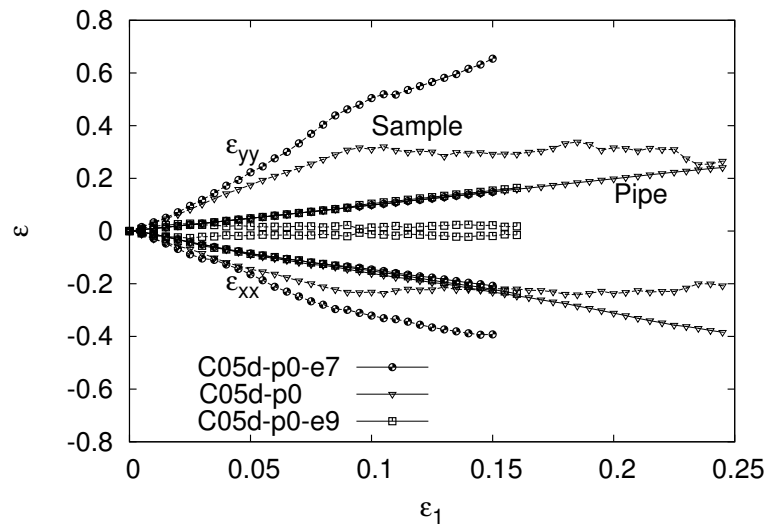
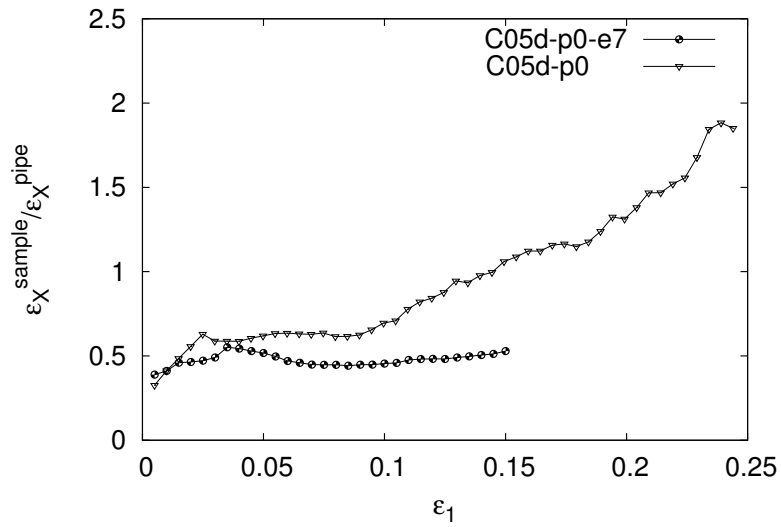

 (a) ϵ_V values

 (b) ϵ_V comparison

 Figure 3.50: Volumetric strains of the sample of $\alpha = 0.5$ clumps containing elastic pipes of different stiffness

The vertical and horizontal strains of the pipe were affected by the pipe stiffness change as well, Figure 3.51. As in the case of volumetric strains, the strains of the stiff pipe were close to zero and therefore the ratio of the granular sample and pipe strains was not presented, Figures 3.51b and 3.51c.

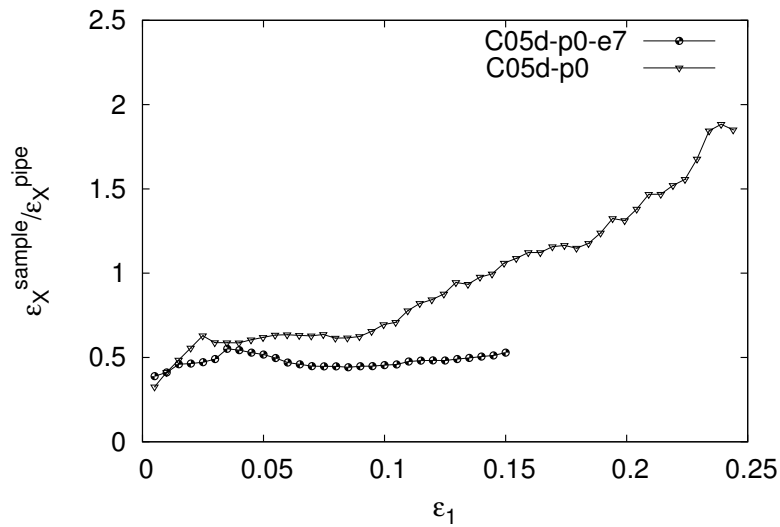


(a) ϵ_X and ϵ_Y values



(b) Horizontal strains

Figure 3.51: Horizontal and vertical strains of the pipe and the whole sample. The value of the pipe stiffness was different in each sample



(c) Vertical strains

Figure 3.51: Horizontal and vertical strains of the pipe and the whole sample. The value of the pipe stiffness was different in each sample

3.4.2.2.2 Displacement Fields

Biaxial Compression By plotting the displacement vector of each particle between two phases of the experiment it was possible to obtain the displacement fields of the samples. In Figures 3.52 the sample of clumps with the shape parameter α equal to 0.5 and the microscopic friction coefficient at the pipe-soil interface equal to $\mu_{int} = 0.5$ is presented. The plots were made every $2.5\epsilon_1$ throughout the test, and each vector is starting at the point occupied by the particle in the isotropic state. Equivalent image for a sample C05d-p0 is presented in Figure 3.53. In each image, the centre of coordinates was placed at the bottom of the pipe.

The displacement fields reveal some discontinuities but are not very informative. Therefore it was decided to subtract the mean field of displacement \bar{u}_i from each displacement field, as it was explained with the equation (3.50) on the page 84. The meaning of these figures can be explained with an example: in the later phases of the compression presented in Figure 3.52 (see Appendix E.1 for larger, scalable images), the grain directly above the top of the pipe moved down more than the grain at the top of the sample which moved the same as mean strain (displacement field minus the mean field close to zero). This difference is not visible in the displacement fields but become clear when the mean field is subtracted.

These plots are presented in Figures 3.54 and 3.55 for the the C05 clump samples with frictional and frictionless pipe boundary respectively (see Appendix E.2 for larger, scalable images). These graphics reveal some interesting patterns of circular displacement. It was possible to observe similar behaviour in the physical samples, Figures 3.36 and 3.37, but in case of $1\gamma 2\epsilon$ wooden sample the “vortexes” were more local and in case of PVC sample the pattern was dominated by multiple reflecting shearbands (compare with Fig. 3.39). Here in both the cases of pipe interface friction, one can observe two large vortex-like patterns, located around the discontinuities of the displacement field at each side of the pipe, that seem to indicate grains above the pipe pushing into it. This would comply with the larger strains of the pipe in comparison with the granular material observed before.

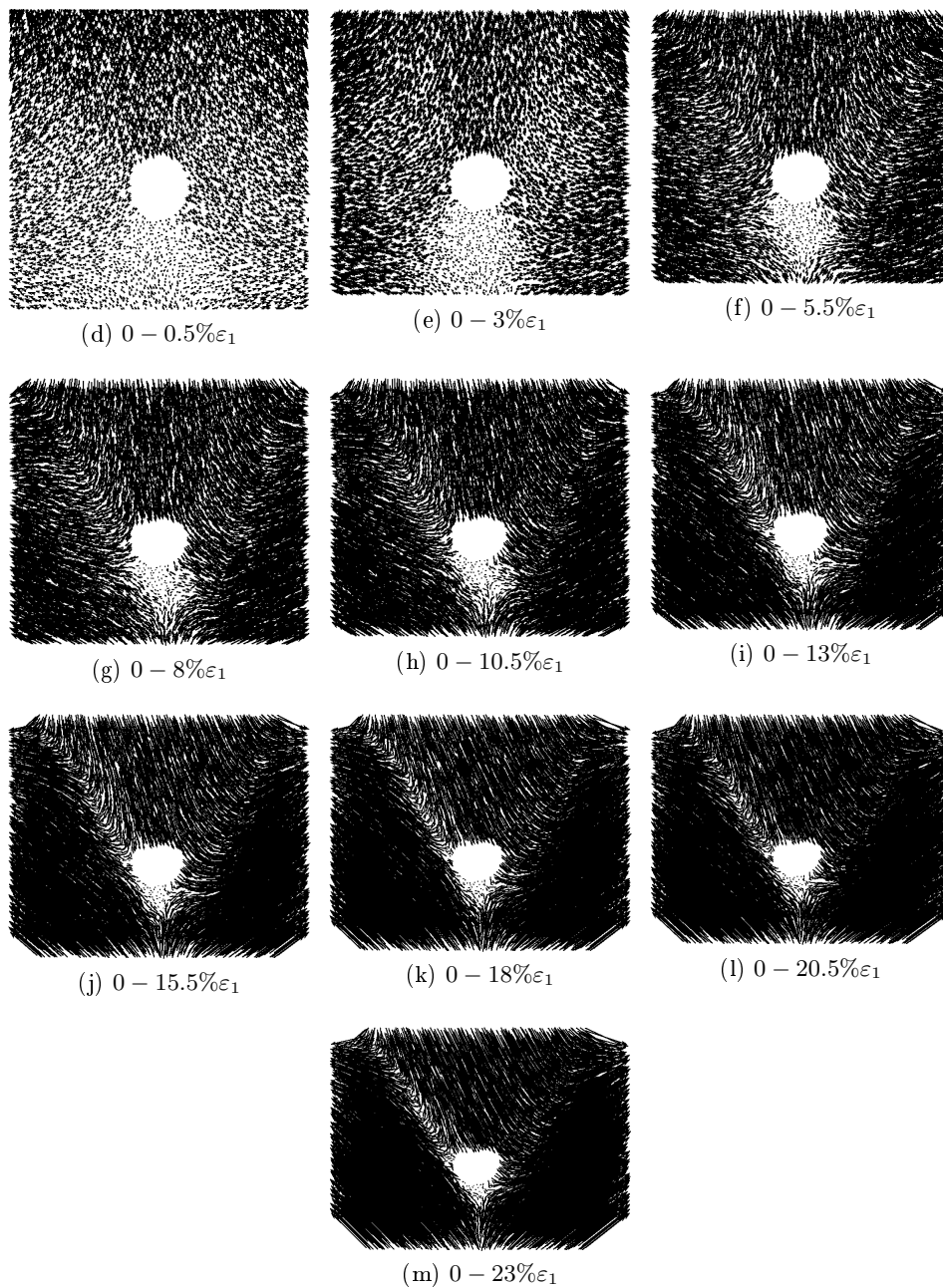


Figure 3.52: Displacement fields of a clump sample with $\alpha = 0.5$ and friction at the boundary of the pipe

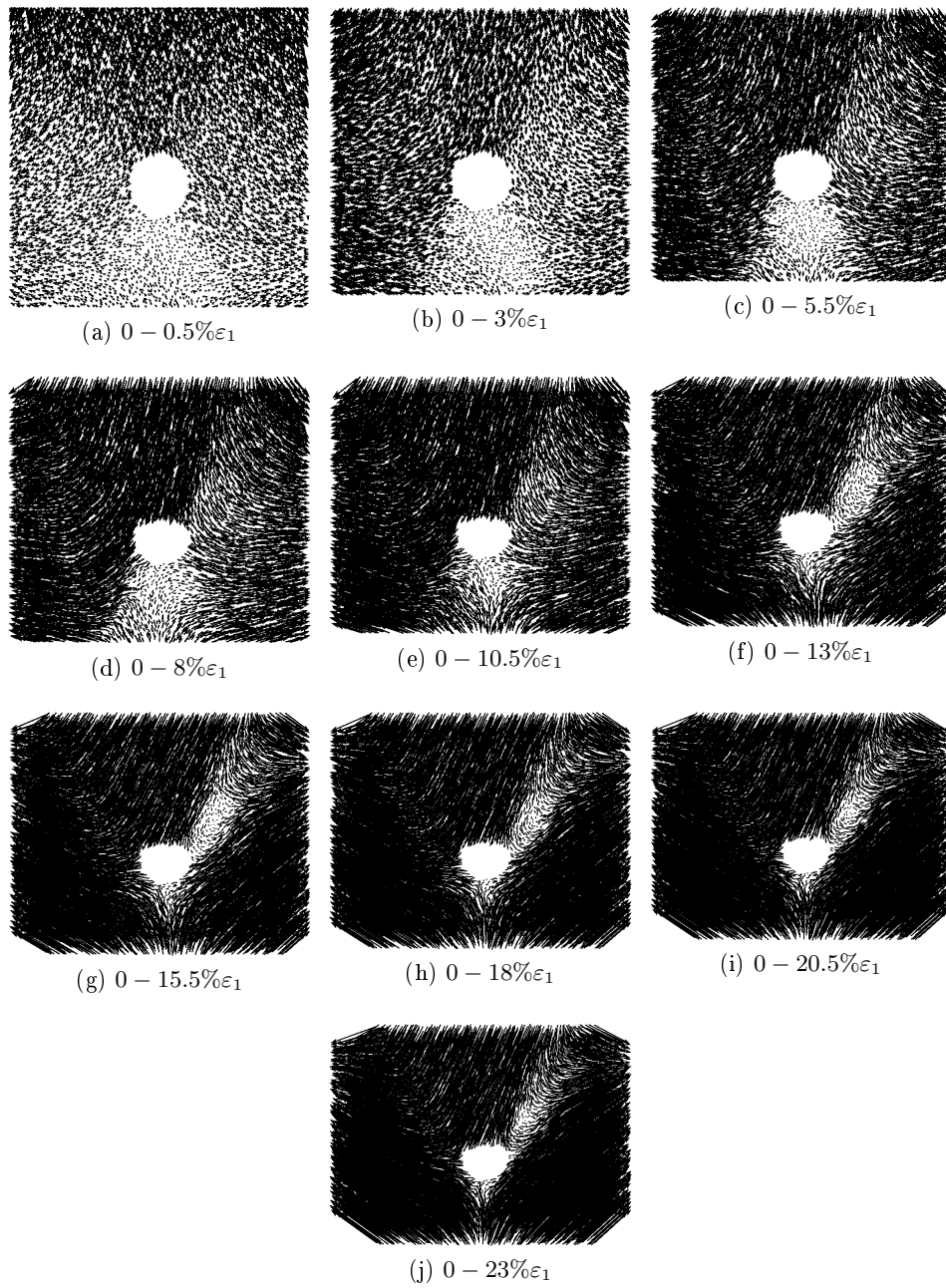


Figure 3.53: Displacement fields of a clump sample with $\alpha = 0.5$ and no friction at the boundary of the pipe

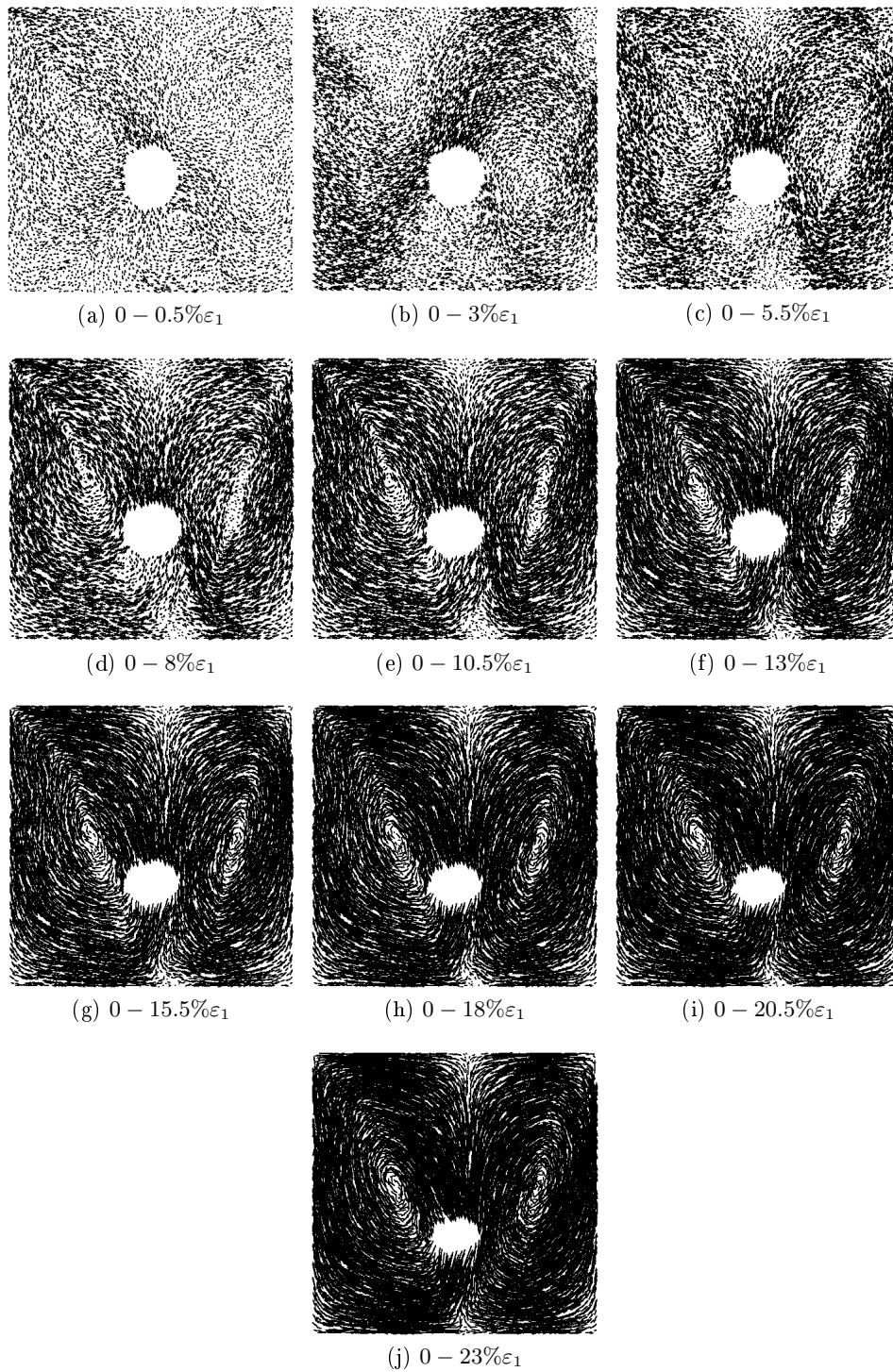


Figure 3.54: Displacement fields reduced by mean field of displacement. Clump sample with $\alpha = 0.5$ and friction at the boundary of the pipe

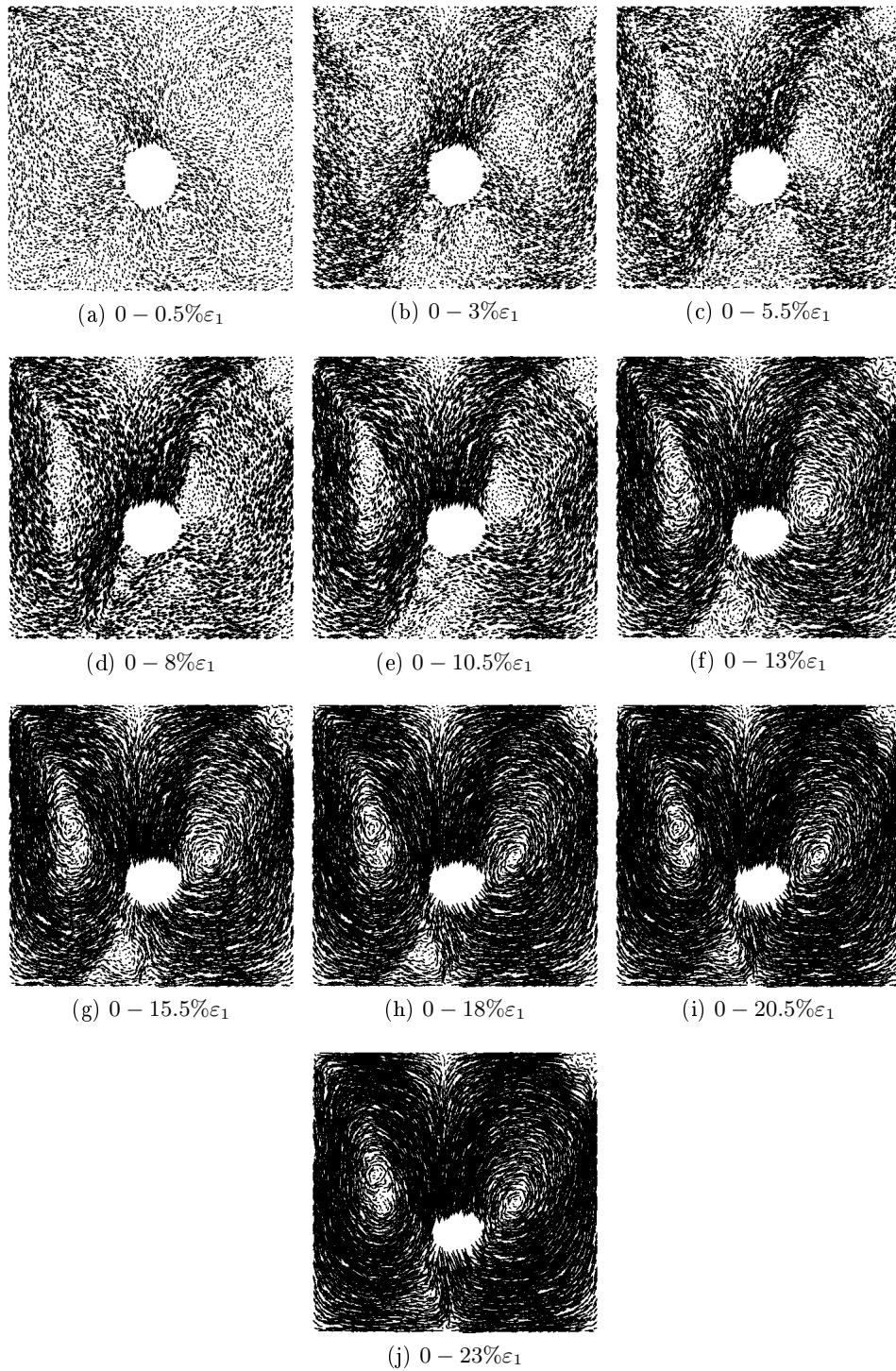


Figure 3.55: Displacement fields reduced by mean field of displacement. Clump sample with $\alpha = 0.5$ and no friction at the boundary of the pipe

3.4.2.2.3 Localisation of Shear

Study of the displacement field revealed some discontinuities that were supposed to be linked with shear localisation. The results for only one shape of clumps, $\alpha = 0.5$ and two values of the friction coefficient at the boundary of the pipe are presented here, Figures 3.56 and 3.57 for frictional and frictionless pipe boundary respectively (see Appendix E.3 for larger, scalable images). The images presents the second strain invariant (see page 40) with symbols, where the size of the symbol for each particle represents the value of the indicator and thus the intensity of shear.

The maps show that the patterns observed in the displacement fields and the ones decreased by the mean field are connected with the shear localisation. As in the case of physical experiments, reflecting bands that include the pipe were observed. Please note, that the localisation patterns in the simulations with pipe were not very different from the patterns observed during the simulations without the pipe, Fig. 2.8.

The localisation patterns for samples with a pipe with different stiffness are presented in Figures 3.58 and 3.59 (see Appendix E.3). The change of pipe stiffness seems to influence the shearband trajectory around the pipe, although it is based on the observation of single samples. The localisation zone in the stiff pipe sample is going around the pipe, which is probably due to the fact the pipe is forming one rigid block with the grains above. In the soft pipe sample the pipe is deforming a lot and it appears the localisation patterns are encouraged to pass through the pipe.

3.4.2.3 Arching Effect Assessment

3.4.2.3.1 Stress Comparison

Thanks to the nature of the DEM simulations it was possible to investigate the interparticle forces in the assembly, which was not possible in the experiments performed in $1\gamma 2\varepsilon$. In order to study the arching effect above the pipe, the forces acting on the specimen were compared with the forces acting on the pipe. It was possible to compute the vertical component of the stress by dividing the sum of vertical forces by the length of the wall or the width of the pipe.

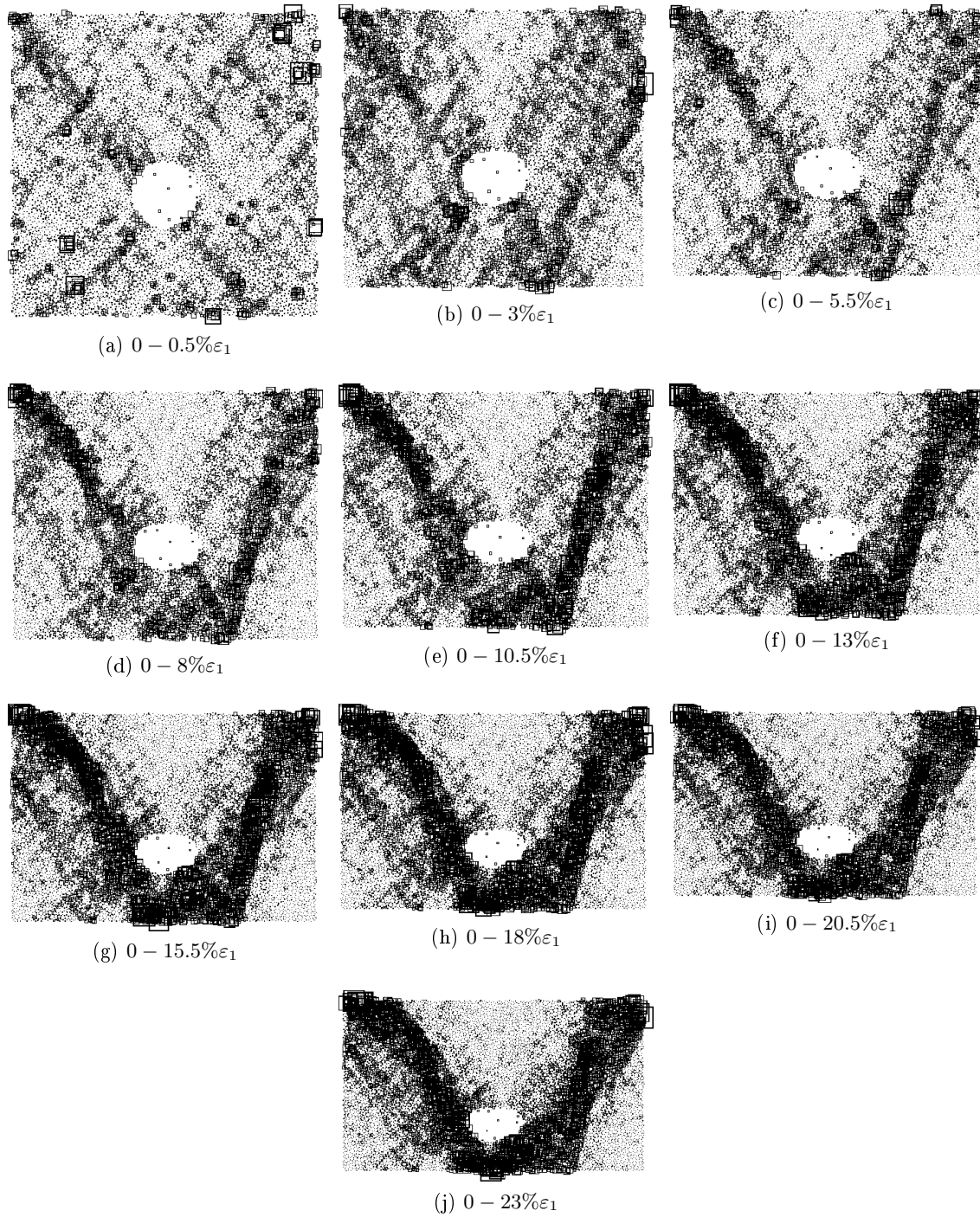


Figure 3.56: *Shear localisation maps of a clump sample $\alpha = 0.5$ with friction at the pipe boundary*

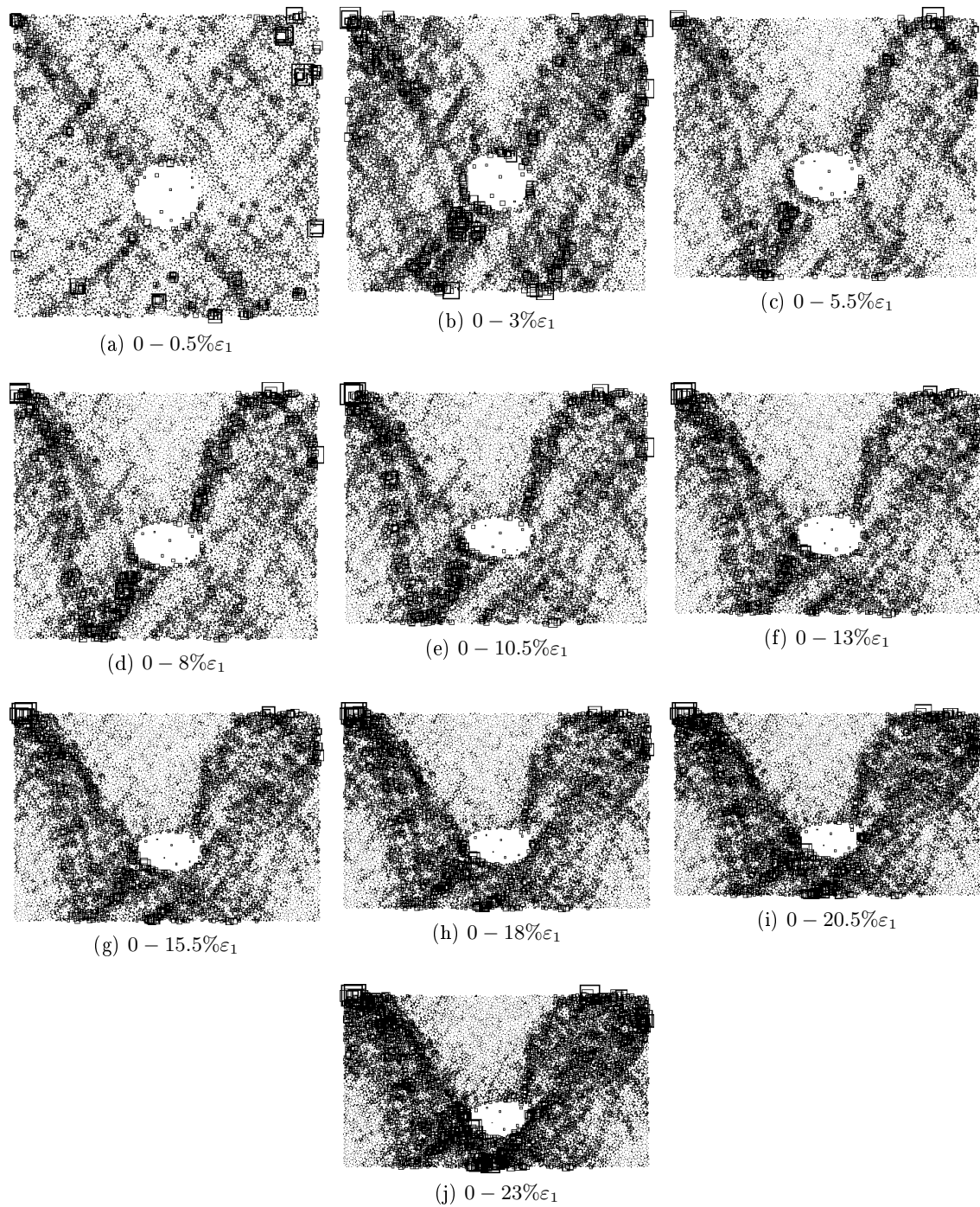


Figure 3.57: *Shear localisation maps of a clump sample $\alpha = 0.5$ with no friction at the pipe boundary*

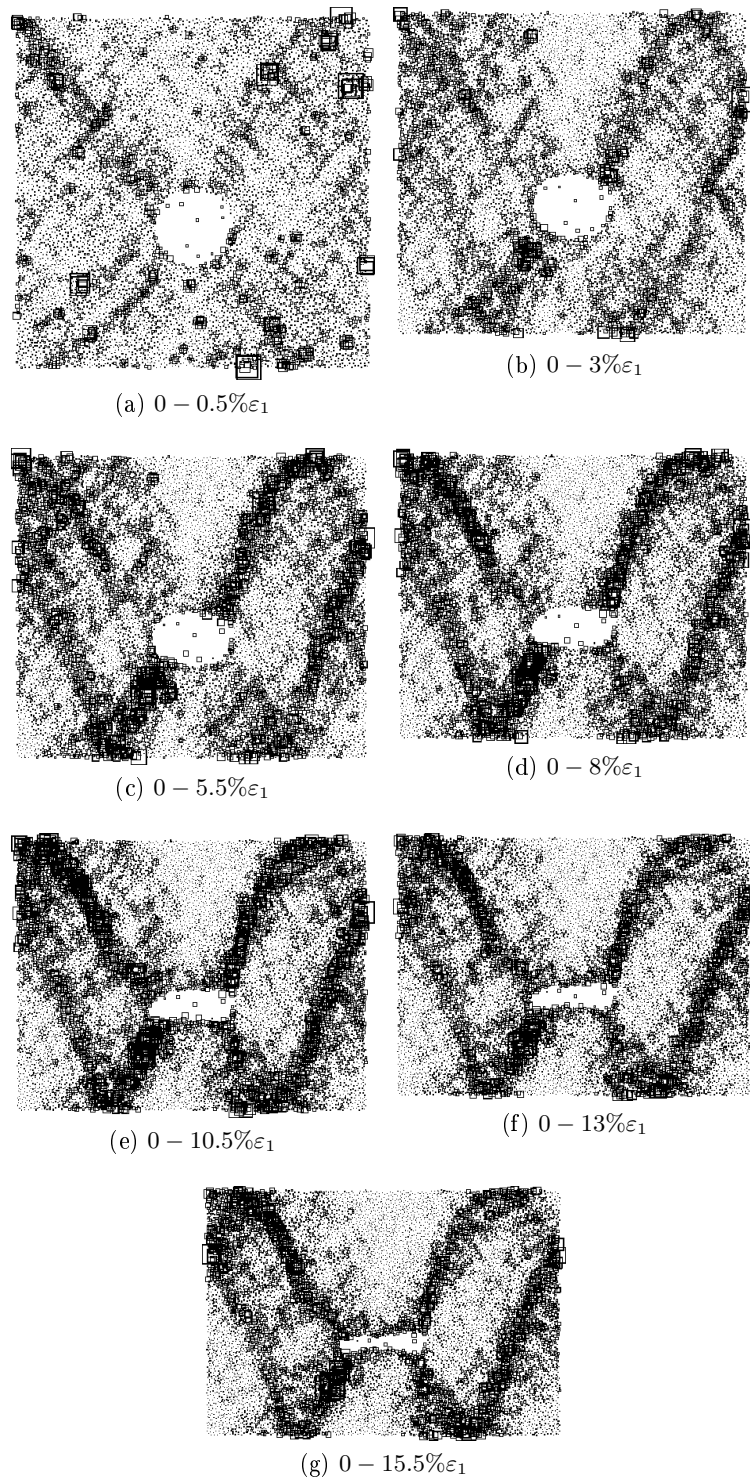


Figure 3.58: Shear localisation maps of a clump sample $\alpha = 0.5$ with soft pipe and no friction at the pipe boundary

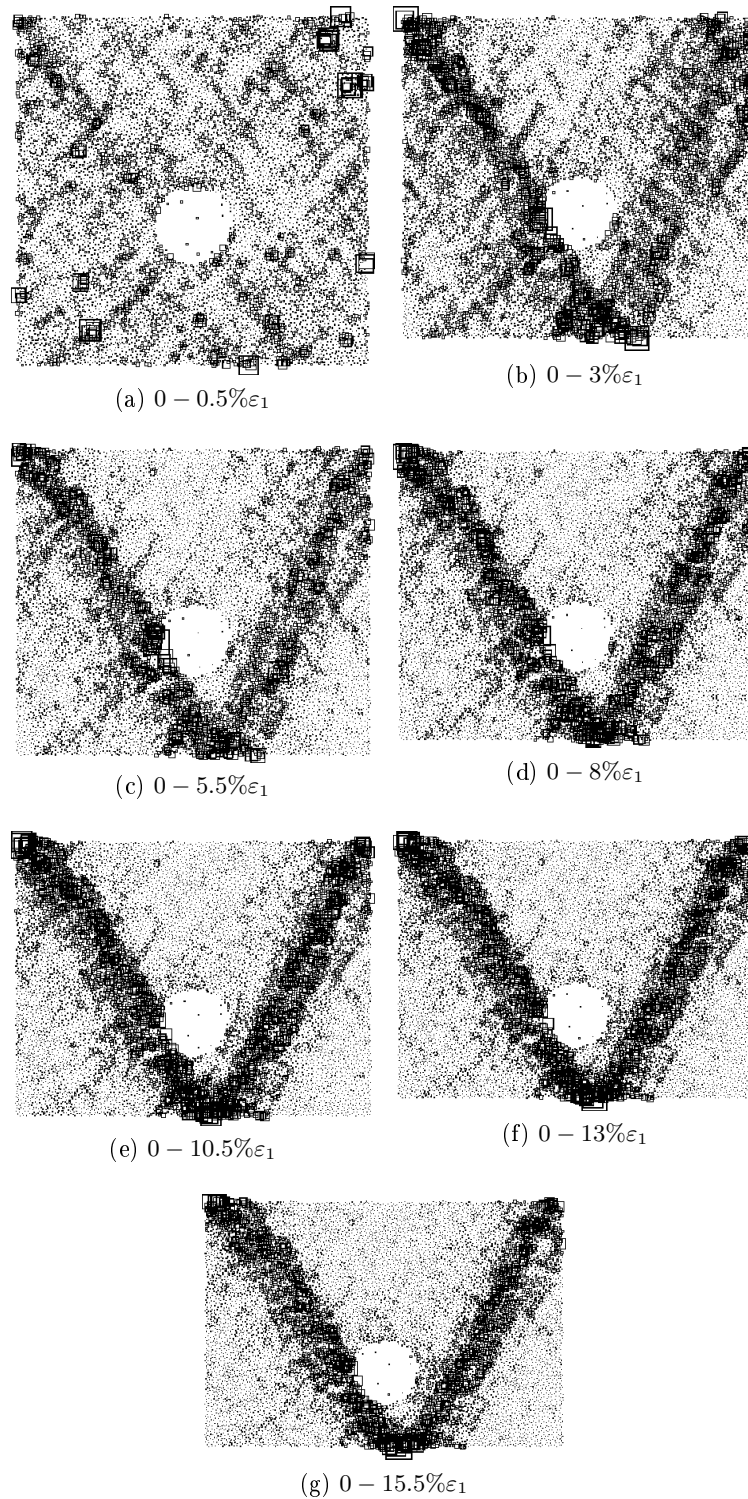


Figure 3.59: *Shear localisation maps of a clump sample $\alpha = 0.5$ with hard pipe and no friction at the pipe boundary*

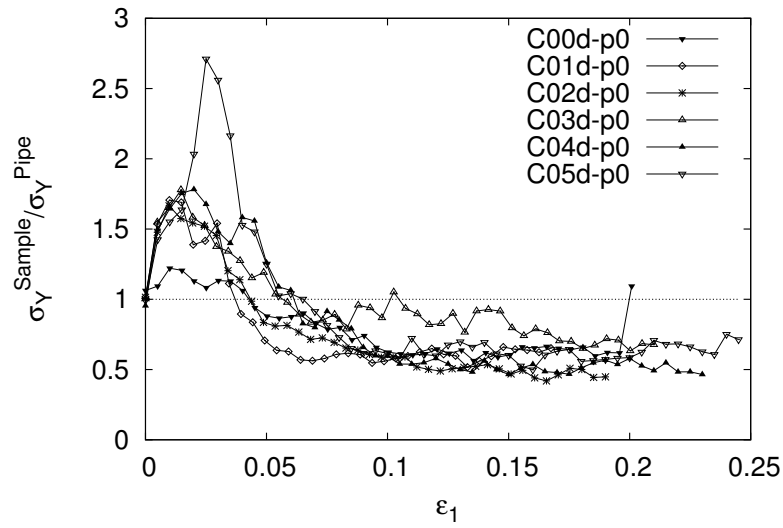
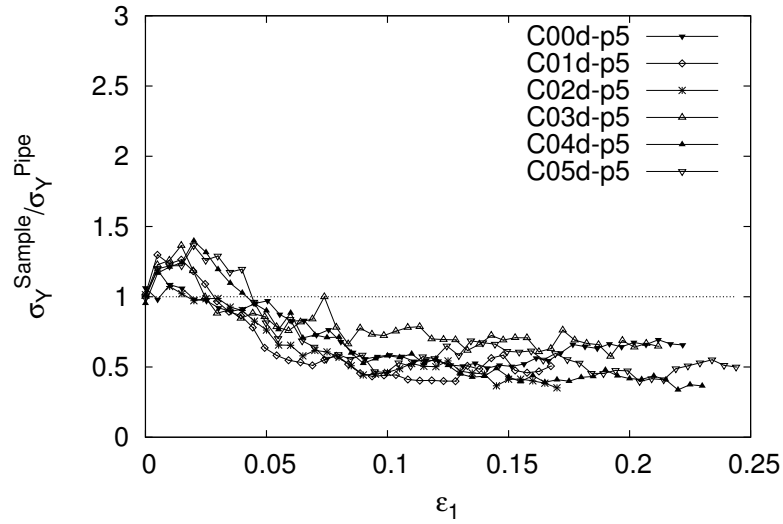

 (a) $\mu = 0.0$

 (b) $\mu = 0.5$

Figure 3.60: *Stress repartition on elastic pipe in DEM simulation with clumps of different α . The vertical stress acting on the pipe was compared with the stress acting on the horizontal walls compressing the sample. The friction coefficient μ between the pipe and the soil is different for each of the two images above*

As presented in Figure 3.60, the loading acting on the elastic pipe was changing during the compression. Initially the pipe was loaded less than the walls above and below. This repartition of stress is characteristic for the arching mechanism; The effect of load transfer was lost after the peak macroscopic stress. The repartition of stress acting on the horizontal wall was bigger in simulations without friction between the pipe and the surrounding soil. It is due to the fact that in frictionless case the forces are acting along the pipe wall and do not add loading to the pipe. Also, it seems that the increase of stress repartition disappeared later in the test without the friction at the boundary. Disc sample induce very small arching effect but it appears the stress

repartition is increasing with the value of shape parameter α .

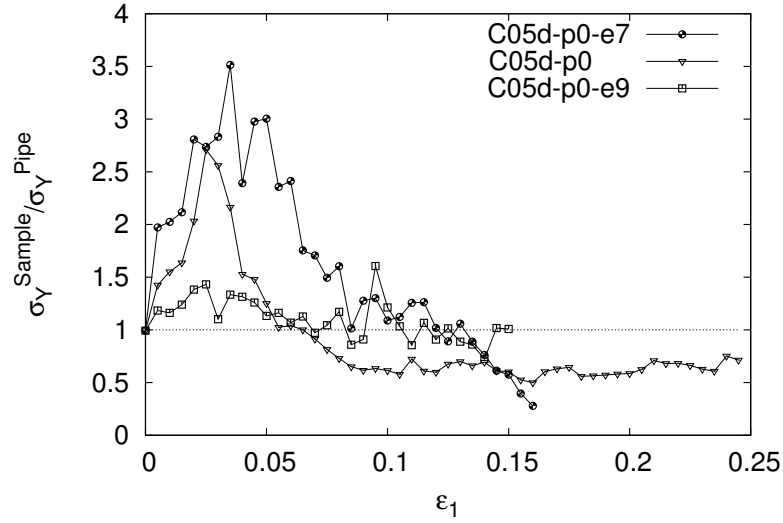


Figure 3.61: *Stress repartition on elastic pipe in DEM simulation with pipe of different stiffness*

It was interesting to observe the difference in the stress repartition between samples with more soft and more stiff pipe, Figure 3.61. The softer pipe C05-p0-e7 with $E = 20e7Pa$ induced greater load transfer mechanism than the reference, stiffer pipe C05-p0 with $E = 20e8Pa$. The curve is dropping below 1 after $\epsilon_1 = 12\%$ which is due to the fact, the pipe buckled and collapsed and did not support the load anymore. On the contrary, the load transfer for the stiffer pipe C05-p0-e9 with $E = 20e9Pa$ that remained virtually undeformed was much smaller than the reference pipe, although it was still more than the surrounding soil ($\frac{\sigma_Y^{Sample}}{\sigma_Y^{Pipe}} > 1$).

3.4.2.3.2 Stress Direction

Apart from the total forces acting at the pipe, it was also interesting to observe the stress in the microscale. The stress acting on every particle was computed using the Weber's homogenisation formula (Weber, 1966):

$$\sigma_{\alpha\beta} = \frac{1}{S} \sum_{N^{ij}} F_{\alpha}^{ij} l_{\beta}^{ij}, \quad (3.53)$$

where:

$\sigma_{\alpha\beta}$ are the components of the Cauchy stress tensor,

α, β are the directions in space, $\{\alpha, \beta\} = \{x, y\}$

S is the surface area of the zone,

N^{ij} is the contact between particles called i and j in a given zone,

F_{α}^{ij} is a component of the force vector interacting between particles i and j ,

l_{β}^{ij} is a component of the branch vector connecting centres of particles i and j .

The formula was applied in such way that instead of using a branch vector, the forces were projected on a vector connecting the particle centre and the contact point. The sum of forces for each particle was divided by the area of a given particle. In case of the circular pipe, the forces acting on each grain forming the pipe were added and the result for the entire pipe was divided by the area of the ring containing all the pipe particles. This way, it was possible to

obtain a stress tensor for each of the particles. In order to present it graphically, each particle was represented with a cross oriented along the principal stress direction with the arm lengths proportional to the principal values of stress. An example of the stress direction plot for a clump sample *C05d* with $\mu_{int} = 0.0$ is presented in Figure 3.62 (see Appendix E.4 for larger, scalable images).

The tensorial nature of stress allows us to compute the difference in stress between two states for each grain, the two states being an increment of vertical strain apart. In Figure 3.63 these stress increments for the same samples of clumps are presented (see Appendix E.4 for larger, scalable images). In the initial phase of the loading, increment $2.5 - 3\% \varepsilon_1$, when the shear is not yet fully localised, the stress network is denser at the sides of the pipe than above or below it. This could indicate that more stress is carried by the soil than by the pipe, which is typical for the arching effect phenomenon. The same strain increment in Figure 3.62 shows an arch-like stress-chain pattern.

One could also say that in the later phases of the test when the shear zones are developed, the stress increments are larger in the zones of shear localisation than in the rigid blocks around. Chains perpendicular to the direction of the shear localisation zone can be observed.

The change of pipe stiffness is influencing the pattern of stress directions a lot. It seems that above and below the soft pipe, Figure 3.64, the stress increment network is less dense and this phenomenon remains until the pipe collapse. In a sample with more rigid pipe, Fig. 3.65, the stress change occurs in the localisation zone mostly (see Appendix E.4 for larger, scalable images).

3.5 Conclusions

In the second part of the study the focus was put on the practical aspect of granular media modeling. The point was to observe the stress repartition above an elastic shell surrounded by grains. Six physical experiments were performed in a 2D apparatus. The results were analysed with the help of Digital Image Correlation method. The results were used to create a numerical model of the experimental setup with the help of the tools developed in the first part of this work.

The experiments were performed in a $1\gamma 2\varepsilon$ apparatus which is able to impose various boundary conditions on a two-dimensional granular material. Thanks to the construction of this apparatus digital photography can be used to gather information about the kinematic behaviour of the samples without the need to engage complicated sensors. The tests were performed on two different types of granular materials, large wooden particles and small PVC particles. In every case a piece of PVC pipe was placed in the centre of the sample as a model of an elastic drain pipe. The mechanical behaviour of the pipe itself was studied in separate vertical compression tests in order to establish the values of the numerical parameters to be used in the numerical model.

The analysis of the stress-strain and volumetric strain macroscopic curves of $1\gamma 2\varepsilon$ showed that the presence of the elastic pipe had no major influence on the behaviour of the assembly. The same could be said about the strain localisation patterns that were basically the same with or without the presence of pipe. The localisation bands were seen going through the pipe. The analysis of the kinematics of the $1\gamma 2\varepsilon$ tests showed different behaviour of the pipe and the surrounding material – the strains of the elastic pipe were bigger than the strains of the grains around. Observations of the displacement fields revealed that the granular material was pushing into the pipe.

In order to perform numerical analysis of the experiments with a DEM code a specific contact interaction was used to model the elastic pipe. The pipe comprised of discs connected with

3.5. CONCLUSIONS

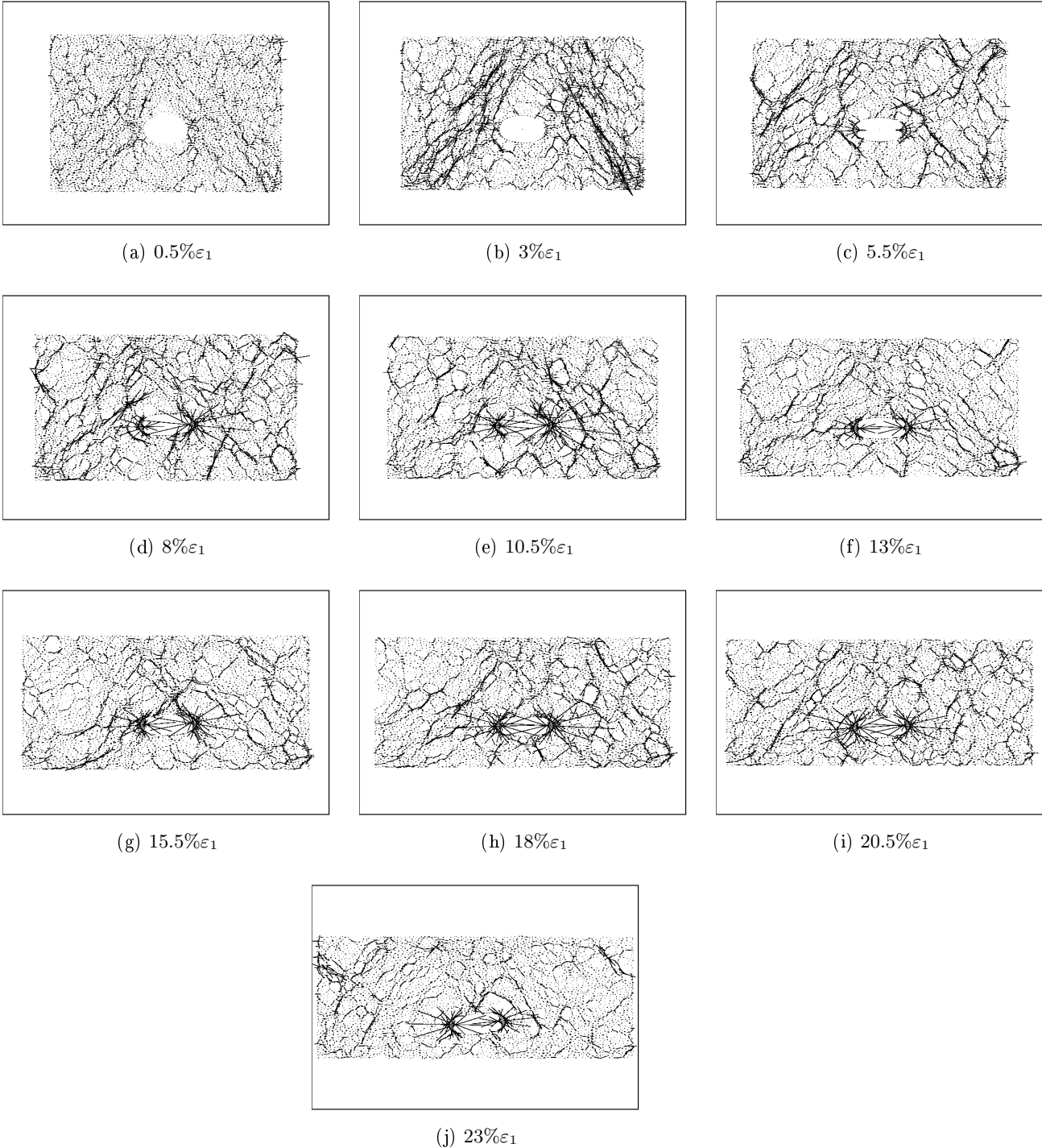


Figure 3.62: Direction of particle stress during biaxial compression of a clump sample with $\alpha = 0.5$ and frictionless pipe

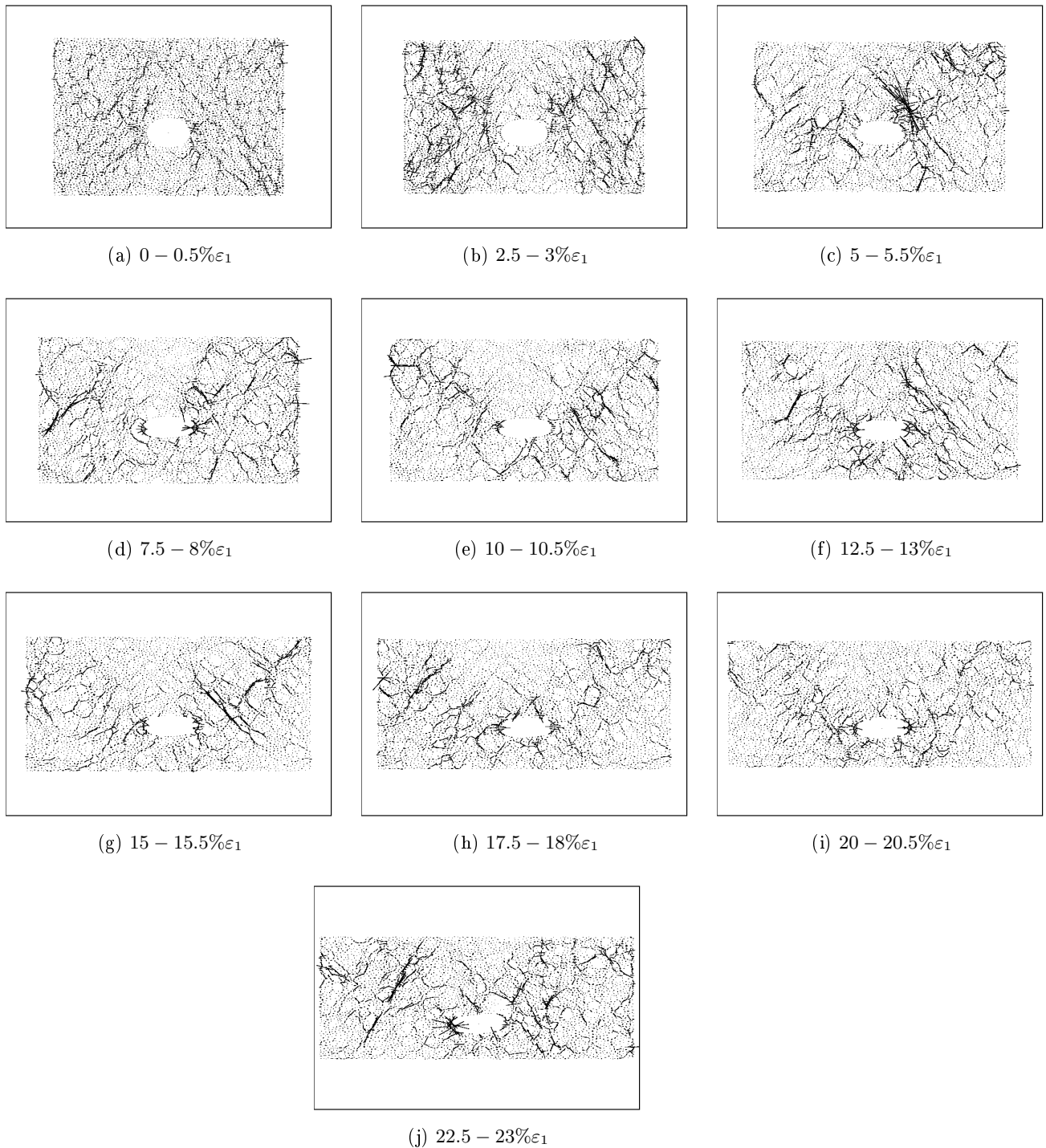


Figure 3.63: *Direction of particle stress increment during biaxial compression of a clump sample with $\alpha = 0.5$ and frictionless pipe*

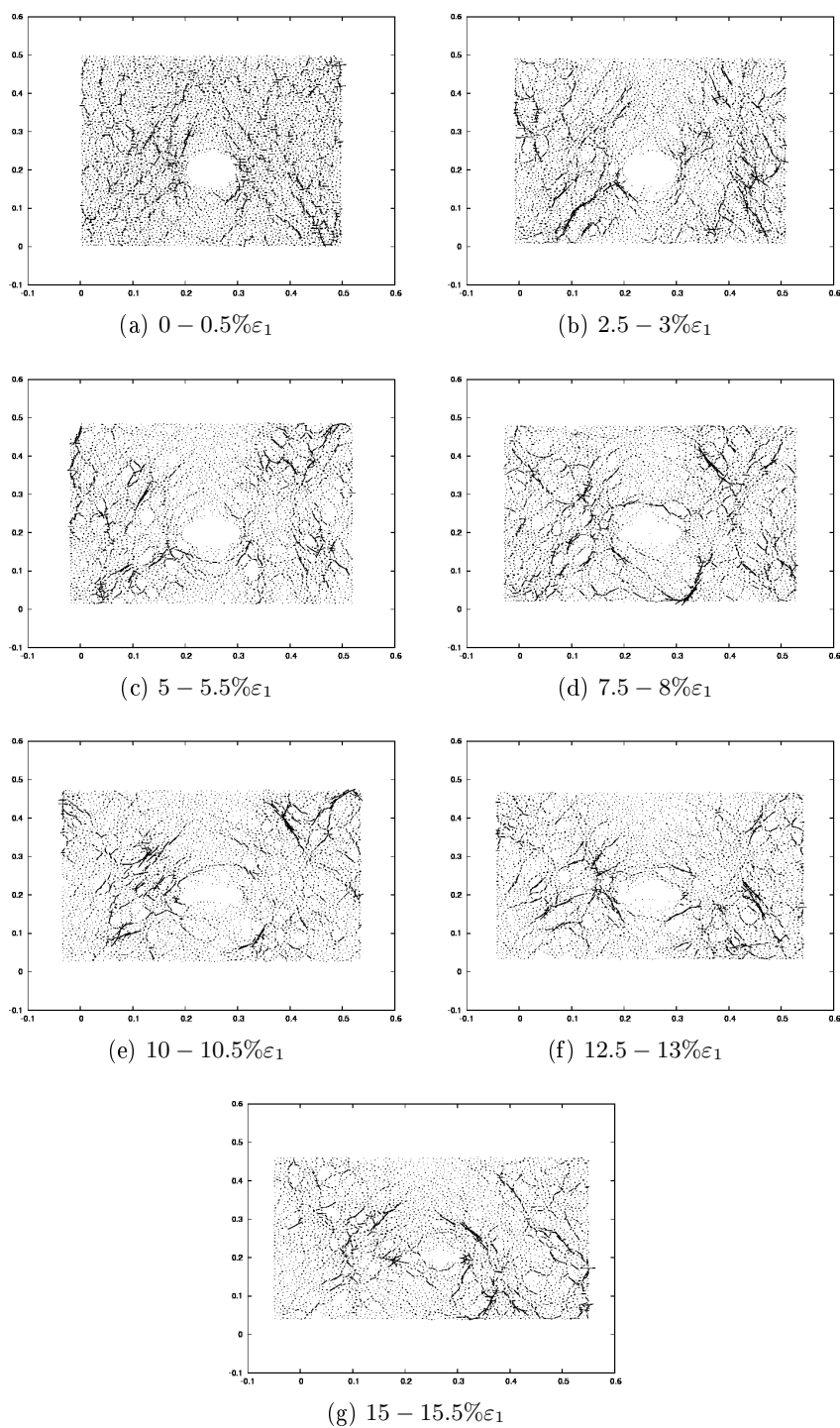


Figure 3.64: Direction of particle stress increment during biaxial compression of a clump sample with $\alpha = 0.5$ and frictionless pipe with Young's modulus $E = 20e7Pa$

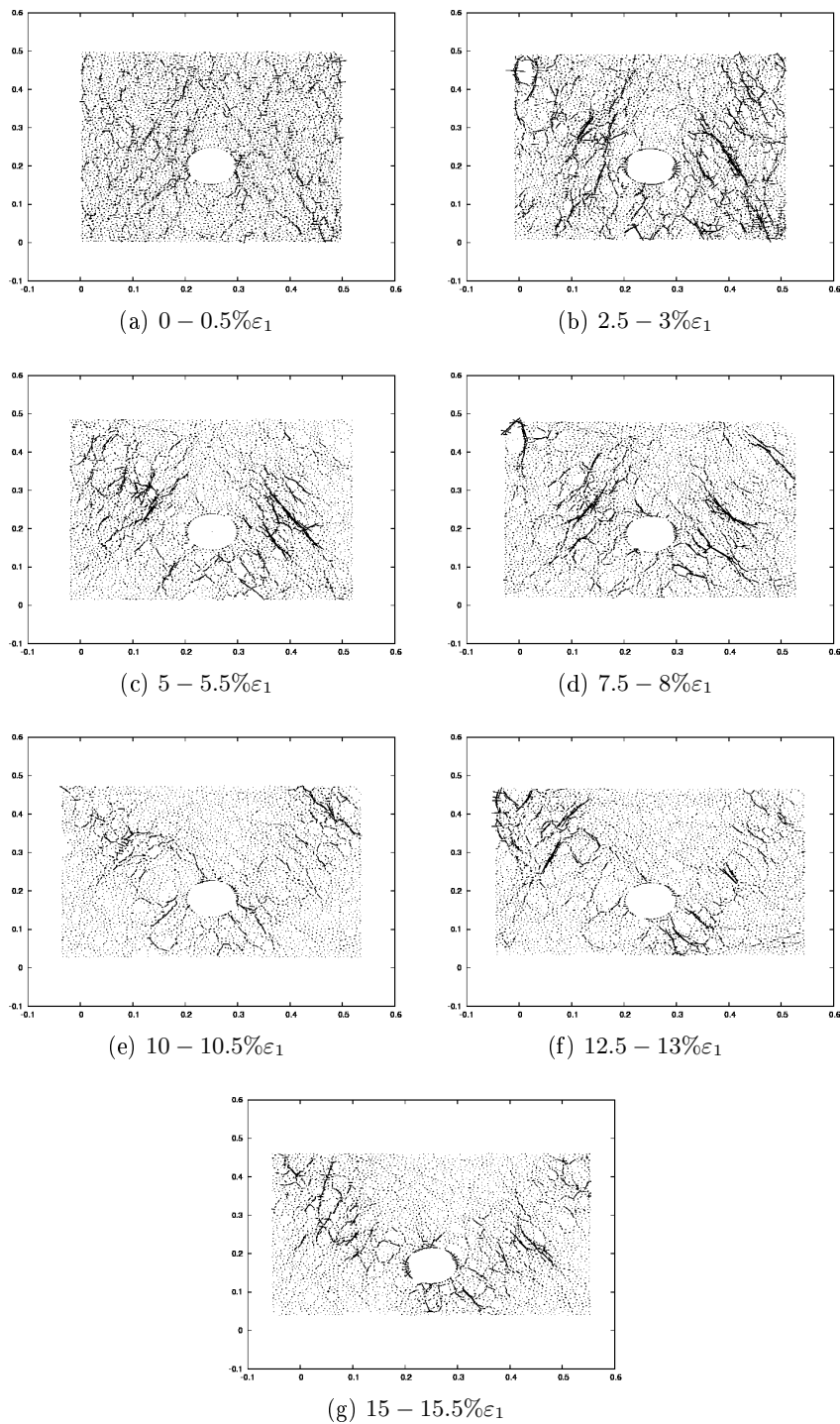


Figure 3.65: Direction of particle stress increment during biaxial compression of a clump sample with $\alpha = 0.5$ and frictionless pipe with Young's modulus $E = 20e9Pa$

unbreakable bonds that were transferring forces and moments of force. This pipe model was implemented into the assemblies of clumps described in the first part of this work. Due to that, it was possible to model all the elements of the setup with a single numerical code.

The pipe and surrounding grains were subjected to vertical loading with constant lateral pressure, as it was done during the experiments in $1\gamma 2\varepsilon$. Two values of the microscopic friction coefficient between the outer boundary of the pipe and the granular material were used but no significant influence was observed. Once again, the macroscopic behaviour was no different with and without the presence of the pipe and the kinematic analysis revealed difference in the values of strains between the pipe and the surrounding material. The numerical results showed some circular vortex-like structures that were pushing the particles into the pipe. Similar but less developed structures were observed in the results obtained with digital images. The localisation of strains was also similar in the simulations with or without the pipe.

Numerical modeling of the elastic pipe in the granular sample allowed us to observe the repartition of stress in the assembly, which generally speaking is not possible in physical experiments. It was possible to observe the stresses acting on the boundaries of the sample and the pipe, and see that in the initial phases of the test the pipe was loaded less than the surrounding material, which is characteristic for the so-called arching effect. The peak of the repartition occurred along with the peak of macroscopic stress. The results of the current study suggests that the peak value is more appropriate, but one must remember that $\phi_{threshold}$ is more reliable and safer.

. It was shown that the arching effect is influenced by the shape of the grains and also by the stiffness of the pipe.

Moreover, the direction of stresses was pointing around the pipe in the initial phases of the compression tests and the stress increment was larger in the zones at the sides of the pipe than in the middle zone containing the pipe. In the later phases of the loading the stress directions were influenced by the localisation of strains.

Conclusions and Perspectives

In many geotechnical problems the deformation of granular materials submitted to loading can be large (localised strains), and related to the irreversible mechanical behaviour of soil. Such problems are difficult to model in the framework of Finite Element Method without using phenomenological constitutive laws with excessive number of parameters that sometimes have little physical meaning. In these cases Discrete Element Method (DEM) might be a better choice because it is intrinsically dealing with discrete particles and therefore allow particle reorganization. However, DEM have some limitations as well; Simulations in this method can be computationally expensive so the number of particles used in simulations is always much smaller than in reality and the shape of modelised grains is idealised and rarely take into account the real variety and complexity. As it is commonly recognised, the shape of grains is an important factor influencing the mechanical response of granular media under loading. In order to simulate realistic behaviour of soil, the granular model must be more complex than simple discs or spheres.

The work presented in this thesis is divided into two parts: the investigation of grain shape influence on the mechanical behaviour of granular media, and its application to the issue of arching effect above underground conduits.

After a short introduction, the first Chapter contains some general considerations about the grain shape and two commonly used parameters for geometrical description of it: sphericity and roundness. Some studies extracted from the literature about the effect of the particle shape on the mechanical behaviour of dry sand were presented. The different possible strategies for modeling complex grain shapes with DEM were presented, including two kinds of shapes (clumps of discs and polygons) specifically studied in the course of this work. Additionally, a description of DEM contact detection method used in this work was given.

Chapter 2 of this work was focused on the investigations of the grain shape influence on the mechanical behaviour of granular assemblies. In Section 2.1 the results of collaboration of three teams in the CEGEO research program are described. The scope of the program was to highlight the effects of grain shapes of dense granular assemblies submitted to biaxial loading. The three teams involved (LTDS – Lyon, LMGC – Montpellier, 3SR – Grenoble) used different rounded and angular particle shapes defined with common rules, namely a parameter α describing particle sphericity, to build samples 5000 particles each. Parameter α was ranging from 0.0 to 0.5, and the teams used different DEM approaches: Contact Dynamics in case of LTDS and LMGC, and Molecular Dynamics in case of 3SR. Even though α is a simple, low order parameter, it was shown that it is related to a number of features of granular assembly.

In the isotropic state it was observed that coordination number was similar for all the grains regardless of α . On the contrary, the solid fraction of assemblies of the samples was clearly dependant on sphericity parameter; The dependence was seen to be non-monotonous and similar for each grain shape. An analytical solid fraction model depending on α and suitable for every grain shape used in the study was proposed. Moreover, analysis of the mechanical behaviour

of samples submitted to vertical loading with constant velocity and constant lateral pressure revealed that the value of residual (i.e. for large vertical strains) macroscopic friction angle was increasing linearly with α . Even though the level of friction angle was different for rounded and angular particles, the inclination of the increase was the same for all the particle shapes. Finally it was observed that Contact Dynamics and Molecular Dynamics methods give very similar results when simulating the same particles.

The work presented in Section 2.2 focused on two particular groups of grains used in CEGEO: concave clumps of three overlapping discs and its polygonal envelope – convex polygons of six edges. Each shape group consisted of several shape variants described with different values of the same parameter α . For α ranging from 0.0 to 0.5 the clump particles changed from three fully overlapping discs (equivalent to a single disc) to three discs distributed every 120° with partial overlap; The depth of “valleys” between the discs was increasing with α . In case of polygons α was ranging from ≈ 0.13 to 0.5 which corresponded to a gradual change from regular hexagon to equilateral triangle.

The numerical samples were studied in both the isotropic state and after biaxial loading. The mechanical response of sheared granular samples proved to be dependant on α . The maximum value of shear strength in dense assemblies of clumps was increasing with α but in dense assemblies of polygons it was decreasing. These observations combined with the results obtained during CEGEO program suggested that the size of the concavities in the particles was the main parameter influencing ϕ_{peak} of granular samples.

For the residual values of macroscopic friction angle, the trend in all the cases was the same: linear increase of $\phi_{threshold}$ with α , which suggest that under large macroscopic strains it was not the depth of concavities but the convex envelope of the grains that influenced the macroscopic behaviour.

Moreover, the study of deformations of the samples showed strain localisation in the form of bands. The width of the bands was increasing with α (with an exception of discs and hexagons) which can be related to grain interlocking. This trend was more clear for samples made of clumps while for samples made of polygons additional computations should be performed. The localisation in clump assemblies occurred earlier (in terms of vertical strain) in the tests comparing to polygons. The final width of the bands was more narrow for clumps than for polygons. These observations combined led to a conclusion, that while assemblies of clumps behave more like a brittle material, assemblies of polygons behave much more like real sands. In any case, the introduction of even slight complexity in the form of particles changed the behaviour of the entire assembly drastically comparing to assemblies of discs.

The information gathered during the first part of the study was used to model granular soil surrounding a flexible pipe, an engineering problem which is still not fully understood. The existing design methods for underground pipes rely heavily on engineering experience, contain parameters that are difficult to measure and include significant simplifications. The performance of flexible pipes depends on the soil-pipe interactions rather than the strength of the pipe itself, therefore the question of load transfer over a buried pipe is both scientifically interesting and practically important.

The work presented in Chapter 3 was focused on the kinematic behaviour of the pipe-soil system and reorganisation of the backfill grains which influence the load transfer mechanism above a flexible pipe. Knowing that in DEM framework it is possible to model granular medium and to obtain the interparticle forces, it was decided to create a model of a flexible pipe and to simulate the whole system in order to assess the arching effect. The pipe was created using a chain of discs connected with a contact law called parallel bonds. The pipe model was validated in series

of simple tests to ensure the contact law is able to model flexible structures well. Basing on laboratory tests on PVC pipe specimens the numerical model input parameters were determined and used in the subsequent simulations.

Numerical DEM simulations of the pipe in granular soil were performed using the pipe model surrounded by disc or clump particles. In parallel to experiments, it was decided to perform laboratory experiments of the same setup using PVC pipe buried in circular grains. In both the cases of numerical and experimental tests, the pipe and surrounding grains were subjected to biaxial and oedometric compressions. The experimental campaign was carried out using a plane strain apparatus $1\gamma 2\varepsilon$ and two kinds of 6 [cm] long Schneebeli material: wooden rods with diameters from 8 [mm] to 20 [mm] (≈ 2000 rods) and PVC rods with diameters from 1 [mm] to 3 [mm] (≈ 40000 rods in a sample). The experimental assemblies were including a $D = 10$ [cm] PVC pipe as a flexible pipe model. During the experiments in $1\gamma 2\varepsilon$, the stress and strains on the boundaries were measured. Additionally series of digital images of the sample were recorded to assess the kinematics of the grains and the pipe using Digital Image Correlation tools.

Surprisingly, it was observed that the presence of elastic pipe had little influence on the macroscopic mechanical behaviour of the assemblies, the stress-strain curves were similar. The strain localisation patterns revealed with the means of DIC seemed to be unaffected by the flexible inclusion as well. The mean strain computed for the pipe specimen was bigger than the macroscopic strain of the whole assembly. Numerical simulations of the experiments were qualitatively in agreement with experiments in terms of the macroscopic response and kinematic behaviour proving it is possible to model an underground pipe in DEM. The advantage of the chosen numerical method was that it was possible to observe the arching effect and quantify it by directly comparing the contact forces between the grains and the pipe. The arching effect was seen to be dependant on the stiffness of the pipe but also on the particle sphericity α of the granular material surrounding the pipe, with more concave grains transferring more load. The load transfer was observed in the initial phases of loading, for small vertical strains ($\varepsilon_1 < 2\%$). A typical question concerning the Terzaghi formula (3.28) is whether the peak or residual value of macroscopic friction angle should be used. The results of the current study suggests that the peak value is more appropriate, but one must remember that $\phi_{threshold}$ is more reliable and safer.

The study of grain shape influence on the behaviour of granular materials is still far from end. A natural continuation of such a study would be investigations of other grain shapes, like for example non-convex polygons, clumps made of 4 or 6 discs with the concavities partially filled, or polygons with rounded corners. More importantly, a similar numerical approach could be used to investigate other grain shape features like particle angularity, roundness or flatness. An important next step for this study would be to create samples characterised by different grain size distributions. In case of regular polygons, hexagons and triangles, the results might have been hindered by spontaneous crystalline patterns in the assemblies. A typical goal of every 2D study is its extension to a third dimension. In this particular case of grain shape investigation the potential advantages of 3D simulations could be obstructed by difficulties to change the grain shape while influencing only its certain aspects. Nevertheless it is necessary to bring the grain shape investigations closer to reality.

There are still a lot of paths that were not travelled in the course of this study concerning the micro-mechanical behaviour of the samples. The reasons for the clear decrease of ϕ_{peak} along with α in assemblies of polygons were not discovered. Some peculiar differences between grains of different shapes were noticed concerning the probability density functions of the contact forces, but were not understood enough to be included in this work. Attempts were made to correlate the grain shape with the intensity of moment of force transfer, but with little result. Discovery of such dependence could lead to development of rolling resistance contact laws. The residual

macroscopic friction angle curves suggested that there are other shapes characterised by even higher values of $\phi_{threshold}$. A question arises what could limit that increase? In the course of this study a promising attempt to characterise the assembly using elements of the graph theory was made (approach similar to (Walker et al., 2011)), but due to difficulties to interpret the results, this study was not continued.

The study of the flexible pipe buried in granular material can be recognised as work in progress. The simplifications in the course of the study should be corrected in order to model an actual engineering problem. Two examples of major simplification of the model used in the current study were the assumption of the elastic behaviour of the pipe and simple sample preparation procedure.

In reality, pipe behaviour is plastic and even in the $1\gamma 2\varepsilon$ experiments the pipe samples were permanently deformed after the tests and revealed some decolouration of the material at the sides. A model of plastic pipe behaviour could be introduced by simply altering the Young's modulus of the pipe during loading. Nevertheless, it seems it was negligible in the particular tests that were performed.

The pipe laying process in the field is performed differently than it was done in this study. An attempt was taken to model a grain pluviation process, but it led to problems connected with the introduction of gravity that was blurring the results, and with different boundary conditions that had to be used and therefore made the comparison with the experiments difficult.

Probably the most important shortcoming of the DEM modeling of underground flexible pipe was the size of the simulated assembly. Most probably the sample should be bigger (considering the pipe size would remain constant) in order to observe the manifestation of soil arching in contact forces or stress direction more clearly. As seen in the physical experiments, the question of the number of contacts between the pipe and the grains is influencing the pipe behaviour a lot. Simulation with much larger number of particles ought to be done.

The initial idea behind the physical experiments and subsequent numerical modeling of the pipe was to record deformations of the pipe with digital images, then to enforce the same deformation of a numerical pipe and to obtain the internal forces between the particles constituting the pipe which would be representative to internal forces in the physical pipe. That way it would be possible to "measure" stress during an experiment without employing instrumentation of the specimen. This was the reason to mark the pipe with 48 points and to model the pipe with 48 particles, and to use a pipe specimen thick enough to be able to record it. Unfortunately, the results were far from expected. The first approach was to impose displacement of the pipe grains equal to displacements obtained from numerical loading with point forces. The model was statically indeterminate and the resulting forces were different from the ones imposed. The use of DIC brought also another problem, the precision of the results. Due to the large stiffness of the pipe, errors in the positioning of the particles led to very large values of internal forces. The rotational stiffness of the pipe was smaller, but the accuracy of the DIC code to measure rotations was also worse and the pattern used to paint the pipe was not sufficient. Nevertheless, the results of the experimental program and its modeling were successful as it was possible to observe the anticipated phenomenon and this approach of underground structure modeling should be continued. At the same time, even though the DIC method proved itself to be a very useful experimental tool, the value of classical large scale experiments with standard instrumentation and real materials should not be forgotten.

Appendix A

Shadow Overlap Method

A.1 Method Description

Contact detection is an important aspect of DEM computations. In this study a method based on the separating axis theorem was used to determine the contact between polygons and to place the contact forces. For each pair of grains from the neighbour list the following tasks are performed, only if the computations in the previous point succeeded (Fig. A.1):

- 1) predetection (Fig. A.7),
- 2) precise contact detection (Fig. A.8),
- 3) establishing the number and position of the contact (Fig. A.9).

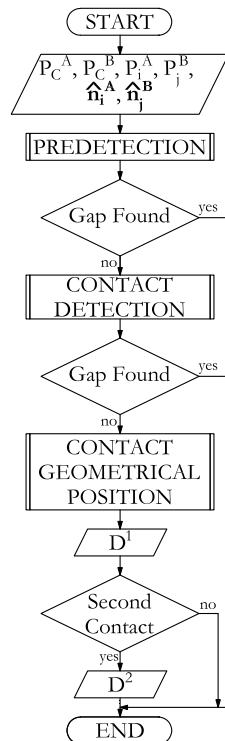


Figure A.1: Flowchart of the Shadow Overlap contact detection method for a single pair of polygonal grains A and B. This algorithm is applied to each record in the neighbour list and can be finished before the end whenever a gap is found

A.1.1 Predetection

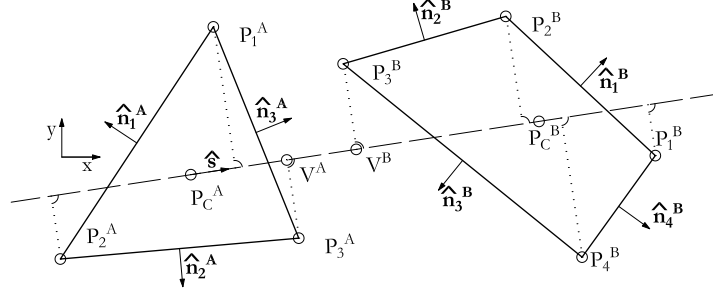


Figure A.2: Geometrical interpretation of the Shadow Overlap predetection phase together with the description of the variables used. Clearly, the difference of the projection of extreme points $V^A - V^B$ is less than null and the particles are not in contact

The predetection part is very simple and makes it possible to eliminate most of the non-existing contacts quickly. It is the practical realisation of the SAT for convex polygons. It is also possible to apply SAT to other objects (Burns and Sheppard, 2011).

The neighbouring particles A and B are described by the position of the mass centre $P_c^N = (x_c^N, y_c^N)$, positions of the corners $P_i^N = (x_i^N, y_i^N)$ in the global frame and the normal unit vectors of the edges \hat{n}_i^N directing outside. $N = \{A, B\}$ and $i = \{j, k\}$, $j, k = \{1, \dots, n_{corners}^N\}$. The numbering of the corners and faces of the polygons is supposed to be anticlockwise. An example of two arbitrary polygons is presented in Figure A.2.

In the first approach a unit vector \hat{s} is computed. This vector connects the centres of mass of the two particles and is directing from the particle A into particle B . Next, each corner of the two particles is orthogonally projected on the vector \hat{s} direction and the extreme projections are chosen:

$$V^A = \max\{\hat{s} \cdot P_j^A\} = \max\{\hat{s}_x \cdot x_j^A + \hat{s}_y \cdot y_j^A\} \quad (\text{A.1})$$

$$V^B = \min\{\hat{s} \cdot P_k^B\} = \min\{\hat{s}_x \cdot x_k^B + \hat{s}_y \cdot y_k^B\} \quad (\text{A.2})$$

If $V^A - V^B \leq 0$ than there is no overlap and therefore no contact. Otherwise, there is a possibility that the two particles are in contact and a more precise test is needed, see Fig. A.3.

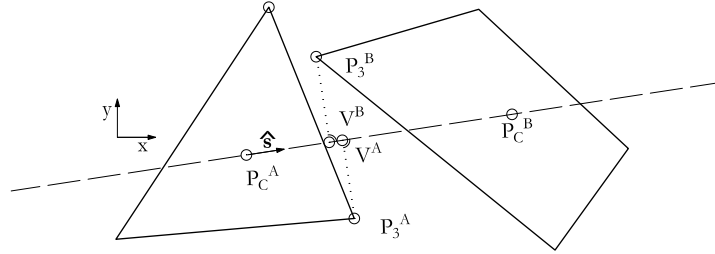


Figure A.3: Example of two neighbouring polygons that would pass the predetection test even though they are not in contact $V^A - V^B > 0$

A.1.2 Contact Detection

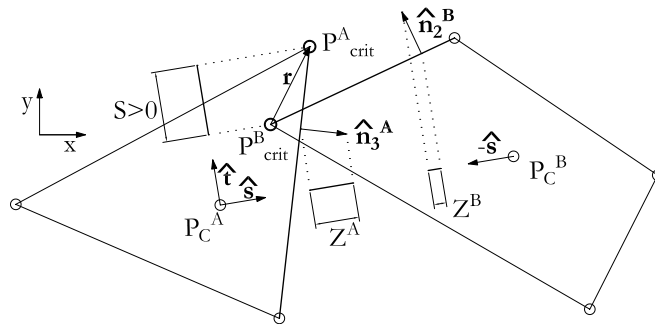


Figure A.4: Geometrical interpretation of the Shadow Overlap contact detection phase. These two particles passed the predetection phase and both the critical corners were found, together with associated critical faces. The critical corner vector \mathbf{r} was projected on the $\hat{\mathbf{t}}$ to obtain the value of S . The critical face unit vectors are projected on the direction of $\hat{\mathbf{s}}$ to obtain the values of Z^A and Z^B . As $Z^A > Z^B$, it is supposed that particle B is intruding particle A. The next step would be to change the critical corner of particle A from 1 to 3 and repeat the process

In the previous step the two particles were not proven to be apart. The next step would be to investigate *each* edge in search for a gap between the particles but this process can be optimised. The anticlockwise numbering of the corners and vertices helps to avoid the unnecessary checks.

Initially the extreme (critical) corners chosen during the predetection phase are connected

with a *critical corner vector* \mathbf{r} directing from P_{crit}^B to P_{crit}^A , see Figure A.4. The critical corner vector is projected onto a vector orthogonal to $\hat{\mathbf{s}}$: $\hat{\mathbf{t}}$. This gives the direction of rotation for the vector $\hat{\mathbf{s}}$.

$$S = \hat{\mathbf{t}} \cdot \hat{\mathbf{r}}, \quad (\text{A.3})$$

where

$$\begin{cases} \hat{\mathbf{t}}_x = -\hat{\mathbf{s}}_y, \\ \hat{\mathbf{t}}_y = \hat{\mathbf{s}}_x \end{cases} \quad (\text{A.4})$$

Then the normal vectors of the polygon faces are taken into account: If $S < 0$ then the critical face is considered; Otherwise, the face preceding the critical one. The dot products of $\hat{\mathbf{s}}$ ($-\hat{\mathbf{s}}$ for particle B) and $\hat{\mathbf{n}}_i^N$ vectors are computed for both the particles. The bigger value of these two dot products indicate which particle's normal unit vector of the considered edge will replace the $\hat{\mathbf{s}}$. Finally the critical corner number of this particle is updated (increased by one in case when $S < 0$ or decreased when $S > 0$). That procedure gives the new critical corner vector which can be projected on the $\hat{\mathbf{t}}$. If the projection would change the sign in comparison to the initial value of S and if the dot product of $\hat{\mathbf{s}}$ and \mathbf{r} is not lower than 0 (which would be a proof of a gap between the polygons), than the particles are in contact and this contact involves the critical vertex. In the other case, the procedure is repeated. For an example see Figure A.4.

A.1.3 Contact Geometrical Position

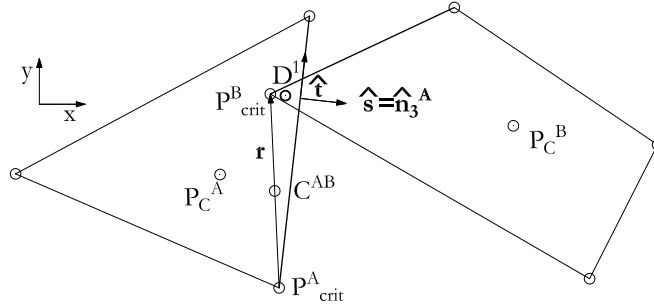


Figure A.5: *Geometrical interpretation of the Shadow Overlap contact positioning phase. After finishing the previous phase it is certain that the two particles are in contact and it is particle B intruding A. The current critical corners and $\hat{\mathbf{s}}$ are presented. The middle of a critical corner vector C^{AB} is presented. The intermediate steps are not presented, but the final position of the first and only contact point D^1 is marked*

Having established that a certain critical corner of the first particle is penetrating the other particle, the next step is to place the contact point in space. It is also important to check whether there is a second contact point or not. This is done by investigating the following and

preceding critical edges of the penetrating particle. Initially the first contact point is assumed to be placed in reference from the critical vertex of the intruding particle (see Fig. A.5):

$$\begin{cases} D_x^1 = x_{crit}^N \pm 0.5 \cdot (\hat{\mathbf{s}} \cdot \mathbf{r}) \cdot \hat{\mathbf{s}}_x, \\ D_y^1 = y_{crit}^N \pm 0.5 \cdot (\hat{\mathbf{s}} \cdot \mathbf{r}) \cdot \hat{\mathbf{s}}_y, \end{cases} \quad (\text{A.5})$$

where $-$ sign is for the case when $N = A$.

Next, the positions of the preceding ($n_{crit} - 1$) and the following ($n_{crit} + 1$) corners of the penetrating particle are compared with the point C^{AB} placed in the middle of the distance between the critical vertices of particles A and B (see Figure A.5):

$$L_1 = (x_{crit-1}^N - C_x^{AB}) \cdot \hat{\mathbf{s}}_x + (y_{crit-1}^N - C_y^{AB}) \cdot \hat{\mathbf{s}}_y, \quad (\text{A.6})$$

$$L_2 = (x_{crit+1}^N - C_x^{AB}) \cdot \hat{\mathbf{s}}_x + (y_{crit+1}^N - C_y^{AB}) \cdot \hat{\mathbf{s}}_y. \quad (\text{A.7})$$

The second point of contact exist if $L_1 > 0$ or if $L_2 > 0$ when A is penetrating B ($L_1 < 0$ or if $L_2 < 0$ when B is penetrating A).

If $L_1 > 0$ ($L_1 < 0$), then the second point of contact is assumed to be placed at

$$\begin{cases} D_x^2 = x_{crit-1}^N - L_1 \cdot \hat{\mathbf{s}}_x, \\ D_y^2 = y_{crit-1}^N - L_1 \cdot \hat{\mathbf{s}}_y. \end{cases} \quad (\text{A.8})$$

If $L_2 > 0$ ($L_2 < 0$) while $L_2 > L_1$ ($L_2 < L_1$), the second point position is computed using the equations (A.8) but using P_{crit+1}^N and L_2 instead.

If both the contact points were identified, the final position of the second contact point is established in relation to the vector $\hat{\mathbf{t}}$. Equation (A.6) is used to compute M_1 by replacing P_{crit-1}^N with P_{crit}^A and $\hat{\mathbf{s}}$ with $\hat{\mathbf{t}}$. M_2 is computed using (A.6) while inserting D_x^2 instead of P_{crit-1}^N and $\hat{\mathbf{t}}$ instead of $\hat{\mathbf{s}}$.

Remembering the direction of rotation computed in the second phase of the procedure (the value of S), the distance between the point C^{AB} and the corners of the particle that is being penetrated are projected on the direction of the vector $\hat{\mathbf{t}}$. In case when $S < 0$ and it is particle A intruding particle B , the critical and the one preceding it are used in equation (A.6) to compute the K_1 and K_2 respectively. In case of $S > 0$ the corners involved are P_{crit+1} and P_{crit} .

The opposite situation, particle B penetrating particle A , the corners used in case of $S < 0$ are P_{crit-1} and P_{crit} , while it is P_{crit} and P_{crit+1} when $S > 0$.

The value of M_2 obtained is compared with the values of K_1 and K_2 . K_2 substitute M_2 when $M_2 > K_2$ and K_1 substitute M_2 when $M_2 < K_1$. Finally, the position of the second point of contact is equal to:

$$\begin{cases} D_x^2 = C_x^{AB} + M_2 \cdot \hat{\mathbf{t}}_x, \\ D_y^2 = C_y^{AB} + M_2 \cdot \hat{\mathbf{t}}_y. \end{cases} \quad (\text{A.9})$$

In fact the two resulting contact points are placed as wide as possible, at the ends of the overlapping area.

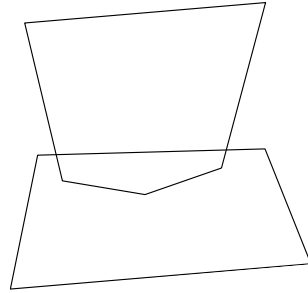


Figure A.6: Configuration of two polygonal particles with large overlap: one particle is penetrated with three corners of the second particle

It is important to know the limitations of the Shadow Overlap method. In case when the grain contacts are very soft comparing to the external forces a situation similar to the one presented in Figure A.6 becomes possible. Such a deep penetration will not be solved properly with the Shadow Overlap method as it is impossible to define a single penetrating corner or edge.

A.2 Block Schemes

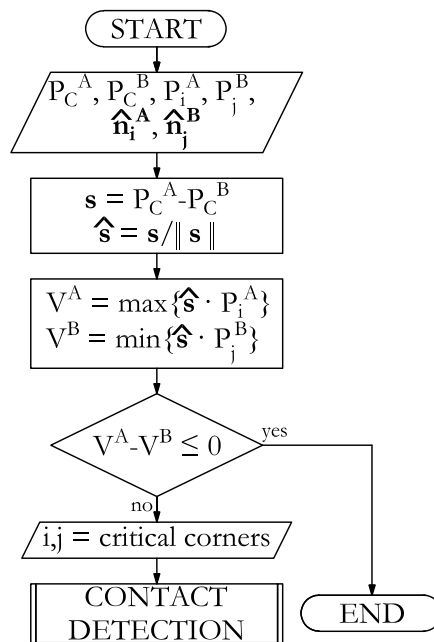


Figure A.7: Flowchart of the contact predetection. The input information needed are the positions of the corners, mass centres of the two particles and the unit vectors of the faces. As an output one learns if a contact is possible and which corners of the particles should be investigated more

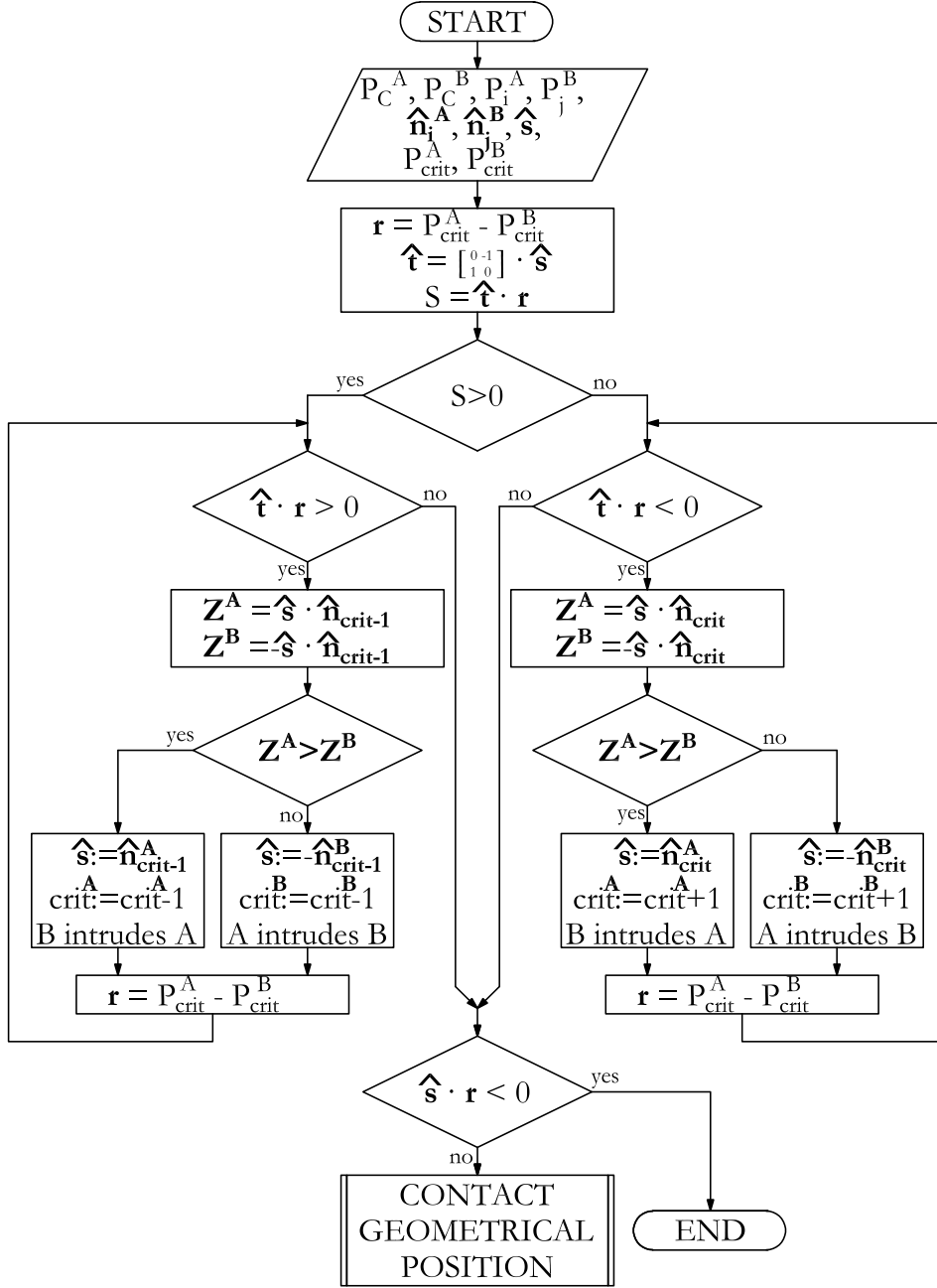


Figure A.8: Flowchart of the contact detection phase. Apart from the basic information about the particles carried from the predetection phase, the input consists of the vector $\hat{\mathbf{s}}$ direction and the initial critical corner numbers

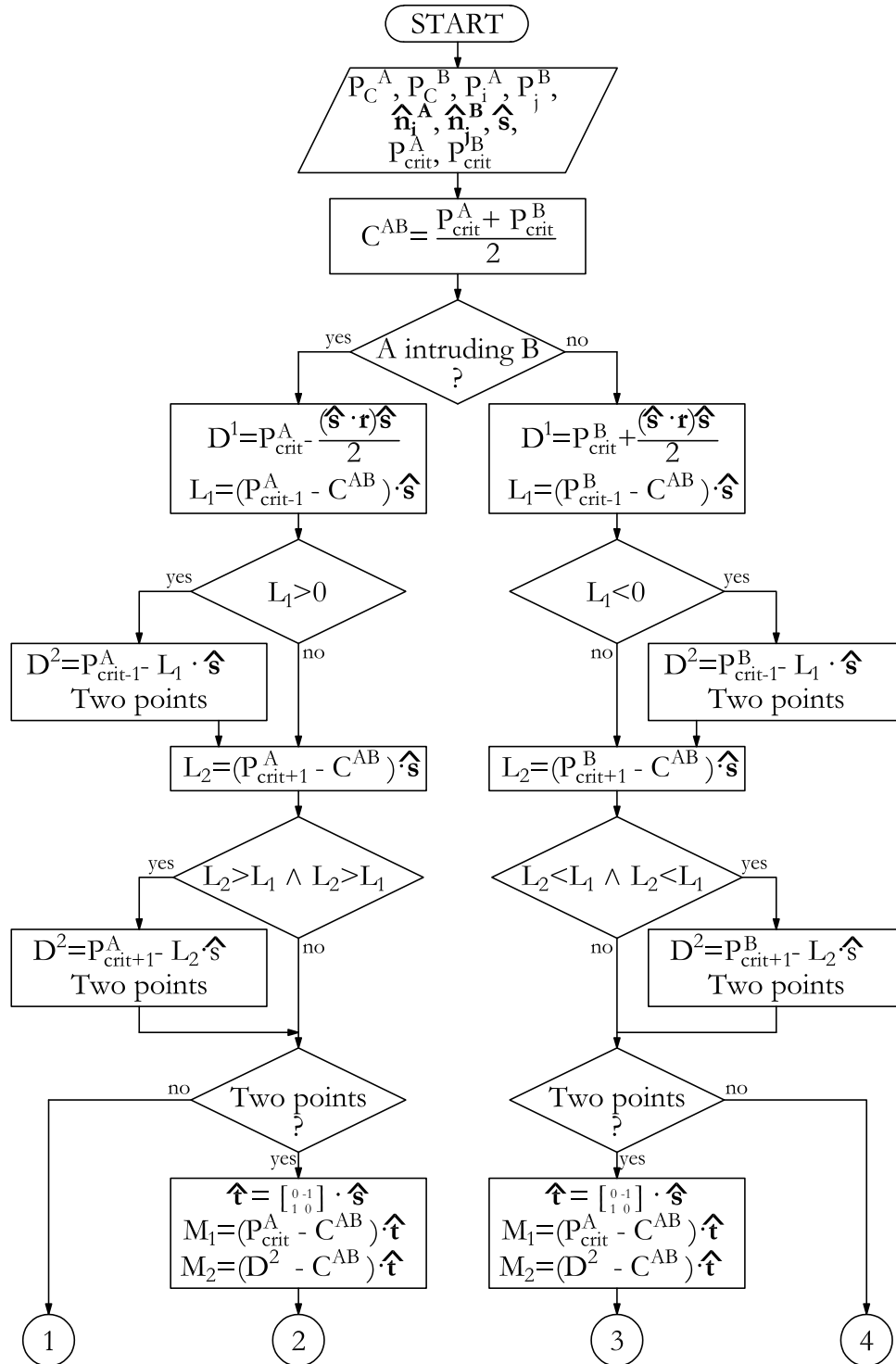


Figure A.9: Flowchart of the contact placing in Shadow Overlap method. The flowchart continues on the next page

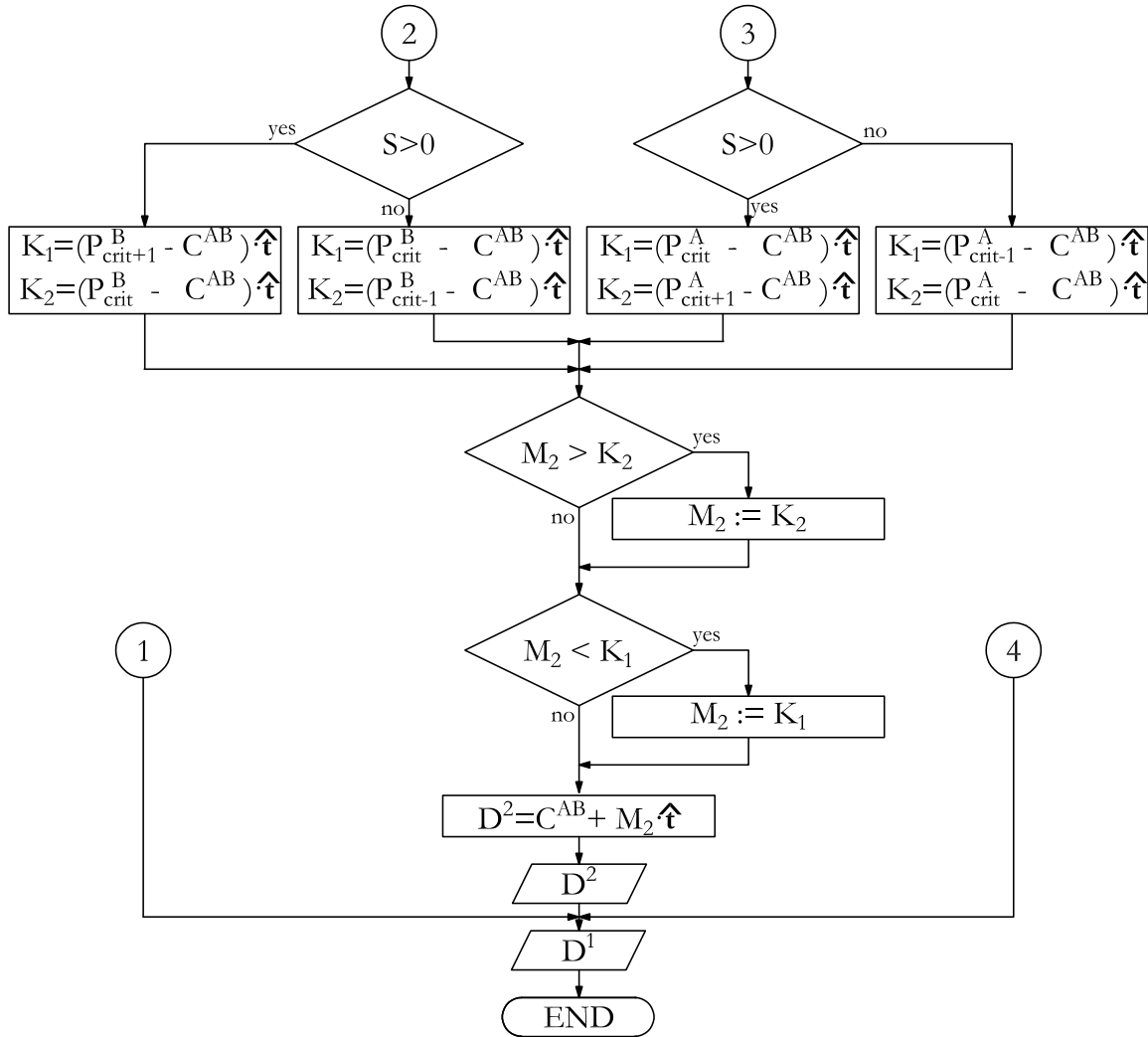


Figure A.9: Flowchart of the contact placing in Shadow Overlap method. The output is either one or two contact point geometrical positions

Appendix B

Particle Area

B.1 Clump Area

As one can see in Figure B.1, any clump in range of α between 0 and 0.5 is made of an equilateral triangle and three circular segments of equal size:

$$S_{clump} = 3 \cdot S_{circular\ segment} + S_{triangle\ a}. \quad (B.1)$$

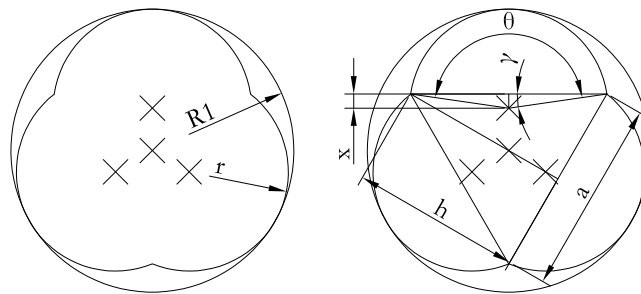


Figure B.1: *Clump area computation*

Let us denote the size of a clump using the circumscribed circle radius R_1 . The vertices of the triangle will be placed on the inscribed circle of the clump, the radius of which can be expressed in function of α and R_1 using the relation (2.1):

$$R_2 = R_1 (1 - \alpha). \quad (B.2)$$

Therefore, the triangle side length is given by:

$$a = \sqrt{3} \cdot R_1 \cdot (1 - \alpha), \quad (B.3)$$

and its height by:

$$h = \frac{3}{2} \cdot R_1 \cdot (1 - \alpha). \quad (\text{B.4})$$

Considering that, the area of the triangle is given by the equation:

$$S_{triangle\ a} = \frac{3}{4} \sqrt{3} \cdot R_1^2 \cdot (1 - \alpha)^2. \quad (\text{B.5})$$

The circular segment is cut from a circle of radius r with a chord denoted by a . The clump circle radius is expressed with the following relation:

$$r = \frac{(\alpha^2 - \alpha + 1) \cdot R_1}{\alpha + 1}. \quad (\text{B.6})$$

The area of the segment is given with a relation:

$$S_{circular\ segment} = \frac{r^2}{2} \cdot (\theta - \sin\theta), \quad (\text{B.7})$$

where θ is expressed in [rad].

The angle θ is:

$$\theta = \pi - 2 \cdot \gamma, \quad (\text{B.8})$$

where γ is the angle of a triangular part with height x :

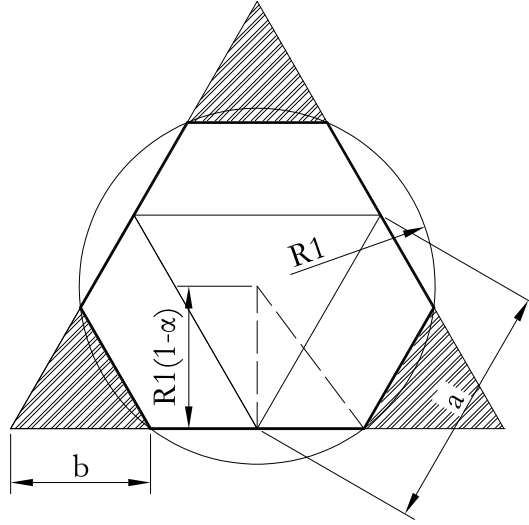
$$x = \frac{h}{3} - (R_1 - r), \quad (\text{B.9})$$

$$\tan\gamma = \frac{x}{\frac{a}{2}}. \quad (\text{B.10})$$

It can be also interesting to present the area of a given clump as a function of the shape parameter α and the outer radius of the particle R_1 . By putting equations (B.3), (B.8), (B.9), (B.10) and (B.6) into equations (B.5) and (B.7) and then to (B.1), a following relation can be obtained:

$$S_{clump}(\alpha, R_1) = \frac{3\sqrt{3}}{4} \cdot R_1^2 \cdot (1 - \alpha)^2 + \frac{3 \cdot R_1^2 \cdot (\alpha^2 - \alpha + 1)^2}{2 \cdot (\alpha + 1)^2}. \quad (\text{B.11})$$

$$\cdot \left\{ \pi + 2 \operatorname{atan} \left(\frac{\alpha^2 - 4\alpha + 1}{\sqrt{3}(\alpha - 1) \cdot (\alpha + 1)} \right) - \sin \left[\pi + 2 \operatorname{atan} \left(\frac{\alpha^2 - 4\alpha + 1}{\sqrt{3}(\alpha - 1) \cdot (\alpha + 1)} \right) \right] \right\}.$$


 Figure B.2: *Polygon area computation*

B.2 Polygon Area

The area of any polygon in agreement with the definition (2.1) can be computed as a sum of equilateral triangles. The polygon area consists of four triangles with a side length denoted as a , reduced by the area of three equilateral triangles with a side length denoted as b , see Figure B.2. The definition of the first a triangle is the same as in case of clump (B.1). The remaining three triangles are placed along the three sides of the base triangle. In Figure B.2 the b triangles are hatched to represent a “negative” area.

$$S_{\text{polygon}} = 4 \cdot S_{\text{triangle } a} - 3 \cdot S_{\text{triangle } b}, \quad (\text{B.12})$$

The side b length of the small triangle might be computed using the Pythagorean equation knowing that the two sides of the dashed triangle in Figure B.2 are equal to the radii of the particle ex- and incircle:

$$R_1^2 = R_1^2 \cdot (1 - \alpha)^2 + (a - b)^2 \quad (\text{B.13})$$

Using the relation (B.3), two solutions are obtained:

$$b = \pm \sqrt{2R_1^2 \cdot \alpha - R_1^2 \cdot \alpha^2 - \sqrt{3}R_1\alpha + \sqrt{3}R_1} \quad (\text{B.14})$$

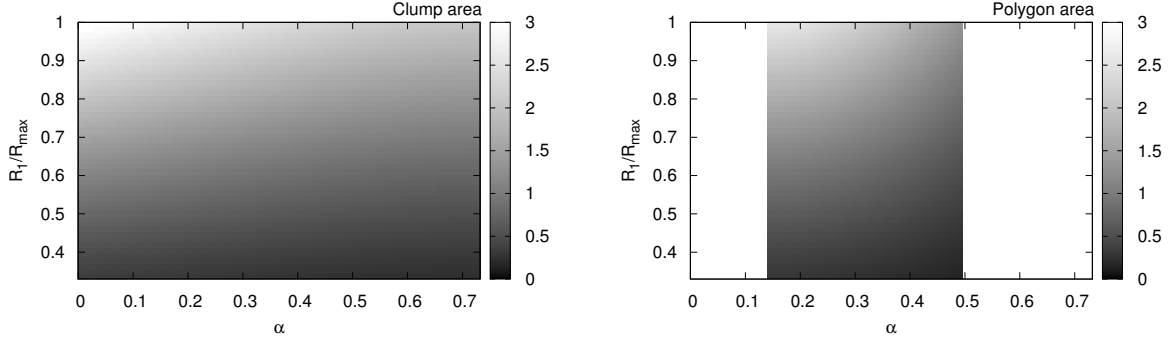
The negative square root denotes the b length that was looked for. Finally, the area of a small triangle can be computed using the following formula:

$$S_{\text{triangle } b} = \frac{\sqrt{3}}{4}b^2. \quad (\text{B.15})$$

As in case of clumps, the area of a particle can be presented as a function of α and R_1 :

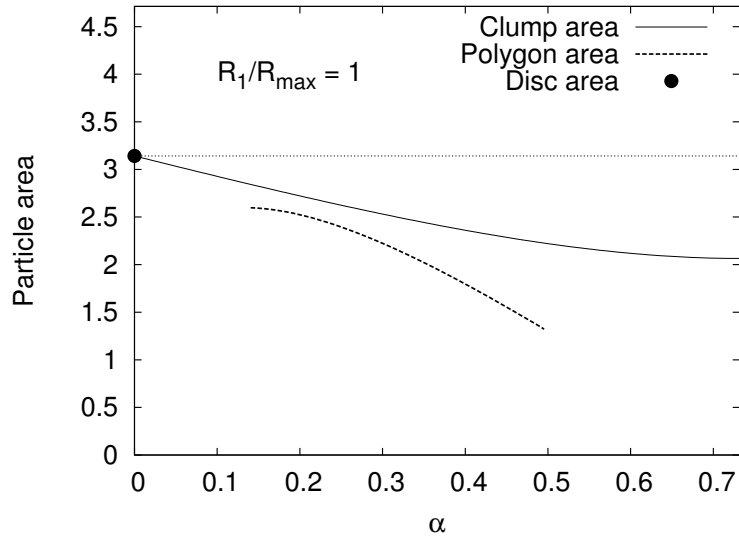
$$S_{\text{polygon}}(\alpha, R_1) = \frac{3}{4}R_1 \cdot \left(\sqrt{3} \cdot R_1 \cdot (2 \cdot (\alpha - 2) \cdot \alpha + 1) - 6 \cdot (\alpha - 1) \cdot \sqrt{R_1^2 \cdot (\alpha - 2) \cdot \alpha} \right). \quad (\text{B.16})$$

The functions (B.11) and (B.16) are nonlinear in α and R_1 . In Figure B.3 the surface maps of the respective functions are presented. In Figure B.3c a cross-section of these two figures for a single value of $R_1 = R_{max}$ is presented.



(a) *Clump*

(b) *Polygon*



(c) *Both maps cross-section*

Figure B.3: *Particle area functions: surface maps and a cross-section for one particular radius. The colour scale is denoting the dimensionless area in function of the shape parameter α and the normalised outer radius of the particle $R_1[-]$. The plots are limited by the extreme values of the α parameter*

Appendix C

Castigliano Theorem

A pipe loaded with a single vertical force can be divided into quadrants. Single quadrant can be regarded as an circularly curved cantilever beam (see Fig. C.1).

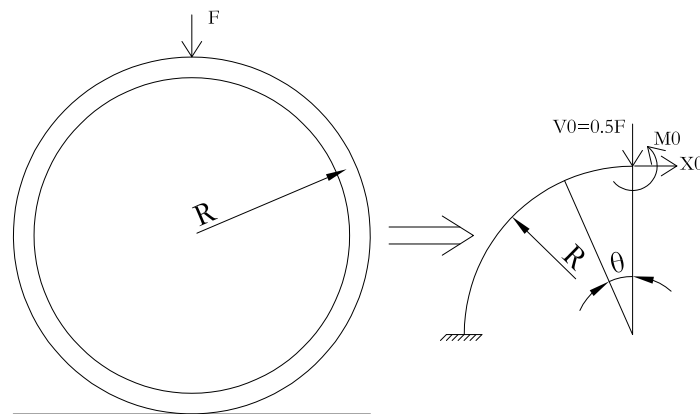


Figure C.1: *Pipe quadrant modelled as a cantilever beam. The beam is fixed on one end and the other end is loaded with half of the external load acting vertically, a bending moment which correspond to internal forces and a horizontal force*

The radius of the beam curvature correspond to the radius of the pipe $((R_{external} + R_{internal})/2)$. The beam is loaded with three forces: vertical, horizontal and a bending moment. The vertical force Y_0 is equal to half of the external load (the other half is loading the upper-right quadrant of the pipe). The bending moment M_0 is in fact equal to the internal bending moment in the pipe and is yet to be determined. Without the external moment the free end of the pipe would rotate and would not be horizontal anymore. The horizontal force X_0 is equal to zero, but it is needed to derive the horizontal displacements.

The beam is circular therefore the forces are correlated with the angle θ . For a given cross-section at θ the strains due to normal and tangential stresses are negligible and only the bending moment is significant. Therefore the equilibrium equation for a cross-section at θ is given:

$$\sum M_{\theta} = M + M_0 - Y_0 R \sin \theta - X_0 R (1 - \cos \theta) = 0 \quad (C.1)$$

and so

$$M = Y_0 R \sin\theta + X_0 R(1 - \cos\theta) - M_0. \quad (\text{C.2})$$

The horizontal force X_0 is null, therefore:

$$M = Y_0 R \sin\theta - M_0. \quad (\text{C.3})$$

The differential equations are given:

$$\frac{\partial M}{\partial Y_0} = R \sin\theta \quad (\text{C.4})$$

$$\frac{\partial M}{\partial X_0} = R(1 - \cos\theta) \quad (\text{C.5})$$

$$\frac{\partial M}{\partial M_0} = -1 \quad (\text{C.6})$$

The Castigliano's Theorem states that

$$\delta G = \int_S \frac{M}{EI} \cdot \frac{\partial M}{\partial G} ds \quad (\text{C.7})$$

where G is a given load, δG is the displacement resulting from the load, s is the length of the beam, I is the moment of inertia of the cross-section and E is the Young's modulus of the material.

By inserting equations (C.4), (C.5) and (C.6) to equation (C.7) is obtained:

$$\begin{aligned} \delta Y_0 &= \frac{1}{EI} \int_0^L M \frac{\partial M}{\partial Y_0} ds = \frac{1}{EI} \int_0^{\frac{\pi}{2}} (Y_0 R \sin\theta - M_0) \cdot R \sin\theta \cdot R d\theta = \\ &= \left(\frac{\pi}{4} Y_0 R - M_0\right) \frac{R^2}{EI} \end{aligned} \quad (\text{C.8})$$

$$\begin{aligned} \delta X_0 &= \frac{1}{EI} \int_0^L M \frac{\partial M}{\partial X_0} ds = \frac{1}{EI} \int_0^{\frac{\pi}{2}} (Y_0 R \sin\theta - M_0) \cdot R(1 - \cos\theta) \cdot R d\theta = \\ &= \left(\frac{Y_0 R}{2} - \left(\frac{\pi}{2} - 1\right) M_0\right) \frac{R^2}{EI} \end{aligned} \quad (\text{C.9})$$

$$\begin{aligned} \delta M_0 &= \frac{1}{EI} \int_0^L M \frac{\partial M}{\partial M_0} ds = \frac{1}{EI} \int_0^{\frac{\pi}{2}} (Y_0 R \sin\theta - M_0) \cdot (-1) \cdot R d\theta = \\ &= \left(-Y_0 R + M_0 \frac{\pi}{2}\right) \frac{R}{EI} \end{aligned} \quad (\text{C.10})$$

The end of the beam is not rotating so $\delta M_0 = 0$ and thus from equation (C.10) can be computed:

$$M_0 = \frac{2}{\pi} Y_0 R \quad (\text{C.11})$$

By inserting equation (C.11) to equations (C.8) and (C.9), while remembering that $Y_0 = \frac{F}{2}$, finally we obtain:

$$2\delta Y = \left(\frac{\pi}{4} - \frac{2}{\pi}\right) \frac{FR^3}{EI} \quad (\text{C.12})$$

$$2\delta X = \left(\frac{2}{\pi} - \frac{1}{2}\right) \frac{FR^3}{EI} \quad (\text{C.13})$$

where δX is the pipe deflection perpendicular to the loading direction and δY is the deflection parallel to the loading direction. Inserting equation (C.11) into equation (C.3) results in the $M(\theta)$ function. The extreme bending moment values are located at $\theta = 0^\circ$ and $\theta = 90^\circ$.

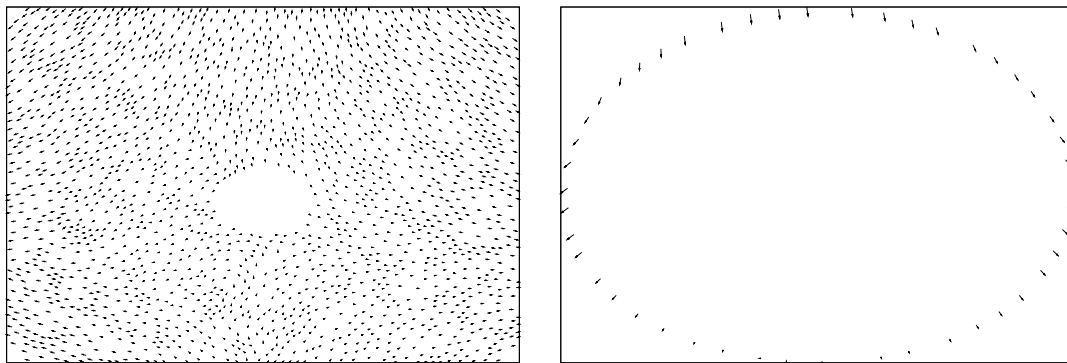
$$M(\theta = 0^\circ) = -\frac{2}{\pi}Y_0R, \quad (\text{C.14})$$

$$M(\theta = 90^\circ) = \left(1 - \frac{2}{\pi}\right) \cdot Y_0R. \quad (\text{C.15})$$

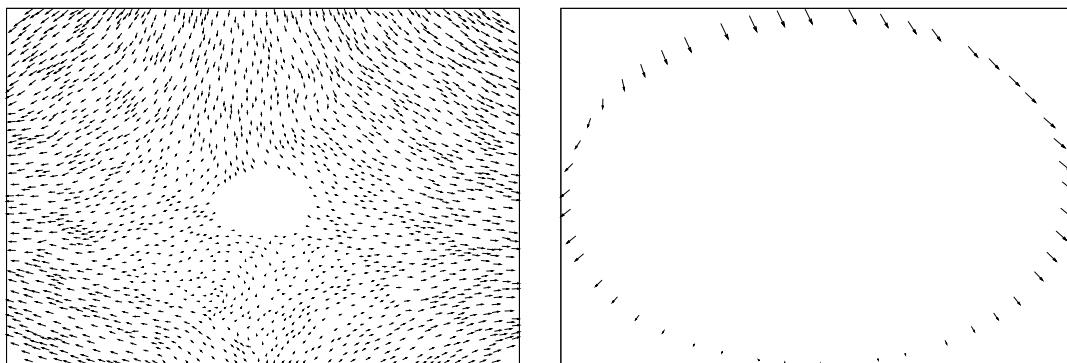
Appendix D

$1\gamma 2\varepsilon$ Results

D.1 Displacement Fields

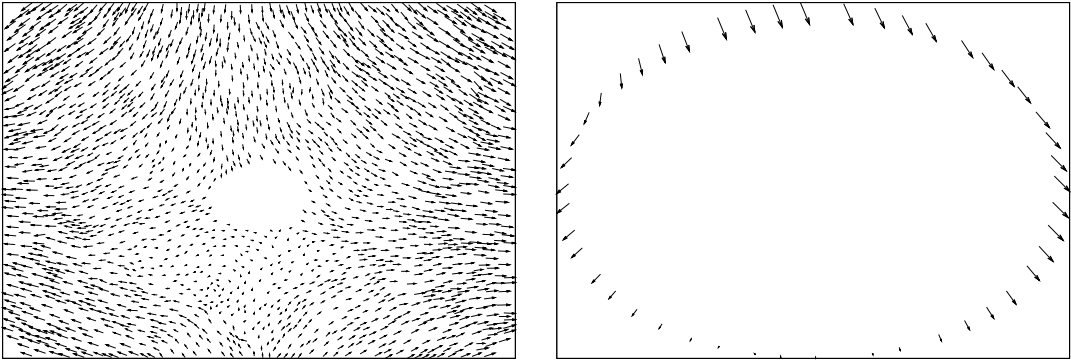


(a) $0 - 1\% \varepsilon_1$

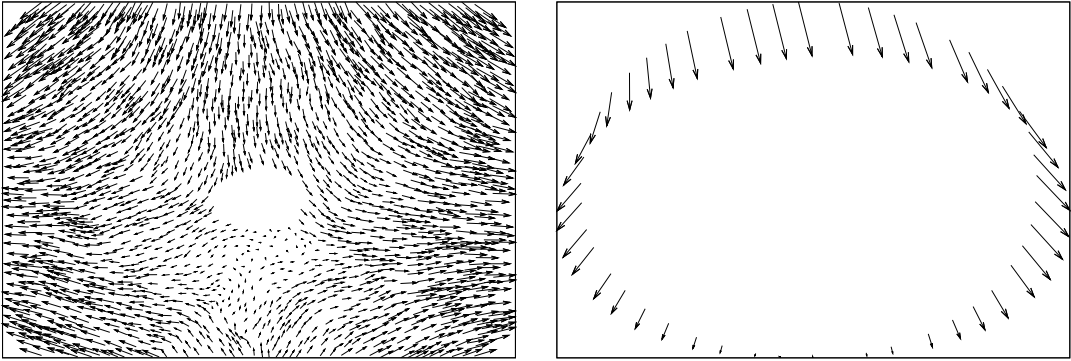


(b) $0 - 2\% \varepsilon_1$

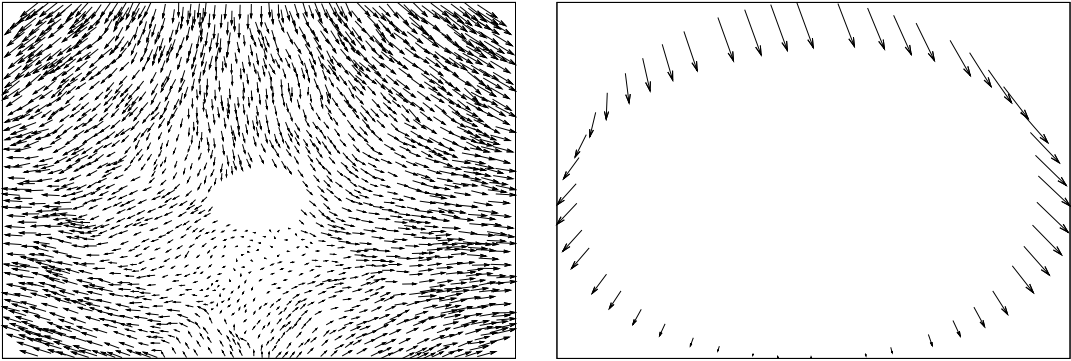
Figure D.1: Wooden grains with a PVC pipe, displacement fields. The longest arrow of particle displacement is equal to $58mm$; The biggest displacement of a point on a pipe is equal to $26mm$



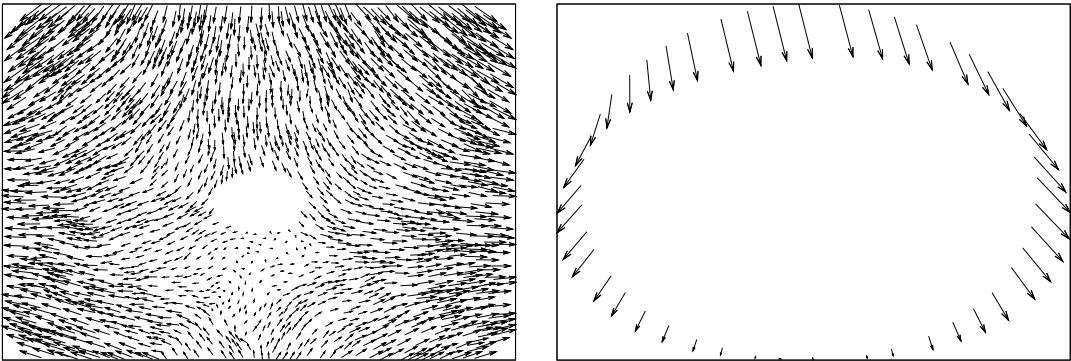
(c) $0 - 3\% \varepsilon_1$



(d) $0 - 4\% \varepsilon_1$

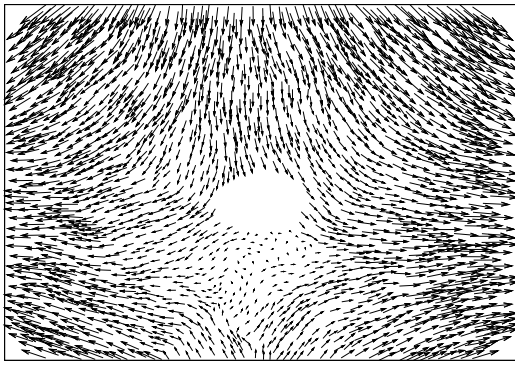
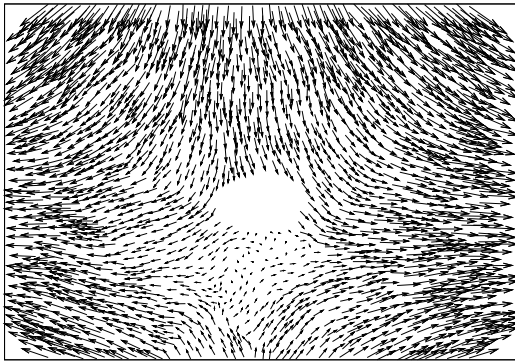
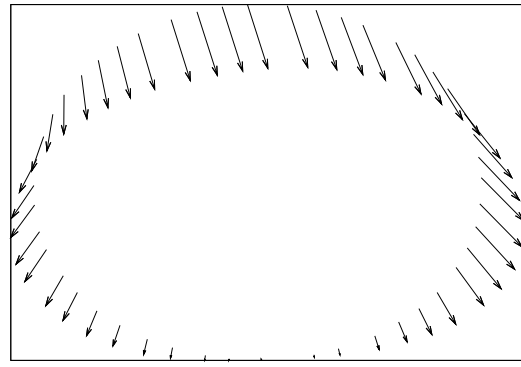
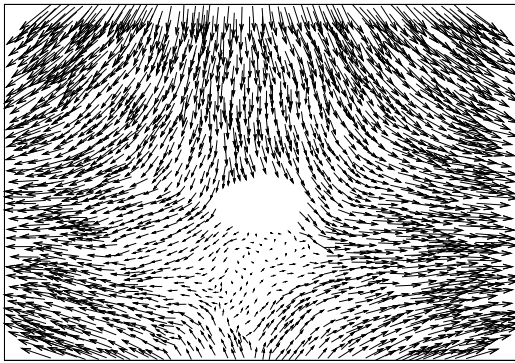
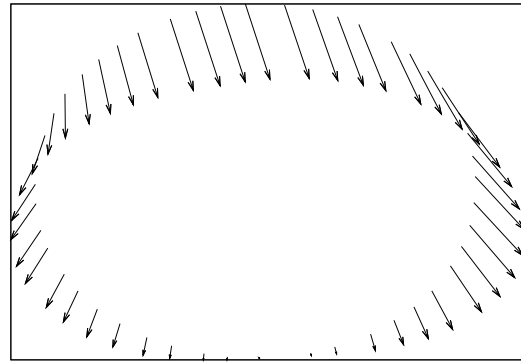
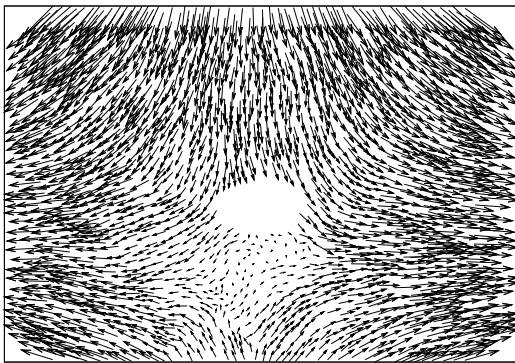
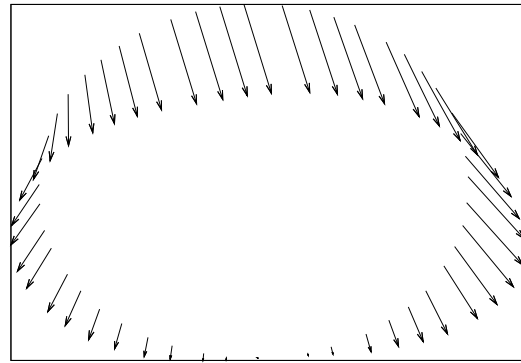
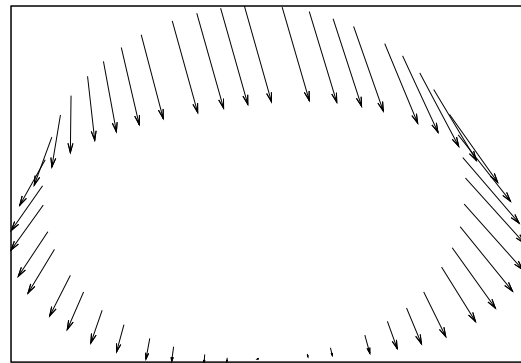


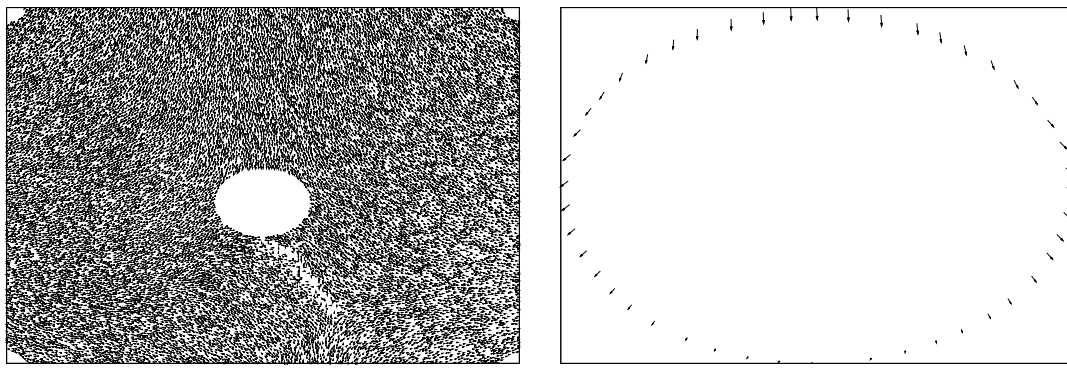
(e) $0 - 5\% \varepsilon_1$



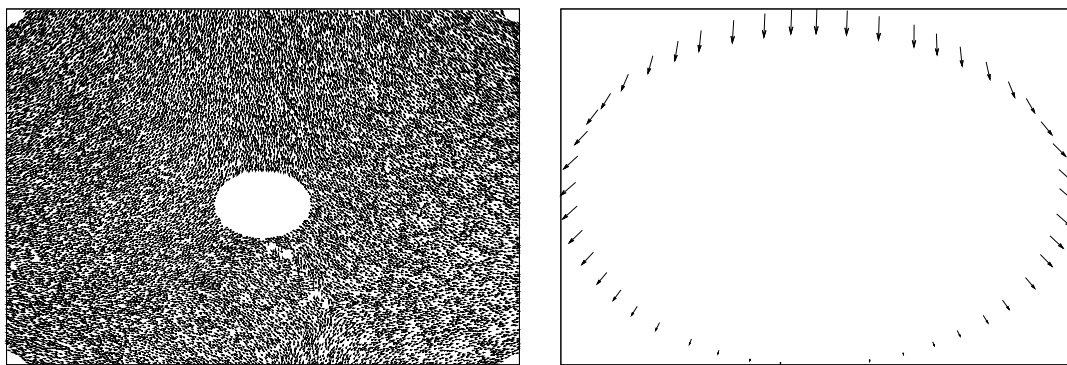
(f) $0 - 6\% \varepsilon_1$

Figure D.1: *Wooden grains with a PVC pipe, displacement fields*

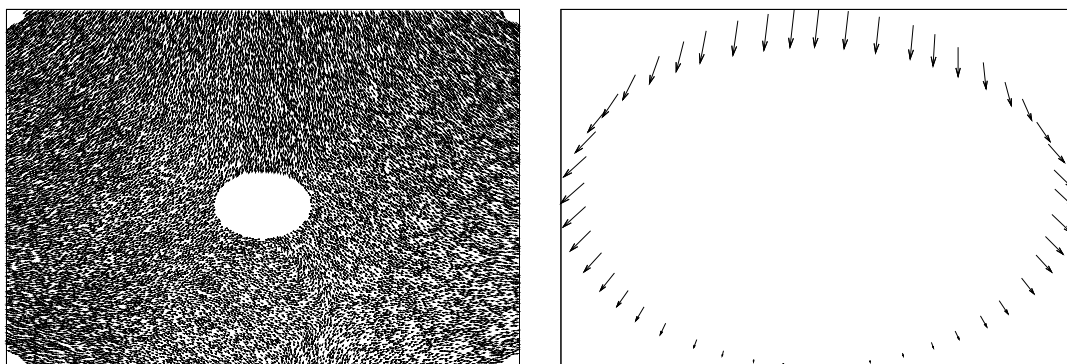
(g) $0 - 7\%\varepsilon_1$ (h) $0 - 8\%\varepsilon_1$ (i) $0 - 9\%\varepsilon_1$ (j) $0 - 10\%\varepsilon_1$ Figure D.1: *Wooden grains with a PVC pipe, displacement fields*



(a) $0 - 1\% \varepsilon_1$

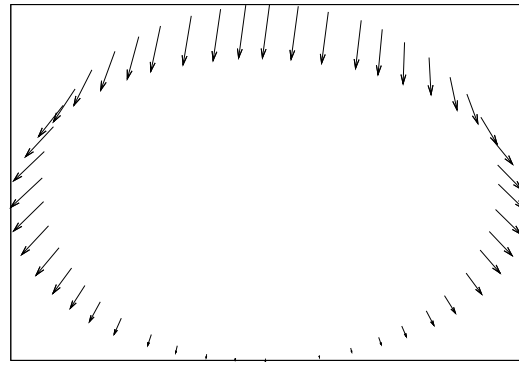
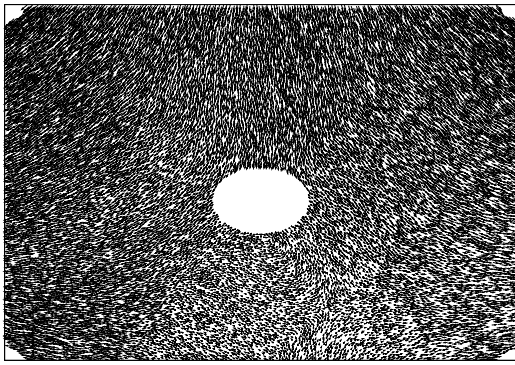
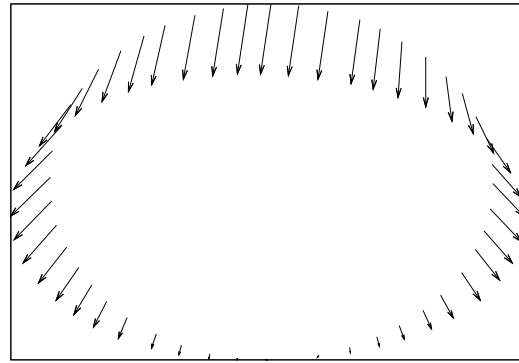
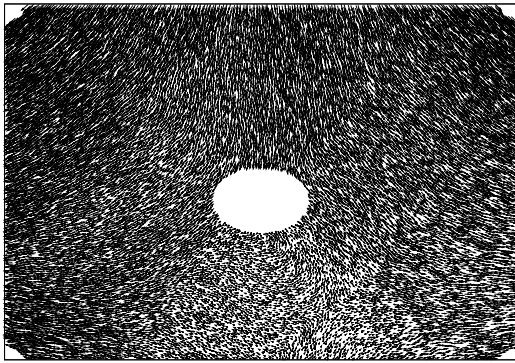
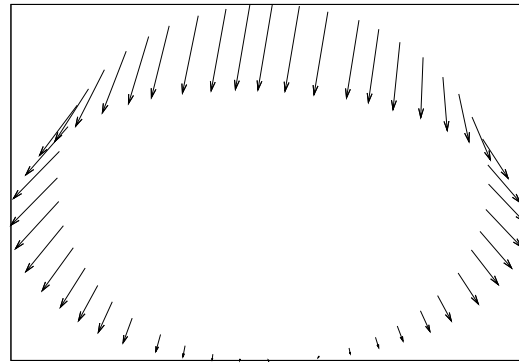
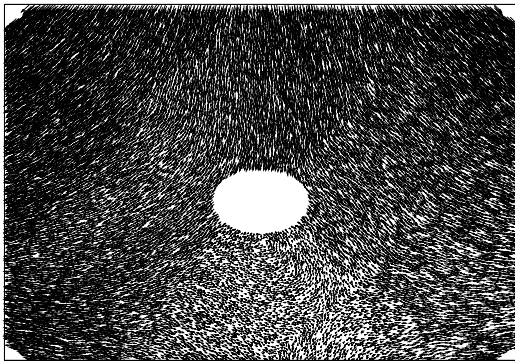
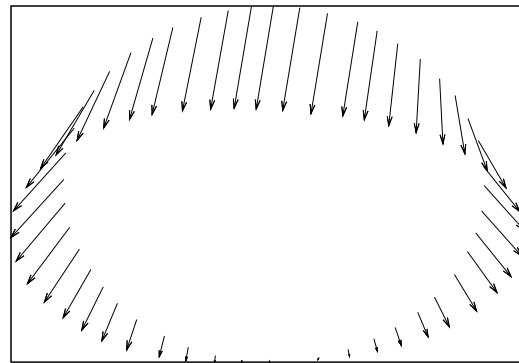
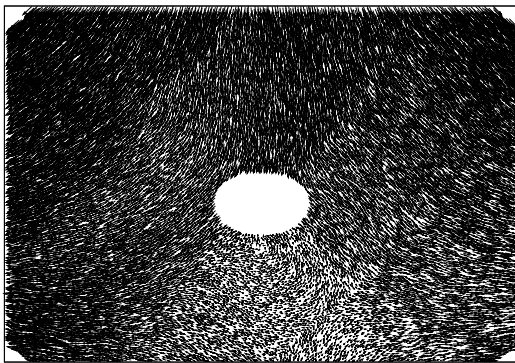


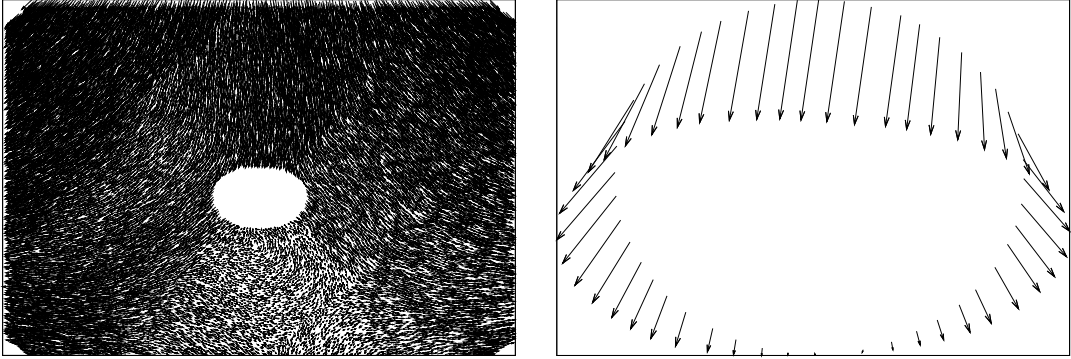
(b) $0 - 2\% \varepsilon_1$



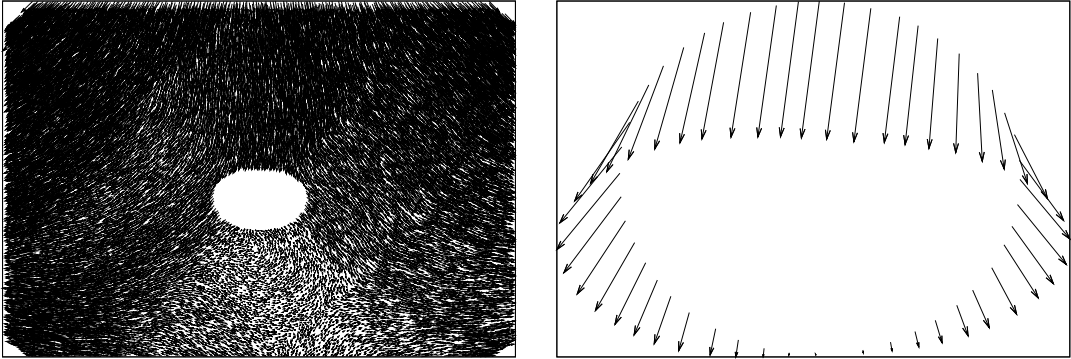
(c) $0 - 3\% \varepsilon_1$

Figure D.2: *PVC grains with a PVC pipe, displacement fields. The longest arrow of particle displacement is equal to 21mm and it was reduced three times in the images for a clearer presentation; The biggest displacement of a point on a pipe is equal to 34mm*

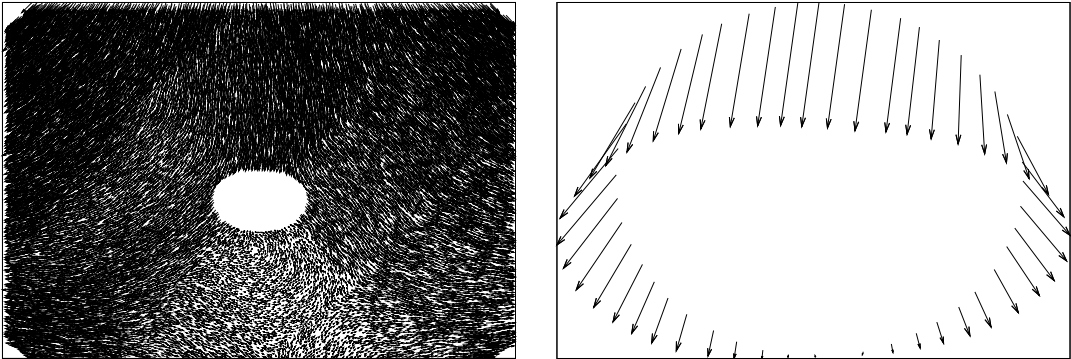
(d) $0 - 4\%\varepsilon_1$ (e) $0 - 5\%\varepsilon_1$ (f) $0 - 6\%\varepsilon_1$ (g) $0 - 7\%\varepsilon_1$ Figure D.2: *PVC grains with a PVC pipe, displacement fields*



(h) 0 – 8% ϵ_1



(i) 0 – 9% ϵ_1



(j) 0 – 10% ϵ_1

Figure D.2: PVC grains with a PVC pipe, displacement fields

D.2 Mean Displacement Field Subtracted from Displacement Field

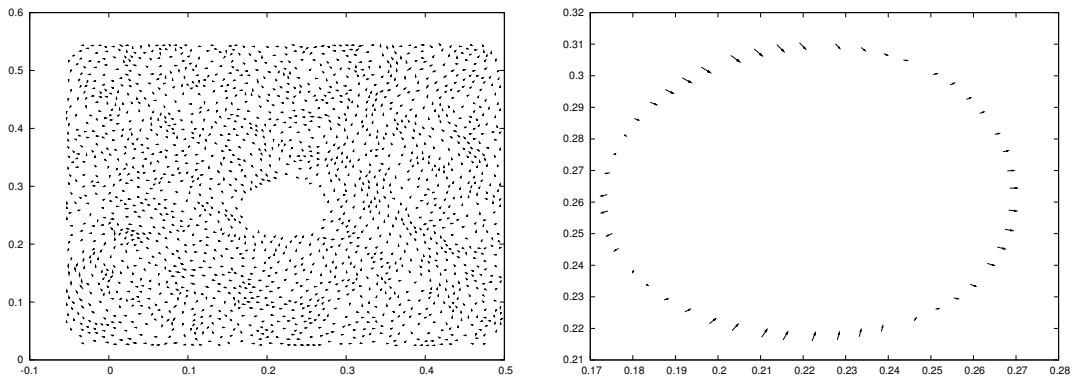
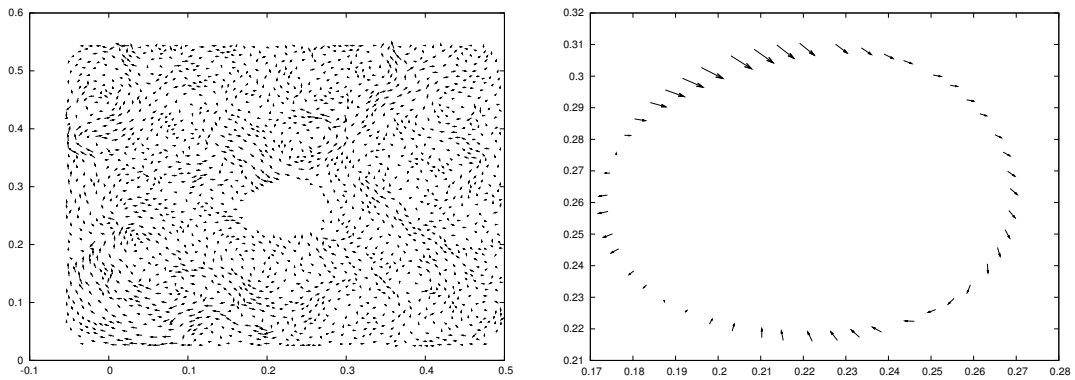
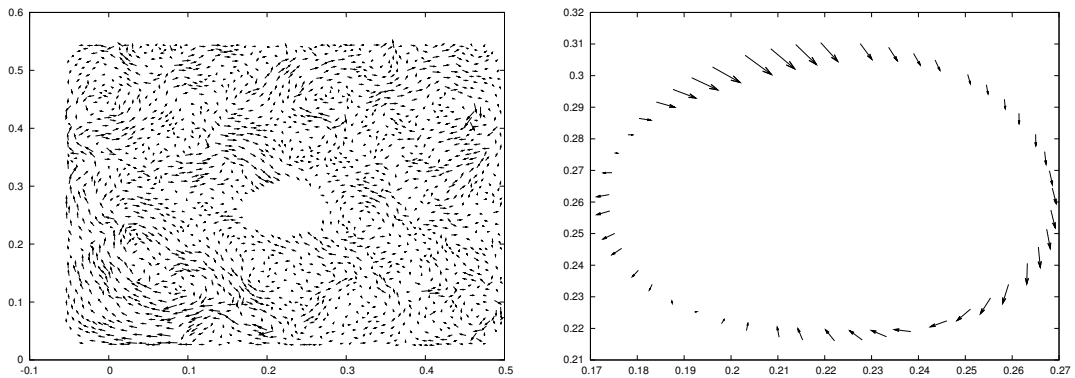
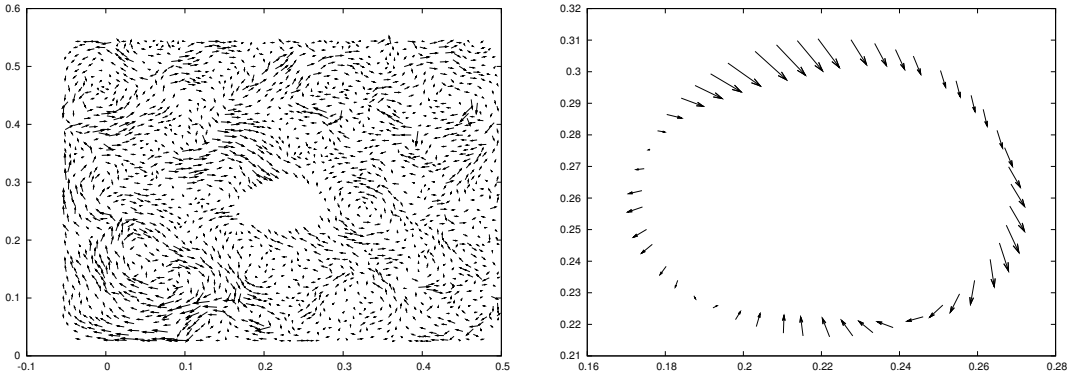
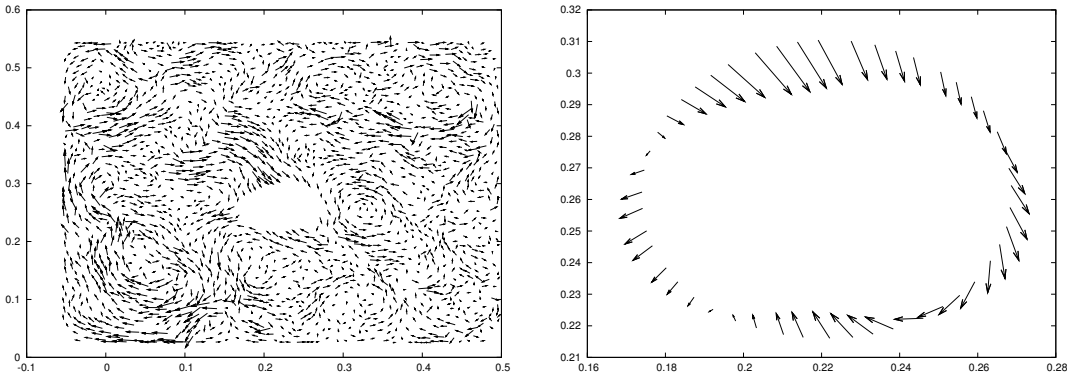
(a) $0 - 1\% \varepsilon_1$ (b) $0 - 2\% \varepsilon_1$ (c) $0 - 3\% \varepsilon_1$

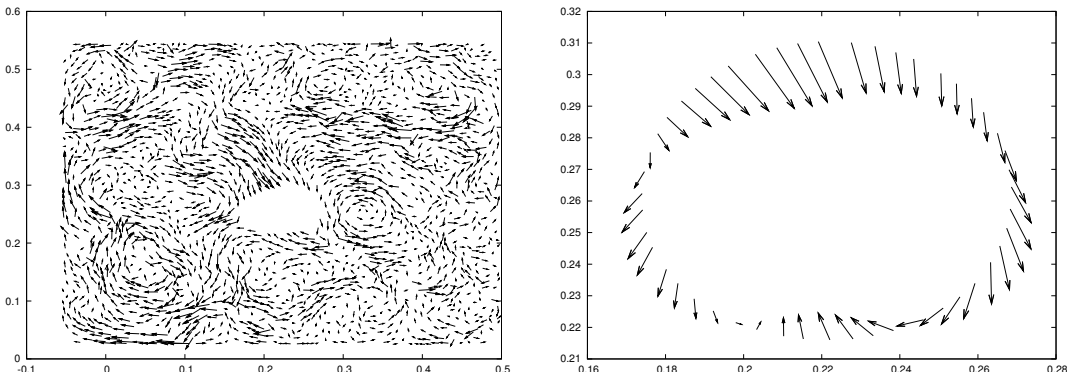
Figure D.3: Wooden grains with a PVC pipe, mean field of displacement subtracted from the displacement field. The longest arrow of displacement in the figures correspond to 4cm



(d) $0 - 4\% \epsilon_1$



(e) $0 - 5\% \epsilon_1$



(f) $0 - 6\% \epsilon_1$

Figure D.3: Wooden grains with a PVC pipe, mean field of displacement subtracted from the displacement field

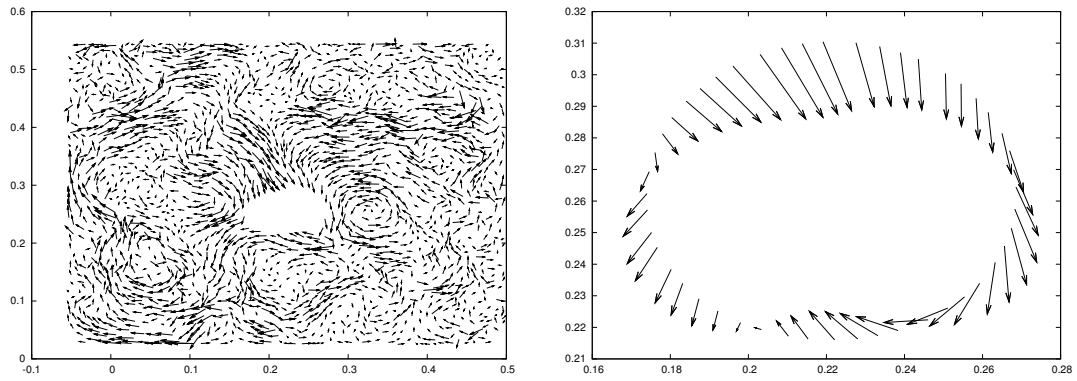
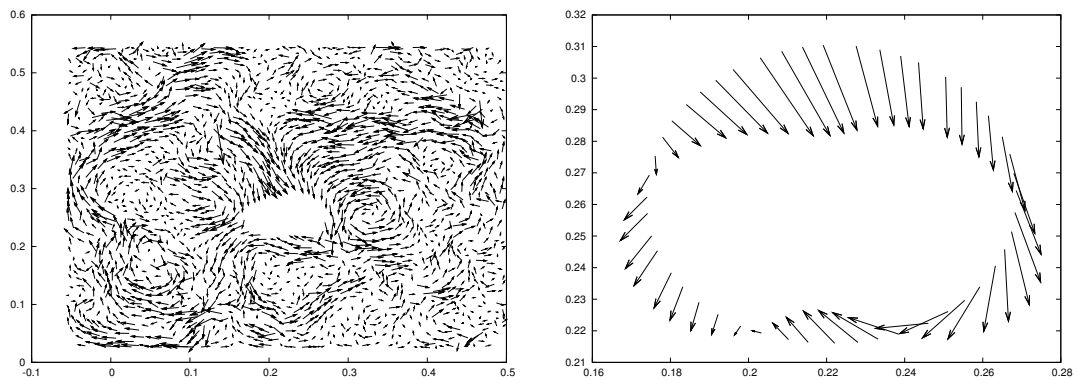
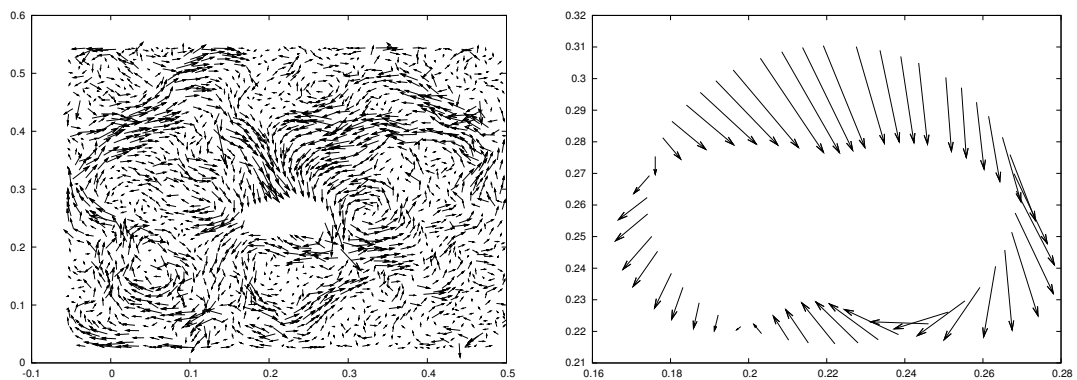
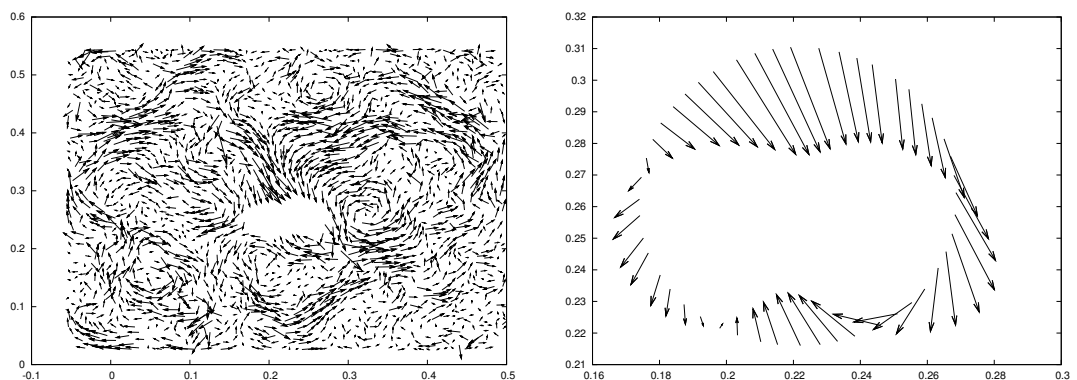
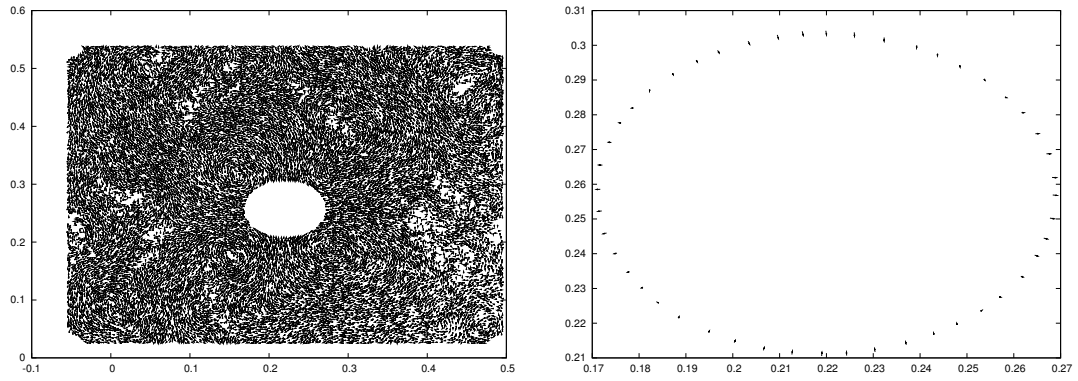
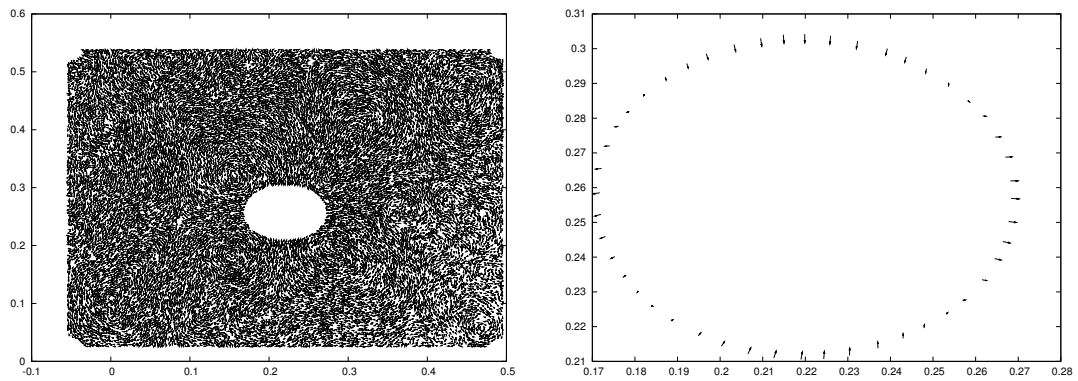
(g) $0 - 7\%\varepsilon_1$ (h) $0 - 8\%\varepsilon_1$ (i) $0 - 9\%\varepsilon_1$ (j) $0 - 10\%\varepsilon_1$

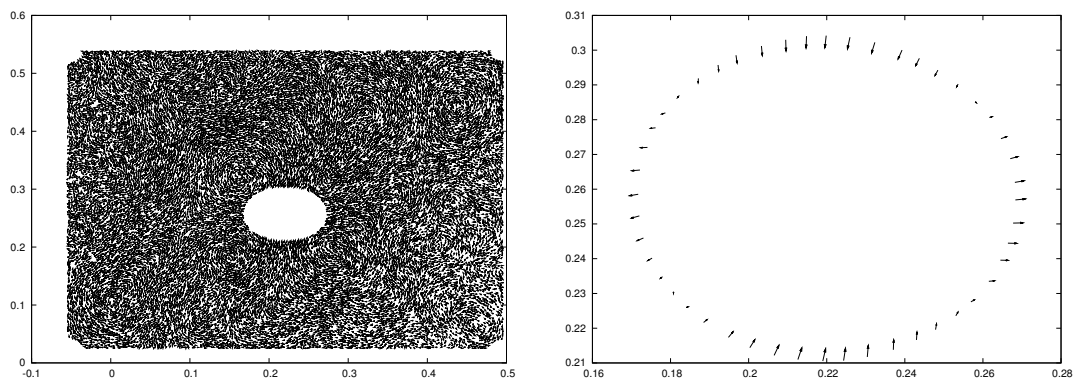
Figure D.3: Wooden grains with a PVC pipe, mean field of displacement subtracted from the displacement field



(a) $0 - 1\% \varepsilon_1$



(b) $0 - 2\% \varepsilon_1$



(c) $0 - 3\% \varepsilon_1$

Figure D.4: PVC grains with a PVC pipe, mean field of displacement subtracted from the displacement field. The longest arrow of displacement in the figures correspond to 1cm

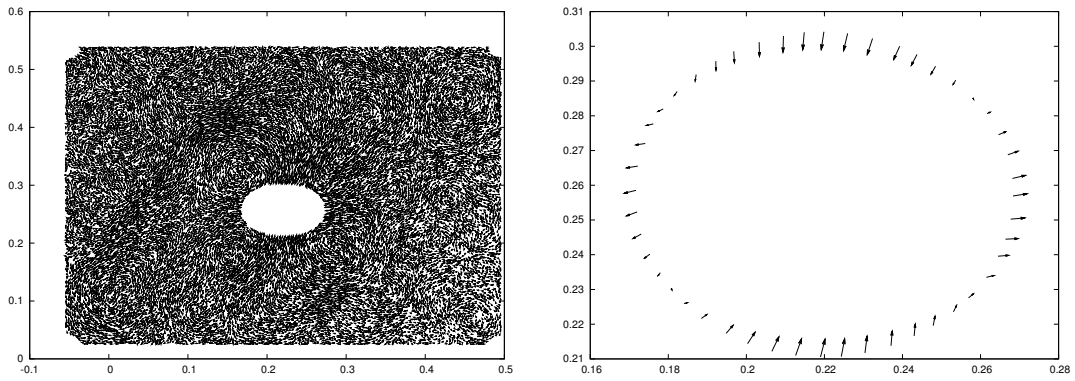
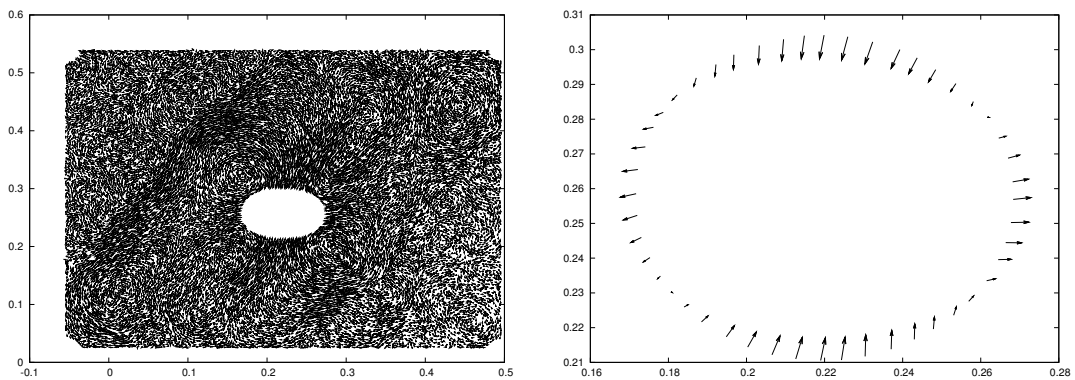
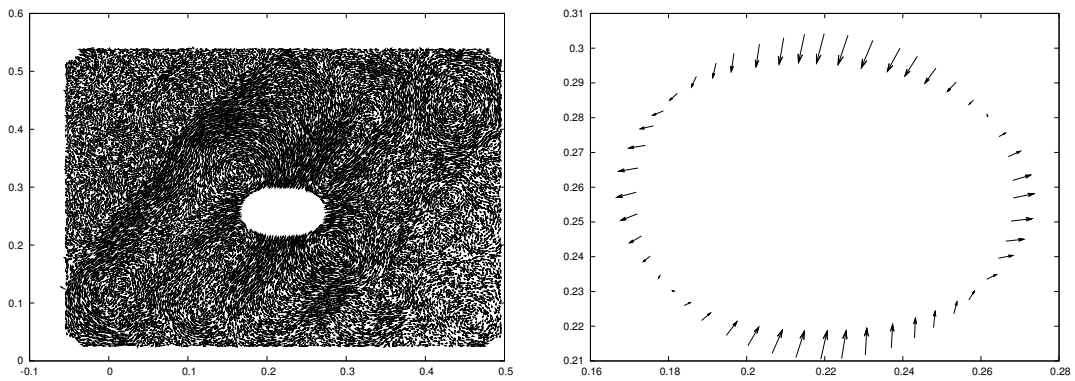
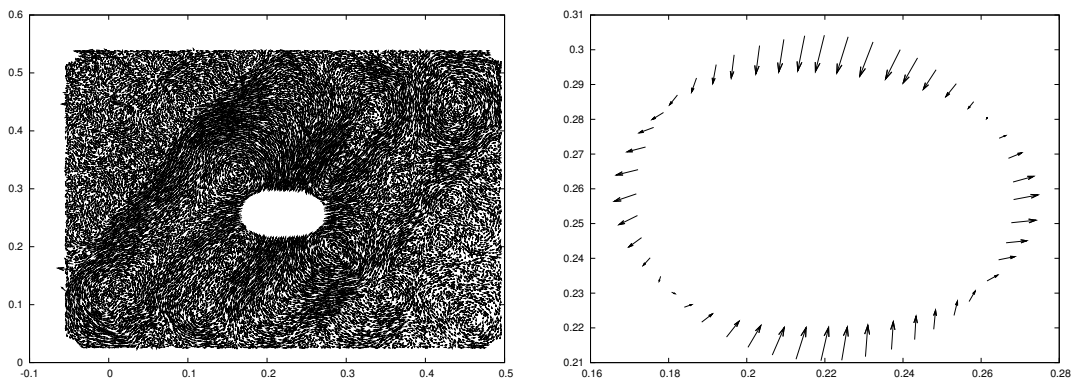
(d) $0 - 4\%\varepsilon_1$ (e) $0 - 5\%\varepsilon_1$ (f) $0 - 6\%\varepsilon_1$ (g) $0 - 7\%\varepsilon_1$

Figure D.4: PVC grains with a PVC pipe, mean field of displacement subtracted from the displacement field

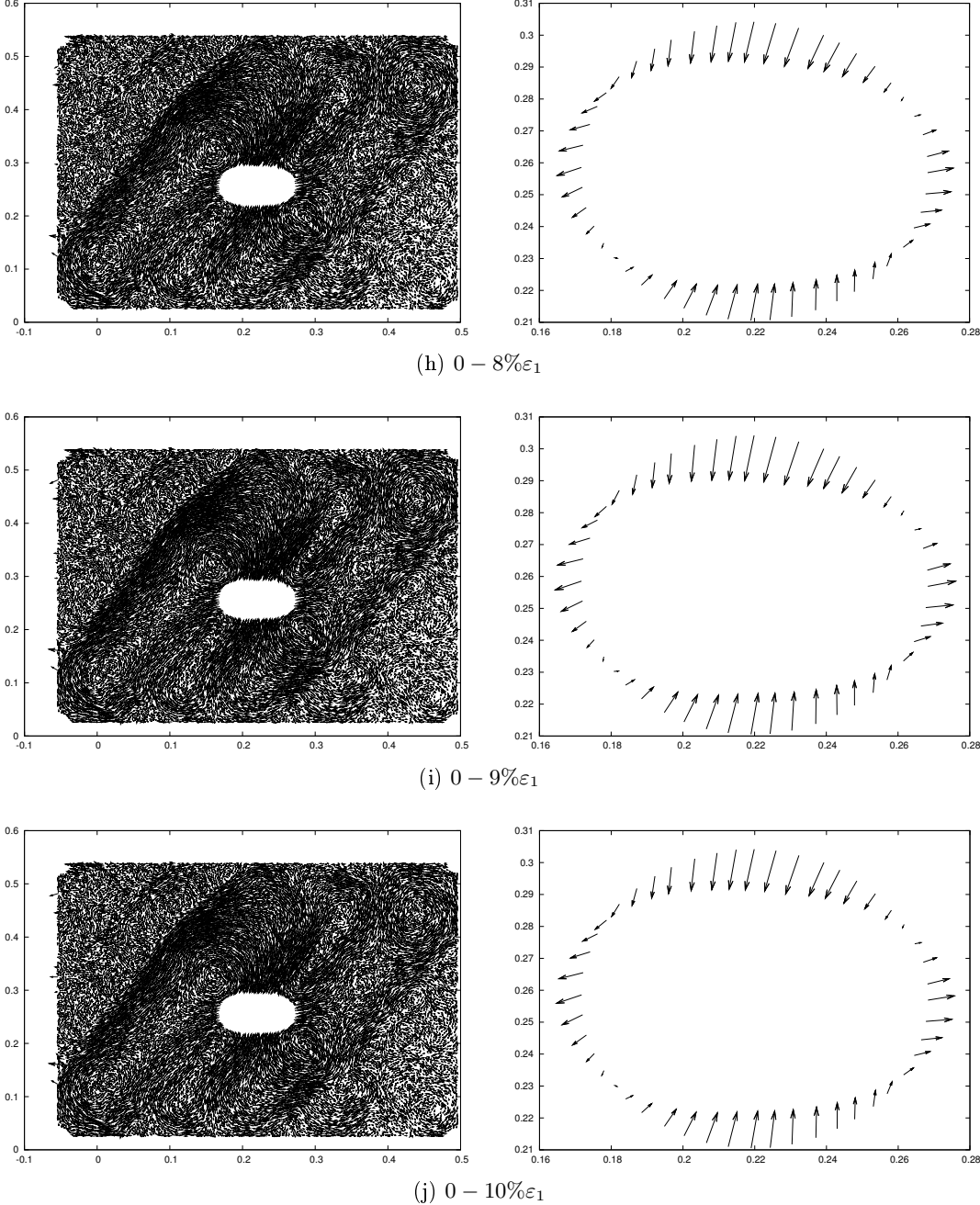


Figure D.4: PVC grains with a PVC pipe, mean field of displacement subtracted from the displacement field

D.3 Strain Localisation

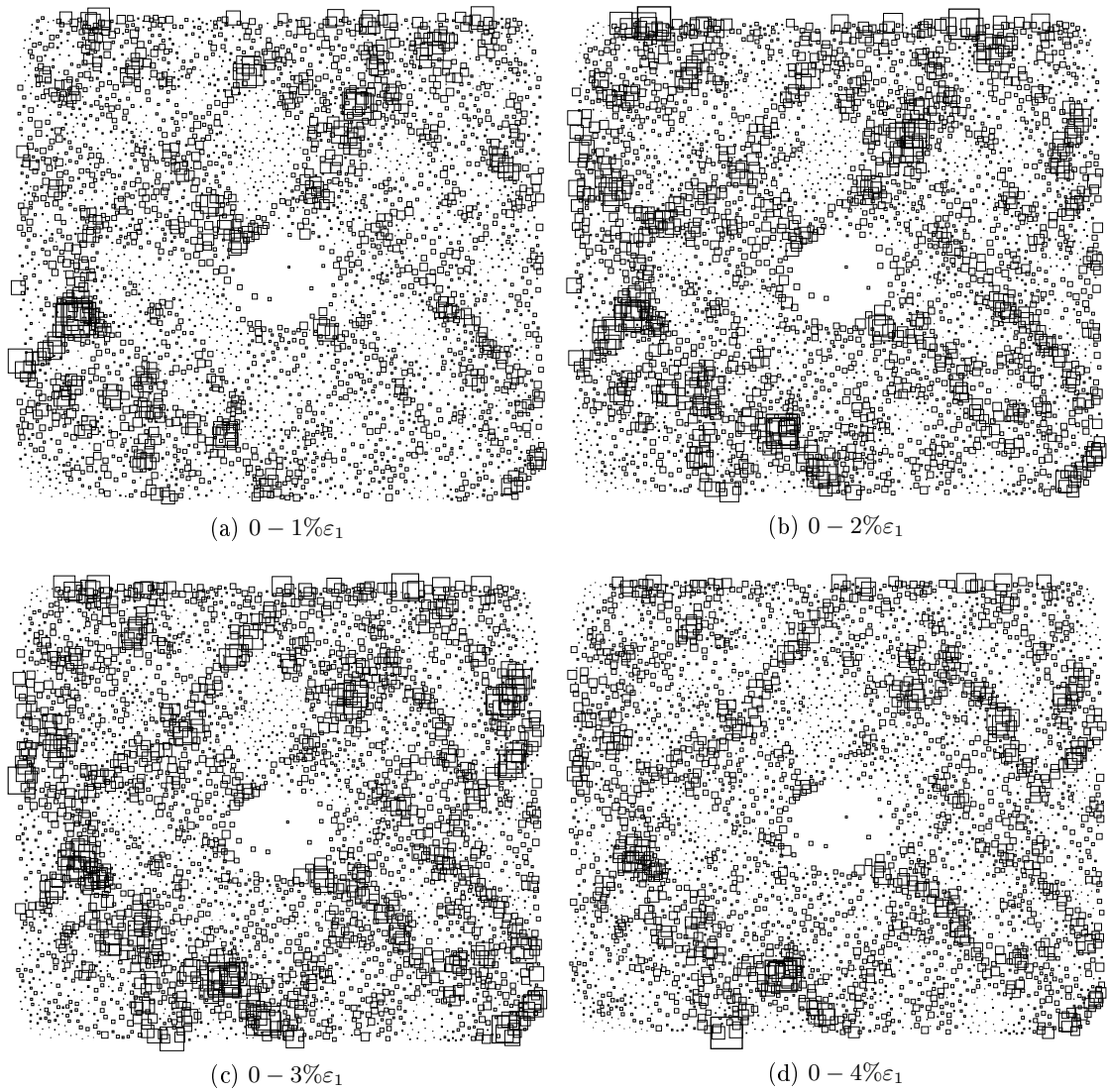


Figure D.5: Wooden grains with a PVC pipe, shear localisation. For the maximum strain the biggest symbol correspond to 300 units while the mean is equal to 35

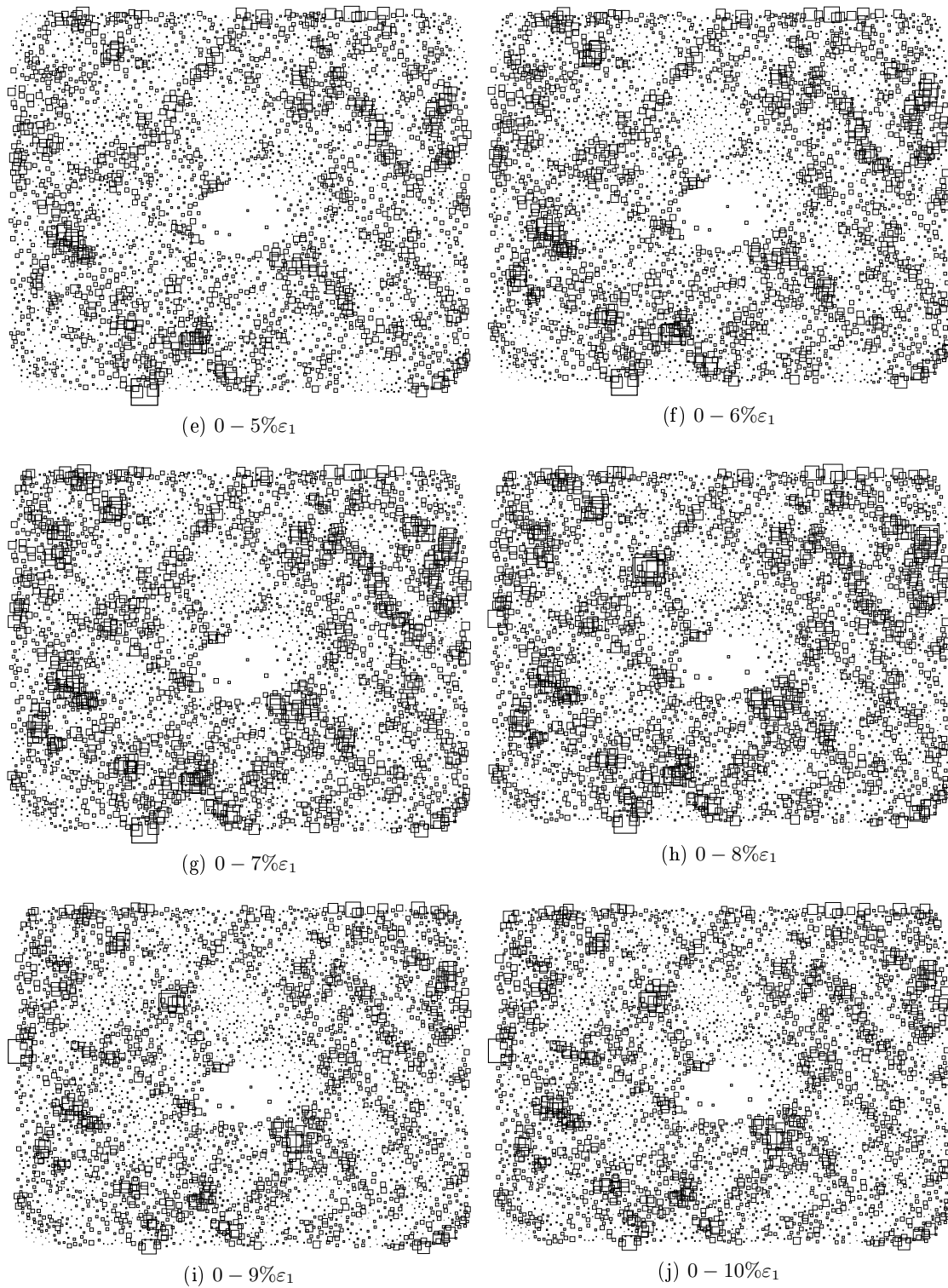


Figure D.5: *Wooden grains with a PVC pipe, shear localisation*

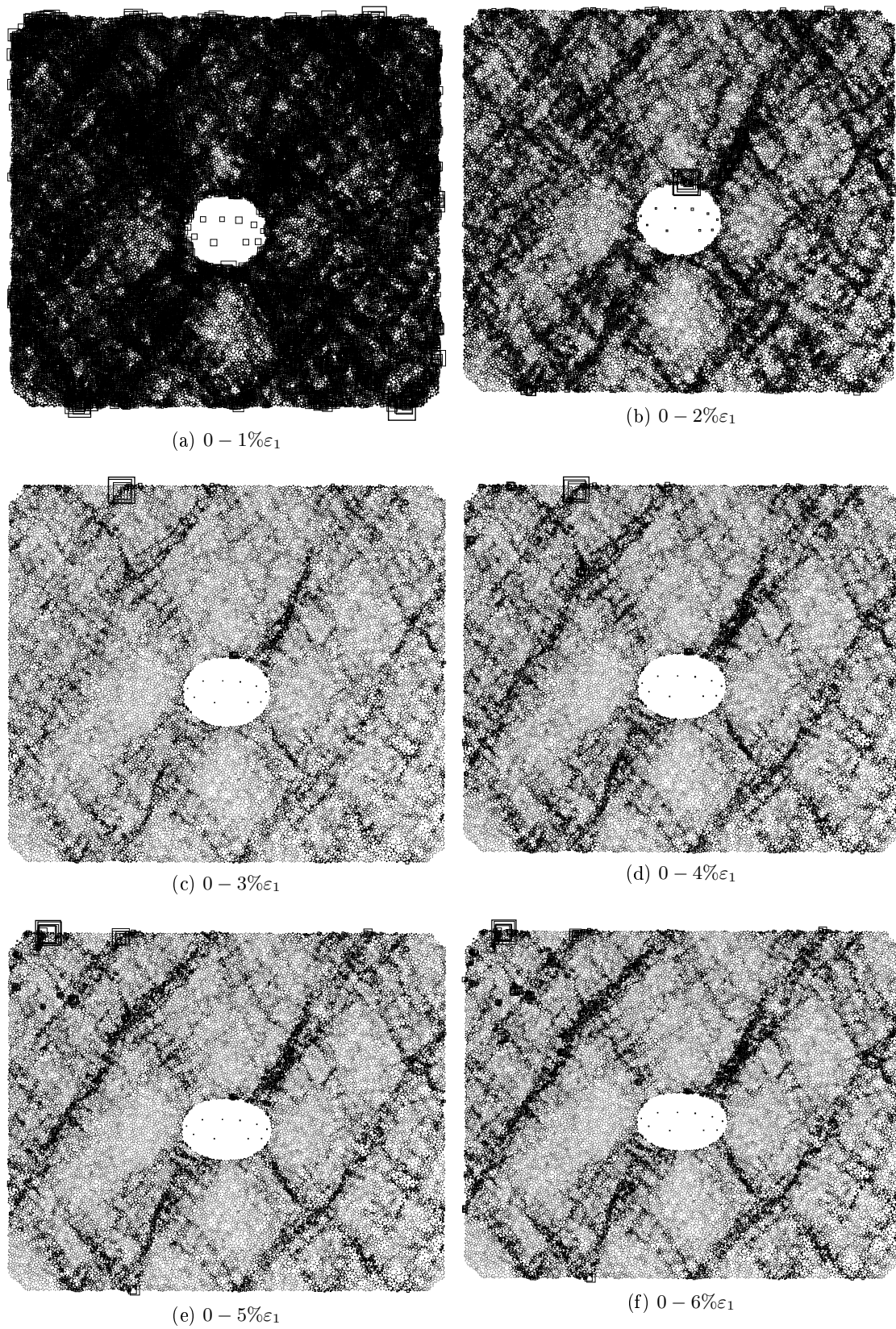


Figure D.6: PVC grains with a PVC pipe, shear localisation. For the maximum strain the biggest symbol correspond to 2500 units while the mean is equal to 32

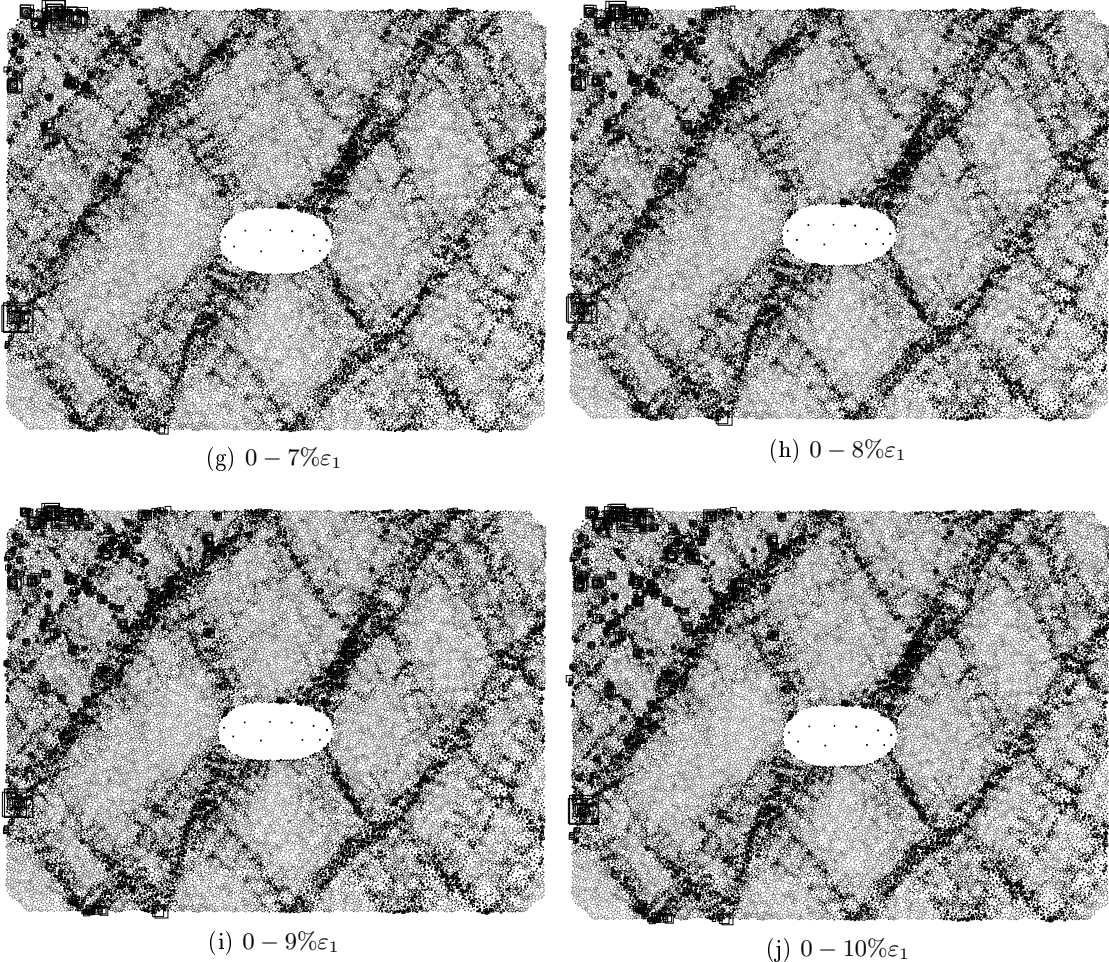
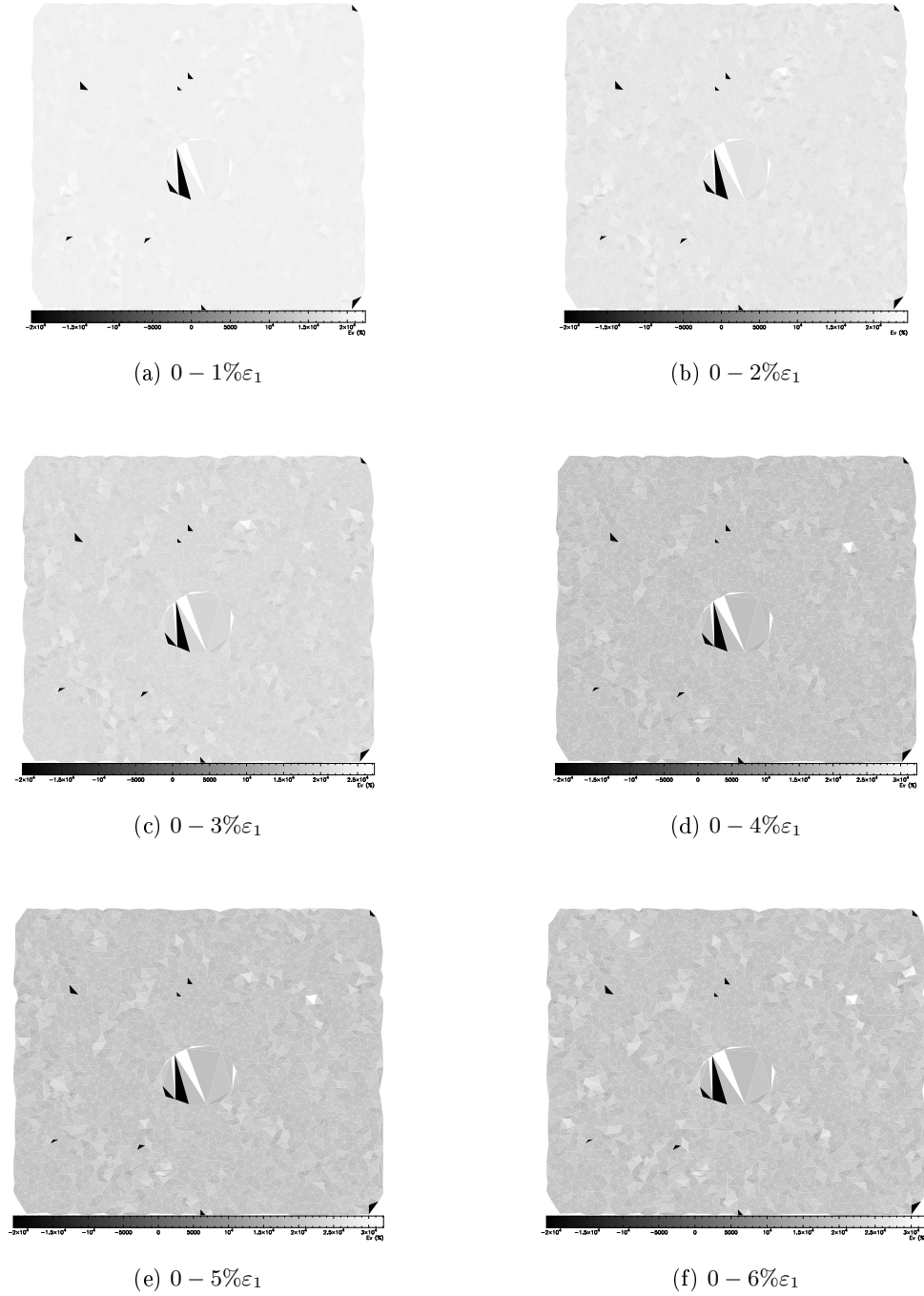
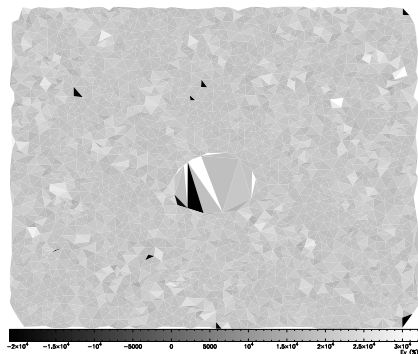


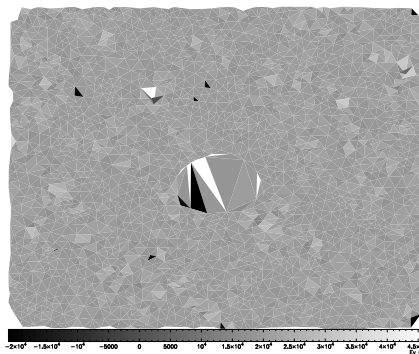
Figure D.6: *PVC grains with a PVC pipe, shear localisation*

D.4 Volumetric Strains

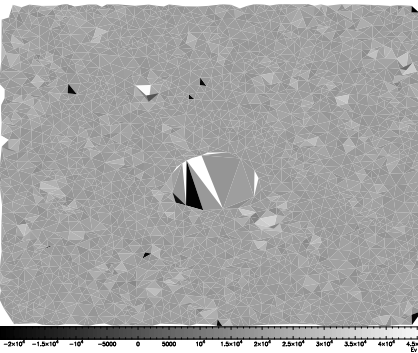
Figure D.7: *Wooden grains with a PVC pipe, volumetric strain*



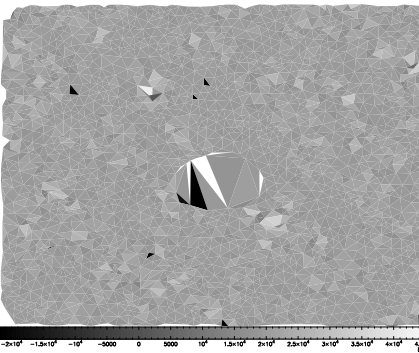
(g) $0 - 7\% \epsilon_1$



(h) $0 - 8\% \epsilon_1$

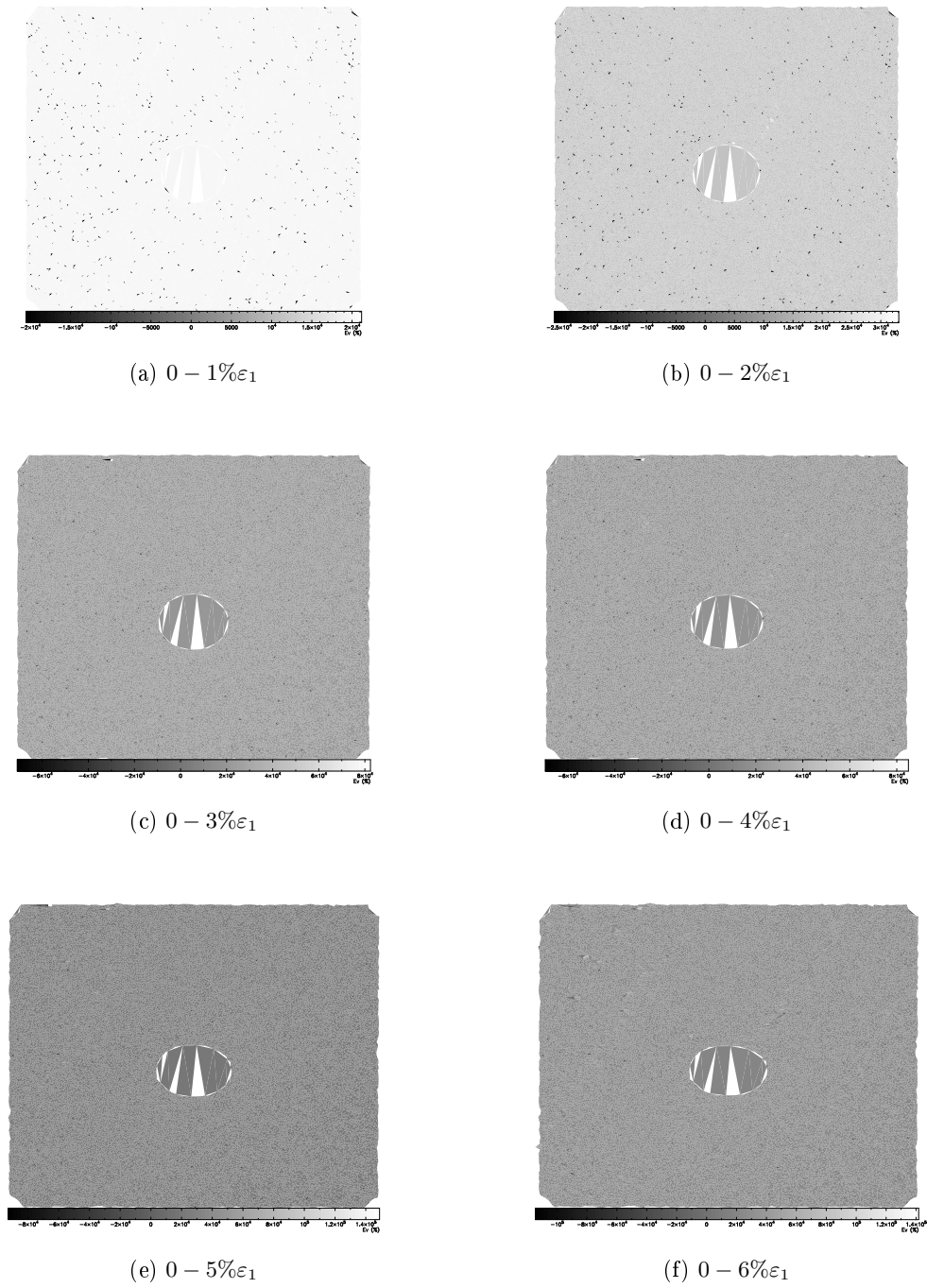


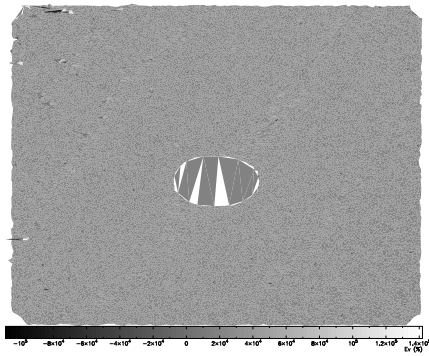
(i) $0 - 9\% \epsilon_1$



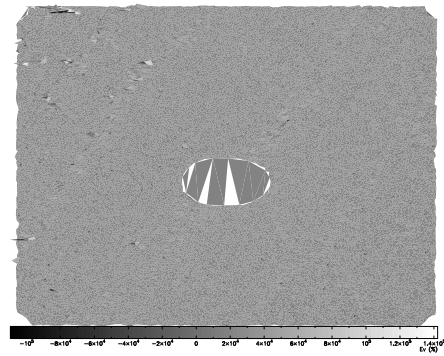
(j) $0 - 10\% \epsilon_1$

Figure D.7: *Wooden grains with a PVC pipe, volumetric strain*

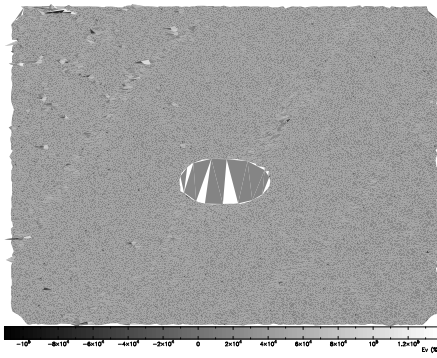
Figure D.8: *PVC grains with a PVC pipe, volumetric strain*



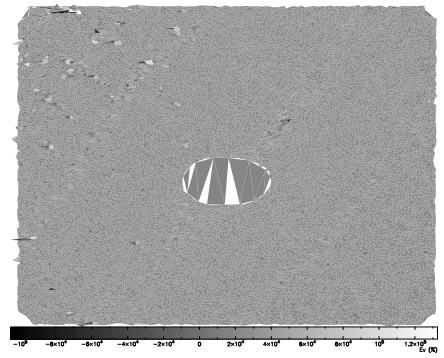
(g) $0 - 7\% \varepsilon_1$



(h) $0 - 8\% \varepsilon_1$



(i) $0 - 9\% \varepsilon_1$



(j) $0 - 10\% \varepsilon_1$

Figure D.8: *PVC grains with a PVC pipe, volumetric strain*

D.5 Horizontal and Vertical Strains

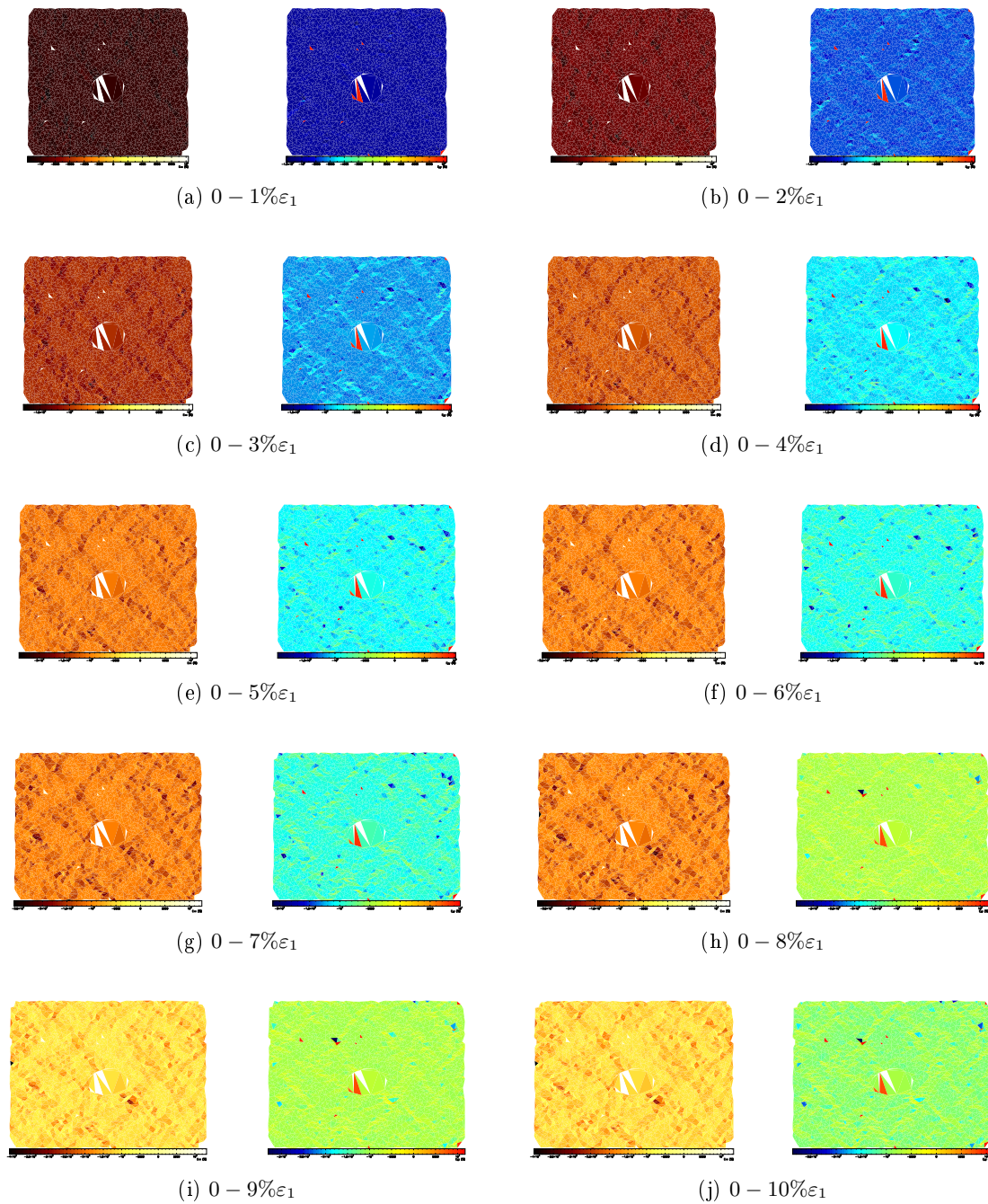


Figure D.9: Wooden grains with a PVC pipe, horizontal (left) and vertical (right) strains

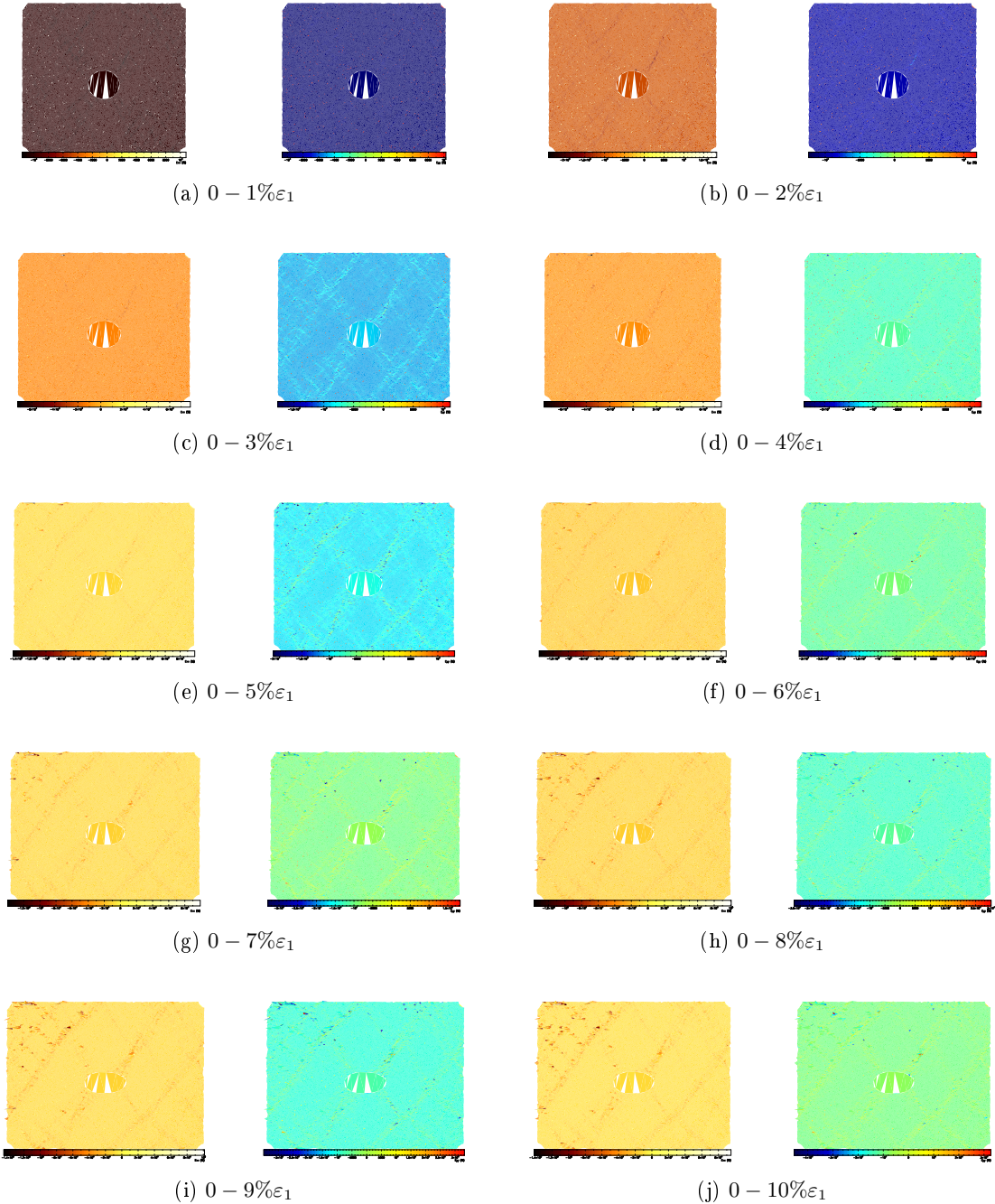


Figure D.10: PVC grains with a PVC pipe, horizontal (left) and vertical (right) strains

D.6 PVC Pipe Unloading after Biax-4-PVC-Pipe Test

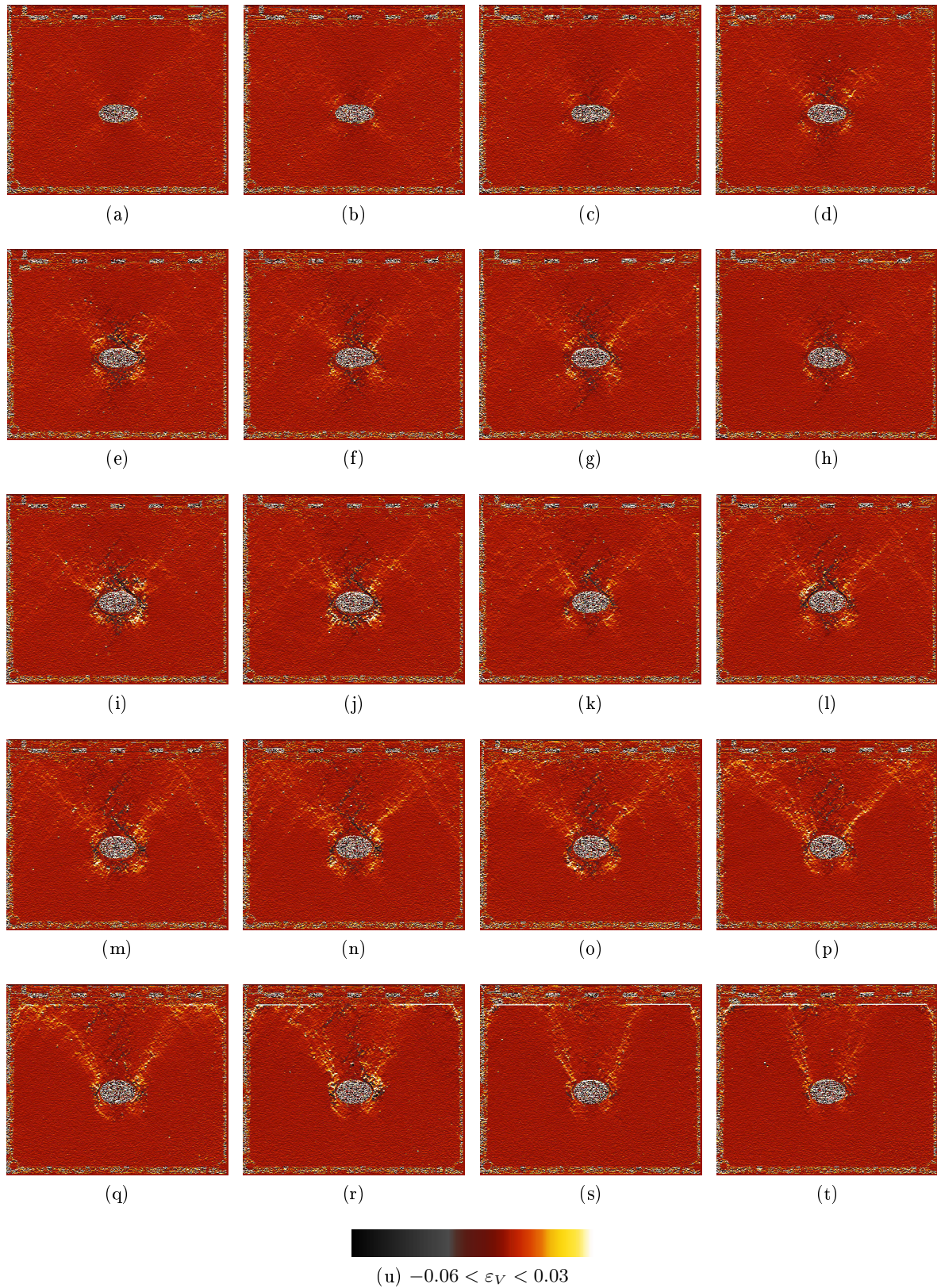


Figure D.11: “Oedometric” unloading of PVC pipe and PVC grain assembly from isotropic state $\sigma_0 = 50kPa$ to $\sigma_1 = 0kPa$. DIC analysis revealed interesting pattern of ε_V

Appendix E

DEM Pipe in Soil Simulation Results

E.1 Displacement Fields

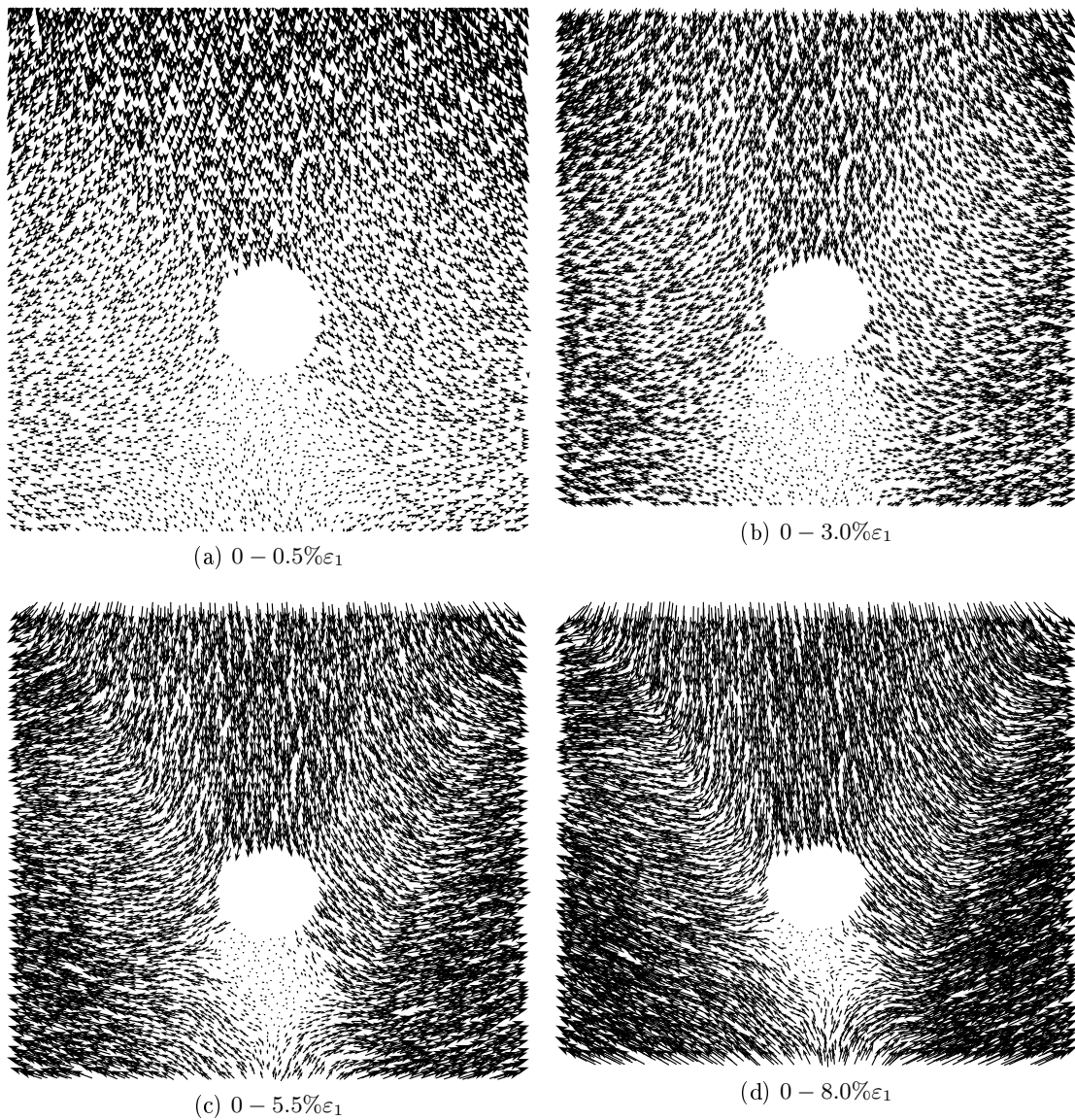


Figure E.1: Simulation of clumps $\alpha = 0.5$ with friction at the pipe boundary. Displacement fields

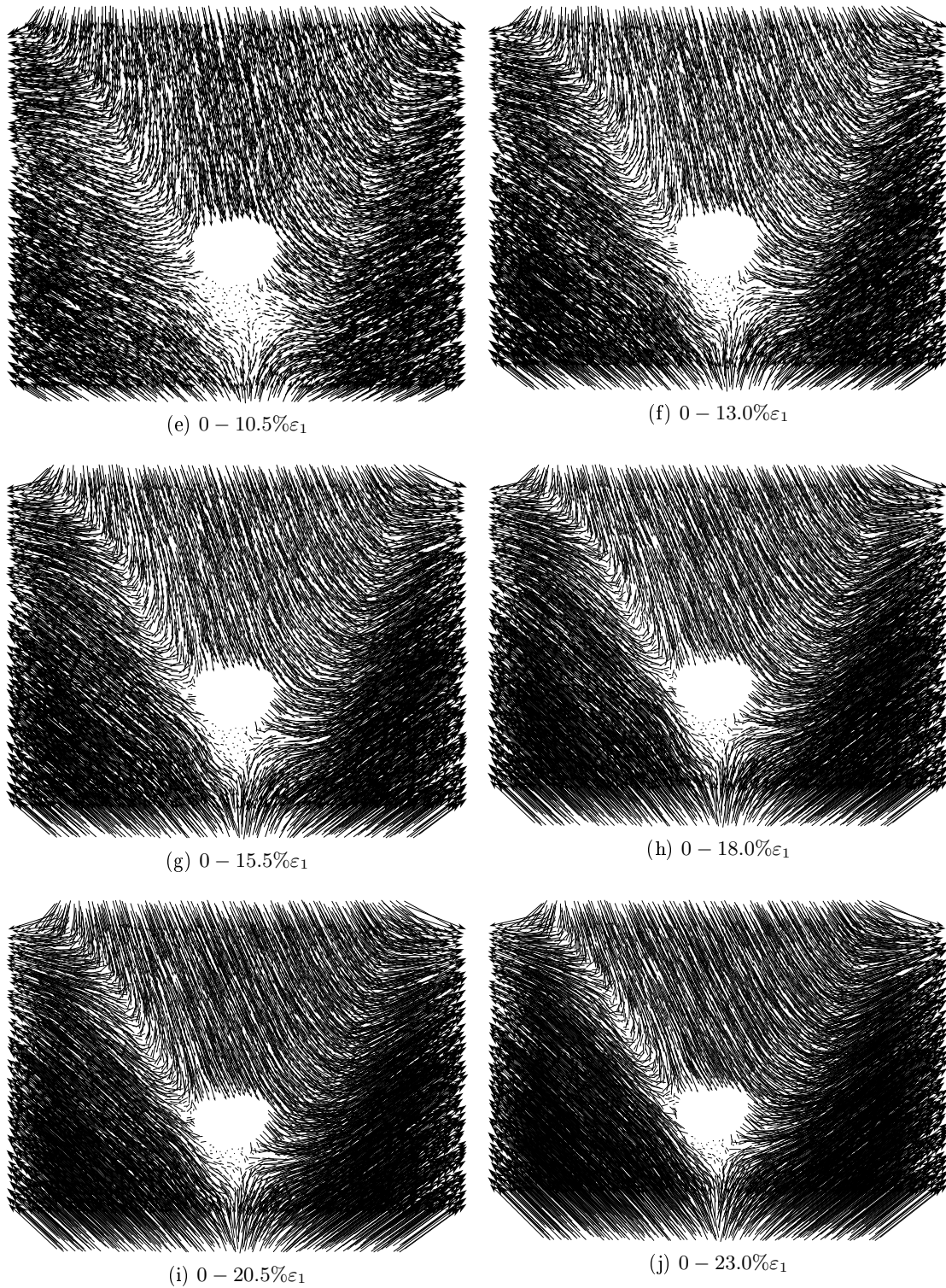


Figure E.1: *Displacement fields. Clumps $\alpha = 0.5$ with friction at the pipe boundary*

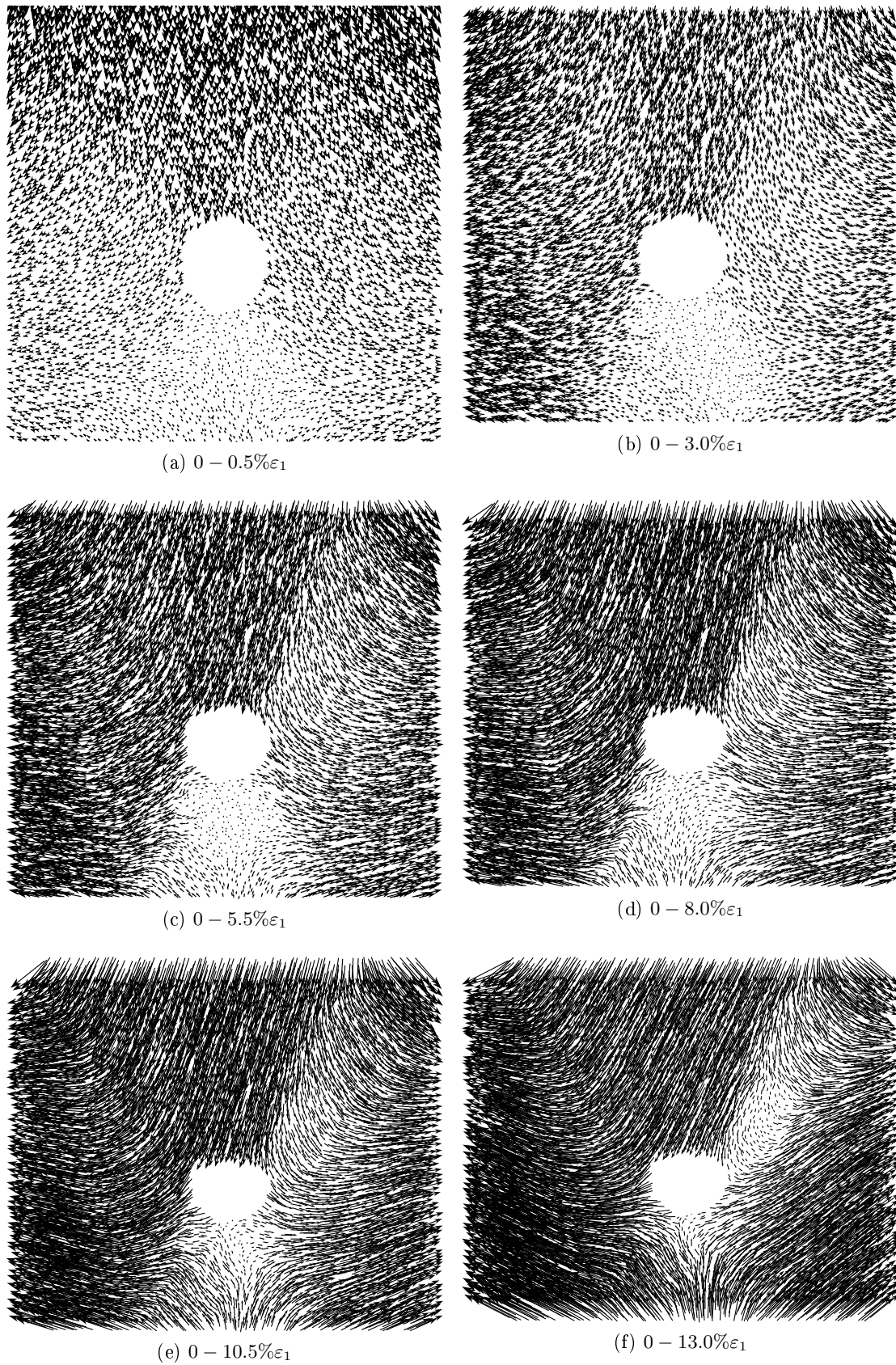


Figure E.2: Simulation of clumps $\alpha = 0.5$ without friction at the pipe boundary. Displacement fields

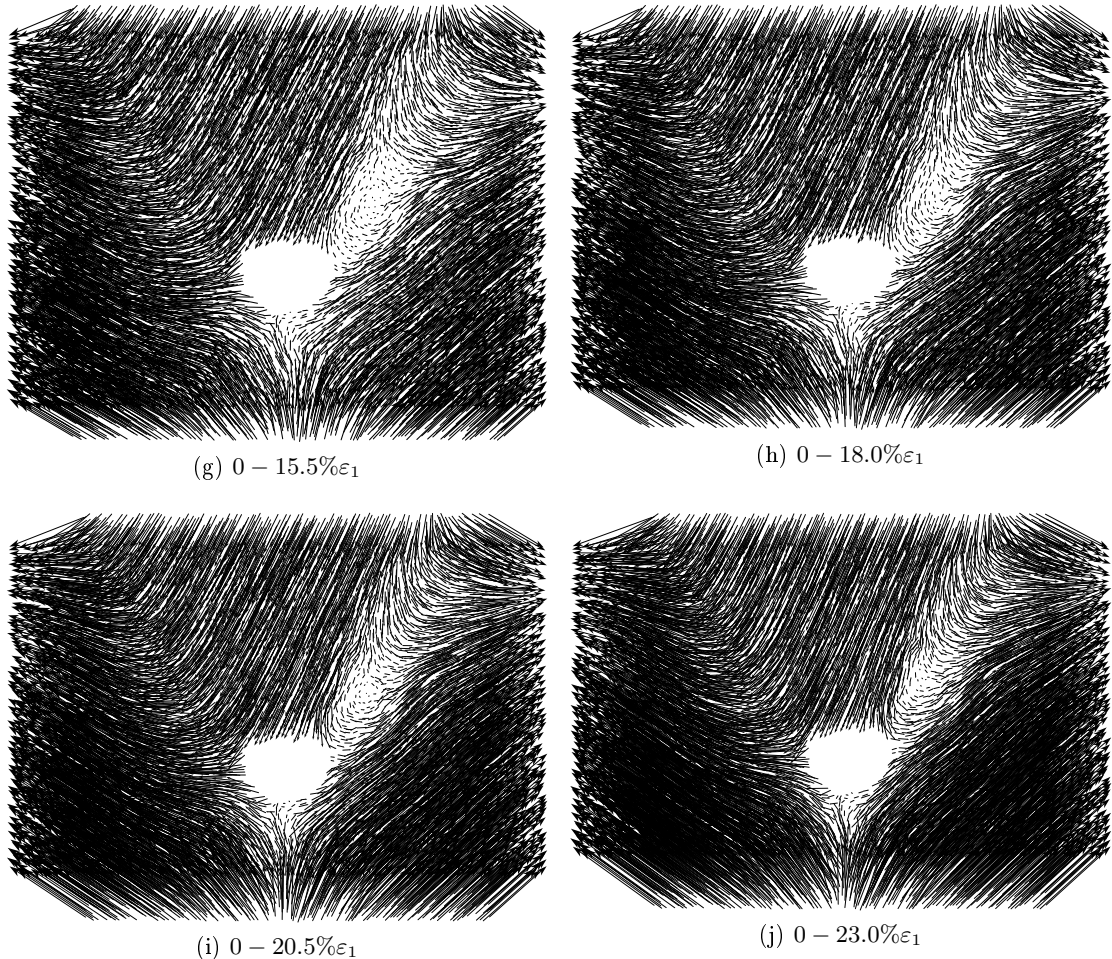


Figure E.2: Displacement fields. Clumps $\alpha = 0.5$ without friction at the pipe boundary

E.2 Mean Displacement Field Subtracted from Displacement Field

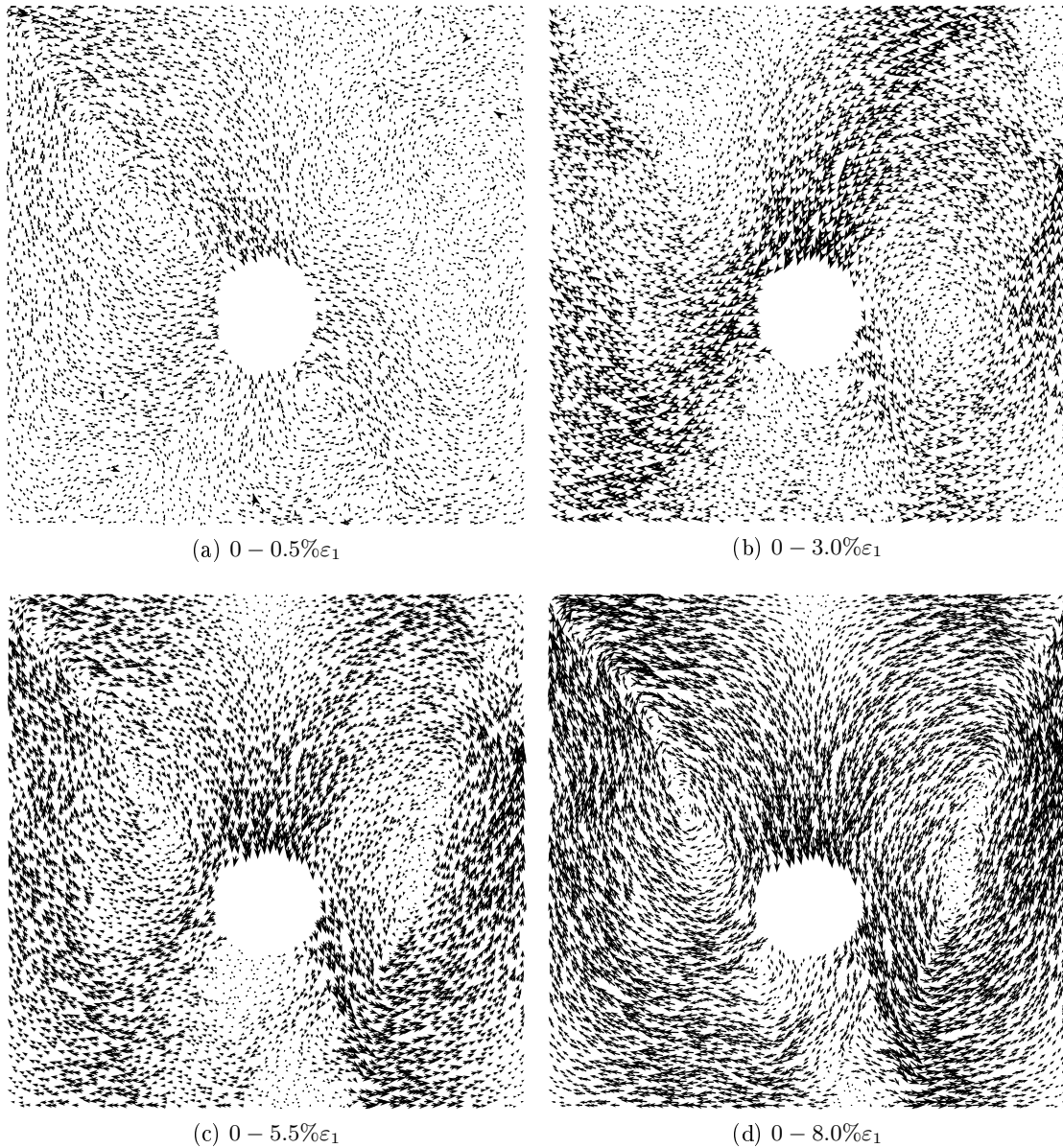


Figure E.3: Simulation of clumps $\alpha = 0.5$ with friction at the pipe boundary. Displacement fields reduced by mean field of displacement

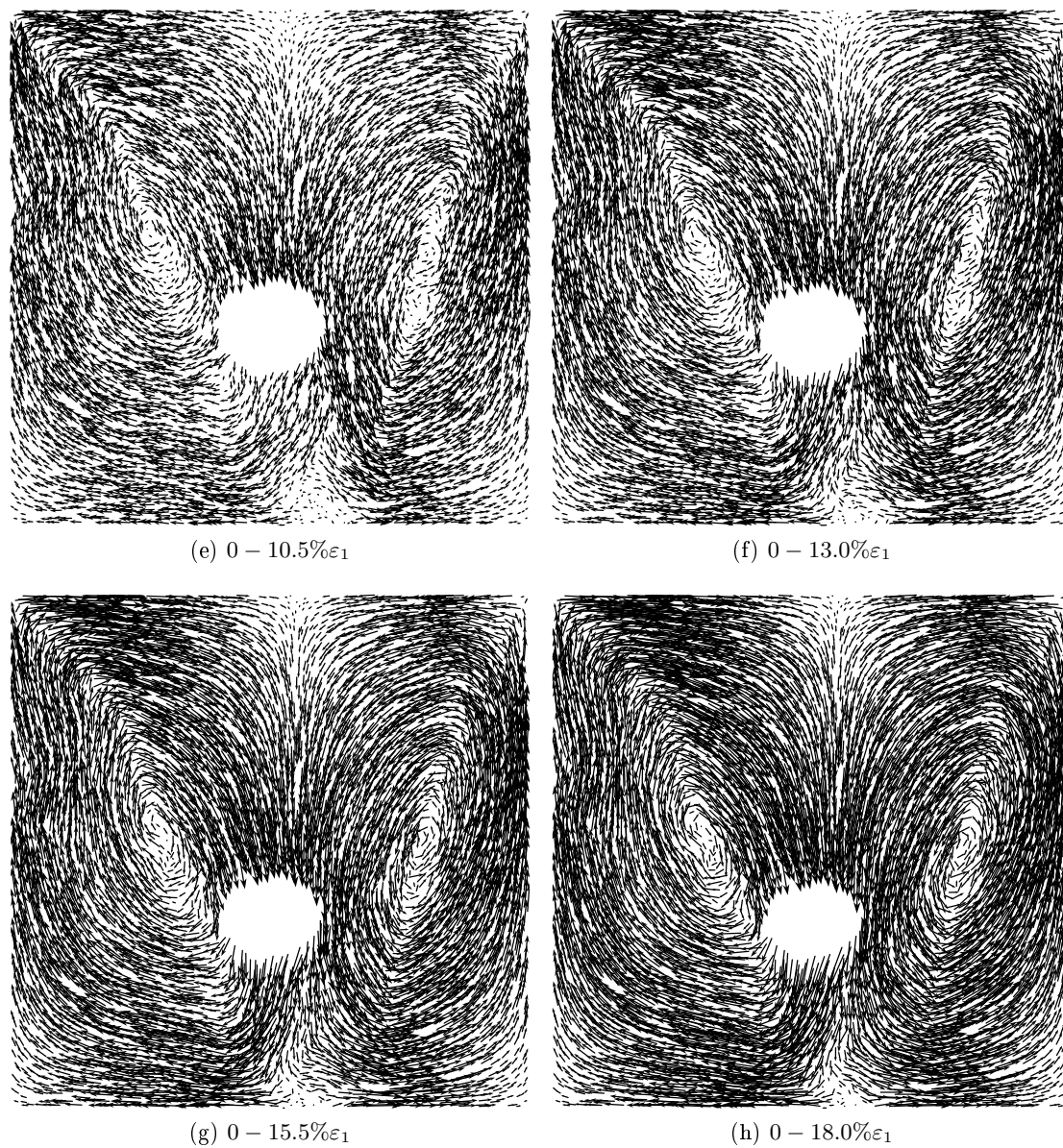


Figure E.3: Displacement fields reduced by mean field of displacement. Clumps $\alpha = 0.5$ with friction at the pipe boundary

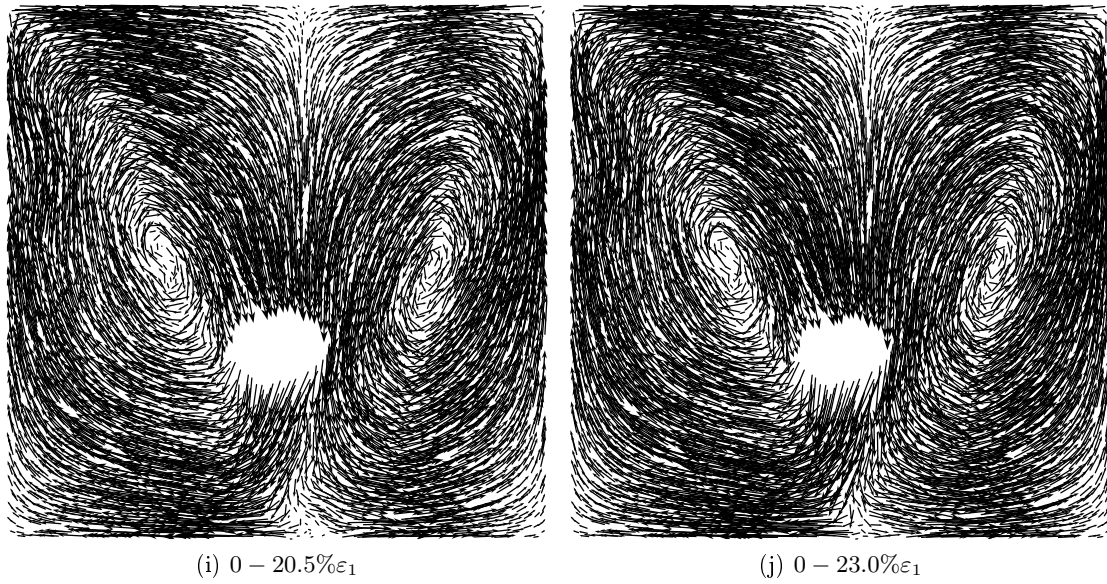


Figure E.3: Displacement fields reduced by mean field of displacement. Clumps $\alpha = 0.5$ with friction at the pipe boundary

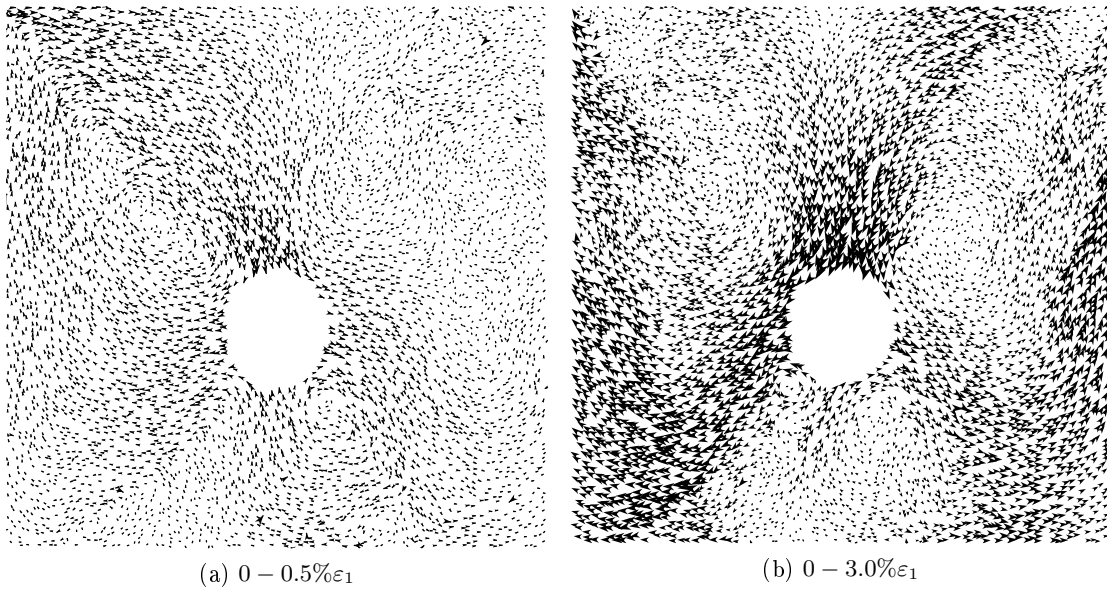


Figure E.4: Simulation of clumps $\alpha = 0.5$ without friction at the pipe boundary. Displacement fields reduced by mean field of displacement

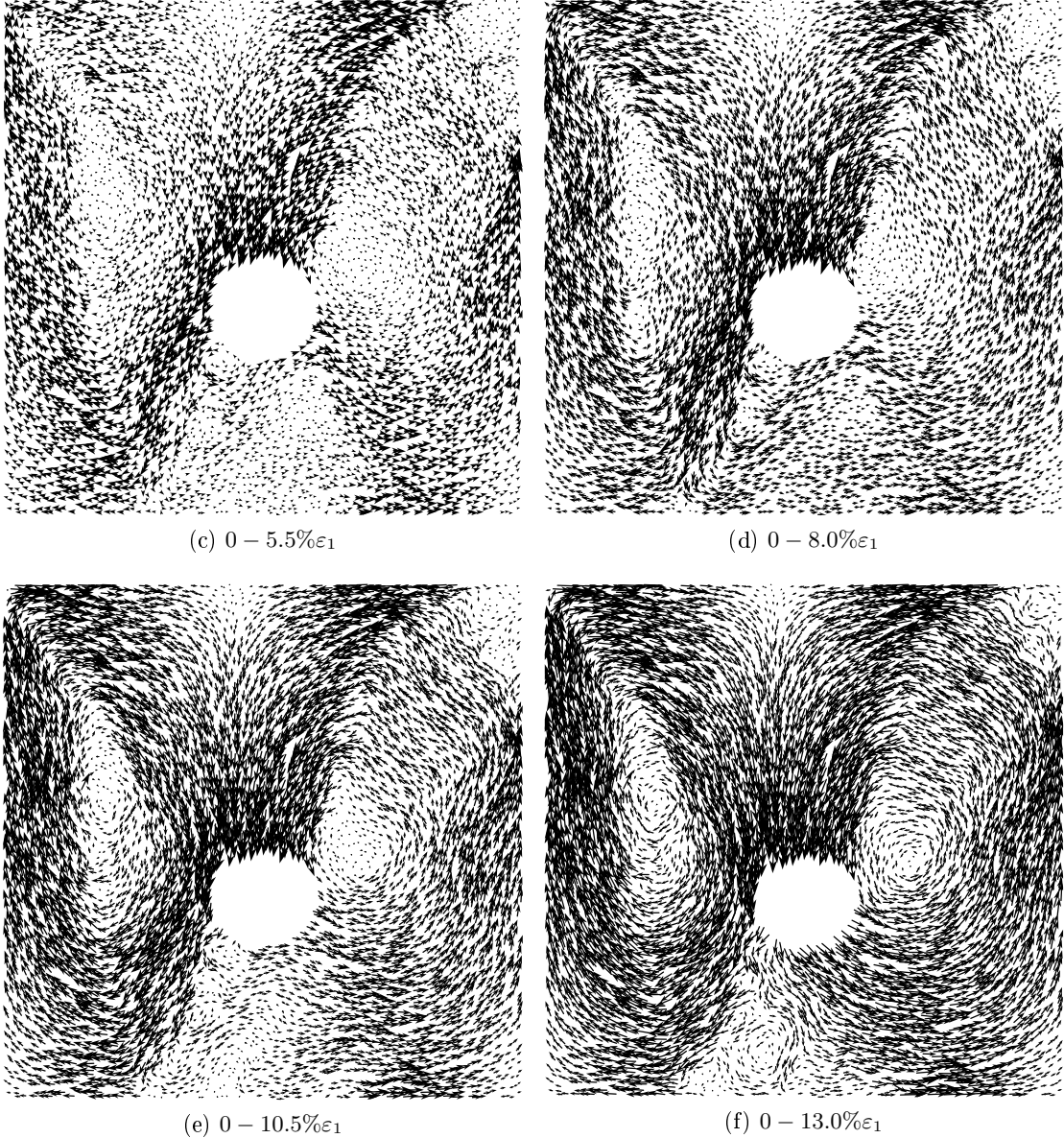


Figure E.4: Displacement fields reduced by mean field of displacement. Clumps $\alpha = 0.5$ without friction at the pipe boundary

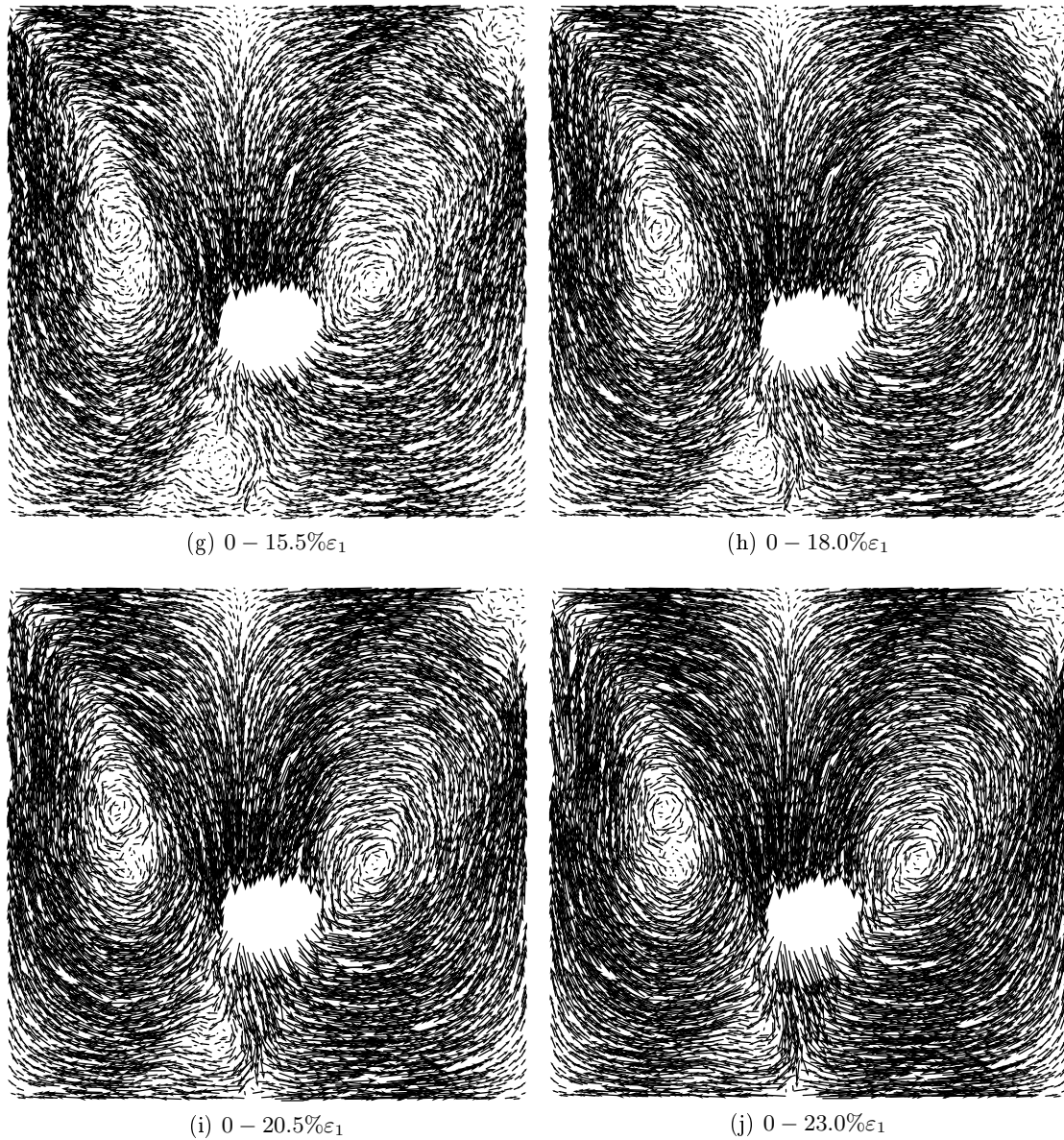


Figure E.4: Displacement fields reduced by mean field of displacement. Clumps $\alpha = 0.5$ without friction at the pipe boundary

E.3 Strain Localisation

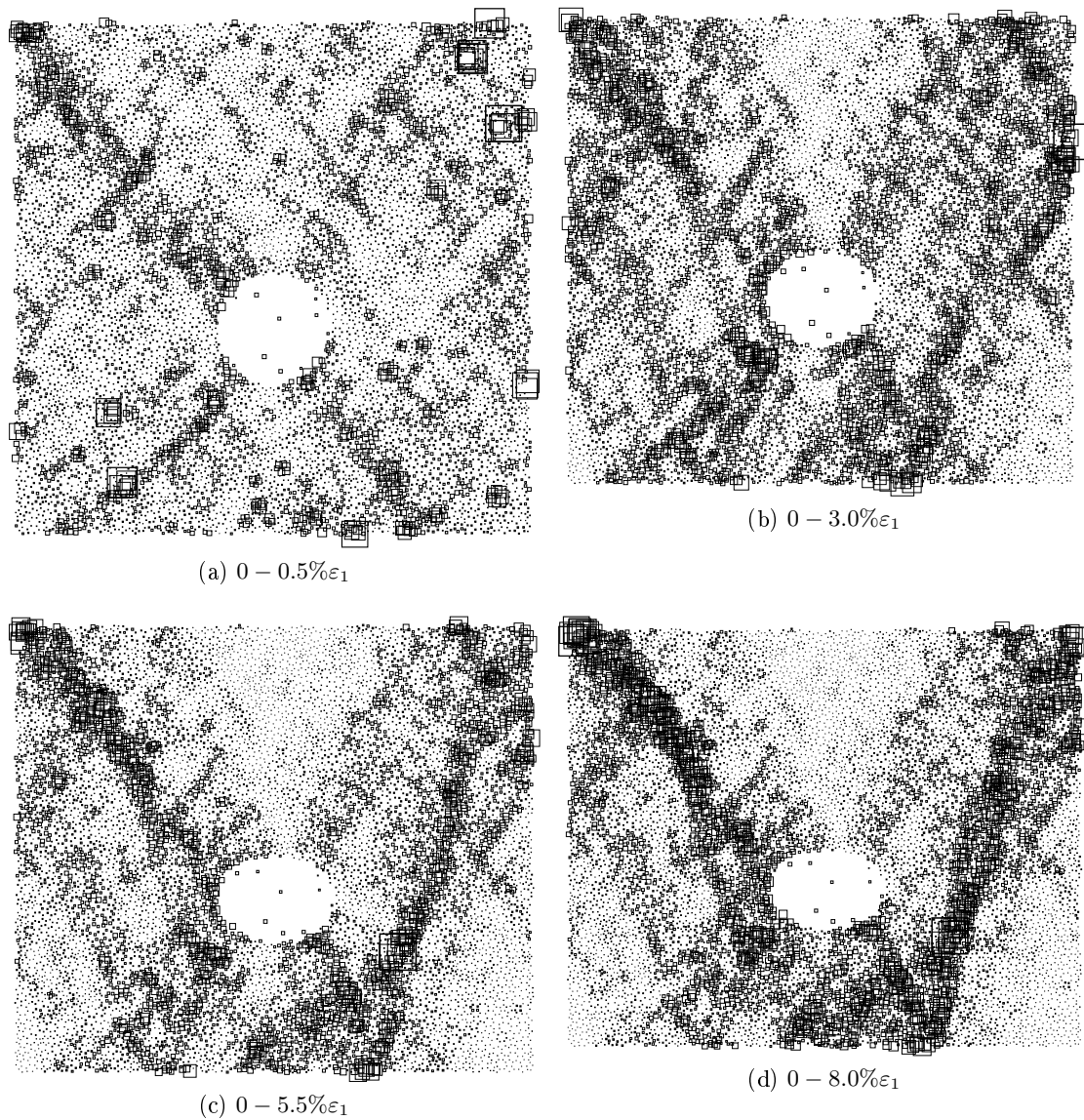


Figure E.5: Simulation of clumps $\alpha = 0.5$ with friction at the pipe boundary. Shear localisation maps

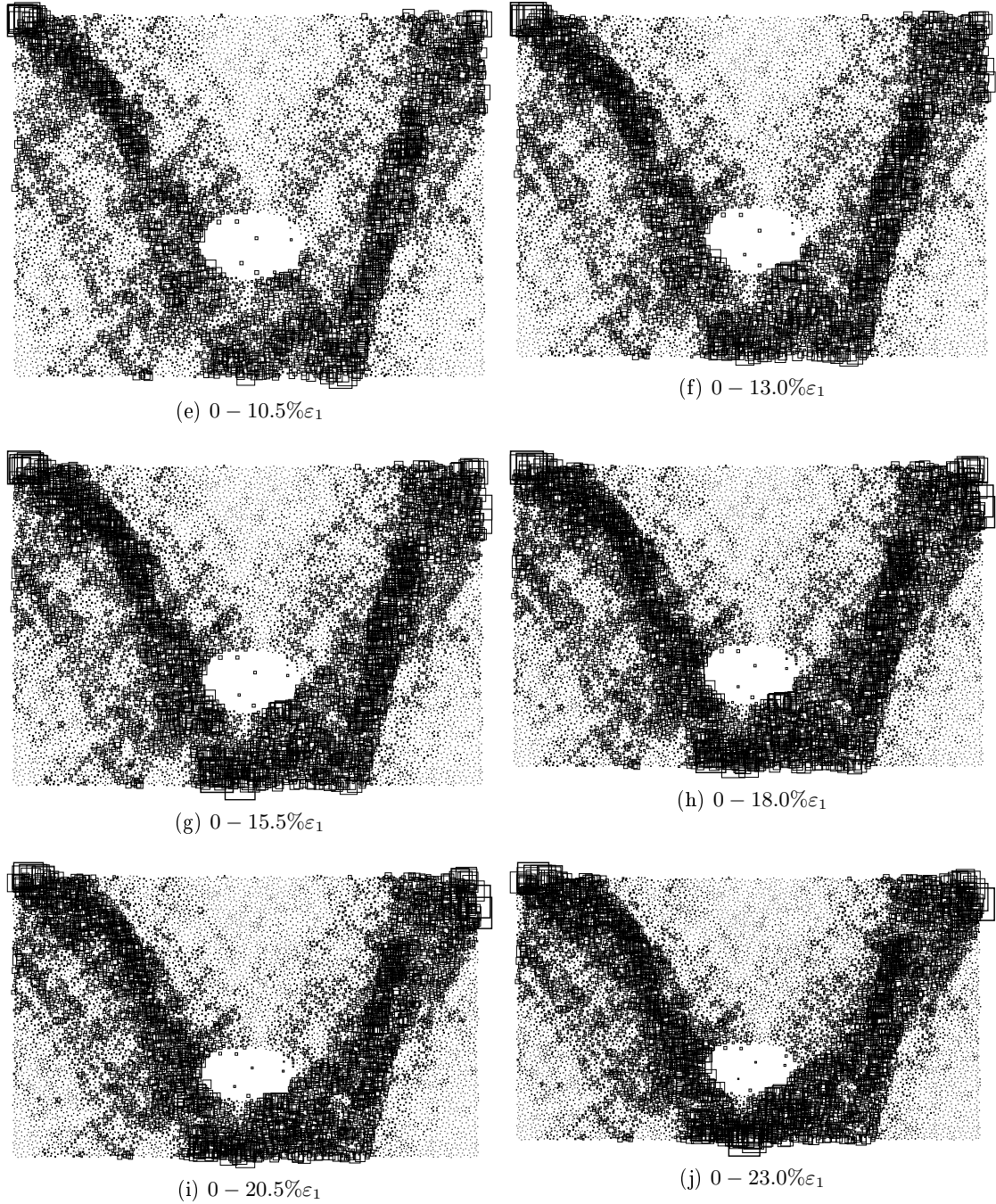


Figure E.5: *Shear localisation maps. Clumps $\alpha = 0.5$ with friction at the pipe boundary*

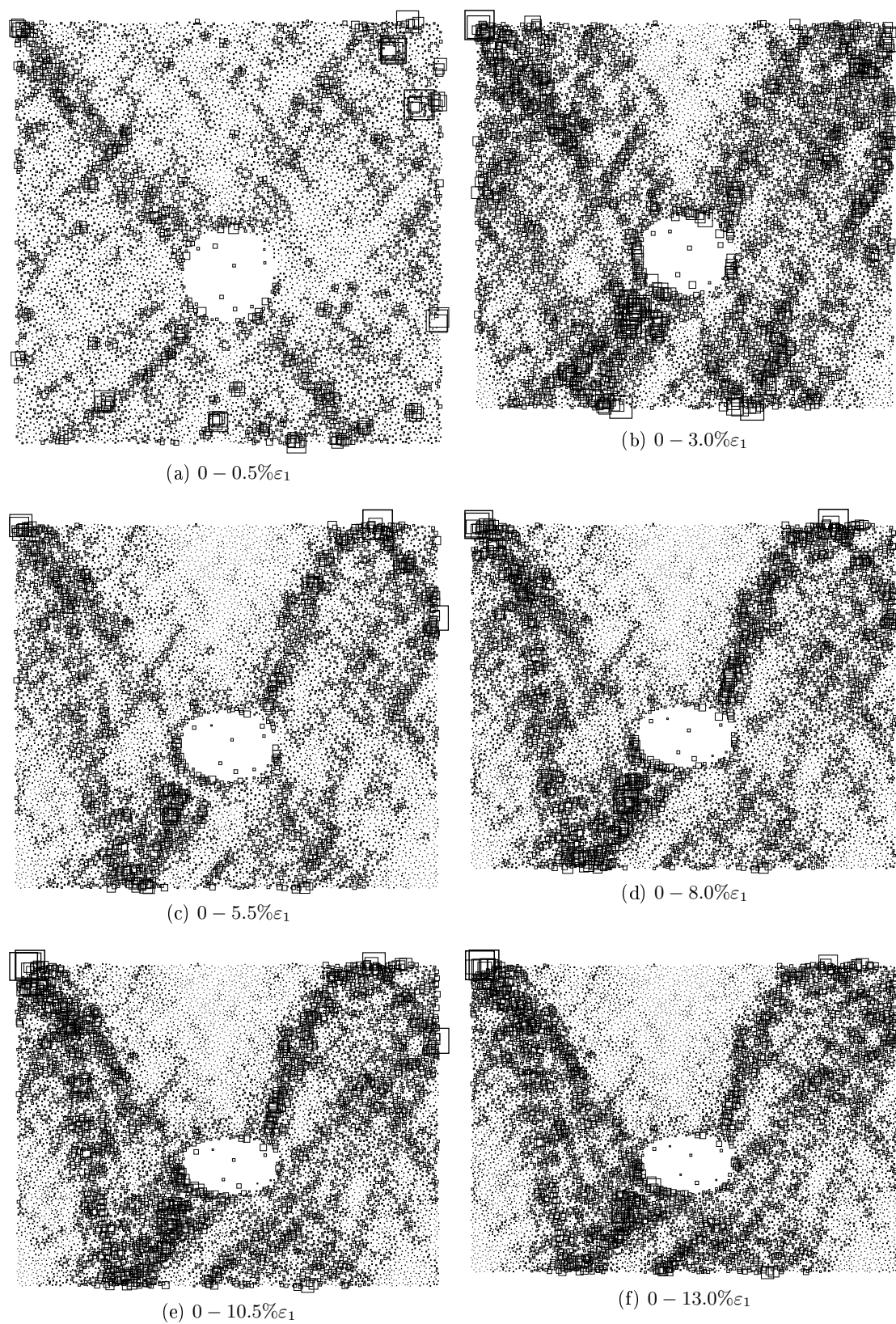


Figure E.6: Simulation of clumps $\alpha = 0.5$ without friction at the pipe boundary. Shear localisation maps

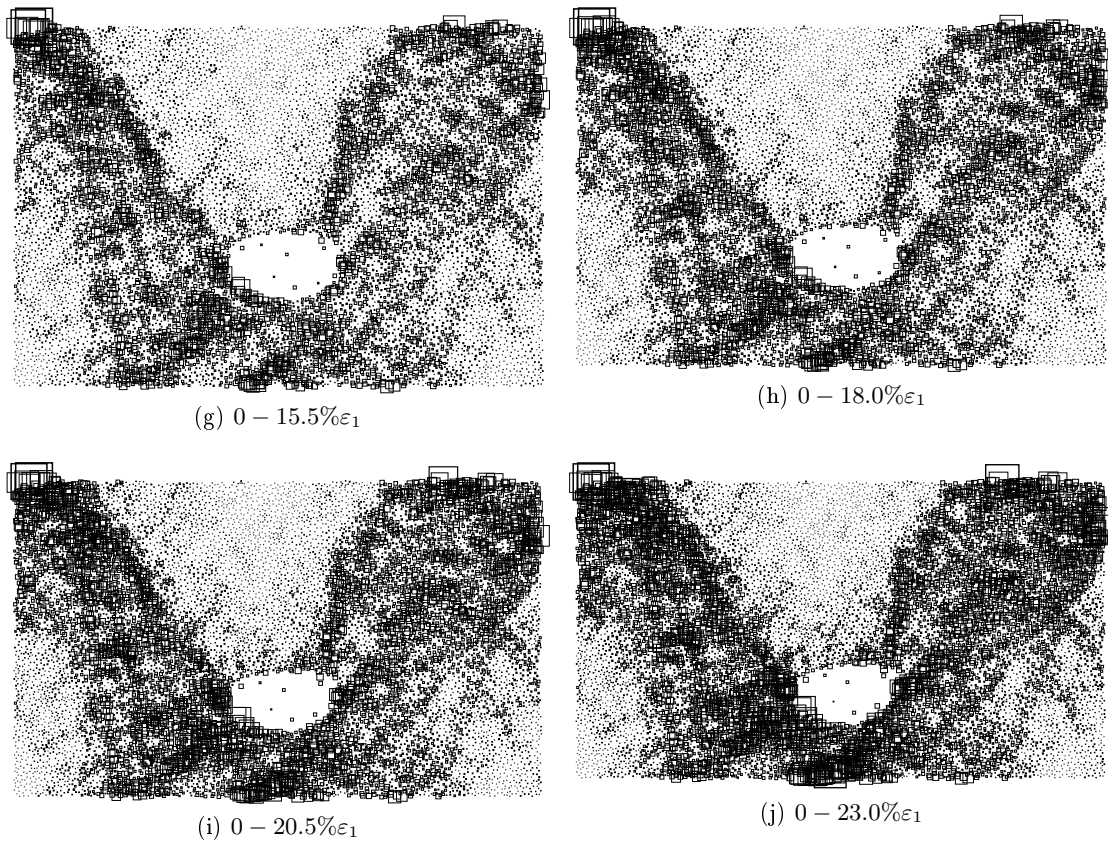


Figure E.6: *Shear localisation maps. Clumps $\alpha = 0.5$ without friction at the pipe boundary*

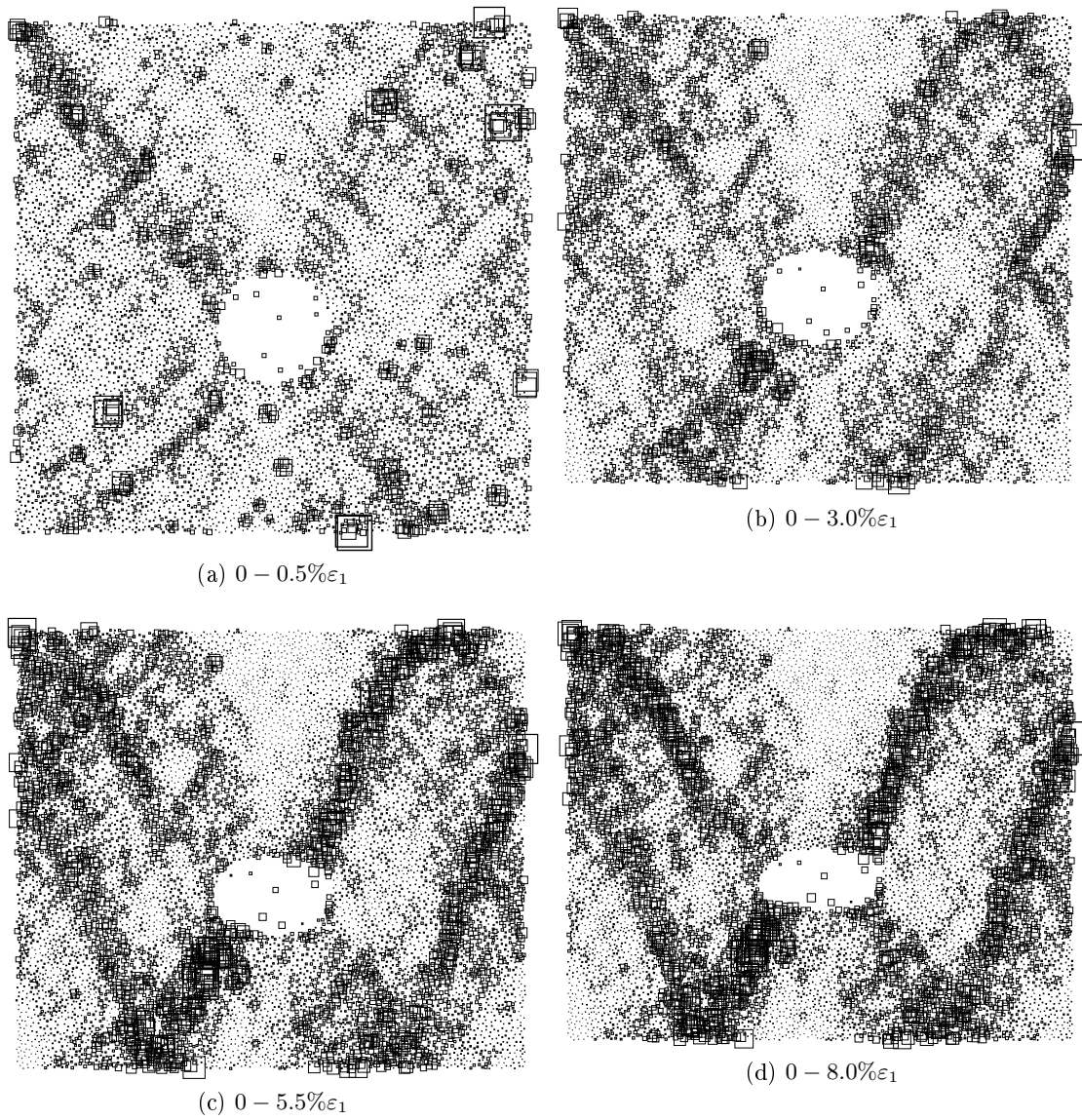


Figure E.7: Simulation of soft pipe $E = 20e7Pa$ with clumps $\alpha = 0.5$ and no friction at the pipe boundary. Shear localisation maps

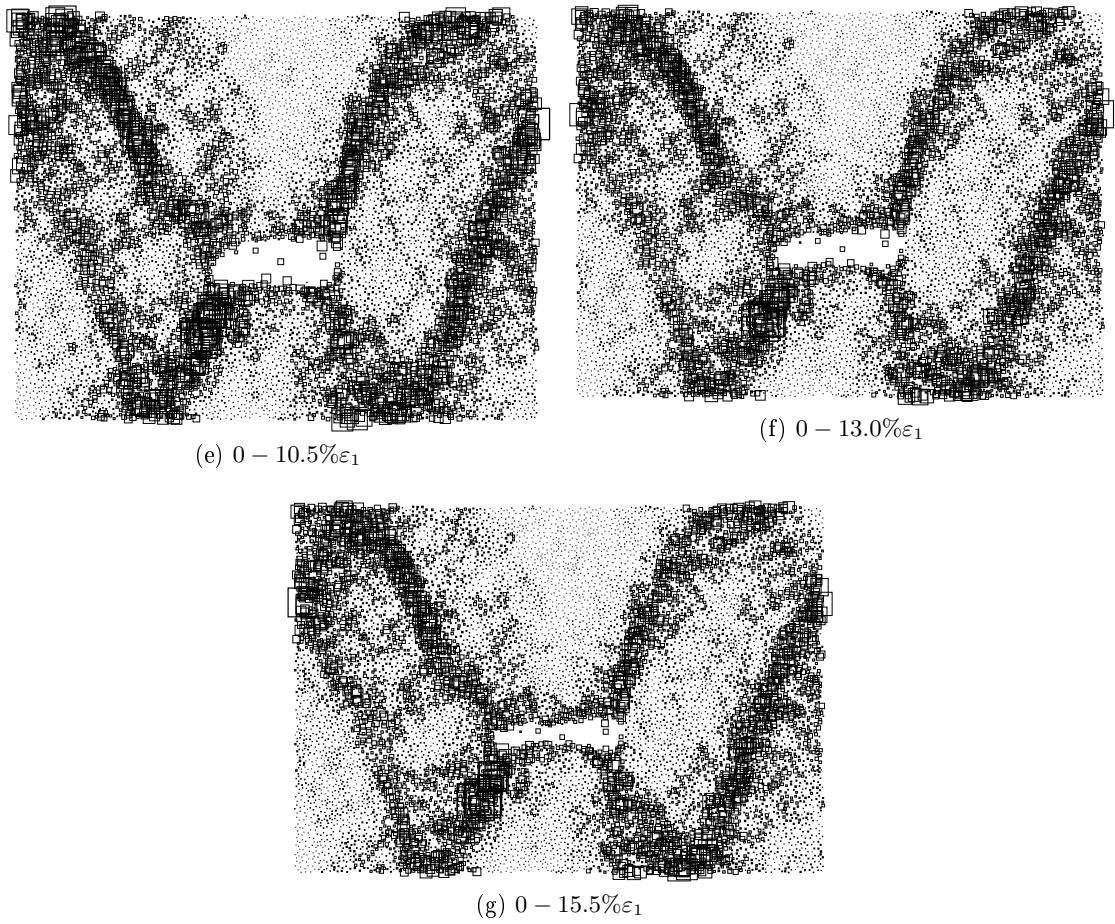


Figure E.7: Simulation of soft pipe $E = 20e7Pa$ with clumps $\alpha = 0.5$ and no friction at the pipe boundary. Shear localisation maps

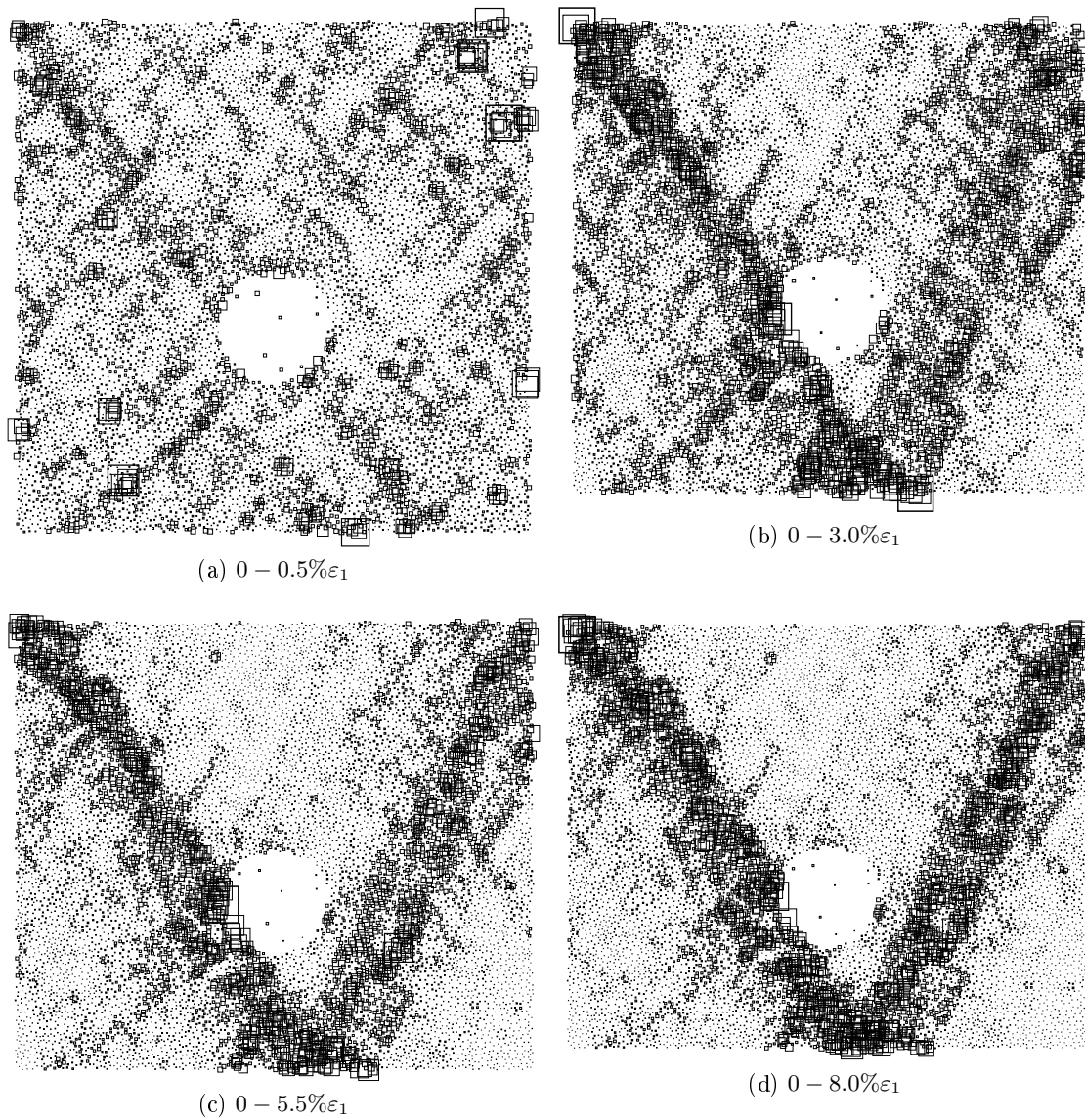


Figure E.8: *Simulation of stiff pipe $E = 20e9Pa$ with clumps $\alpha = 0.5$ and no friction at the pipe boundary. Shear localisation maps*

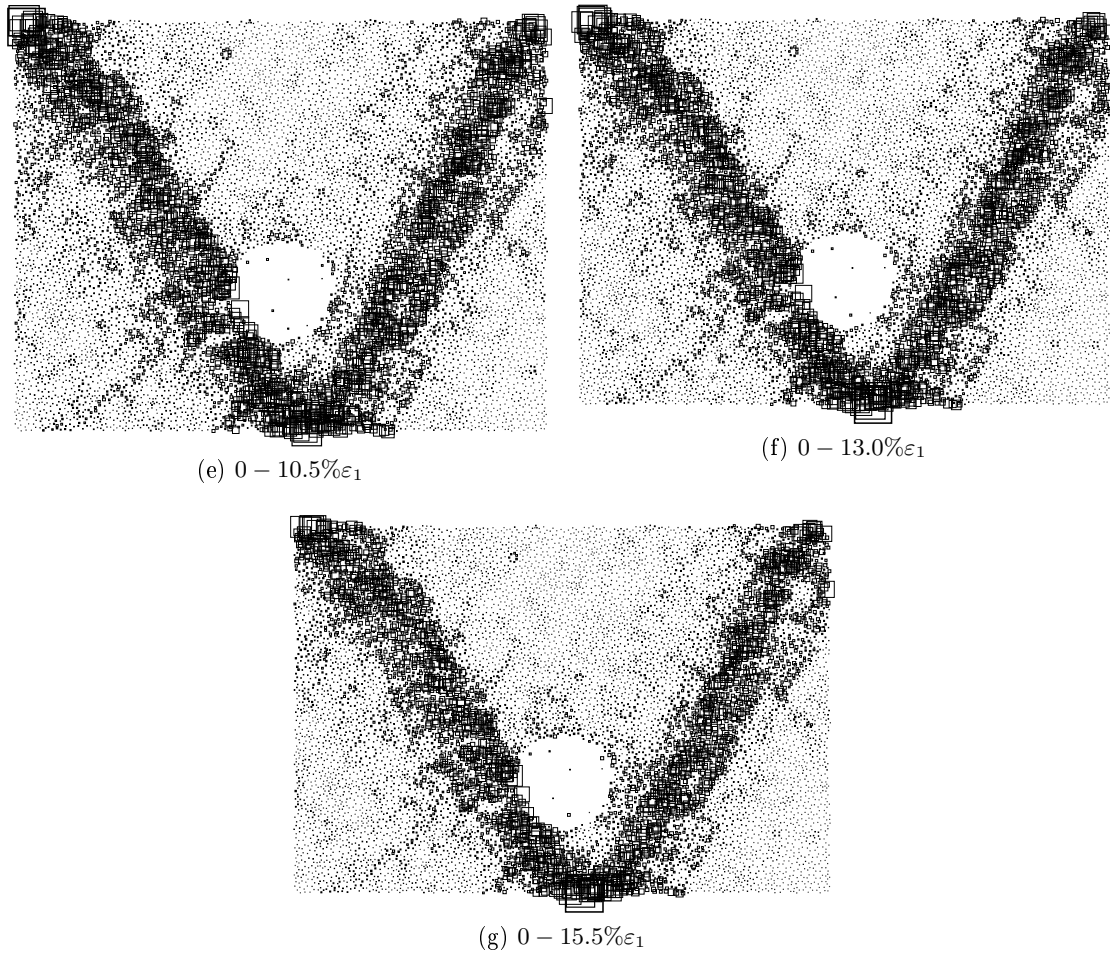


Figure E.8: Simulation of stiff pipe $E = 20e9Pa$ with clumps $\alpha = 0.5$ and no friction at the pipe boundary. Shear localisation maps

E.4 Stress Direction

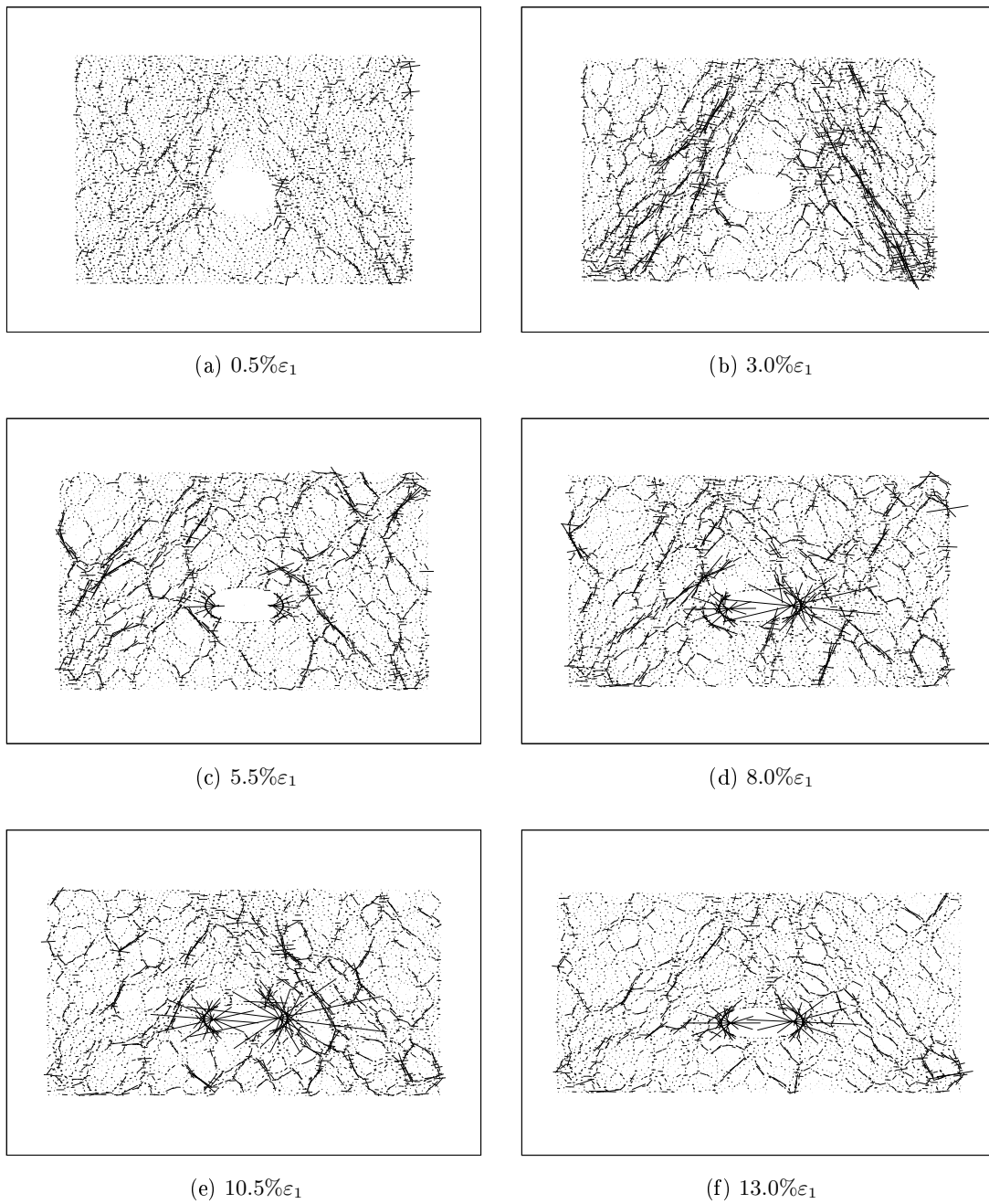


Figure E.9: Simulation of clumps $\alpha = 0.5$ without friction at the pipe boundary. Direction of particle stress

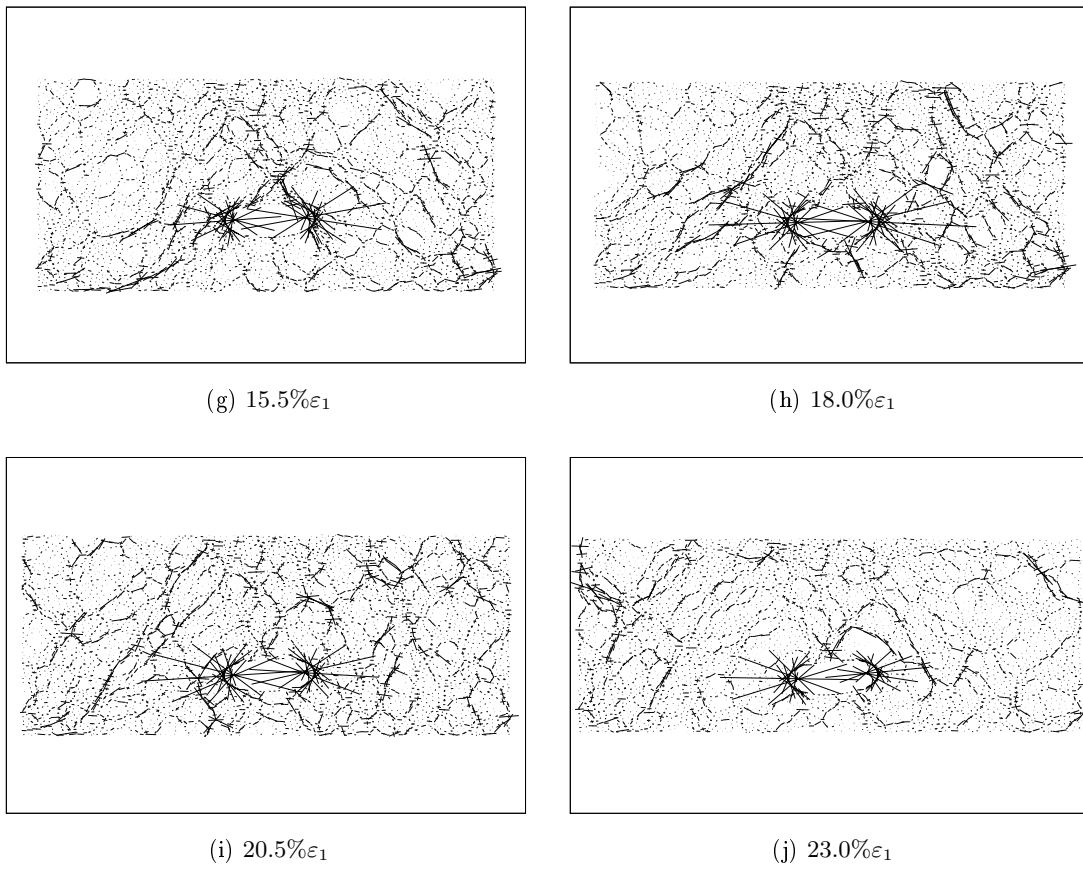


Figure E.9: *Direction of particle stress. Clumps $\alpha = 0.5$ without friction at the pipe boundary*

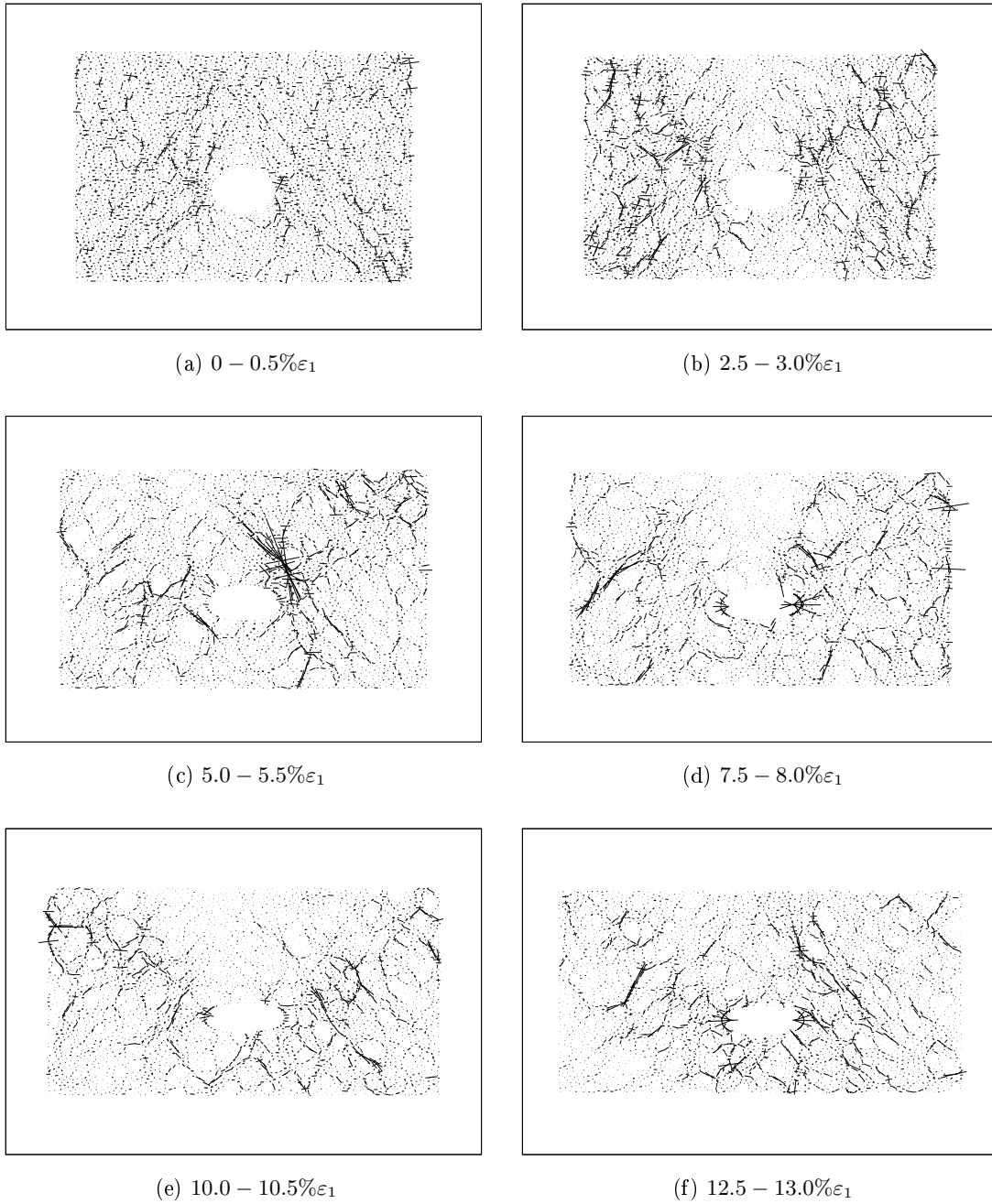


Figure E.10: *Simulation of clumps $\alpha = 0.5$ without friction at the pipe boundary. Direction of particle stress increment*

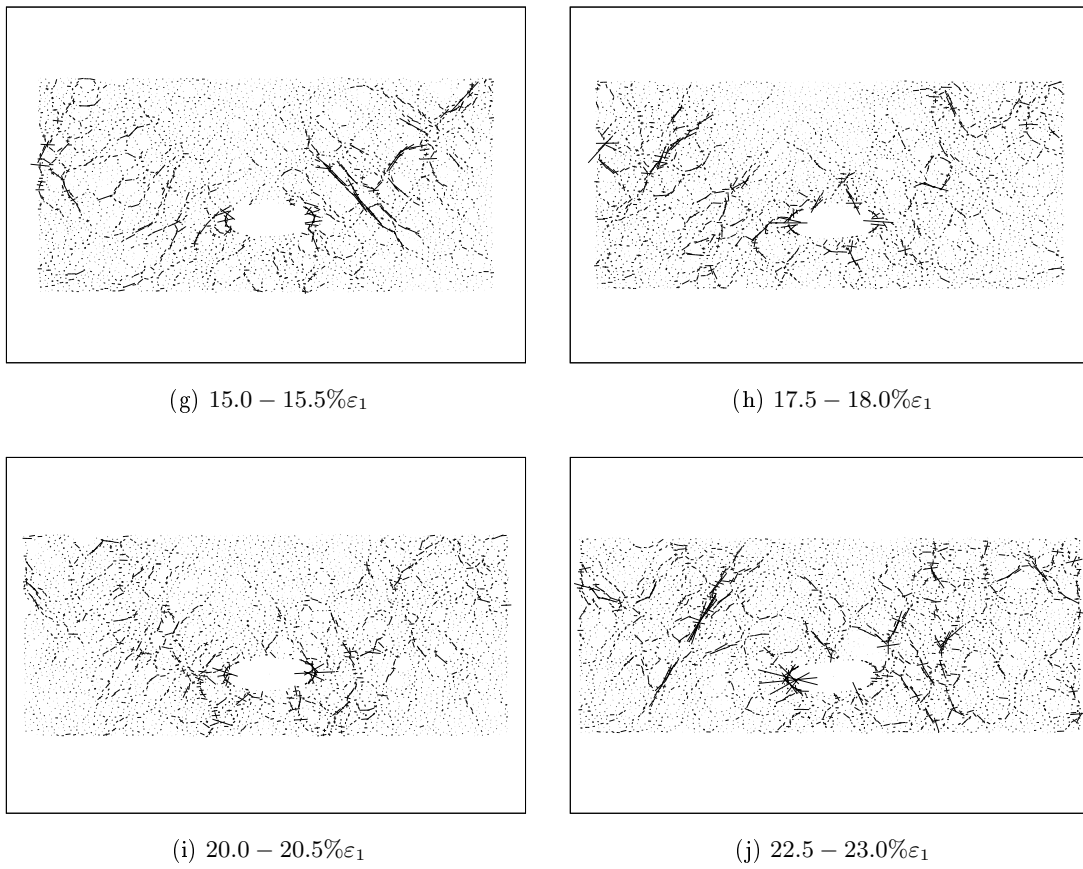


Figure E.10: *Direction of particle stress increment. Clumps $\alpha = 0.5$ without friction at the pipe boundary*

E.4. STRESS DIRECTION

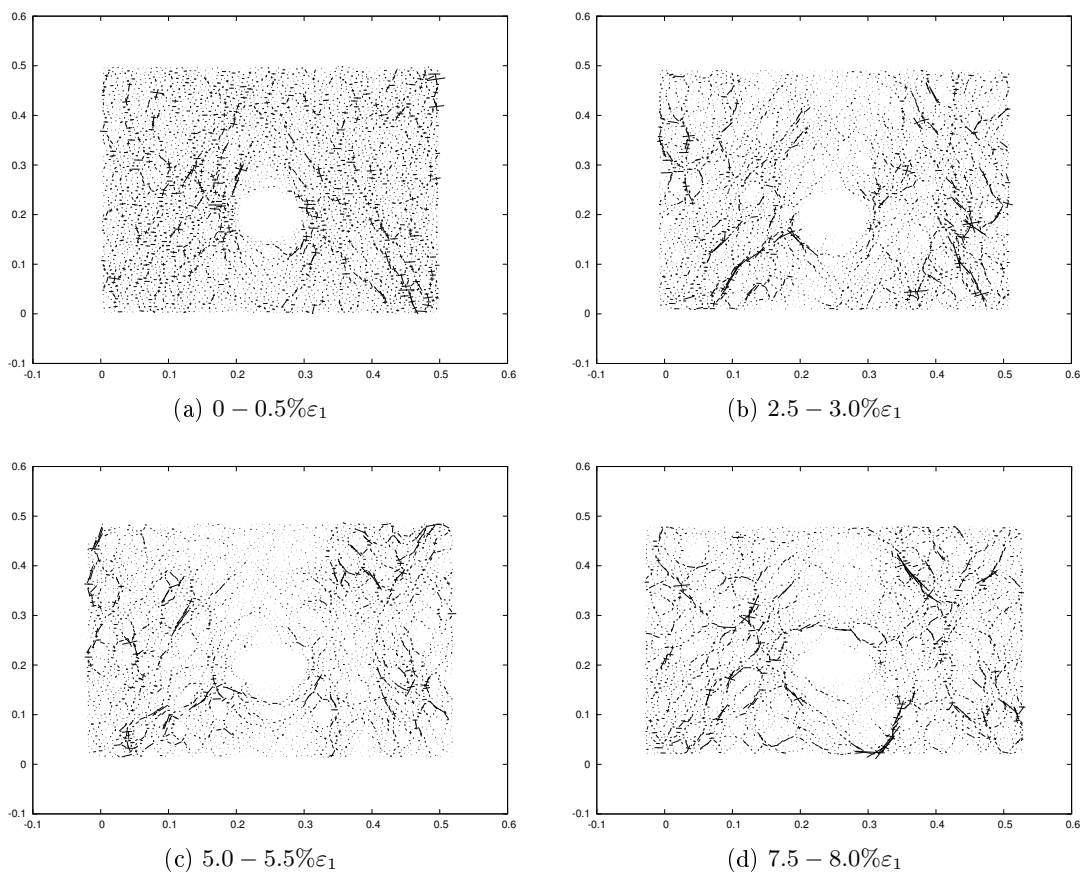


Figure E.11: Simulation of soft pipe $E = 20e7Pa$ with clumps $\alpha = 0.5$ and no friction at the pipe boundary. Direction of particle stress increment

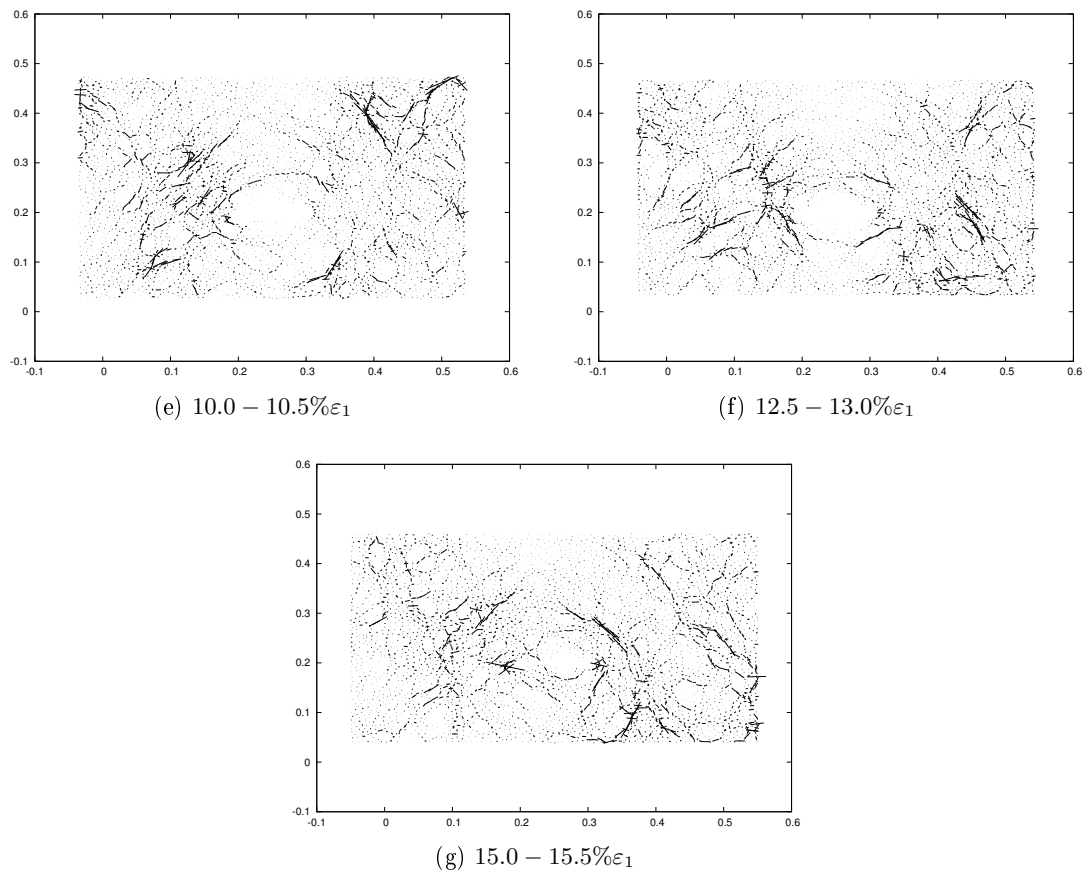


Figure E.11: Simulation of soft pipe $E = 20e7 Pa$ with clumps $\alpha = 0.5$ and no friction at the pipe boundary. Direction of particle stress increment

E.4. STRESS DIRECTION

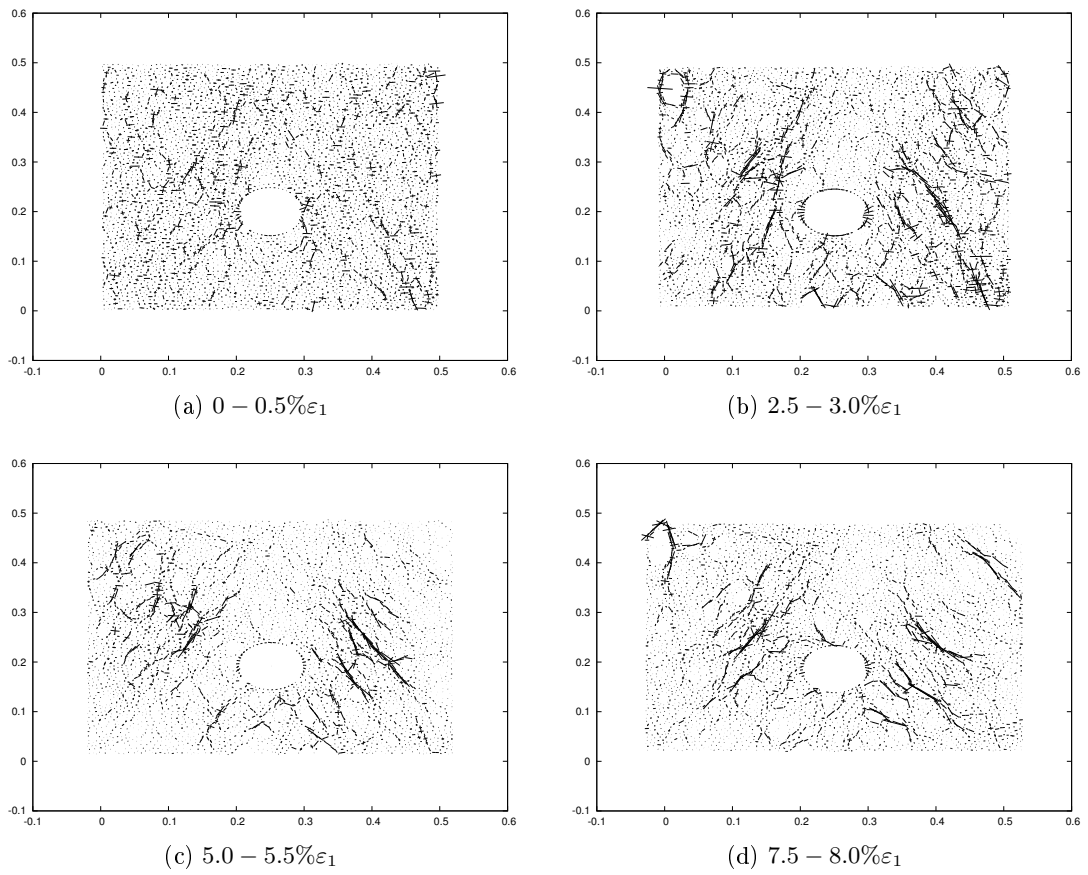


Figure E.12: Simulation of stiff pipe $E = 20e9Pa$ with clumps $\alpha = 0.5$ and no friction at the pipe boundary. Direction of particle stress increment

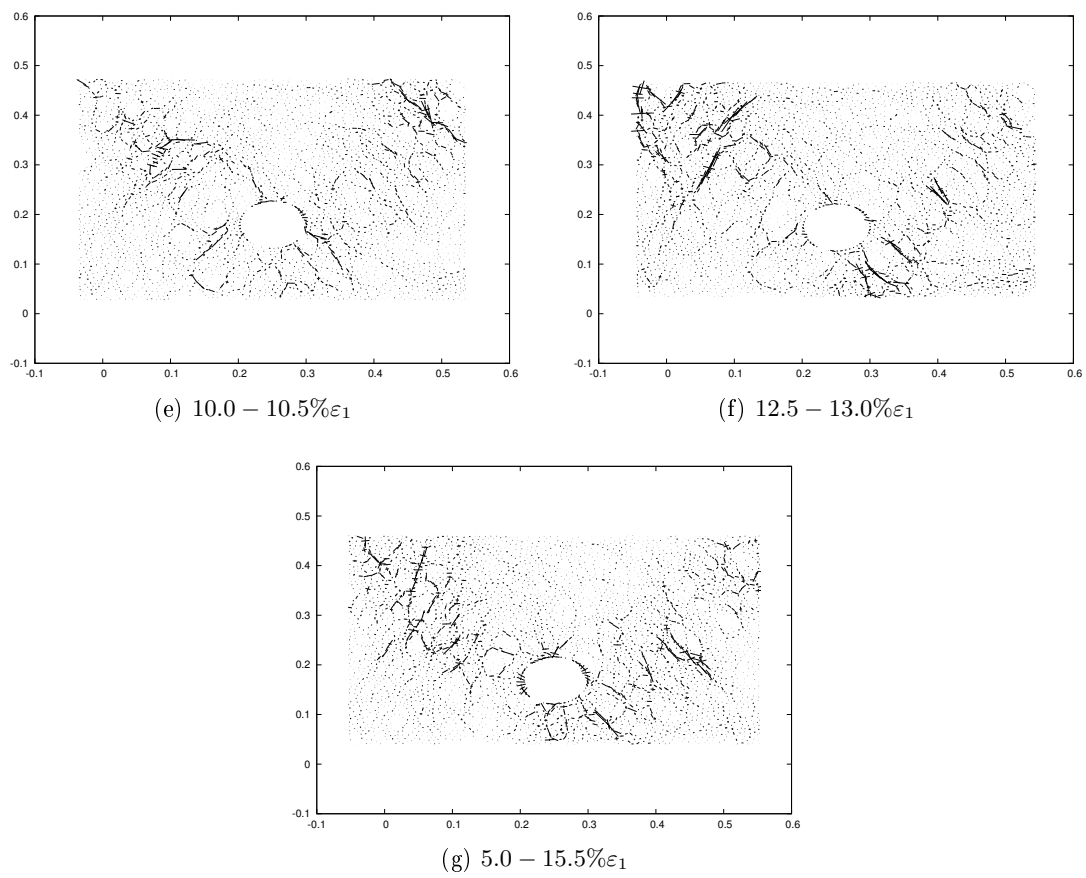


Figure E.12: Simulation of stiff pipe $E = 20e9Pa$ with clumps $\alpha = 0.5$ and no friction at the pipe boundary. Direction of particle stress increment

Bibliography

- Abe, S., Latham, S., and Mora, P. (2006). Dynamic rupture in a 3-d particle-based simulation of a rough planar fault. *Computational Earthquake Physics: Simulations, Analysis and Infrastructure, Part I*, pages 1881–1892.
- Allen, M. and Tildesley, D. (1994). *Computer simulation of liquids*. Oxford Science Publications.
- Alonso-Marroquin, F. (2008). Spheropolygons: A new method to simulate conservative and dissipative interactions between 2D complex-shaped rigid bodies. *EPL (Europhysics Letters)*, 83:14001.
- Alonso-Marroquin, F., Luding, S., Herrmann, H. J., and Vardoulakis, I. (2005). The role of the anisotropy in the elastoplastic response of a polygonal packing. *Physical Review E (Statistical, Nonlinear, and Soft Matter Physics)*, 71:051304.
- Alves, L. and Martins, P. (2009). Nosing of thin-walled pvc tubes into hollow spheres using a die. *The International Journal of Advanced Manufacturing Technology*, 44:26–37.
- Arockiasamy, M., Chaallal, O., and Limpeteepakarn, T. (2006). Full-scale field tests on flexible pipes under live load application. *Journal of performance of constructed facilities*, 20(1):21–27.
- Ashmawy, A., Sukumaran, B., and Hoang, V. (2003). Evaluating the influence of particle shape on liquefaction behavior using discrete element modeling. In *Proc. Offshore and Polar Engineering Conference*, pages 542–550.
- Åström, J., Herrmann, H., and Timonen, J. (2000). Granular packings and fault zones. *Physical review letters*, 84(4):638–641.
- Azéma, E., Radjaï, F., and Saussine, G. (2009). Quasistatic rheology, force transmission and fabric properties of a packing of irregular polyhedral particles. *Mechanics of Materials*, 41(6):729–741.
- Bareither, C., Edil, T., Benson, C., and Mickelson, D. (2008). Geological and physical factors affecting the friction angle of compacted sands. *Journal of geotechnical and geoenvironmental engineering*, 134:1476.
- Barrett, P. J. (1980). The shape of rock particles, a critical review. *Sedimentology*, 27(3):291–303.
- Blake, A. (1959). Deflection of a thick ring in diametric compression. *Journal of Applied Mechanics*, 26(2).
- Burns, R. and Sheppard, M. (2011). Collision detection and response. <http://www.metanetsoftware.com/technique/tutorialA.html>. Accessed: VIII 2012.

- Calvetti, F., Combe, G., and Lanier, J. (1997). Experimental micromechanical analysis of a 2D granular material: relation between structure evolution and loading path. *Mechanics of Cohesive-frictional materials*, 2:121–163.
- Calvetti, F., Di Prisco, C., and Nova, R. (2004). Experimental and numerical analysis of soil-pipe interaction. *Journal of geotechnical and geoenvironmental engineering*, 130(12):1292–1299.
- Calvetti, F., Viggiani, G., and Tamagnini, C. (2003). A numerical investigation of the incremental behavior of granular soils. *Rivista italiana di geotecnica*, 37(3):11–29.
- CEGEO, Saint-Cyr, B., Szarf, K., Voivret, C., Azéma, E., Richefeu, V., Delenne, J.-Y., Combe, G., Nouguier-Lehon, C., Villard, P., Sornay, P., Chaze, M., and Radjaï, F. (2012). Particle shape dependence in granular media. *EPL (Europhysics Letters)*, 98(4):44008.
- Charalampidou, E.-M., Combe, G., Viggiani, G., and Lanier, J. (2009). Mechanical behavior of mixtures of circular and rectangular 2D particles. In *Powders and Grains 2009*, pages 821–824.
- Cheng, Y., Bolton, M., and Nakata, Y. (2005). Grain crushing and critical states observed in dem simulations. *P&G05*, 2:1393–1397.
- Cho, G., Dodds, J., and Santamarina, J. (2006). Particle shape effects on packing density, stiffness, and strength: natural and crushed sands. *Journal of Geotechnical and Geoenvironmental Engineering*, 132:591.
- Christensen, N. (1967). Rigid pipes in symmetrical and unsymmetrical trenches. *Geoteknisk Institut Bulletin*, 24.
- Cleary, P. and Sawley, M. (2002). Dem modelling of industrial granular flows: 3d case studies and the effect of particle shape on hopper discharge. *Applied Mathematical Modelling*, 26(2):89–111.
- Coulomb, C. (1821). *Théorie des machines simples: en ayant égard au frottement de leurs parties et à la roideur des cordages*. Bachelier.
- Cundall, P. (1971). A computer model for simulating progressive large scale movements of blocky rock systems. *Proceedings of the symposium of the international society of rock mechanics*, 1.
- Cundall, P. A. and Strack, O. D. L. (1979). A discrete numerical model for granular assemblies. *Géotechnique*, 29(1):47–65.
- Das, N. (2007). *Modeling three-dimensional shape of sand grains using Discrete Element Method*. Doctoral thesis, University of South Florida, Tampa, USA.
- Delaney, G. and Cleary, P. (2010). The packing properties of superellipsoids. *EPL (Europhysics Letters)*, 89:34002.
- Desrues, J. (1984). *La localisation de la déformation dans les matériaux granulaires*. Doctoral thesis, INP-USM Grenoble, Grenoble, France.
- Desrues, J. and Chambon, R. (2002). Shear band analysis and shear moduli calibration. *International Journal of Solids and Structures*, 39(13 - 14):3757 – 3776.

- Desrues, J. and Viggiani, G. (2004). Strain localization in sand: an overview of the experimental results obtained in grenoble using stereophotogrammetry. *International Journal for Numerical and Analytical Methods in Geomechanics*, 28(4):279–321.
- di Prisco, C. and Galli, A. (2006). Soil-pipe interaction under monotonic and cyclic loads: experimental and numerical modelling. In *Proceedings of the First Euro Mediterranean Symposium in Advances on Geomaterials and Structures. Hammamet, Tunisia*, pages 3–5.
- Doanh, T., Ibraim, E., and Matiotti, R. (1997). Undrained instability of very loose hostun sand in triaxial compression and extension. part 1: experimental observations. *Mechanics of Cohesive-frictional Materials*, 2(1):47–70.
- Emeriault, F. and Claquin, C. (2004). Statistical homogenization for assemblies of elliptical grains: effect of the aspect ratio and particle orientation. *International journal of solids and structures*, 41(21):5837–5849.
- Estrada, N., Azéma, E., Radjaï, F., and Taboada, A. (2011). Identification of rolling resistance as a shape parameter in sheared granular media. *Physical Review E*, 84(1):011306.
- Ganter, M. A. and Isarankura, B. P. (1993). Dynamic collision detection using space partitioning. *Journal of Mechanical Design*, 115(1):150–155.
- Gilabert, F. A., Roux, J.-N., and Castellanos, A. (2007). Computer simulation of model cohesive powders: Influence of assembling procedure and contact laws on low consolidation states. *Phys. Rev. E*, 75:011303.
- Gilbert, E., Johnson, D., and Keerthi, S. (1988). A fast procedure for computing the distance between complex objects in three-dimensional space. *Robotics and Automation, IEEE Journal of*, 4(2):193 –203.
- Gottschalk, S., Lin, M., and Manocha, D. (1996). OBBTree: a hierarchical structure for rapid interference detection. In *Proceedings of the 23rd annual conference on Computer graphics and interactive techniques*, pages 171–180. ACM.
- Haile, J. (1992). *Molecular Dynamics Simulation, Elementary Methods*. Wiley professional paperback series. John Wiley & Sons. New York. US.
- Hall, S., Muir Wood, D., Ibraim, E., and Viggiani, G. (2010). Localised deformation patterning in 2D granular materials revealed by digital image correlation. *Granular Matter*, 12:1–14. 10.1007/s10035-009-0155-1.
- Hartley, J. and Duncan, J. (1987). E' and its variation with depth. *Journal of transportation engineering*, 113(5):538–553.
- Iron, A. and Institute, S. (1994). *Handbook of steel drainage & highway construction products*. American Iron and Steel Institute.
- Iwashita, K. and Oda, M. (2000). Micro-deformation mechanism of shear banding process based on modified distinct element method. *Powder Technology*, 109(1-3):192 – 205.
- Jean, M. and Moreau, J. (1992). Unilaterality and dry friction in the dynamics of rigid body collections. In *Proceedings of Contact Mechanics International Symposium*, pages 31–48. Presses Polytechniques et Universitaires Romandes.

- Jensen, R., Bosscher, P., Plesha, M., and Edil, T. (1999). Dem simulation of granular media–structure interface: effects of surface roughness and particle shape. *International Journal for Numerical and Analytical Methods in Geomechanics*, 23(6):531–547.
- Joer, H. (1991). $1\gamma 2\varepsilon$: *une nouvelle machine de cisaillement pour l'étude du comportement des milieux granulaires*. Doctoral thesis, Université J. Fourier, Grenoble, France.
- Joer, H., Lanier, J., Desrues, J., and Flavigny, E. (1992). $1\gamma 2\varepsilon$: A new shear apparatus to study the behavior of granular materials. *Geotechnical Testing Journal*, 15.
- Krizek, R. (1971). *Structural Analysis and Design of Pipe Culverts*. Number no. 116 in Report (National Cooperative Highway Research Program). Highway Research Board, National Research Council.
- Krumbein, W. and Sloss, L. (1951). *Stratigraphy and sedimentation*. A Series of books in geology. W. H. Freeman.
- Kruyt, N. and Rothenburg, L. (2004). Micromechanical study of macroscopic friction and dissipation in idealised granular materials: the effect of interparticle friction. In *Proceeding of the 21st International Conference on Theoretical and Applied Mechanics*.
- Kunecki, B. (2006). Zachowanie się ortotropowych powłok walcowych w ośrodku gruntowym pod statycznym i dynamicznym obciążeniem zewnętrznym.
- Lanier, J. and Combe, G. (1995). An experimental study of deformation in 2D-granular media. In Dembicki, E., Auriault, J.-L., and Sikora, Z., editors, *Proceeding of the International Workshop on Homogenisation, Theory of migration and granular bodies*, pages 143–149, Gdańsk.
- Le Ngoc, L. (2011). Experimental determination of inter-granular forces using 2D digital image correlation. Master thesis, UJF, Grenoble.
- Lirer, S., Flora, A., Lanier, J., and Viggiani, G. (2005). Analisi sperimentale dell'influenza della forma delle particelle sul comportamento di un materiale granulare 2D. In *Incontro annuale ricercatori di geotecnica (IARG)*.
- Maclaurin, C. (1774). *A Treatise of Fluxions*. Edinburgh.
- Markauskas, D. and Kačianauskas, R. (2011). Investigation of rice grain flow by multi-sphere particle model with rolling resistance. *Granular Matter*, 13(2):143–148.
- Marston, A. (1930). *The theory of external loads on closed conduits in the light of the latest experiments*. Bulletin (Iowa Engineering Experiment Station). Iowa State College.
- Matsushima, T., Katagiri, J., Uesugi, K., Tsuchiyama, A., and Nakano, T. (2009). 3d shape characterization and image-based dem simulation of the lunar soil simulant fjs-1. *Journal of Aerospace Engineering*, 22:15.
- Matsushima, T. and Saomoto, H. (2002). Discrete element modeling for irregularly-shaped sand grains. In Mestat, P., editor, *5e Conférence Européenne Méthodes Numériques en Géotechnique*. LCPC.
- Matuttis, H., Luding, S., and Herrmann, H. (2000). Discrete element simulations of dense packings and heaps made of spherical and non-spherical particles. *Powder Technology*, 109(1–3):278 – 292.

- McAfee, R. and Valsangkar, A. (2008). Field performance, centrifuge testing, and numerical modelling of an induced trench installation. *Canadian Geotechnical Journal*, 45(1):85–101.
- McDowell, G., Li, H., and Lowndes, I. (2011). The importance of particle shape in discrete-element modelling of particle flow in a chute. *Géotechnique Letters*, 1(3):59–64.
- Moser, A. (2001). *Buried Pipe Design, 2nd Edition*. McGraw-Hill Professional Engineering, McGraw-Hill.
- Muir Wood, D. and Maeda, K. (2008). Changing grading of soil: effect on critical states. *Acta Geotechnica*, 3:3–14.
- Nouguier-Lehon, C., Cambou, B., and Vincens, E. (2003). Influence of particle shape and angularity on the behaviour of granular materials: a numerical analysis. *International journal for numerical and analytical methods in geomechanics*, 27(14):1207–1226.
- Orford, J. and Whalley, W. (1983). The use of the fractal dimension to quantify the morphology of irregular-shaped particles. *Sedimentology*, 30(5):655–668.
- PFC^{2D} Manual (2004). *PFC^{2D} Particle Flow Code in 2 Dimensions — Theory and Background, Version 3.1*. Itasca Consulting Group, Inc.
- Plassiard, J.-P. (2007). *Modélisation par la méthode des éléments discrets d’impacts de blocs rocheux sur structures de protection type merlons*. Doctoral thesis, UJF, Grenoble, France.
- Potapov, A. and Campbell, C. (1998). A fast model for the simulation of non-round particles. *Granular Matter*, 1(1):9–14.
- Radjai, F. and Dubois, F., editors (2011). *Discrete-element Modeling of Granular Materials*. ISTE; Wiley. ISBN 18-4821-260-7.
- Radjai, F., Jean, M., Moreau, J., and Roux, S. (1996). Force distributions in dense two-dimensional granular systems. *Physical review letters*, 77(2):274–277.
- Rothenburg, L. and Bathurst, R. (1992). Micromechanical features of granular assemblies with planar elliptical particles. *Geotechnique*, 42(1):79–95.
- Roux, J.-N. and Chevoir, F. (2005). Discrete numerical simulation and the mechanical behavior of granular materials. *Bulletin des Laboratoires des Ponts et Chaussées*, 254:109–138.
- Salot, C., Gotteland, P., and Villard, P. (2009). Influence of relative density on granular materials behavior: Dem simulations of triaxial tests. *Granular Matter*, 11:221–236.
- Santamarina, J. and Cho, G. (2004). Soil behaviour: The role of particle shape. In *Proceedings of Skempton Conference, London*.
- Saussine, G., Cholet, C., Gautier, P.-E., Dubois, F., Bohatier, C., and Moreau, J. (2006). Modelling ballast behaviour under dynamic loading. part 1: A 2D polygonal discrete element method approach. *Computer Methods in Applied Mechanics and Engineering*, 195:2841–2859.
- Sazzad, M. and Suzuki, K. (2010). Micromechanical behavior of granular materials with inherent anisotropy under cyclic loading using 2D dem. *Granular Matter*, 12:597–605.
- Schneebeli, G. (1956). Une analogie mécanique pour les terres sans cohésion. *Comptes rendus de l’académie des sciences*, 243, No. 1:125–126.

- Schneider, P. J. and Eberly, D. (2002). *Geometric Tools for Computer Graphics*. Elsevier Science Inc., New York, NY, USA.
- Sibille, L. and Froiio, F. (2007). A numerical photogrammetry technique for measuring microscale kinematics and fabric in schneebeli materials. *Granular Matter*, 9:183–193.
- Sornette, A., Davy, P., and Sornette, D. (1993). Fault growth in brittle-ductile experiments and the mechanics of continental collisions. *Journal of geophysical research*, 98:12111–12140.
- Spangler, M. (1933). *The supporting strength of rigid pipe culverts*. Iowa State College.
- Spangler, M. and Shafer, G. (1941). The structural design of flexible pipe culverts. In *Highway Research Board Proceedings*.
- Suiker, A. S. J. and Fleck, N. A. (2004). Frictional collapse of granular assemblies. *Journal of Applied Mechanics*, 71(3):350–358.
- Sutton, M. A., Ortu, J.-J., and Schreier, H. (2009). *Image Correlation for Shape, Motion and Deformation Measurements: Basic Concepts, Theory and Applications*. Springer Publishing Company, Incorporated, 1st edition.
- Szarf, K., Combe, G., and Villard, P. (2009a). Influence of grain shape on the mechanical behaviour of granular materials. In *Colloque "Science et Technologie des Poudres et Matériaux Frittés 2009" (STPMF)*, Montpellier, France. ISBN 9782952814010.
- Szarf, K., Combe, G., and Villard, P. (2009b). Influence of the grains shape on the mechanical behavior of granular materials. In *6th Int. Conf. on Micromechanics of Granular Media "Powders and Grains 2009"*, Golden, CO, USA.
- Szarf, K., Combe, G., and Villard, P. (2011). Polygons vs. clumps of discs: A numerical study of the influence of grain shape on the mechanical behaviour of granular materials. *Powder Technology*, 208(2):279 – 288. Special Issue: Papers presented to the Symposium STPMF 2009, Science and Technology of Powders and Sintered Materials.
- Tengattini, A. (2010). Experimental study of turbulent-like transitions in quasi-static flow of granular media : velocity field analysis from particle tracking with the $1\gamma 2\varepsilon$ apparatus. Master thesis, UJF, Grenoble.
- Terzaghi, K. (1943). *Theoretical soil mechanics*. J. Wiley and Sons, inc.
- Tien, H.-J. (1996). A literature study of the arching effect. Master thesis, Massachusetts Institute of Technology, Massachusetts.
- Ting, J. (1992). A robust algorithm for ellipse-based discrete element modelling of granular materials. *Computers and Geotechnics*, 13(3):175–186.
- Titov, W., editor (1984). *PVC technology*. Springer. ISBN 978-0-85334-249-6.
- Tordesillas, A. (2007). Force chain buckling, unjamming transitions and shear banding in dense granular assemblies. *Philosophical Magazine*, 87(32):4987–5016.
- Viggiani, G. and Hall, S. (2008). Full-field measurements, a new tool for laboratory experimental geomechanics. In *Fourth Symposium on Deformation Characteristics of Geomaterials*.
- Voivret, C. (2008). *Texture et comportement des matériaux granulaires à grande polydispersité*. Doctoral thesis, Université Montpellier 2, Montpellier, France.

- Wadell, H. (1932). Volume, Shape, and Roundness of Rock Particles. *Journal of Geology*, 40:443–451.
- Walker, D. M., Tordesillas, A., Einav, I., and Small, M. (2011). Complex networks in confined comminution. *Phys. Rev. E*, 84:021301.
- Warman, D., Hart, J., and Francini, R. (2009). Development of a pipeline surface loading screening process & assessment of surface load dispersing methods. Technical report, Canadian Energy Pipeline Association.
- Watkins, R., Reeve, R., and of Agricultural Engineers. Meeting, A. S. (1980). *Structural Performance of Buried Corrugated Polyethylene Tubing*. American Society of Agricultural Engineers.
- Watkins, R. and Spangler, M. (1958). Some characteristics of the modulus of passive resistance of soil: A study in similitude. In *Highway Research Board Proceedings*.
- Weber, J. (1966). Recherches concernant les contraintes intergranulaires dans les milieux pulvérulents. *Bulletin de Liaison des Ponts et Chaussées*, 20:1–20.
- Willardson, L. and Watkins, R. (2002). Minimum-risk bedding for flexible drain pipes. *Journal of irrigation and drainage engineering*, 128(2):74–77.
- Wiłun, Z. (2009). *Zarys geotechniki: podręcznik akademicki*. Wydawnictwa Komunikacji i Łączności WKL.
- Youd, T. (1973). Factors controlling maximum and minimum densities of sands. *Evaluation of Relative Density and Its Role in Geotechnical Projects Involving Cohesionless Soils*, page 98.
- Zhou, Y., Xu, B., Yu, A., and Zulli, P. (2001). Numerical investigation of the angle of repose of monosized spheres. *Physical Review E*, 64(2):021301.